Hydrodynamics of Stirred Tank using Radioactive Particle Tracking (RPT) Technique and CFD

Submitted in partial fulfilment of the requirements for the award of the degree of

DOCTOR OF PHILOSOPHY

in

CHEMICAL ENGINEERING

by

PATIL HARSHAL SOMNATH
Roll No: 715068

Under the Supervision of

Dr. A VENU VINOD
Professor
Department of Chemical Engineering

and

Dr. AJEY KUMAR PATEL
Assistant Professor
Department of Civil Engineering

DEPARTMENT OF CHEMICAL ENGINEERING
NATIONAL INSTITUTE OF TECHNOLOGY WARANGAL
TELANGANA – 506004, INDIA.

September 2020

NATIONAL INSTITUTE OF TECHNOLOGY

Warangal – 506004, Telangana, INDIA.

CERTIFICATE

This is to certify that the thesis entitled **"Hydrodynamics of Stirred Tank using Radioactive Particle Tracking (RPT) Technique and CFD"** being submitted by Mr. **Patil Harshal Somnath** for the award of the degree of Doctor of Philosophy (Ph.D) in Chemical Engineering to the National Institute of Technology, Warangal, India is a record of the bonafide research work carried out by him under our supervision. The thesis has fulfilled the requirements according to the regulations of this Institute and in our opinion has reached the standards for submission. The results embodied in the thesis have not been submitted to any other University or Institute for the award of any degree or diploma.

Date: 01/09/2020

Dr. A. Venu Vinod
Thesis Supervisor
Professor
Department of Chemical Engineering
National Institute of Technology, Warangal,
India.

Dr. Ajey Kumar Patel
Thesis Supervisor
Assistant Professor
Department of Civil Engineering
National Institute of Technology, Warangal,
India.

DECLARATION

This is to certify that the work presented in the thesis entitled **"Hydrodynamics of Stirred Tank using Radioactive Particle Tracking (RPT) Technique and CFD"** is a bonafide work done by me under the supervision of Dr. A. Venu Vinod and Dr. Ajey Kumar Patel and it was not submitted elsewhere for award of any degree.

I declare that this written submission represents my ideas in my own words and where others' ideas or words have been included, I have adequately cited and referenced the original source. I also declare that I have adhered to all principles of academic honesty and integrity and have not misrepresented or fabricated or falsified any idea/data/fact/source in my submission.

I understand that any violation of the above will be a cause for disciplinary action by the Institute and can also evoke penal action from the sources which have thus not been properly cited or from whom proper permission has not been taken when needed.

PATIL HARSHAL SOMNATH

Roll No.715068

ACKNOWLEDGMENTS

First and foremost I would like to thank my supervisors ***Prof. A. Venu Vinod*** and ***Dr. Ajey Kumar Patel*** for their disciplined, patient guidance, timely appreciation, extraordinary support enormous enlightening discussion with constructive criticism, inspiring, enticing pieces of advises and sustain inputs during the research work and preparation of thesis. Their guidance is a great learning experience to me throughout my stay at National Institute of Technology Warangal, by strengthening me all the time. I owe a lot to them for their positive encouragement and guidance.

I wish to sincerely thank university authorities, ***Prof. N.V. Ramana Rao,*** Director, National Institute of Technology, Warangal and other officials who gave me an opportunity to carry out research work.

I also sincerely thank ***Prof. Shirish H. Sonawane,*** Head, Chemical Engineering Department, National Institute of Technology, Warangal for his continuous support towards carrying out research work.

I wish to express my sincere thanks and gratitude to my doctoral scrutiny committee (DSC) members ***Dr. S. Srinath, Dr. S. Vidya Sagar,*** Department of Chemical Engineering and ***Prof. K. V. Jayakumar,*** Department of Civil Engineering, National Institute of Technology Warangal, for their kind help, encouragement and valuable suggestions for successful completion of research work.

I would like to extend my thanks to all the faculty members in Department of Chemical Engineering for their valuable suggestions and encouragement.

I take this opportunity to sincerely acknowledge the ***Board of Research in Nuclear Science (BRNS)*** and ***Bhabha Atomic Research Center (BARC), Government of India*** for providing the financial assistance and radioactive source to conduct research work at NITW.

I would like to express my sincere thanks to ***Dr. Harish J. Pant, Scientist, Bhabha Atomic Research Center (BARC), Government of India*** for helping in provision of a radioactive source to conduct research work at NITW. Also, I would like to thanks ***Dr. Rajesh Kumar Upadhyay, Associate Professor, IIT BHU,*** for providing training on RPT data processing.

I am extremely thankful to Marathi family in NIT Warangal ***Dr. Vinay Rangari, Dr. Uday Bagale, Dr. Prashant Suryawanshi, Dr. Abhay Lingayat, Mr. Gajanan Suryawanshi, Mr.***

Roshan Bodile, Mr. Ganesh Gawale, Mr. Upendra Maurya, Mr. Swapnil Adsul, Mr. Avinash Borgaonkar, Mr. Vikas Hakke, Mr. Kishor Ingle, Mr. Sandip Khobragade, Mrs. Vividha Landage, Mrs. Shital Potdar and my dear friends ***Mr. Devrajan K., Mr. Yashwant Gowda, Mr. Abdullah Sheikh, Mr. Sukhesh,*** for their companionship, many fruitful conversations, help, and quality time spent together throughout my stay at NIT Warangal.

Last but not least, I would like to express my deepest thanks to family members ***Dr. Somnath Patil*** (Father), ***Surekha*** (Mother), ***Yogesh*** (Brother) and ***Nayana*** (Sister in law) for their understanding, patience, continuous support and heartiest love.

PATIL HARSHAL SOMNATH

Abstract

Stirred tank reactors are widely used in various chemical process and its allied industries to enhance the rate of heat and mass transfer. The rotating impellers in stirred tanks generate the highly turbulent and complex three dimensional flow structure. In present work, radiation based non-invasive Radioactive Particle Tracking (RPT) technique was used and a steady state computational fluid dynamics (CFD) model was developed to study complex flow structures in a stirred tank agitated by Rushton turbine (RT).

In the calibration measurement of RPT technique, the effect of fluid motion on radiation intensity was addressed by analysis of variance (ANOVA) technique. Through the ANOVA analysis it was found that fluid motion has no effect on radiation intensity. RPT correctly shown the radial discharge stream coming out from impeller tip. RPT accurately measured the mean radial, tangential and axial velocities and compared well with established Laser Doppler Anemometry (LDA) technique data.

A steady state CFD model was developed for a standard configured stirred tank. Initially, variants of the k-ε turbulence models such as standard, realizable, renormalized group (RNG) were tested. Among them standard k-ε model has given better prediction of mean velocities in comparison with realizable and RNG k-ε models. Further, the optimal dimensions of inner-rotating fluid zone for multiple reference frame (MRF) technique in CFD modelling of stirred tank were determined. In this study, a series of CFD simulations were performed at various dimensions of inner-rotating fluid zones and the optimal zone dimensions were considered when the results for mean velocities were found to be in good agreement with literature data. The efficiency of CFD model with optimized inner-rotating fluid zone was validated by comparing the prediction of mean velocities, power number at various Reynolds number, radial pumping number, classical flow pattern of double re-circulation loops and turbulence parameters with the RPT and the literature data.

The effect of impeller clearance (from bottom of the tank) on flow hydrodynamics in RT stirred tank was investigated, as it has paramount importance in various applications. A series of CFD simulations were conducted for the clearance ranging from C/T = 0.15 to 0.85. The mean and turbulence flow fields from the stirred reactor configuration having RT impeller at standard as well as lower clearances were validated with the experimental results available in the literature. A critical clearance of C/T = 0.78 and 0.18 were determined at which the standard double re-

circulation loop flow pattern was transformed into single re-circulation loop with more than 30% and 44% reduction in the power number as well as radial pumping number respectively. Thus, double re-circulation loop exists in the range of $0.19 \leq C/T \leq 0.77$ and single re-circulation loop occurs in the range of $C/T \leq 0.18$ and $C/T \geq 0.78$. Therefore, the radial flow pattern associated with the standard RT clearance changed into axial flow pattern. The higher clearances provided higher magnitudes of mean velocity, turbulence kinetic energy as well as its dissipation rate near the top surface of the tank. This phenomenon is extremely suitable for surface aeration process in wastewater treatment plants which leads to superior mixing and transfer of oxygen from atmosphere to the water. The lower clearances developed strong axial pumping action and maintain sufficient values of radial velocity and turbulence quantities till the tank wall which helps in solid-liquid suspension process in the agitated vessels at low power consumption.

The effect of impeller diameter ranging from $D/T = 0.2$ to 0.46 (fully turbulence regime) on flow hydrodynamics in RT stirred tank was investigated through CFD simulations. The magnitudes of power number as well as radial pumping number increase slightly with impeller diameter. The power number calculated using energy dissipation rate was found to be lower than that calculated by torque and the overall percentage deviation was found to be 15%. The distribution velocity field and turbulence kinetic energy increased with increase in impeller diameter. The peak value of mean velocities and turbulence parameters were observed at angle of 50° behind the impeller blades.

Table of Contents

List of Figures

List of Tables

Nomenclature

A	=	Source strength (Ci)
b	=	Baffle width (m)
C	=	Impeller clearance (m)
D	=	Impeller diameter (m)
d	=	Penetration depth of photons in the detector crystal (m)
H	=	Height of water in tank (m)
k	=	Kinetic energy of turbulence (m^2/s^2)
l	=	Impeller blade length (m)
L_1-L_{14}	=	Locations of tracer particle
N	=	Rotational speed of impeller (rev/s)
NaI	=	Sodium iodide
N_P	=	Power number
N_r	=	Radial pumping number
N_{Re}	=	Impeller Reynolds number
N_Q	=	Impeller pumping number
P	=	Power (J/s)
Q	=	Fluid circulation rate (m^3/s)
r, z, θ	=	Radial, axial and tangential coordinate
R	=	Impeller radius (m)
Sc-46	=	Scandium 46
T	=	Tank diameter (m)

T_S = Sampling time (s)

V_r = Mean radial velocity (m/s)

V_{tip} = Impeller tip speed (m/s)

V_z = Mean axial velocity (m/s)

V_θ = Mean tangential velocity (m/s)

w = Impeller blade width (m)

Greek letters

γ = Gamma radiations

μ = Dynamic viscosity (kg/ m.s)

ρ = Density (kg/m^3)

τ = Torque (N.m)

ε = Turbulence dissipation rate (m^2/ s^3)

ν = Number of gamma ray photons emitted per disintegration

ε_{abs} = Absolute efficiency of detector

ϕ = Photo-peak fraction

τ_d = Detector dead time (s)

μ_D = The mass attenuation coefficient of the detector crystal material

μ_j = The mass attenuation of all materials between the source and detector

Abbreviations

ANOVA	Analysis of Variance
CARPT	Computer Automated Radioactive Particle Tracking
CFD	Computational Fluid Dynamics
DNS	Direct Numerical simulation
DSM	Differential Stress Model

HWA	Hot Wire Anemometry
IBC	Impeller boundary condition
IO	Inner-outer
LDA	Laser Doppler Anemometry
LLD	Lower Level Discriminator
LES	Large Eddy Simulation
MDG	Moving Deforming Grid
MIDAS	Multi Input Data Acquisition System
MRF	Multiple Reference Frame
MRI	Magnetic Resonance Imaging
PBT	Pitched Blade Turbine
PEPT	Positron Electron Particle Tracking
PIV	Particle Image Velocimetry
PPU	Pulse Processing Unit
RANS	Reynolds Averaged Navier-Stokes
RNG	Renormalized Group
RPT	Radioactive Particle Tracking
RT	Rushton Turbine
RSM	Reynolds Stress Model
SCA	Single Channel Analyzer
SIMPLE	Semi Implicit Method for Pressure Linked Equations
SM	Sliding Mesh
SS	Source-Sink
ULD	Upper Level Discriminator

Chapter 1

Introduction

Mixing and agitation in stirred vessels are widely used unit operations in the various process industries such as chemical, pharmaceutical, food, oil, and bio-chemical as well as municipal and industrial wastewater treatment plants to enhance the mass and heat transfer rate. Superior mixing of contents is the prime importance for producing high yields of product. In comparison to worlds' chemical production, more than 50% processes involve stirred tanks for production of high value added products (Hemrajani and Tatterson, 2004). The main objectives of mixing process in stirred tanks are to achieve the uniform concentration of contents, physical properties and temperature. Mixing in stirred vessels is carried out by the physical movement of contents by rotating impellers which generates complex and three dimensional flow structure. Stirred tanks have been used for various industrial applications and these are classified based on the number of phases involved in the tanks (Table 1.1).

Table 1.1 Some industrial applications of stirred tanks (Ranade, 2002; Debangshu, 2007)

Phases handled	Applications
Liquid	Alkylations, sulfonations, esterifications, bulk and solution polymerizations (styrene, acrylonitrile, ethylene, propylene)
Gas-Liquid	Oxidations (ethylene, paraffins), chlorinations (acetic acid, dodecane), carbonylations (methanol, propanol), manufacture of sulfuric acid, adipic acid, oxamide, esterifications
Gas-Liquid-Solid	Hydrogenations (olefins, edible oils, several chloro and nitro aromatics), oxidations (p-xylene), fermentations (alcohol, single cell proteins, antibiotics), wastewater treatment
Liquid-Liquid	Suspension and emulsion polymerizations (styrene, vinyl chloride), extractions
Liquid-Solid	Calcium hydroxide (from calcium oxide), regeneration of ion exchange resins, anaerobic fermentations
Gas-Liquid-Liquid	Bi-phase hydroformylations, carbonylations

In stirred tanks, scaling of tank affects flow hydrodynamics and finally its performance. It is reported that the small scale stirred tanks have higher shear rate and high circulation rate compared to large scale tanks. Hence, the analysis of scale-up/scale-down of stirred reactors is crucial for the pilot plant tests (Ranade, 2002). A different types of impellers with different shapes have been used in practice. Impellers located at different clearances are used for different applications. A stirred reactor has to perform several functions simultaneously for many industrial situations. For example, blending and heat transfer processes require more bulk flow and less shear, while gas-liquid dispersion and mass transfer processes requires high shear rate (Tatterson, 1991). Hence, it is difficult to get the desired flow hydrodynamics for such a conflict requirement. The cost of production in US chemical industry through stirred tank was half of the $750 billion per year and $20 billion per year was the major loss to the industry due to inefficient design of stirred tanks (Roy et al., 2010). A compromise between conflicting process requirement needs to be achieved in order to get the desired output. Hence, in the optimal design and process economic point of view, it is the job of reactor engineer to have a prior knowledge of complex flow hydrodynamics and its relation with design parameters and with process of interest.

1.1 Stirred Tank Technology

A conventional stirred tank comprises of vertical cylinder, a rotating impeller mounted on a vertical shaft (Figure 1.1). Sometimes, horizontally placed, or square or rectangular shape of stirred tanks are also used and these are called as nonstandard geometries. The stirred vessel consists of several components such as rotating impeller, shaft, wall baffles, motor drive and gear box. Sometimes impellers with bottom entrance can be used in tall tanks to reduce shaft length and maintain mechanical stability. For the large product storage and blending tanks impellers with side entrance or entering from top at an angle for unbaffled tanks can be used. Mixing in stirred tank takes places under laminar regime or turbulence regime. It is decided based on the impeller Reynolds number and it is defined as $N_{\mathrm{Re}} = \frac{ND^2\rho}{\mu}$. N represents the rotational speed of impeller, D is the impeller diameter, ρ and μ are density and dynamic viscosity of fluid respectively. When the Reynolds number is below 10, the flow condition becomes laminar and when its value is more than 10^4, the flow is fully turbulence. The flow is considered to be transitional when Reynolds number finds in between above mentioned two regimes (Bates et al., 1963). The various components of stirred tanks are explained briefly in the following section.

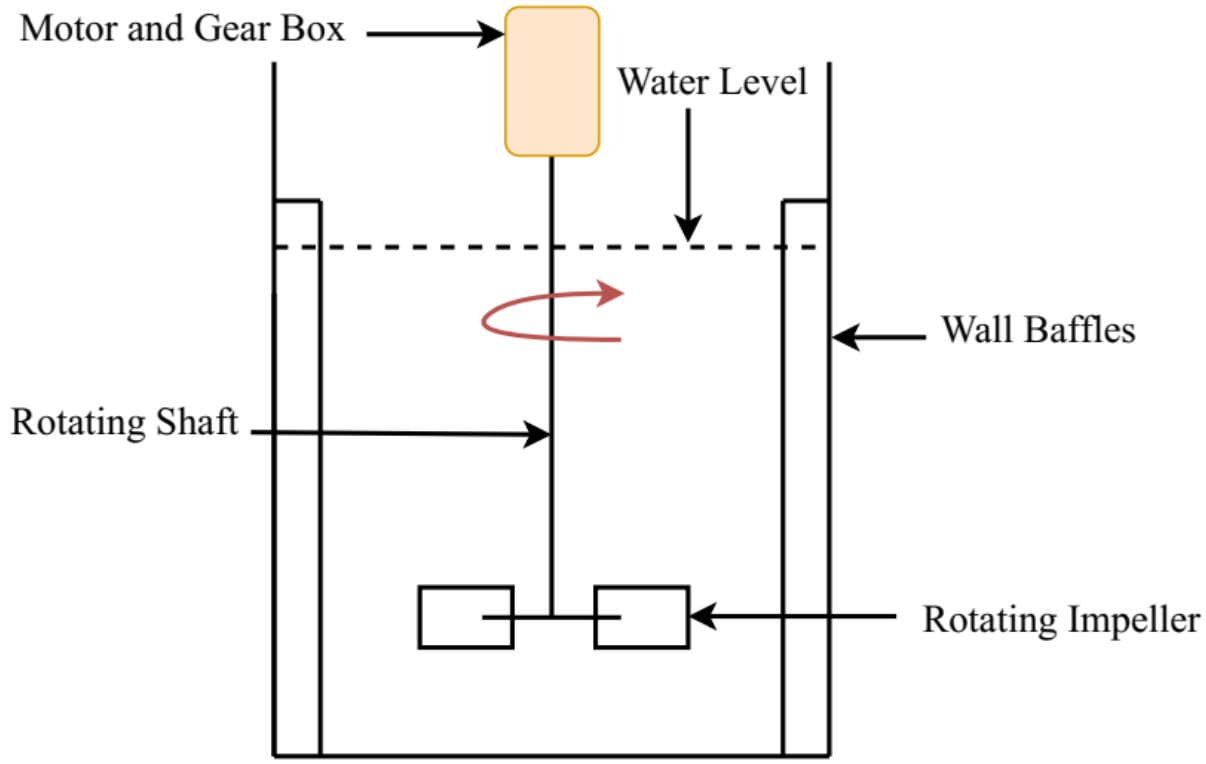

Figure 1.1 A conventional stirred tank

1.1.1 Rotating Impellers

Rotating impellers are broadly classified based on the flow patterns generated and specific application for which these are employed. The commonly used impellers are given as:

Radial flow impellers – Disk turbine (Rushton), flat blade impeller, hollow blade turbine

Axial flow impellers – Propeller, pitched blade turbine, hydrofoils

Maximum input energy provided for radial flow impellers is used for generating turbulence while axial flow impellers consume it for convection. Radial flow impellers are extremely suitable for the process involving gas-liquid, liquid-liquid and multiphase dispersions. While, axial flow impellers are employed for the process involving suspension of solids, enhancing the heat transfer rate and blending.

The commonly used different types of impellers in mixing processes are shown in Figure 1.2 (a-d). Marine propeller is the axial type of impeller which is often used for large tanks with side entrance and small tanks with top entrance. These are generally operated at high speed and used for low viscosity liquids. Flat blade impeller and disk turbine are the radial type of impellers and these are used for low to medium viscous fluids. These impellers produce high

levels of turbulence and shear in comparison with axial flow impellers. The difference between flat blade impeller and disk turbine is that, without disk, impeller discharge stream does not move completely in the radial direction because of pressure difference created between each side of impeller. Disk turbine is more power intensive and produces uniform radial discharge than the flat blade impeller. Even though pitched blade turbine comes under the category of axial flow impeller, it is mixed flow impeller as it generates the flow pattern in both radial as well as axial direction. If the ratio of impeller diameter to tank diameter ratio goes above 0.55, pitched blade turbine behaves like radial flow impeller (Joshi et al., 2011).

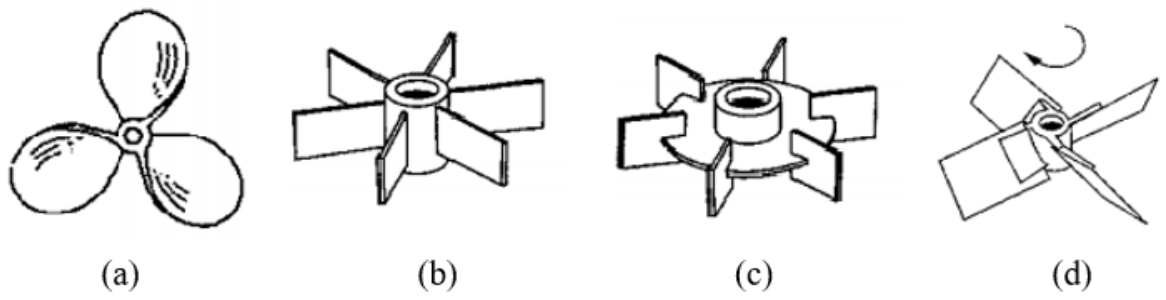

Figure 1.2 Different types of impellers, marine propeller (a), flat blade impeller (b), disk turbine (c), and pitched blade turbine (d) (Walas, 1990; McCabe et al., 1993)

1.1.2 Wall Baffles

Baffles are commonly employed for turbulence and transitional mixing processes. Generally, baffles are not used in case of laminar mixing. Wall baffles consists of flat plates attached to wall of mixing tank to alter the tangential flows produced by rotating impellers and enhance the mixing quality. Baffles disturb the solid body rotation and transform the tangential flows into axial flows. Baffles increase the drag in the flow while it consumes more power for the rotation of impellers. Stirred tanks are commonly employed with three or four baffles (Torre et al., 2007).

1.1.3 Bottom of Tank

Cylindrical stirred tanks comprise of flat or dished bottom. The tanks with different bottoms generate the different flow patterns below the impeller and result in different mixing efficiencies. The dished bottoms are preferred for solid suspension process, because solids accumulate at the corner of flat bottom tanks.

1.1.4 Motor and Gear Box

The motor and gear box comprises the drive system of stirred tank. A gearbox is used to obtain the required impeller rotational speed from the motor speed.

1.2 Impeller Characteristics

The flow characteristics of different impellers are represented in terms of power number, pumping number and flow patterns.
The power applied to stirring process produces volumetric circulating capacity (Q)

$$Q \; \alpha \; ND^3 \qquad (1.1)$$

Where Q (m^3/s) represents fluid circulation rate, N (rev/s) is impeller rotational speed and D (m) is the impeller diameter.

1.2.1 Impeller Pumping Capacity and Pumping Number

Pumping capacity of the impeller represents the amount of fluid discharged by the rotating impeller. After solving Equation 1.1, it can be written as

$$Q = N_Q \, N \, D^3 \qquad (1.2)$$

Where, proportionality constant N_Q represents the impeller pumping number which depends upon the impeller diameter (D) to tank diameter (T) ratio and impeller Reynolds number.

The values of N_Q for commonly used impellers under turbulence flow conditions are given in Table 1.2.

Table 1.2 Type of impellers with their pumping number (N_Q) under turbulence flow conditions (Walas, 1990)

Type of impeller	N_Q
Marine Propeller	0.4-0.6
Disk flat blade turbine (Rushton turbine)	0.72
Pithed blade turbine	0.79
Hollow blade turbine (Smith)	0.76
Flat blade turbine	0.7
Hydrofoil impellers	0.55-0.73

1.2.2 Power Consumption and Power Number

The power required for mixing process is defined as

$$P = N_p \rho N^3 D^5 \qquad (1.3)$$

where N_P represents the power number. N_P depends on the impeller type and impeller Reynolds number (N_{Re}). Relationship between N_P and N_{Re} for various impeller designs is shown in Figure 1.3. It is observed that impeller blade width, number of blades, blade angle, the impeller to tank dimeter ratio, baffle configuration affects the power number. N_P sharply decreases with N_{Re} < 10 (laminar regime), it changes slightly for 10 < N_{Re} < 10^4 (transitional regime) and becomes constant for N_{Re} >10^4 (turbulence regime).

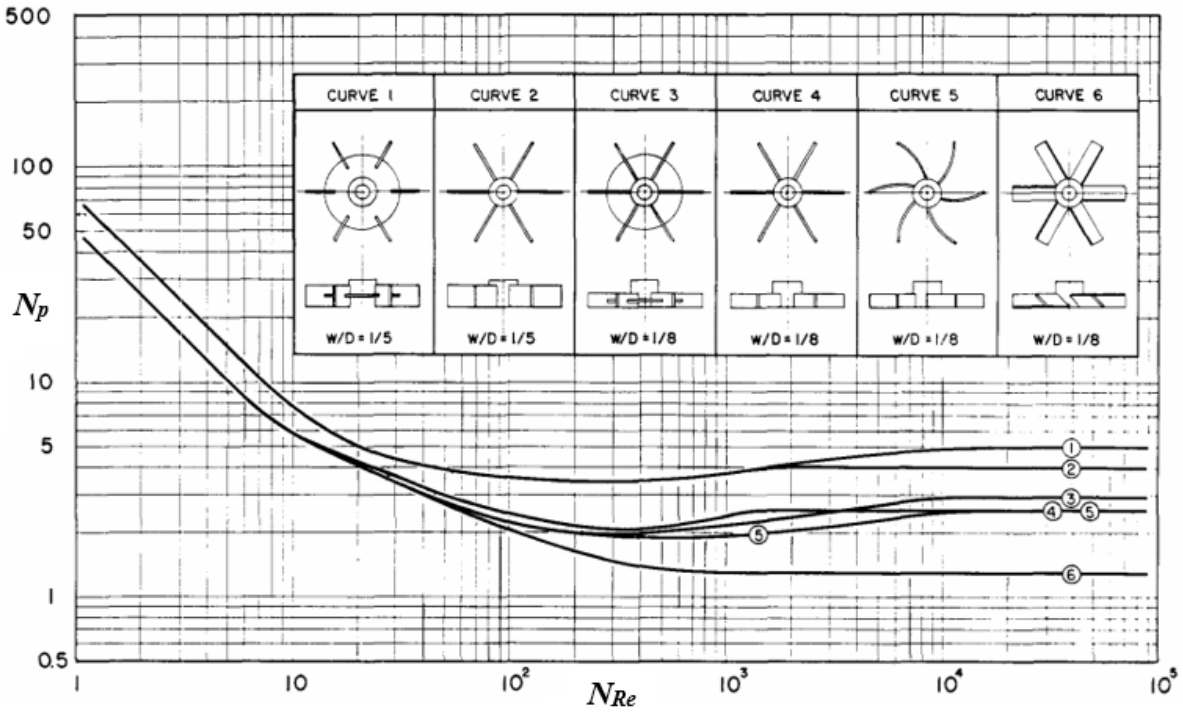

Figure 1.3 Relationship between power number and impeller Reynolds number for various impeller designs (Bates et al., 1963)

1.3 Flow Patterns in Stirred Tanks

Each impeller with its characteristic flow pattern results in different levels of shear rate and pumping capacity. Mostly, axial flow impellers provide high pumping and low-shear while radial flow impellers provide high-shear but low pumping.

The flow patterns produced by impellers result in different mixing efficiencies. The typical flow patterns produced by axial as well as radial type of impellers are shown in Figure 1.4(a-

b). The single loop flow pattern throughout the entire vessel volume is provided by axial flow impellers (Figure 1.4a) such as pitched blade turbines and hydrofoils. The pitched blade turbine (PBT) is a mixed flow impeller which provides high pumping capacity and shear rate as well. PBT has a high shear and turbulence level in comparison with hydrofoils, however both have the same pumping capacity.

The classical flow pattern of two circulating loops one below and one above the impellers is generated by radial flow impellers as shown Figure 1.4(b). In stirred vessels, distribution of shear rate and energy dissipation rate varies with the flow pattern. The impeller which is suitable for a particular operation can be employed based on the flow patterns and shear rates. The double circulation loops associated with disk impellers are efficient for gas-dispersion operation while single circulation loop associated with axial flow impeller is well suited for liquid bending operation. The classical flow patterns generated by impellers can be transformed with the proper adjustment of geometrical parameters such as location of impeller, diameter of impeller, use of impellers and by baffling etc. (Montante et al., 1999; Ranade, 2002; Joshi et al., 2011).

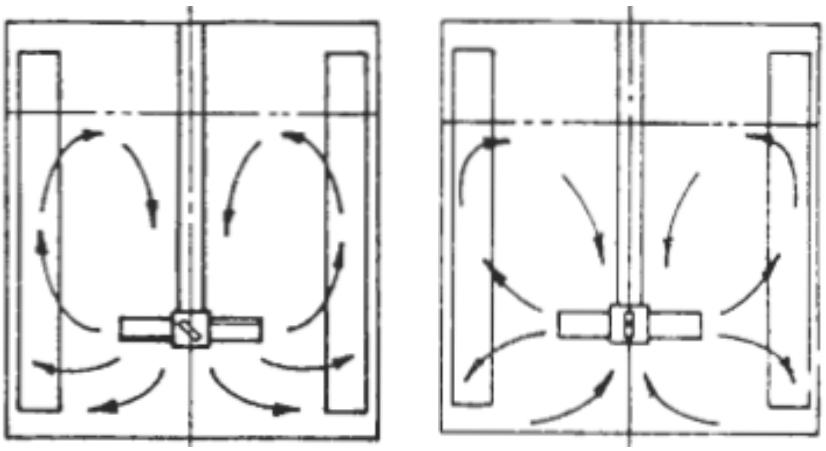

(a) Axial flow impeller (b) Radial flow impeller

Figure 1.4 Flow patterns for different impellers (Walas, 1990)

The mixing process in a stirred tank is strongly affected by the complex and the turbulence flow hydrodynamics. Hence, for optimal design of stirred tanks, it is of prime importance to have a knowledge of flow hydrodynamics, mixing level and overall performance of stirred reactor (Yapici et al., 2008). To have more insights in these aspects, efforts have been done over last three decades through the experimental fluid dynamics and Computational Fluid Dynamics (CFD). In the following sections, both experimental and CFD approaches are explained for the estimation of flow fields.

1.4 Experimental Techniques for Velocity Measurement

Various experimental techniques have been used for the measurement of flow fields in processes involving single phase and multiphase as well. However, each of the techniques have their merits and demerits (Chaouki et al., 1997). Generally, these measurement techniques can be classified into invasive and non-invasive. The details of these measurement techniques have been presented in the following section.

1.4.1 Invasive Velocity Measurement Techniques

The invasive techniques disturb the flow during the velocity measurement, wherein the probe needs to be inserted into the phase flow under consideration. Some of the widely adopted invasive techniques for the velocity measurement are briefly described as below.

(i) Pitot Tube

The Pitot tube works on the principle of measuring the pressure difference at a given location in the flow field. In this, the direct pressure of flow is measured at the point of contact pitot tube and another measurement is the static pressure. The difference between direct pressure and static pressure gives the dynamic pressure. Then the flow rate is determined by taking square root of dynamic pressure and subsequently flow velocity can be obtained. This technique has advantages of low cost, easy for installation into an existing system, however use of this technique is limited due to the difficulties in measuring two phase differential pressure and low accuracy (Ligarani et al., 1989).

(ii) Hot Wire Anemometry (HWA)

HWA technique is based on the principle of change in the electrical resistance wire due to the liberation of heat by flowing fluid and estimates the local fluid velocity with respect to change in resistance of wire. When fluid moves around the probe, it transfers a certain amount of heat by convection, which can be calibrated against fluid velocity. HWA is relatively cheaper and has a good accuracy at lesser cost. But it is not suitable for high velocity gas-solids or gas-liquid-solids systems, as the probes used in HWA are thin (Muller, 1992).

(iii) Optical Probes

The working principle of optical fibers is the difference in refractive index of different materials under consideration in flow field. In optical fiber, light emits at one end of the optical

fiber with a pulse laser and some of this light reflects back at the other end (through total internal reflection). The intensity of the reflected light can be determined by use of a photo-detector, which depends on the refractive index of the surrounding fluid optical probes are less effective for multiphase systems. (Cartellier, 1992; Xue et al., 2008).

1.4.2 Non-Invasive Velocity Measurement Techniques

The non-invasive techniques measure the velocity and velocity fluctuations without disturbing the flow in any way. These techniques are indirect measurement techniques which involve the multistep, i.e., the recorded data in form of the signals or photographs needs to be processed further to get the velocity and velocity fluctuations. Usually, these techniques involve some rigorous mathematics calculations during data processing. The non-invasive techniques are costlier than the invasive techniques due to the indirect measurement method and the associated hardware and software requirements. Some of widely used non-invasive velocity measurement techniques are briefly described below.

(i) Laser Doppler Anemometry (LDA)

In LDA, when a narrow laser beam is illuminated on fluid, the beam reflects back to the source. But there will be difference in the frequency of a laser beam received back from transmitted beam when the fluid is moving. This difference in the frequency (Doppler shift) is used to measure the velocity of moving fluid. LDA does not requires the calibration which is advantage over the use of invasive techniques. The LDA has major problem for multiphase flow monitoring, it is limited to low-volume fractions of the dispersed phase and does not provide the clear information regarding the phase holdup distributions (Rammohan et al., 2001 (a,b); Khopkar et al., 2005). LDA is restricted to transparent flows and transparent tank walls, due to the inherent use of a laser (Bashiri et al., 2016).

(ii) Particle Image Velocimetry (PIV)

In PIV, a high energy laser beam is incident through a cylindrical lens arrangement which shapes the transmitted laser beam into a thin planar sheet of high intensity laser light. Later, this sheet of laser light is aligned parallel to the fluid flow direction. The neutrally buoyant particles are seeded into the flow and these particles scatter the planar laser sheet when they pass through it. The digital camera is placed perpendicular to planar sheet which captures the photograph of scattering seed particles. After one photograph, laser sheet pulses again and again camera captures the photograph of scattering of seed particles. However, during this short

time, seed particle would have moved away to the new location in flow streamline, subsequent change is captured by the pulsing laser and associated camera. Comparing these photographs and particle position, instantaneous velocity of fluid is obtained (Li et al., 2011). With the use of laser like LDA, PIV cannot be used for multiphase systems having a high holdup of the dispersed phase (Upadhyay, 2010).

(iii) Radioactive Particle Tracking (RPT)

RPT uses γ-radiations for the measurement of flow fields. In this technique, the motion of a radioactive source emitting γ-radiations is determined by an array of scintillation detectors strategically placed around the vessel of interest. Before experiments, the radioactive particle needs to be prepared in a such way that it should mimic the flow i.e. neutrally buoyant with the phase of interest. For solid phase tracking size, shape and density of tracer particle should be similar to a solid phase and for liquid phase tracking, tracer particle should be neutrally buoyant with liquid phase (Meek, 1972; Lin et al., 1985; Moslemian et al., 1989; Devanathan et al., 1990; Degaleesan, 1997; Rammohan et al., 2001; Roy et al., 2002; Upadhyay and Roy, 2010).

During experiment, the tracer particle moves freely inside the vessel, and the position of the tracer particle is determined by an array of scintillation detectors that monitor the γ-radiations emitted by the tracer particle. The intensity of radiation recorded at each detector decreases exponentially as the distance between the particle and detector increases. In order to estimate the position of the tracer particle from the measured radiation intensities, a calibration step needs to be performed prior to the RPT experiment by placing the tracer particle at various known locations. Using the data acquired, calibration curves can be established that relate the intensity received at a detector to the distance between the tracer particle and the detector. Once the distance of the particle from the set of detectors is known, a suitable reconstruction algorithm can be used to estimate the position of the particle at a given sampling instant in time. The instantaneous velocities are calculated by time differentiation between two successive instantaneous positions. From this information, it is possible to evaluate the other flow quantities such as mean velocity, kinetic energy of turbulence, shear stresses etc. Figure 1.5 shows the steps involved in RPT for data processing. RPT has advantages over LDA and PIV, it successfully used in multiphase flows having high-volume fractions of dispersed phase such as bubble columns, liquid-solid risers, stirred tanks etc. (Rammohan et al., 2001 (a,b); Khopkar et al., 2005). RPT provides the Lagrangian information about velocity fields and turbulence parameters, however LDA gives Eulerian data (Bashiri et al., 2016).

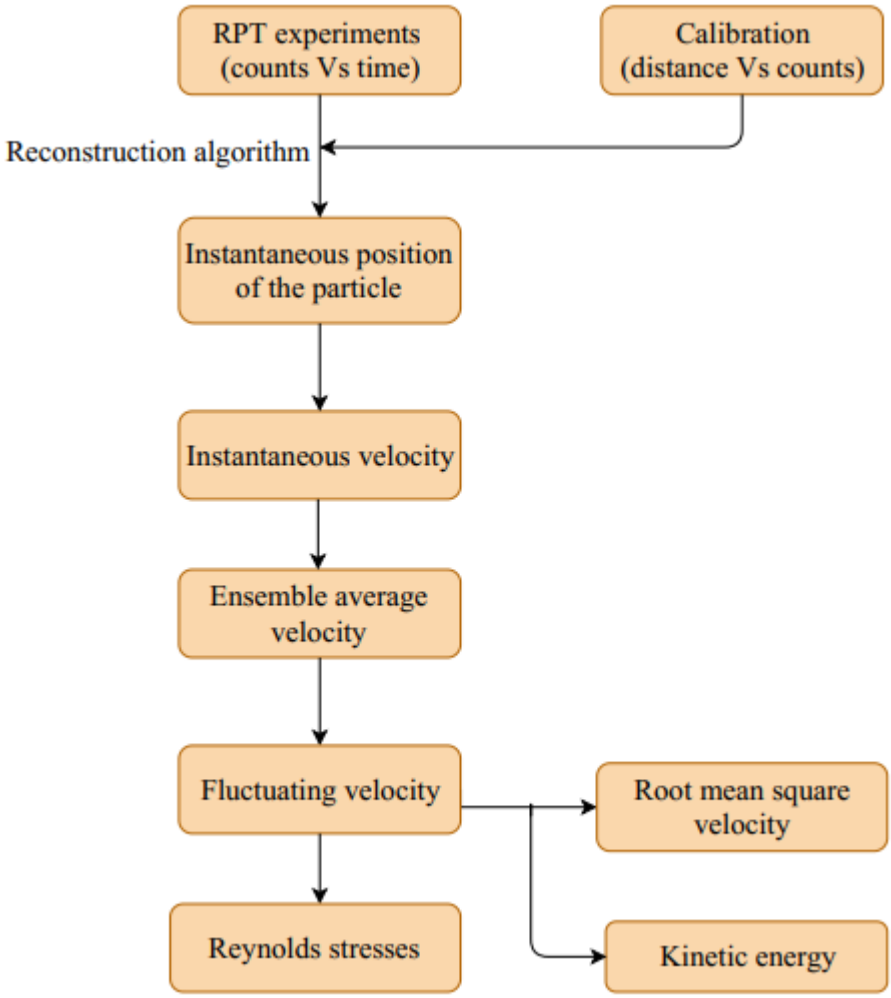

Figure 1.5 Radioactive Particle Tracking (RPT) technique data processing steps

(iv) Positron Emission Particle Tracking (PEPT)

PEPT is very similar to RPT, the motion of a γ-ray source is determined in RPT, however the motion of a single positron emitting tracer is determined in PEPT. Like RPT, the tracer particle is designed specifically to track the phase of interest. When a positron is emitted by the tracer particle, it almost immediately vanishes with the free electron present in its surrounding area, and produces a pair of 511 keV γ-ray which travel in opposite directions along straight line paths. These γ-ray photons are detected by the two large positron sensitive detectors (positron cameras) which are placed on either side of the vessel of interest. The location of the positron emitted tracer particle is then reconstructed by finding the point of interaction of the two lines that connect the location of γ-incidence. Subsequently, the velocity of positron is obtained (Wildman et al., 1999). The use of high detection system (positron camera) made limitations for widespread application of PEPT (Bashiri et al., 2016).

(v) Magnetic Resonance Imaging (MRI)

In MRI technique, high magnetic field is generated by placing magnet of power around 5 Tesla outside the reactor. A radio wave antenna is used to send the signal and then receive it back. In this technique, the phase velocity is obtained by imaging spatial variation in magnitude of magnetization. This technique has successfully measured the flow parameters such as velocity distribution, phase holdups etc. However, this technique is less attractive as it has high expenditure associated with requirement of high magnetic field (Upadhyay, 2010).

In summary, from all of these flow measurement techniques each technique has its own advantages and disadvantages. The selection of the suitable flow measurement technique can be based on the following points.

- Non-invasive nature
- Accuracy
- Suitable for single and multiphase situations
- Portable and less complex for development
- less expensive

Considering all above points, no technique satisfies all above requirement. RPT does satisfy all above requirements at acceptable level of flow measurement. Hence, RPT technique is considered in present work for flow field measurement.

1.5 Computational Fluid Dynamics (CFD)

Various sophisticated flow measurement techniques, such as LDA, PIV, PEPT and RPT have been used to study the three-dimensional, highly turbulence flow structure in stirred tanks (Wu and Patterson, 1989; Li et al., 2011; Rammohan et al., 2001; Fishwick et al., 2005; Bashiri et al., 2016). Even though these experimental studies measured flow fields accurately, these techniques are neither economical nor practical because the best choice of tank geometry and impeller type vary depending on the purpose of operation carried out in stirred tank. Different materials may require different types of impellers and tank geometries in order to get the desired product quality at reasonable operational costs. Other important parameters like impeller clearance from the tank bottom, proximity of the vessel walls, baffle length and number also affect the generated flow (Yapici et al., 2008).

With the significant improvements in computer technology and numerical techniques, CFD simulations has been widely used to solve complex fluid mechanics problems. CFD simulation provides an economical way to obtain the comprehensive information regarding flow behavior, circulation pattern and vortex structures needed for optimizing the tank design in a shorter time (Yapici et al., 2008). Therefore, rather than conducting an experimental study to understand fluid hydrodynamics inside the stirred tank, it is convenient to conduct CFD simulations. However, to test the predictive capability of CFD model, it needs to be validated with experimental data.

1.6 The Present Work

In this work, the flow hydrodynamics in a fully baffled stirred tank agitated by Rushton turbine have been investigated by using RPT technique and a steady state CFD model.

The thesis has been organized into five chapters. In Chapter 1, introduction to stirred tank technology, the flow characteristics in stirred tank and various flow field measurement techniques have been presented. Chapter 2 presents a detailed literature review with reference to RPT and its widespread application in measurement of flow hydrodynamics, various turbulence models and various impeller rotation modelling techniques used in CFD modelling of stirred tanks and experimental as well as numerical studies on investigating the effect of geometrical parameters on flow hydrodynamics in stirred tank. In Chapter 3, the details of the Materials and Methods used in the present work i.e. experimental details of RPT setup for stirred tank, CFD methodology and governing equations used in solving the flow variables have been discussed. Results obtained from the RPT and CFD studies are analyzed in Chapter 4, (Results and Discussion). In Chapter 5, conclusions drawn from the studies and scope for the future work have been presented.

Chapter 2

Literature Review

This chapter presents a detailed literature review of the previous work to identify the gaps in the literature regarding the Radioactive Particle Tracking (RPT) technique and flow hydrodynamics inside the Rushton turbine stirred tank. The chapter has been divided into the following sections.

1. Studies using RPT: This section gives an overview of literature related to implementation of RPT and its application for various single as well as multiphase systems.
2. CFD modelling of stirred tank: This section includes literature related to (i) various impeller rotation modelling approaches, (ii) various turbulence models and (iii) CFD simulations using Reynolds Averaged Navier-Stokes (RANS) equation in Rushton turbine stirred tank.
3. Effect of geometrical parameters on hydrodynamics: This section contains the literature related to the effect of geometrical parameters such as impeller clearance and impeller diameter on hydrodynamics in stirred tanks.
4. Scope and motivation for the present study: This section sets up the objectives for the present study based on the gaps found in the literature.

2.1 Studies using RPT

As part of non-invasive technique, ionizing radiation based Computer Automated Radioactive Particle Tracking (CARPT) or generally called as Radioactive Particle Tracking (RPT) technique has already been proved to be a powerful tool for modeling industrial units and process control (Degaleesan et al., 2002). RPT has been successfully implemented and used to analyze flow hydrodynamics for various kinds of single and multiphase systems such as bubble columns, gas-solid fluidized bed, circulating fluidized, stirred tank, etc. In RPT, there are several key factors such as the tracer particle selection, calibration of the detectors and signal processing which strongly affects the reliability and accuracy in measurement (Degaleesan, 2002). This section gives the details of developments in RPT and its application over the years.

Kondukov et al. (1964) introduced the concept of a single tracer particle to study phase velocities. They used six scintillation detectors to track the motion of solid phase. Due to lack of sufficient acquisition system, they could produce only qualitative information.

Meek (1972) used six scintillation detectors to identify the solid motion in a turbulent liquid. Detectors were arranged on a vertically moving carriage which was designed to move with the solid particles so that particles can be seen by detector. Meek determined the tracer locations with the help of prior calibration. Since it was very difficult for detector carriage to maintain the same speed of the tracer particle, the particle often went out of the control volume of investigation, resulting in loss of data. However, it was the first appropriate attempt for the evaluation and measurement of instantaneous velocities, ensuring RPT for measurement of flow fields.

Lin et al. (1985) developed computer automated particle tracking to investigate the solid motions in a gas fluidized bed. They prepared the tracer particle from gamma (γ) ray emitter Scandium-46 (Sc-46) source and the density of tracer particle was closely matched with solid phase under investigation. Photomultiplier tubes incorporating sodium iodide (NaI) crystals were used for continuous monitoring of γ-ray emission. Twelve detectors were used and placed in staggered configuration around the bed at three different heights with four at each level. Such arrangement has been found to be optimal as the tracer particle can be detected by all detectors. They observed the fluctuations in the signal from secondary emissions produced due to interaction of γ-rays with the bed material. Secondary emissions have low energies which was removed by employing Schmitt trigger with an adjustable threshold. Reconstruction of particle position was done with the use of weighted least square algorithm. Instantaneous solid velocities were obtained by subtracting two successive particle locations and then multiplying with known sampling frequency.

Moslemian et al. (1989) used RPT to study the solid motion in gas-solid fluidized bed. The Sc-46 was used as tracer particle in experiment. Sixteen scintillation detectors were used to track the motion of solid particle. The speed of signal acquisition was increased by using digital pulse counting system which resulted in increase of accuracy of position reconstruction. The instantaneous velocity was obtained by time differencing the instantaneous position. The percentage error in the mean velocity measurement was found to be 2-5 %.

Devanathan et al. (1990) used first time CARPT for tracking the liquid flow in gas-liquid bubble column. Experiments were conducted in 12-inch column for the air water system. The

radioactive particle was made by embedding Scandium cylinder (1mm diameter and 0.7 mm long) into 2.4 mm diameter polypropylene sphere such that the composite particle density was 1.01 g/cc and made it neutrally buoyant with water. The particle was activated to Sc-46 with source strength of 200 μCi. Sixteen NaI scintillation detectors were used to monitor the particle position in the column. The data was acquired at sampling rate of 33 Hz for 5 hours. Weighted linear regression scheme as described by Lin et al. (1985) was used for particle position reconstruction.

γ-radiations sensed by detectors were converted into current signal and then amplified by fast filter amplifier. A signal discriminator was used to remove the secondary γ-emissions produced due to interaction of primary γ-radiations with column and its contents. With the use of CAPRT, they investigated mean liquid circulation profiles and liquid phase turbulence (mean velocity, Reynolds shear stress and eddy viscosity). Later, experiments and CFD simulations were conducted by researchers to investigate the particle paths through bubble column (Devanathan et al., 1995).

Yang et al. (1992) used RPT in gas-liquid bubble columns with different diameters (0.114, 0.192, 0.292 m) and height (height to diameter ratio varied from 2.5 to 8) at varying gas superficial velocities from 0.02 m/s to 0.184 m/s. They used sixteen scintillation detector system. They adopted the similar hardware for signal processing and data acquisition system which was used by Devanathan et al. (1990). In their setup, the interaction of γ- rays with the detector crystal generated the photoelectric pulse from photo-multiplier tube (PMT) of the detector. This signal was made to pass through a separate timing amplifier which amplified the weak signal. The main development brought in this setup was the manner by which the acquired information (photon counts) were stored, through which long acquisition times for the RPT experiment became possible. The tracer particle (density 1.01 g/cc) was prepared from Sc-46 and made neutrally buoyant with water. This tracer particle preparation method was also an important development in RPT.

Yang et al. (1993) found that the liquid flow pattern in bubble column is a single re-circulation cell where the gas drives the liquid to ascend at the centre of the column and descend near the wall. They evaluated both axial and radial normal stresses, shear stresses and found that both the types of stress increases with increase in gas superficial velocity. Axial normal stresses were found to be significantly higher than radial normal stresses.

After Devanathan et al. (1990) and Yang et al. (1993), the major developments in RPT were brought by Larachi et al. (1994, 1995, 1997). Larachi et al. (1994) used RPT to track the solids motion in three phase fluidized bed reactor. They used eight NaI scintillation detectors to monitor γ-ray. The tracer particle was prepared from a mixture of soda ash lime powder and scandium oxide melted at high temperature. The particle was coated with a diamond-like carbon layer in order to prevent its rupture due to erosion in flow. The density of prepared tracer particle was matched with solid phase of interest. Larachi et al. (1994) introduced Monte-Carlo model for the first time in RPT. They used Monte-Carlo model to generate distance-count map (i.e., functional relationship between the distance between radioactive source and detector, and the radiation photon counts recorded at detector) for various known locations. During calibration, they verified the count rate calculated by Monte-Carlo model with the count rate measured in actual experiments for 19200 known locations. Once the distance count map was obtained, least square approach was used for reconstruction of particle position. They were able to obtain the solid phase velocities with adequate precision.

The capability of developed Monte-Carlo model was tested by Larachi et al. (1995, 1997) by performing experiments in both the spouted bed and the fluidized bed under the actual flow conditions. Later, test of Monte-Carlo model was performed on circulating and turbulence gas-solid fluidized bed. They found that the spatial resolution was improved by increasing the number of detectors, reducing the distance between column walls and the detectors and increasing sampling time (Larachi et al., 1995).

Degaleesan (1997) and Degaleesan et al. (1998, 2001) used RPT for investigation of flow hydrodynamics in bubble columns. Degaleesan et al. (1998) studied the liquid back mixing and axial dispersion coefficient in bubble column. The fluid dynamic parameters such as time averaged velocities and eddy diffusivities needed for the evaluation of axial dispersion coefficient were obtained through RPT experiments. Further, they studied the effect of operating conditions i.e. column diameter and gas superficial velocity on axial dispersion coefficient.

Godfroy et al. (1997) used artificial neural network (ANN) algorithm for real time flow visualization. It is less time consuming than the least-square (Devanathan, 1991). It directly calculates the tracer position from the detector signals. In this algorithm, some part of the calibration data was used to design the ANN model and to obtain the model constants

(weighting functions) and the remaining data was used to check the accuracy of the model. This model used a large number of fitting parameters (159) and that need to be tuned as per required accuracy, which is the major drawback associated with the ANN model. They reported that the accuracy of ANN was less compared to that of Devanathan et al. (1990). However, the major advantage was the ability of real-time reconstruction and quick convergence.

Degaleesan et al. (2001) performed RPT experiments in bubble columns for air-water system. The experiments were conducted in different flow regimes, different sizes of bubble columns, different distributor configuration. Velocity vector plot, Reynolds stresses, turbulence kinetic energy and eddy diffusivity were obtained for all the conditions.

Rammohan et al. (2001a) implemented RPT for the first time in the investigation of flow hydrodynamics in a single phase Rushton turbine stirred tank. Researchers used sixteen scintillation detectors to track the motion of tracer particle. They found that conventional laser based techniques take more time than RPT for data collection. RPT was able to capture key phenomena of stirred tank i.e. eye of re-circulating loops above and below the impeller and shapes of the dead zones at the tank bottom. In extension of this work, Rammohan et al. (2001b) investigated the various flow parameters such as radial pumping number, mean radial velocity, mean tangential velocity and turbulence kinetic energy and these parameters were found to be in a reasonable agreement with experimental techniques like LDA and Hot Wire Anemometry (HWA). They found that RPT experiments have limitations over the large tracer particle size which was found during the comparison of fluctuating components like root mean squared error and turbulence kinetic energy.

Rammohan (2002) found an error during measurement called as ‘dynamic bias’. The tracer particle is stationary during calibration, while during the experiments tracer particle is in motion. In experiments, even in a short time period of acquisition, the tracer particle may be forced to move in the domain when the fluid is moving at high speed. Reconstruction algorithm would take a single position of tracer particle while it may be moved to another position, resulting to dynamic bias in the reconstructed positions. Such bias depends on the past particle trajectory, fluid velocity and the sampling rate. He suggested that if fluid velocity increases, the rate of data sampling needs to be increased, so that effect of dynamic bias can be minimized.

In order to implement RPT for large scale plants, careful and systematic planning is required. Roy et al. (2002) developed Monte-Carlo nuclear radiation based model for an optimal design of RPT experiments. They defined the two terms as resolution and sensitivity to predict the

optimal configuration of RPT setup in terms of source strength, detector size, shape and number of detectors and their configuration.

Degaleesan et al. (2002) proposed filtering algorithm based on wavelet analysis for the removal of intrinsic noise in the instantaneous position data generated in CARPT experiments for bubble column. They got some important findings with the use of wavelet based filtering algorithm as it removed 80-90% noise in the data and it is more suitable than the Fourier transform based algorithm for removal of such type of noise.

Bhusarapu (2005) used RPT experiment to study the hydrodynamics in gas–solid circulating fluidized bed. Sc-46 radioactive source was used for tracer particle. He made the tracer particle similar to solid particles in shape size and density, having a very small diameter 0.15 mm. He used twenty scintillation detectors to monitor motion of solid phase. The use of cross-correlation model for reconstruction of tracer particle position was the novelty in the work. With the help instantaneous position data, instantaneous and mean velocities, Reynolds stresses, turbulence kinetic energy, dispersion coefficient and time of flight for gas-solid fluidized bed were evaluated.

Khopkar et al. (2005) used CAPRT to characterize the flow generated in a gas-liquid Rushton turbine stirred tank. CARPT was able to capture the Eulerian liquid flow characteristics. Guha et al. (2007) studied the solids flow field in solid–liquid suspensions in a Rushton turbine stirred tank. They used sixteen scintillation detectors to monitor the motion of solid phase. CARPT provided Lagrangian solid flow field which was used to obtain the time-averaged velocity fields and the turbulence quantities. CARPT provided the solids sojourn time distributions at various axial location in the tank.

Upadhyay et al. (2010) used RPT to study hydrodynamics of binary mixture fluidized bed for particles having same size but different densities. They investigated the effect of air inlet velocity and bed composition on hydrodynamics and mixing behavior. Upadhyay et al. (2013) investigated the liquid flow patterns in rectangular air-water bubble column. Through RPT, the effect of different operating conditions and different aspect ratio of column on flow fields were investigated.

Dube et al. (2014) introduced an optimization strategy to find optimal positions of scintillation detectors and orientations used in the RPT setup. In this strategy, the objective function was to maximize the resolution of detectors and a mesh adaptive direct search algorithm was used to solve the optimization problem. The detector configuration suggested by this strategy was

found to be similar with Roy et al. (2002). They observed that optimization technique leads to a considerable reduction in the error during tracer particle reconstruction. They recommend that depending on the experimental conditions, the objective function may be sensitive to both resolution as well as sensitivity, while this strategy was based on resolution only.

Bashiri et al. (2016) used RPT to analyze the fully turbulence fluid flows in stirred tank equipped with Rushton turbine and pitched blade turbine. They benchmarked the RPT measurements with their CFD simulations and LDA measured literature data for Rushton turbine. RPT measured mean velocities at various axial locations were found to be in good agreement with other methods. Poincare maps for visualization of flow structures in stirred tanks and mixing time were well predicted by RPT.

Sharma et al. (2017) used RPT-Time of Flight and RPT-Volume of Fraction for oil-water two phase flow measurement in coiled geometries. RPT-Time of Flight was able to measure the exit age distribution which provided an accurate extent of radial mixing. RPT-Volume of Fraction measured occurrence density distribution. Through both methods, they collected the phase holdup and mixing behavior information by which different flow regimes in two-phase coiled flow were identified. Azizi et al. (2017) and Kalaga et al. (2017) investigated the flow hydrodynamics in bubble column using RPT. RPT efficiently provided the information about fractional gas distribution, axial mean liquid velocities and liquid phase mixing characteristics.

Kalo et al. (2019) investigated the hydrodynamics of binary gas-solid fluidized bed using RPT. They used twelve scintillation detectors to track the solid motion. Sc-46 was used as radioactive source and the tracer particle was made with the same shape, size and density of solid under consideration. They performed time series analysis to study the bed dynamics at different gas inlet velocities and bed compositions. They evaluated the Hurst exponent, autocorrelation coefficient and mixing index by using time series data.

Al-Juwaya et al. (2019) used RPT for first time to study the hydrodynamics and mixing behavior of binary solids mixture in gas-solid spouted bed. The binary mixture was prepared from glass beads and steel particles. Two separate tracer particles were prepared for glass and steel. For glass, a radioactive source Cobalt-60 (Co-60) having diameter of 0.6mm was encapsulated in an Aluminium particle to get the same density of the glass beads. For steel, a radioactive source Cobalt-60 (Co-60) was encapsulated in a steel particle to get same density like steel particles. They found that segregation always takes place in binary spout bed due to the dissimilar behavior of different solids phases in terms of the solids velocity field and

turbulence parameters. They demonstrated that, the particle-particle interaction between solids having same size but different densities play an important role for hydrodynamics in binary spout bed.

Table 2.1 Brief of literature on RPT development and its application (Upadhyay, 2010)

Author	System Investigated	Tracer used	Remarks from literature
Kondukov et al. (1964)	Fluidized bed (gas-solid)	Sc-46	• Concept of RPT introduced to study the phase velocity. They could able to get only qualitative information due to lack of sufficient data acquisition system
Meek (1972)	Fluidized bed (liquid -solid)	Sc-46	• Axially moving carriage was designed so that detectors positioned on it can move with the solid particle
Lin et al. (1985)	Fluidized bed (gas-solid)	Sc-46	• Twelve detectors were arranged in a staggered configuration at three different heights with four detectors at each level. Weighted linear least-square algorithm was used for reconstruction of particle position
Moslemian et al. (1989)	Fluidized bed (gas-solid)	Sc-46	• Digital pulse counting system was used to increase the speed of signal acquisition which resulted in increase in the accuracy of particle position reconstruction
Devanathan et al. (1990)	Bubble Column (gas-liquid)	Sc-46	• RPT was used for first time to investigate gas-liquid flow
Yang et al. (1993)	Bubble column (gas-liquid)	Sc-46	• Used same method as used by Devanathan et al. (1990). Modification in acquisition system to get longer acquisition time of photon counts during experiments
Larachi et al. (1994)	Fluid bed (solid-liquid-gas)	Sc-46	• Used RPT for three phase, developed Monte-Carlo algorithm to generate the

			distance count map for various known locations
Larachi et al. (1995)	Spouted bed (gas-solid)	Sc-46	• Monte-Carlo algorithm was tested by performing various experiments
Degaleesan (1997)	Bubbble column (gas-solid)	Sc-46	• Extensively studied the hydrodynamics of bubble column for different conditions and for different diameters of bubble column
Godfroy et al. (1997)	Fluidized bed (gas-liquid-solid)	Sc-46	• Used artificial neural network algorithm for real time position reconstruction
Roy et al. (2002)	Circulating fluidized bed (liquid-solid)	Sc-46	• Used Monte-Carlo nuclear radiation based model for an optimal design of RPT experiments
Rammohan (2002)	Stirred tank (liquid, liquid-gas)	Sc-46	• Used RPT for the first time to characterize the flow behaviour in stirred tank for single phase and gas-liquid phase
Bhusarapu (2005)	Circulating fluidized bed (gas-solid)	Sc-46	• Developed cross-correlation reconstruction algorithm for reconstruction of instantaneous tracer particle position
Guha et al. (2007)	Stirred tank (gas-solid)	Sc-46	• Used RPT to investigate the flow hydrodynamics in solid-liquid suspension operation
Upadhyay (2010)	Multiphase flow analysis (bubble column)	Cs-137, Au-198, Sc-46	• Implemented next generation RPT. Studies on bubble column for different aspect ratios for a wide range of air flow rate. Implemented RPT for binary fluidized bed using two different tracers.
Dube et al. (2014)	Cylindrical tumbler	Sc-46	• Introduced an optimization strategy to find the optimal position of detectors and orientation used in RPT based on the objective function of maximizing detector resolution

Bashiri et al. (2016)	Stirred tank	Sc-46	• Used RPT to analyze the flow fields and turbulence flows in stirred tank equipped with Rushton turbine and pitched blade turbine
Sharma et al. (2017)	Coiled geometry (oil-water)	Sc-46	• RPT-Time of Flight and RPT-Volume of Fraction were used to study the exit age distribution, radial mixing, flow regimes
Al-Juwaya et al. (2019)	Spouted bed (binary solid-gas)	Co-60	• Through RPT, they investigated the segregation phenomena, particle-particle interaction for hydrodynamics in binary spouted bed

2.2 CFD Modelling of Stirred Tank

In baffled stirred tanks, rotating impellers generate highly turbulent and complex three-dimensional flow structure, as the flow induced by them interacts with the stationary baffles mounted on the tank wall. The flows in stirred tank can be modelled by two approaches, the phenomenological models and the numerical solution of the complete Navier-Stokes equations. The phenomenological models oversimplify the complexity of flow and hence these models can represent only mean velocity fields (Rammohan, 2002).

In order to capture the three-dimensional flow structure in stirred tank, rigorous numerical models are needed. With the advancement in computer technology, CFD techniques based on the Navier-Stokes are being used to solve such a complex flow structure in stirred tanks. The flow field prediction in stirred tanks through CFD is achieved by the turbulence models and impeller rotation model. The details of these aspects are given the following sub-sections.

2.2.1 Modelling of Turbulence

For optimal design of stirred tanks, engineer should have knowledge of velocity and turbulence parameters distributed in space and time domain. The transport equations for incompressible Newtonian fluids are given as follows. These are the continuity and momentum equations and referred as Navier-Stokes equations.

$$\frac{\partial u_i}{\partial x_i} = 0 \qquad (2.1)$$

$$\frac{\partial(\rho u_i)}{\partial t}+\frac{\partial(\rho u_i u_j)}{\partial x_j}=-\frac{\partial p}{\partial x_i}+\frac{\partial}{\partial x_j}\left[\mu\left(\frac{\partial u_i}{\partial x_j}+\frac{\partial u_j}{\partial x_i}-\frac{2}{3}\frac{\partial u_k}{\partial x_k}\delta_{ij}\right)\right]+\rho\vec{g}+\vec{F} \qquad (2.2)$$

These transport equations are solved in three ways in CFD, i) direct numerical simulations (DNS), (ii) large eddy simulations (LES), and (iii) Reynolds-averaged Navier-Stokes (RANS) equations. These approaches are represented on an energy spectrum which is shown in Figure 2.1 (Joshi et al., 2011). Energy spectrum tells the transfer of energy from large scales of motion to the small scales. Energy containing eddies contain most of the kinetic energy whereas the smallest eddies are responsible for the viscous dissipation of turbulence kinetic energy. At intermediate scales, there is neither a direct forcing of the flow nor a significant amount of viscous dissipation, but there is a net nonlinear transfer of energy from the large scales to the small scales. This is called as inertial subrange. In the inertial subrange, negligible dissipation occurs and the dominant energy process is the transfer of kinetic energy from large eddies to smaller eddies by inertial forces (Hemrajani and Tatterson, 2004).

DNS solves the transport equations directly, but it requires huge computational cost. Due to the high computational cost, the transport equations can also be solved using LES and RANS approaches. LES and RANS use the turbulence models and solves the additional equations which arises from space filtering (LES) or ensemble averaging (standard *k*-*ε* model) in Navier-Stokes equations. The overall classification of strategy to solve the Navier Stokes equation is shown in Figure 2.2.

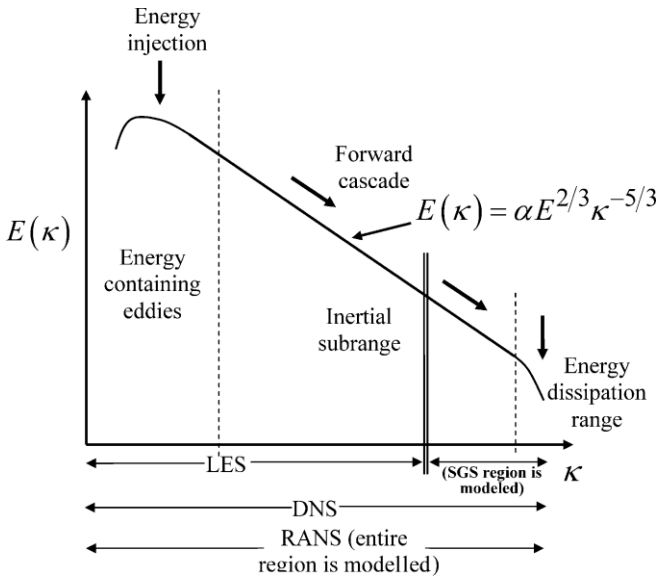

Figure 2.1 CFD model equations based on energy spectrum (Joshi et al., 2011)

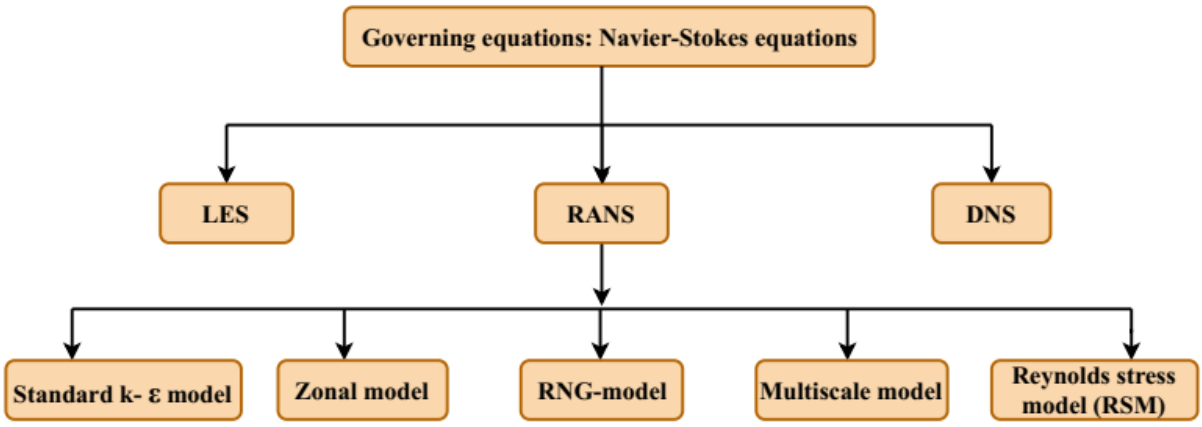

Figure 2.2 Overall classification of CFD models for stirred tanks

(i) Direct Numerical Simulation (DNS)

DNS does not require any turbulence modelling, as all the transport equations are solved exactly. All the scales ranging from small scales (Kolmogorov length scale) to the largest scales are resolved in DNS. For that, accurate estimation of derivatives in RANS equations are required. Earlier, spectral methods are used in DNS method for simple geometries to estimate the derivatives and these methods are extremely accurate. With the advancement in computational technology, numerical techniques such as finite difference and finite element methods are used for DNS computations in the complex geometries like stirred vessels. However, computations using DNS are highly time consuming and requires the large storage space and hence DNS computation are limited to simple geometries and at low Reynolds number (Dewan et al., 2006; Buwa et al., 2006).

Bartels et al. (2000) used RANS based standard *k-ε* model and DNS approaches for modelling stirred tank agitated by flat blade disk turbine at low Reynolds number of 7275 and compared their results with Schafer et al. (1998). DNS as well as *k-ε* model qualitatively predicted the flow fields. In comparison, DNS accurately predicted the secondary vortical structure behind the blades, however, *k-ε* model was unable to capture it. The turbulence kinetic energy and its peak close to the impeller was well predicted by DNS, while, *k-ε* was able to do the same in the region away from the impeller.

(ii) Large Eddy Simulation (LES)

In this approach, the small scale eddies are modelled with the help of subgrid scale (SGS) models, while, large scale eddies are resolved. The SGS models properly incorporates distribution of energy transfer from the large scales to small scales.

The flow fields in the Navier-Stokes equations are decomposed into a large-scale and a small-scale component.

$$u = \bar{u} + u' \tag{2.3}$$

By putting the above decomposition in the Equations 2.1 and 2.2, taking constant density (incompressible flow), the modified equations are written as.

$$\frac{\partial \bar{u}}{\partial x_i} = 0 \tag{2.4}$$

$$\frac{\partial \bar{u}}{\partial t} + \frac{\partial \left(\bar{u}\bar{u}\right)}{\partial x_i} = -\frac{1}{\rho}\frac{\partial \bar{p}}{\partial x_i} + \nu \frac{\partial^2 \bar{u}}{\partial x_i^2} - \frac{\partial \tau}{\partial x_i} \tag{2.5}$$

Subgrid scale models such as Smagorinsky model, scale similarity model, etc are required to estimate the effect of subgrid scale stresses (τ).

LES investigations have important advantages - these are cheaper than the experimental measurements and provide the detailed three dimensional flow structure. Even though LES requires less computational cost compered to DNS, LES still needs high computational power for the optimization of complicated process equipment (Buwa et al., 2006).

(iii) Reynolds Averaged Navier-Stokes (RANS) Approach

RANS is another approach which has been used to solve flow problems in stirred tanks. It is computationally less expensive compared to LES as well as DNS and hence it is extensively used for practical engineering applications (Khopkar et al., 2004; Li et al., 2004). In this approach, basic Navier-Stokes equations are ensemble averaged, then the modified equations can be written in following form.

$$\frac{\partial \langle u_i \rangle}{\partial x_i} = 0 \tag{2.6}$$

$$\frac{\partial}{\partial t}\left(\rho u_i\right) + \frac{\partial}{\partial x_j}\left(\rho u_i u_j\right) = -\frac{\partial p}{\partial x_i} + \frac{\partial}{\partial x_j}\left[\mu\left(\frac{\partial u_i}{\partial x_j} + \frac{\partial u_j}{\partial x_i} - \frac{2}{3}\delta_{ij}\frac{\partial u_k}{\partial x_k}\right)\right] + \frac{\partial}{\partial x_i}\left(-\rho\overline{u_i' u_j'}\right) + \rho\vec{g} + \vec{F} \tag{2.7}$$

The Reynolds stresses term $(-\rho\overline{u_i'u_j'})$ in Equation (2.7) coming out due to the ensemble averaging, it can be modelled using Boussinesq hypothesis :

$$-\rho\rho\left\langle u_i'u_j'\right\rangle = \frac{2}{3}k\rho\delta_{ij} - \mu_t\left(\frac{\partial\left\langle u_i\right\rangle}{\partial x_j} + \frac{\partial\left\langle u_j\right\rangle}{\partial x_i}\right) \tag{2.8}$$

The effective viscosity (μ_t) in Equation 2.8 can be defined by various turbulence models reported in literature from simplest zero-equation model to most complex Reynolds stress model (RSM). The commonly used RANS based turbulence models are discussed in the following section.

Standard *k*-*ε* Model

The basic assumptions associated with the Standard *k*-*ε* model are isotropic turbulence condition and high Reynolds number. In this model, μ_t is determined using kinetic energy of turbulence (k) and its dissipation rate (ε) and the modified equation is given by:

$$\mu_t = C_\mu\rho\frac{k^2}{\varepsilon} \tag{2.9}$$

k-*ε* model results in additional five different turbulence parameters C_μ, $C_{\varepsilon 1}$, $C_{\varepsilon 2}$, σ_k and σ_ε. These turbulence parameters have been obtained from experimental studies. The standard *k*-*ε* model predicts the flow fields satisfactorily in many studies but inaccurate prediction of turbulence kinetic energy distribution due to isotropic nature of model.

Zonal Model

In this model, whole fluid domain is divided into various small zones. Sahu et al. (1998) employed the zonal model for investigation of hydrodynamics in stirred tanks. It has significant advantages, as it identifies the different zones having a specific flow structure and determines the value of turbulence parameters accordingly for further modifications.

Renormalized Group (RNG) *k*-*ε* Model

This is two equations based model which are obtained from renormalized group methods. In RNG *k*-*ε* model, the inertial sub-range eddies are removed from eddy viscosity equation. This model efficiently predicts the turbulence quantities. It is more fundamental compared to semi-empirical models and appropriately predicts flows near the wall (Joshi et al., 2011; Ansys theory guide, 2013).

Multiscale Models

The non-spectral energy equilibrium and two time scales assumptions based multiscale model was developed by Placek et al. (1986). The standard k-ε model assumes equilibrium spectrum and hence a single time scale. As mentioned earlier (Figure 2.1), the CFD simulation models are divided into three energy spectrum regions viz., production region, a transfer region and turbulence dissipation region. The multiscale model has two time scales for the production region and turbulence dissipation rate region. This model consists of two equations, one for the transport of kinetic energy of turbulence of the large-scale vortices and second one for transport of kinetic energy of turbulence of inertial sub-range eddies. It is well suited for the prediction of flow patterns in stirred tanks.

Reynolds Stress Model (RSM)

RSM assumes the isotropic flow condition, also, it properly incorporates streamline curvature, rotational strains and body force effects (Murthy et al., 2008). It is seven equations based model which solves six equations for the Reynolds stresses and one equation for turbulence energy dissipation rate. In RSM, the model parameters for Reynolds stresses are not constant and it varies with the type of flow and hence model needs to be calibrated. It takes the large computational power to get the converged solutions for the system with complex flow. These are the major disadvantages associated with the use of RSM which make its less attractive.

2.2.2 Modelling of the Impeller Rotation

In the CFD modelling of stirred tanks, the impeller rotation can be modelled by the various techniques and these are broadly classified into steady state and unsteady state.

Steady state techniques

The model equations associated with these techniques are solved under steady state condition. Some of the steady state techniques are briefly described in this section. Figure 2.3(a-d) shows the schematic representation of various impeller rotation modelling techniques.

(i) Impeller boundary condition technique (IBC)

In this technique, impeller is considered as a black box (Figure 2.3-a). The impeller is encapsulated with the surface area around it and the boundary conditions are provided on it which are obtained from experimentally measured flow fields and turbulence parameters (Kresta and Wood, 1991). The boundary needs to be changed, if the tank or impeller

configuration changes. After providing boundary conditions, the solution for flow variables for entire flow domain is obtained. The dependency on experimental boundary conditions is the major drawback associated with the use of this technique. It is difficult to predict the fluid dynamics for various tank designs and configurations; as geometrical design parameters strongly affect the flow hydrodynamics (Yapici et al., 2008). Further, it is difficult to get the exact boundary conditions from experiments for the processes involving the multiphase flows.

(ii) Source-sink technique (SS)

Source-sink technique was developed by Pericleous and Patel (1987) wherein rotating impeller is modelled as momentum source and stationary baffles are considered as momentum sinks. In this technique, the impeller blade is divided into number of vertical strips from hub to impeller tip. If the blade is placed at different angle with axis of rotation, then the strip is further divided into number of subsection so that every section (of the blade) is assumed to be practically flat. The blade section inside each strip is approximated to an airfoil and airfoil aerodynamics is applied. The tank wall, baffles and impeller blades are considered as solid surfaces for boundary conditions.

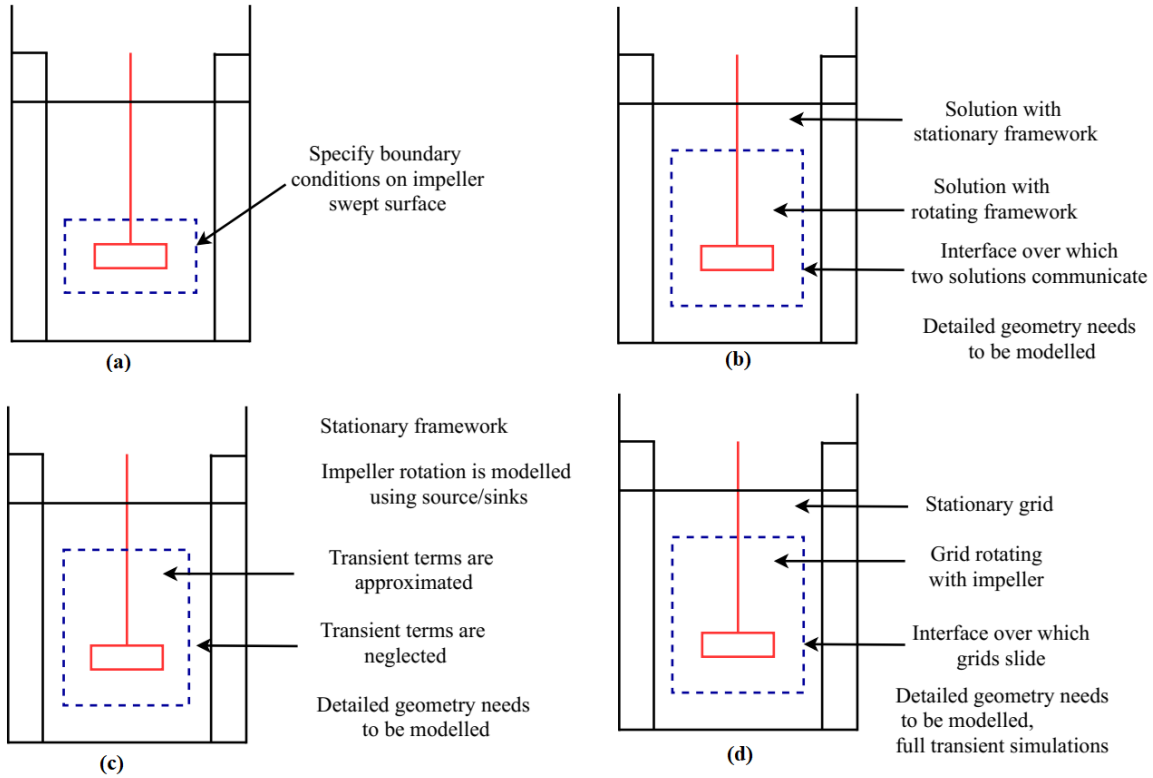

Figure 2.3 Schematic representation of various impeller rotation modelling techniques (Joshi et al., 2011)

(iii) Inner-outer technique (IO)

IO technique has been developed by Brucato et al., (1996) and subsequently used by Daskopoulos and Harris (1996) and Brucato et al., (1998) for prediction of flow hydrodynamics in stirred vessels. In this technique, the region encapsulating the impeller is the inner region and the region of bulk flow with baffles is the outer region. The arbitrary boundary conditions are provided at surface of inner region and simulations are conducted. Thus, it has provided the flow fields and turbulence quantities inside the inner region as well as at the boundary of inner surface. This information is used as boundary conditions for the bulk flow simulations (bulk region). Now, the flow fields are known at the outer boundary surface of inner region and this information is used for second inner simulation. This iterative process continues, until system reaches to an acceptable numerical error. In this approach, a steady state assumption was used for the simulations in each of the inner as well as outer region in its own frame of reference.

(iv) Multiple reference frame technique (MRF)

MRF technique was put forward by Luo et al. (1994) for modeling of impeller rotation. In this approach, stirred vessel is partitioned into two frames, i.e. a moving frame and stationary frame. The moving reference frame encapsulates the impeller and the flow confined by it, and the stationary frame involves the vessel, the baffles and the flow outside moving frame (Figure 2.3-b). MRF approach was used by Naude et al. (1998) for modeling of baffled stirred tank with propeller rotor; the results obtained for time averaged computational mean velocities were found to be in good agreement with LDA measurements. Khopkar et al. (2004) and Dewan et al. (2006) have reported that MRF technique does not require any experimental boundary conditions and has a capability for reasonable prediction of flow fields at less computational cost.

(v) Snapshot technique

Snapshot technique was proposed by Ranade and Dommeti (1996) for modeling of impeller rotation. In this technique, the whole flow domain is divided into inner and outer regions (Figure 2.3-c). The inner region encapsulates the impeller in which time dependent terms are decomposed into spatial gradient and impeller rotation speed. However, outer region neglects the time dependent terms. The spatial derivative term is incorporated to the source term in steady state transport equation. The suction and ejection of the fluid from back and front side

of the blade have been considered by adding the mass sink and source respectively in the transport equations.

The assumptions associated with negligible time dependent terms in the outer region removes the momentum in the transport equations. This model assumes that the baffle does not affect the flow between the blades. Further, this technique is not validated for all flow variables in the entire flow domain. These are the major drawbacks of this technique.

Unsteady state techniques

Some of the time dependent impeller rotation modelling techniques are discussed in this section.

(i) Sliding mesh technique (SM)

SM is fully transient simulation technique which was developed by Luo et al. (1993). In this technique, whole fluid domain is divided into two inner and outer non-overlapping cylindrical zones (Figure 2.3-d). Both zones require separate block grid. The grid associated with the inner zone rotates with impeller, while, the grid associated with outer stationary zones remains under stationary condition. The rotating impeller blades are modelled as solid rotating walls. This technique is used for various studies, because, it does not require any kind of experimental data.

Acceleration terms needs to be added explicitly in momentum equations in order to incorporate the moving grid system. The care should be taken at the interfaces, as the inner zone gird moves with rotating impeller. The solution for this method become complex and also it requires few days to get the solution convergence. Hence, SM requires huge computational cost compared to other approaches. Due to the excessive computational cost, it restricts the use of number of cells for simulation which ultimately affects the prediction of turbulence quantities and shear rate near the blades.

(ii) Moving deforming grid technique (MDG)

Perng and Murthy (1994) proposed MDG method in which single type of time dependent grid is employed for both moving as well as stationary parts. The impeller rotation causes the movement of gird connected to it and this results the deformation of grid over the entire flow domain. The grid around the impeller rotates and after certain deformation is accomplished,

the grid is brought back to its original form and the properties are transferred to the restored grid in a conservative fashion.

In this technique, it is very difficult to maintain the grid quality which ultimately affects the numerical accuracy in the results. The computational requirement is highest for this approach compared all other impeller modelling approaches (Coroneo et al., 2011).

(iii) Impeller modelling within lattice–Boltzmann-LES framework (adaptive force field technique (AFT))

The basic assumption of this technique is that the entire flow domain constitutes of small particles. The transport equations are applied to each of these particles and form the equations like incompressible Navier–Stokes equations. This technique assumes, after each time step, each particle travels a lattice distance which was located at the corner of lattice and collide with other particle. The calculation of forces acting on flow is adjusted in such a way that the prescribed velocities at points within the domain should be maintained and this is called as AFT technique. The impeller and tank wall are considered as a set of control points on their surface. For the points on the impeller surface, the tangential velocities are provided same as that of rotational speed of impeller. The distance of surface point from axis of rotation is also provided. The tangential velocities on tank wall are set to zero. The force fields are adapted by a control algorithm at each interval in such a way that it should suppress the mismatch between actual flow velocity and prescribed values and it should provide control values at the surface points.

Even though this technique properly models the impeller rotation and provides the accurate prediction of flow hydrodynamics, still it has limitations associated with requirement of high computational power. It helps more in understanding the flows near walls and impeller swept region where measurements by experimental technique is difficult (Joshi et al., 2011).

2.2.3 CFD Simulations using Reynolds Averaged Navier-Stokes (RANS) Equation with Multiple Reference Frame (MRF) Technique in a Rushton Turbine (RT) Stirred Tanks

As explained above, the three different turbulence modelling approaches have their respective range of application, advantages and drawbacks. The model should be selected in such a way that it has to predict the results with reasonable accuracy at less computational cost. The use of LES or DNS as a research design tool makes less attractive as both approaches requires huge computational cost. In this view, RANS approach is suitable for CFD modelling of stirred tank

which gives the results with reasonable accuracy at less computational cost compared to former approaches. Similarly, MRF technique is capable of investigating the flow hydrodynamics in stirred tank with a reasonable accuracy and less computational expenses in comparison with all other impeller rotation modelling approaches.

Among the various types of impellers used in baffled stirred tanks, disk turbine (RT) is one of the most generally used and extensively studied radial type of flow impeller. In present work, CFD simulations have been conducted to investigate the flow hydrodynamics in a stirred tank agitated by Rushton turbine using RANS approach in combination with MRF technique. This section deals with literature review on various CFD studies using RANS model with MRF approach for RT stirred tank.

Luo et al. (1993) have used k-ε turbulence model in combination with MRF technique for the first time. They compared only the profiles of tangential and axial velocity while no comparison of turbulence parameters was reported. Large deviations in the prediction of tangential velocity was reported, while, axial velocity was better predicted with maximum percentage deviation of 20%.

Dong et al. (1994) have employed the k-ε with MRF technique to simulate the flow in stirred tank. The prediction of flow pattern was good in the bulk flow region; however radial and axial velocities magnitudes were overestimated in the impeller vicinity. Over estimation of turbulence kinetic energy was found in the impeller stream. The velocity vectors plots were accurately predicted by model.

Luo et al. (1994) used CFD model using MRF technique for impeller rotation modelling. Radial and axial velocities are qualitatively predicted by CFD model with the maximum deviation of 20% and 15% respectively. But, the tangential velocity was poorly predicted. The comparison of turbulence parameters was not provided.

Ciofalo et al. (1996) have employed MRF technique and the k-ε turbulence model as well as the second-order differential stress model (DSM). The predictions of free surface shape and tangential velocity were found in good agreement with experimental results. The predicted values of power number were found considerably smaller than experimental values (15-30%).

Tabor et al. (1998) used MRF and SM techniques for modelling of impeller rotation and the standard k-ε model for turbulence modelling. The flow close to the impeller was well predicted by SM, but MRF missed it. However, MRF predicted the overall vortex pattern at much lesser

computational power compared to SM. A good comparison for prediction of velocity components close to the impeller blade edges between MRF and literature was found. But, over prediction was provided by SM technique. MRF much accurately predicted the radial and tangential velocities near impeller, while considerable deviations in axial velocity were found (around 100%). Axial velocity near tank edges was well predicted with maximum deviation of less than 10% while other two components shown the maximum deviation of 30%. They found that MRF predicts the impeller stream flow behavior in much better way compared to SM.

Bartels et al. (2000) conducted the CFD simulations using standard k-ε model and the DNS with MRF technique for impeller rotation modelling. They performed simulations at low Reynolds number of 7275. DNS accurately predicted the contours plots of turbulence kinetic energy compared to k-ε model. DNS successfully identified the secondary vortices near the hub and disk while k-ε model missed it. Simulation results by both the models qualitatively predicted the upward inclination of flow in the impeller discharge region and existence of ring vortices. Researchers concluded that the flow features predicted by both models showed good agreement while DNS shown better prediction compared to standard k-ε model during close comparison.

Kukukova et al. (2005) carried out CFD simulations to investigate the flow pattern with use of one and two impellers. They used MRF along with standard k-ε model. The prediction of flow fields such as radial, axial and tangential velocities were found in good agreement with those obtained from experiments. In addition, they investigated the concentration profile, mixing time, power number and impeller pumping number. The values of mixing time were under predicted compared to experiments with deviation of 20-45%.

Deglon and Meyer (2006) have conducted CFD simulations using MRF and standard k-ε turbulence model. They considered four different grids and different discretization schemes such as upwind, central and Quadratic Upstream Interpolation for Convective Kinematics (QUICK) to investigate the effect on flow fields and turbulence parameters. They observed that the predictions of mean velocities were not significantly affected by either the grid resolution or discretization scheme. However, predictions of turbulence kinetic energy were strongly affected by both the grid resolution and discretization scheme. They observed that with a significant increase in grid resolution, simulation results accurately predicted the turbulence kinetic energy. Researchers concluded that poor prediction of turbulence parameters may be due to of numerical errors (grid resolution) rather than inadequacies in the turbulence model.

Guha et al. (2006) have developed CFD based compartmental model and investigated the effect of turbulence mixing on the performance of stirred tank reactors. The model was able to capture all the important features of macromixing in stirred reactor. They studied the effect of location of feed on product yield and selectivity for multiple reactions. Researchers found some important conclusions from studies such as, the consideration of dispersion term in the transport equation is important when the reactant feed point is located far from impeller. While, convection is important when reactant feed location is near to impeller.

Alopaeus et al. (2009) used zonal modelling for CFD simulation. In this model, the tank volume is divided into small regions with increasing inner volume from impeller swept volume to total tank volume. They obtained the continuous small and large scale mixing curves for each volume. They investigated the two important parameters (i) pumping number and (ii) turbulence dissipation rate. They conducted various kind of simulations for varying tank size, grid size, discretization schemes, turbulence model and type of impeller.

Coroneo et al. (2011) have carried out RANS based CFD simulations and highlighted the effect numerical errors on prediction of fluid dynamics parameters. They suggested that the errors in the predictions of turbulence parameters can be considerably minimized by reducing grid size. Particularly, the deviation between the power number predicted by torque and by integration of turbulence dissipation rate decreased with decrease in grid size. They observed considerable improvement in the predictions of tracer homogenization dynamics with decrease in grid size. Finally, they concluded that the numerical errors can be reduced with the use of much finer computational grid.

2.3 Effect of Geometrical Parameters on Flow Hydrodynamics inside the Stirred Tanks

In baffled stirred tank reactors, the required mixing can be achieved with the proper adjustment of reactor hardware as well as operating conditions at less energy consumption. It is reported that the performance of stirred tank mainly depends on the geometric and dynamic parameters of the tank as well as the physico - chemical properties of the fluid. The geometric parameters include shape and aspect ratio of stirred tank, impeller clearance, impeller diameter, number and size of the impeller, width of baffles etc. (Montante et al., (1999, 2001); Karcz et al., 2005; Kumaresan and Joshi, 2006; Karcz et al., 2005; Montante et al., 2006; Ochieng et al., 2008; Rao et al., (2009, 2010); Devi et al., 2011; Joshi et al., 2011; Li et al., 2011). Among these

parameters, clearance of the impeller from the tank bottom and diameter of impeller are crucial which control the flow patterns and suitability of the stirred reactor for various processes concerned (Montante et al., 1999; Rao et al., (2009, 2010); Devi et al., 2011; Li et al., 2011; Joshi et al., 2011; Kulkarni and Patwardhan, 2014).

Generally, in a standard configured stirred tanks, the impeller is placed at the 1/3 of tank diameter (*T*) from bottom of tank and the impeller diameter (*D*) is 1/3 of tank diameter. However, the flow hydrodynamics in stirred tanks is considerably affected with the variation in these parameters. This section deals with review on various experimental and numerical investigations reported to analyze the effect of impeller clearance (*C*) and impeller diameter on flow hydrodynamics in stirred tanks.

In a standard configured stirred tank, the double loop flow pattern phenomenon i.e. one above the impeller and one below the impeller, is generally observed (Figure 2.4). However, Nienow (1968) has conducted the experiments at different impeller clearances for solid-liquid system and found that the double loop flow pattern changed into single loop flow pattern when impeller clearance is reduced to 1/6 of tank diameter. This flow pattern resulted in different types of solid distribution throughout the tank. He concluded that suspension of solids can be achieved with lowering the impeller clearance at low impeller speed. Following this, Conti et al. (1981) have developed a correlation for estimation of impeller speed over wide range of impeller clearances. Ibrahim and Nienow (1995) observed that the radial discharge stream of RT changed to axial when the impeller clearance lowered to *T*/6, which means that double circulation loop flow patterns change to single loop flow pattern. The power consumption also dropped with lowering the clearance and the power number was reduced by 25% to that of standard clearance.

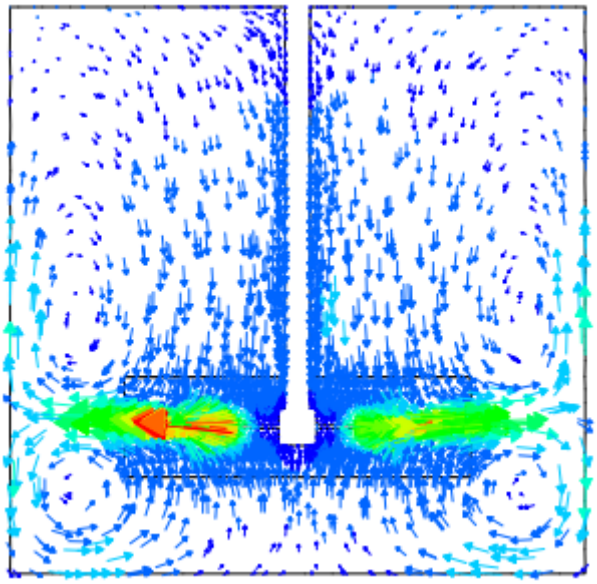

Figure 2.4 Double loop flow pattern associated with standard configured stirred tank (Zhu et al., 2019)

Armenante and Nagamine (1998) have conducted the experiments for four different types of impeller and investigated the effect of impeller clearance on impeller speed for suspension of solids and power consumption. Further, they developed a correlation quantifying the effects of impeller clearance and other parameters on impeller speed for solid suspension when the impeller was placed near the tank bottom. They found that the mixed and axial flow impellers were more energy efficient than radial flow impellers. Researchers noticed that the minimum speed of impeller for complete suspension of solid increases with lowering *C/T* ratio when it approaches to zero.

Montante et al. (1999) have investigated the effects of impeller clearance and its rotational speed on flow characteristics by experimental LDA technique in Rushton turbine stirred tank. The transition of flow pattern from double loop to single loop occurred at the impeller off-bottom clearance around *T*/5 with impeller discharge stream inclined towards the tank bottom at angle around 25° to 30°. The inclination angle of impeller discharge stream varied in radial direction from impeller as well as with angular position between blades. Flow patterns, mean velocities and normalized turbulence parameters were found unchanged with impeller speed for impeller clearances (*C/T* >0.20 or *C/T*<0.15). Therefore, for solid-liquid mixing processes solids can be suspended at lower power with minimum agitator speed. Montante et al. (2001) have tested the capability of CFD model in prediction of flow pattern at various impeller clearances by comparing CFD results with their experimental LDA data (Montante et al.,

1999). The single loop flow pattern was correctly predicted by CFD model. A reasonable agreement between CFD predictions and experimental results was observed for mean flow fields but the angle of impeller discharge stream was overestimated at high clearances. The power number was also well predicted by CFD model and dropped down with lowering impeller clearance. Researchers investigated the details of flow characteristics at $C/T = 0.15$ and a good agreement was found with experimental results. Periodic component of kinetic energy was well predicted, but the random component was underestimated in comparison with experimental results. They tried to improve the CFD predictions with grid refinements and different turbulence models and suggested that further improvements in turbulence model is needed for predictions.

Patil et al. (2004) have experimentally studied the effect of impeller submergence and impeller diameter on mass transfer characteristics in surface aerators. At high impeller submergence the liquid jet stream found deflected towards the liquid surface and this phenomenon resulted in rise of gas-in-liquid dispersion. Subsequently, increase in mass transfer coefficient, bubble entrapment and vortex was observed at the liquid surface. They found the liquid side mass transfer coefficient was high for lower impeller diameter. Deshmukh and Joshi (2006) have reported the similar observations with decreasing power number near gas-liquid interface.

Yapici et al. (2008) have conducted the CFD simulations using LES along with clicking mesh for impeller rotation modelling in Rushton turbine stirred tank. They investigated the effect of design as well as operating parameter on flow hydrodynamics. The design parameters included the impeller off-bottom clearance and the impeller disk thickness, while operating parameter included the Reynolds number based on impeller rotational speed. The mean velocities were well predicted by CFD model when compared to experimental literature data. A smoother circulation flow pattern was observed when impeller was located close to tank bottom. Power number linearly decreased in laminar range while power number was found to be invariant in turbulence regime. They found that the power number decreases with increase in disk thickness.

Ochieng et al. (2008) have carried out the LDV experiments and the CFD simulations at low impeller clearance in Rushton turbine stirred tank and investigated the velocity fields and the mixing time. They observed the transformation of double loop flow pattern to single loop with lowering the impeller clearance and the mixing time was reduced by 35% compared to that of observed standard clearance. Researchers also found that the use of draft tubes at low clearance

enhanced the mixing rate and suppressed the dead zones, and the mixing time reduced by 50%. CFD model over-predicted the mixing time compared to that obtained from experiments. Researchers reported that the reason for over-prediction was k-ε model which under predicted the turbulence intensity.

Nurtono et al. (2008) have performed CFD simulations using LES and sliding mesh to investigate the effect of impeller clearance on Macro-instabilities. The identification of macro-instabilities occurrence was done by visually observing velocity vectors and time series analysis of both velocity fields in bulk flow and dynamic pressure on the tank wall. They observed the secondary circulation loop and asymmetric flow pattern beside the mean flow pattern.

Rao et al. (2009) have experimentally found that the oxygen transfer rate in both baffled and unbaffled surface aeration tanks increases with the impeller clearance up to the optimum clearance and decreases further. The optimum clearance (C/D) for baffled and unbaffled surface aerators have been reported to be 1.0 and 0.94 respectively. They also found high oxygen transfer rate at lower values of impeller diameter for baffled surface aerators. Continuing this, Rao et al. (2010) have found that the power number was almost constant for C/H <1 and decreased thereafter.

Devi et al. (2011) investigated the effect of impeller clearance on oxygen transfer rate and power consumption at various impeller diameters. They found that at high clearance the power consumption for mixing reduced and increased in oxygen transfer rate. They found the optimal clearance range of 0.7 to 0.9 times the impeller diameter.

Li et al. (2011) have carried out the PIV experiments and large eddy simulations at clearance of C/T = 0.15 (low clearance) to investigate the single loop flow field in RT stirred tank. They observed that behind the blades the regions with high level of turbulence kinetic energy were affected by movement of trailing vortices. Two counter-rotating vortices generated behind the blades gradually moved towards the tank bottom with angular rotation when $D = T/3$. They investigated the effect of impeller diameter as well as Reynolds number on flow hydrodynamics. Reynolds number has not significantly affected the mean flow fields and turbulence parameters for configuration of impeller diameter (D) = $T/3$, C/T = 0.15. They observed that the single loop flow pattern was gradually transformed into a double loop at C/T = 0.15 when impeller diameter (D) was increased from $T/3$ to $T/2$.

Kulkarni and Patwardhan (2014) have investigated the phenomenon of gas entrainment in stirred tank using CFD model. They found that the surface aeration process at gas-liquid interface was characterized by exchange of momentum across the interface from liquid side to air side. The instantaneous axial velocities on air side, strain rates on air side, interfacial momentum exchange and air side vorticities were maximum during the gas entrainment.

Basavarajappa et al. (2015) have performed the steady state CFD simulations for stirred tank agitated by Rushton turbine and floatation impeller. The mean flow fields predicted by Rushton turbine were found in a reasonable agreement with literature LDA data. For Rushton turbine, the mean flow characteristics were invariant with Reynolds number. For flotation impeller, impeller size (D) as well as impeller clearance (C) were varied. Researchers observed the transition of double loop flow pattern to a single loop when impeller clearance was decreased for $D = T/3$. However, no such phenomenon was observed for $D = T/4$ with decreasing impeller clearance. Based on this, they suggested that impeller size and impeller location from tank bottom may affect the critical flow transition clearance. The power number calculated by dissipation rate was severely underestimated by Reynolds stress model.

Chara et al. (2016) investigated the velocity fields in a Rushton turbine stirred tank by using experimental PIV technique and detached eddy simulations (DES) when impeller was located in the mid height of tank. The velocities in impeller vicinity were in a reasonable agreement with the experimental data in radial and axial direction, but tangential velocities were slightly under predicted. Further researchers were able to determine the position and strength of trailing vortices. They concluded that DES is suitable research tool for prediction of turbulence flow fields in a stirred tank agitated by RT.

Zhu et al. (2019) investigated the transition of double loop flow pattern to single loop at low impeller clearance and its effect on macro mixing efficiency using CFD simulations. They found that the critical range of impeller clearance wherein such a flow transition occurred, decreased with increase in impeller diameter and suggested such phenomenon may be easily formed at small Rushton turbines. Researchers observed that at low impeller clearances discharge deflected towards tank bottom, if it hits the tank wall first then the double loop will form, if it hits tank bottom then the single loop will form. They suggested that a single loop flow pattern is helpful to enhance rate of macromixing as the mixing time decreased by 35% at same power input. Further they compared the single loop formed by Rushton turbine and 45° pitched blade turbine. Single loop formed by RT was found less efficient than that of pitched

blade turbine and generally it takes 60% more time to accomplish the same level of macromixing at same power input.

Table 2.2 Brief of literature on effect of geometrical parameters on flow hydrodynamics in stirred tank

Author	Impeller type	Methods	Remarks from literature
Nienow (1968)	RT	Flow Visualization	• Double loop flow pattern changed into single loop flow pattern when impeller clearance is reduced to 1/6 of tank diameter • Suspension of solids can be achieved with lowering the impeller clearance at low impeller speed
Ibrahim and Nienow (1995)	RT	Flow visualization	• Radial discharge stream changed to axial at $C = T/6$ • Power number also reduced by 25% at $C = T/6$
Armenante and Nagamine (1998)	Flat blade turbine, RT, PBT, Fluidfoil chemineer	Flow visualization	• Mixed and axial flow impellers were more energy efficient than radial flow impellers at low clearances • Minimum speed of impeller for complete suspension of solid increases with lowering C/T ratio when it approaches to zero
Montante et al. (1999)	RT	LDA	• Double loop to single loop occurred at $C = T/5$ with impeller discharge stream inclined towards the tank bottom at angle around 25° to 30° • Flow patterns, mean velocities and normalized turbulence parameters were found unchanged with impeller speed for impeller clearances ($C/T > 0.20$ or $C/T < 0.15$)

Montante et al. (2001)	RT	CFD	• Experimental work conducted by Montante et al. (1999) was computationally modelled
Patil et al. (2004)	RT	Experimental	• At high impeller submergence, discharge stream deflected towards liquid surface and increases the gas dispersion rate • Lower impeller diameter has given high value of mass transfer coefficient
Yapici et al. (2008)	RT	CFD	• A smoother circulation flow pattern was observed at low clearance • The power number decreases with increase in disk thickness
Ochieng et al. (2008)	RT	LDV and CFD	• Mixing time was reduced by 35% compared at lower clearances to that of observed standard clearance • CFD model over-predicted the mixing time compared to that obtained from experiments
Rao et al. (2009)	RT	Experimental	• The optimum clearance (*C/D*) for oxygen transfer rate for baffled and unbaffled surface aerators reported to be 1.0 and 0.94 respectively. • High oxygen transfer rate at lower values of impeller diameter for baffled surface aerators
Rao et al. (2010)	RT	Experimental	• Power number was almost constant for $C/H<1$ and decreased thereafter
Devi et al. (2011)	RT	Experimental	• At high clearance the power consumption for mixing reduces and oxygen transfer rate increases

Li et al. (2011)	RT	PIV and CFD	• At *C/T*=0.15, high level of turbulence kinetic energy behind the blades affected by movement of trailing vortices
Kulkarni and Patwardhan (2014)	RT and PBT	CFD	• At gas liquid-interface, the instantaneous axial velocities on air side, strain rates on air side, interfacial momentum exchange and air side vorticities were maximum during the gas entrainment
Basavarajappa et al. (2015)	RT, Flotation impeller	LDA and CFD	• For Rushton turbine, the mean flow characteristics were invariant with Reynolds number • For flotation impeller, impeller size and impeller location from tank bottom may affect the critical flow transition clearance
Chara et al. (2016)	RT	PIV and DES	• A reasonable comparison between experiments and model for mean velocities was observed when impeller was located at *C=T/2*
Zhu et al. (2019)	RT	CFD	• Critical range of flow pattern transition decreases with increase in impeller diameter • At low clearance, the rate of macromixing increased while mixing time decreased by 35%

2.4 Scope and Motivation for the Present Study

As observed from various studies reported in the literature (Moslemian et al., 1989; Degaleesan, 1997; Rammohan et al., 2001(a,b) ; Upadhyay, 2010), there are several key factors

such as the tracer particle selection, calibration of the detectors and signal processing which strongly affect the reliability and accuracy in the RPT measurement. Calibration is an important step in RPT wherein radiation intensity emitted by the fixed radioactive tracer particle in the fluid domain needs to be recorded by detectors placed around the stirred tank. No specific data is available in the literature whether the calibration step is to be performed under stationary or moving condition of the fluid inside the stirred tank (Rammohan, 2002; Guha et al., 2007; Bashiri et al., 2016). Thus, it is proposed to address this gap in the present work by conducting the calibration measurement at various known locations in both conditions of fluid motion. The radiation intensity (counts) obtained under both these conditions will be analyzed by Analysis of Variance (ANOVA) statistical method. Further, RPT technique data will be compared with the well-established LDA technique data.

Due to the inherent limitations in the experimental techniques, it is proposed to develop CFD model of stirred tank for investigating the flow hydrodynamics. In the CFD model of stirred tank using MRF technique for modelling of impeller rotation, the dimensions of inner-rotating fluid zone are required to be determined. Though various researchers have used MRF technique (Dong et al., 1994; Ciofalo et al., 1996; Deglon and Meyer, 2006; Ochieng et al., 2008; Basavarajappa et al., 2015), they have not studied the optimality of the dimensions of inner-rotating fluid zone. This gap is addressed in the present work by performing a series of steady state CFD simulations at various dimensions of inner-rotating zone. The optimal dimensions of inner-rotating fluid zone will be determined by comparing the flow characteristics with the experimental literature data. Further, CFD model with optimal inner-rotating fluid zone will be validated with the current RPT work and literature data.

The calibrated and validated CFD model will be used to investigate the effect of geometrical parameters such as impeller clearance and impeller dimeter on flow hydrodynamics. The location of impeller has a strong impact on flow hydrodynamics inside the stirred tank (Nienow, 1968; Conti et al, 1981; Montante et al., (1999, 2001); Patil et al., 2004; Deshmukh and Joshi, 2006; Ochieng et al., 2008; Rao et al., (2009, 2010); Li et al., 2011; Devi et al., 2011; Basavarajappa et al., 2015; Zhu et al., 2019). The impeller located near the tank bottom and mid height of tank have been well studied. But the impeller located at the tank top near gas-liquid interface has not been much investigated. While, impeller located at tank top are very useful in various gas-liquid operations to enhance oxygen transfer rate (Patil et al., 2004; Deshmukh and Joshi, 2006; Rao et al., 2009; Devi et al., 2011; Kulkarni and Patwardhan, 2014). This gap is addressed in the present work by performing a series of steady state CFD

simulations for impeller located from tank bottom to tank top and their effects on the flow patterns, global flow fields, mean velocity fields and turbulence parameters will be investigated. The impeller diameter is one of the geometrical parameters which affects the flow hydrodynamics. Some of the researches (Patil et al., 2004; Deshmukh and Joshi, 2006; Rao et al., (2009, 2010) have investigated the effect of impeller diameter on rate of oxygen transfer and power consumption. But the effect of impeller diameter on flow hydrodynamics (flow fields and turbulence parameters) has not been investigated. This gap is addressed in the present work by performing a series of steady state CFD simulations at various impeller dimeters and their effects on power number, mean velocities and turbulence parameters will be investigated.

To accomplish the above mentioned research gaps, in the present work, a standard configured stirred tank equipped with rotating impeller and four equally spaced baffles will be used (Holland and Chapman, 1966; Rammohan et al., 2001 (a,b)). The widely investigated radial type of six bladed disk turbine (Rushton turbine) is selected as stirrer. The rotational speed of impeller will be kept at 200 rpm for RPT experiments as well as CFD simulations. This is the range of impeller speed where fully turbulence flow condition is achieved for standard configured stirred tank and generally used in the various mixing operations (Wu and Patterson, 1989; Rammohan et al., 2002; Montante et al., 1999; Basavarajappa et al., 2015). For current RPT experiments, a radioactive source of Sc-46 emitting γ-radiations will be used. It has been widely used for various RPT studies in the literature (Rammohan et al., 2001; Guha et al., 2007; Bashiri et al., 2016). NaI(Tl) scintillation detectors were used for determination of γ-radiations emitted by radioactive source and these detectors are robust, rugged and relatively inexpensive (Upadhyay, 2010). In CFD modelling of stirred tank, Reynolds Averaged Navier-Stokes (RANS) approach was used to solve transport equations of flow variables. It is computationally less expensive in comparison with large eddy simulation (LES) and direct numerical simulation (DNS) approaches (Murthy et al., 2008; Joshi et al., 2011). A steady state multiple reference frame (MRF) technique was used for modelling of impeller rotation. This technique does not require any experimental boundary conditions and has a capability for reasonable prediction of flow fields at less computational cost (Khopkar et al., 2004; Dewan et al., 2006).

Chapter 3

Materials and Methods

This chapter presents the details of steps involved in the implementation of experimental Radioactive Particle Tracking (RPT) setup for stirred tank, data processing and analysis methods, and CFD methodology used for modelling of stirred tank. It is broadly divided into the following sections:

3.1 Experimental Work
3.2 Monte-Carlo Algorithm
3.3 Analysis of Variance (ANOVA) Technique
3.4 CFD Methodology

3.1 Experimental Work

The following experimental aspects have been described in this section:

- The Stirred Vessel Configuration and Experimental Conditions
- The RPT Technique
- The RPT Setup for Stirred Tank
- Preparation of Neutrally Buoyant Tracer Particle
- Calibration of Detectors and Data Acquisition System
- Calibration Measurement in RPT Experiment

3.1.1 The Stirred Vessel Configuration and Experimental Conditions

The standard type of stirred tank was used in the study. It consists of a cylindrical tank with four equally spaced baffles of width $b = T/10$ and six bladed Rushton Turbine (RT) as a stirrer (Figure 3.1). All parts of stirred vessels were made from transparent material (acrylic). Water was used as working fluid. The diameter of the stirred tank (T) is 0.3 m and water is filled up to a height $H = T$. The impeller diameter (D) was kept at $T/3$. The length (l) and width (w) of the blade were kept at $D/4$ and $D/5$ respectively. The thickness of blade and turbine disk was 0.002 m. The impeller was kept at off-bottom clearance (C) of $T/3$. The rotational speed of impeller (N) was 200 rpm. The details of dimensions of stirred vessels and operating conditions are given in Table 3.1.

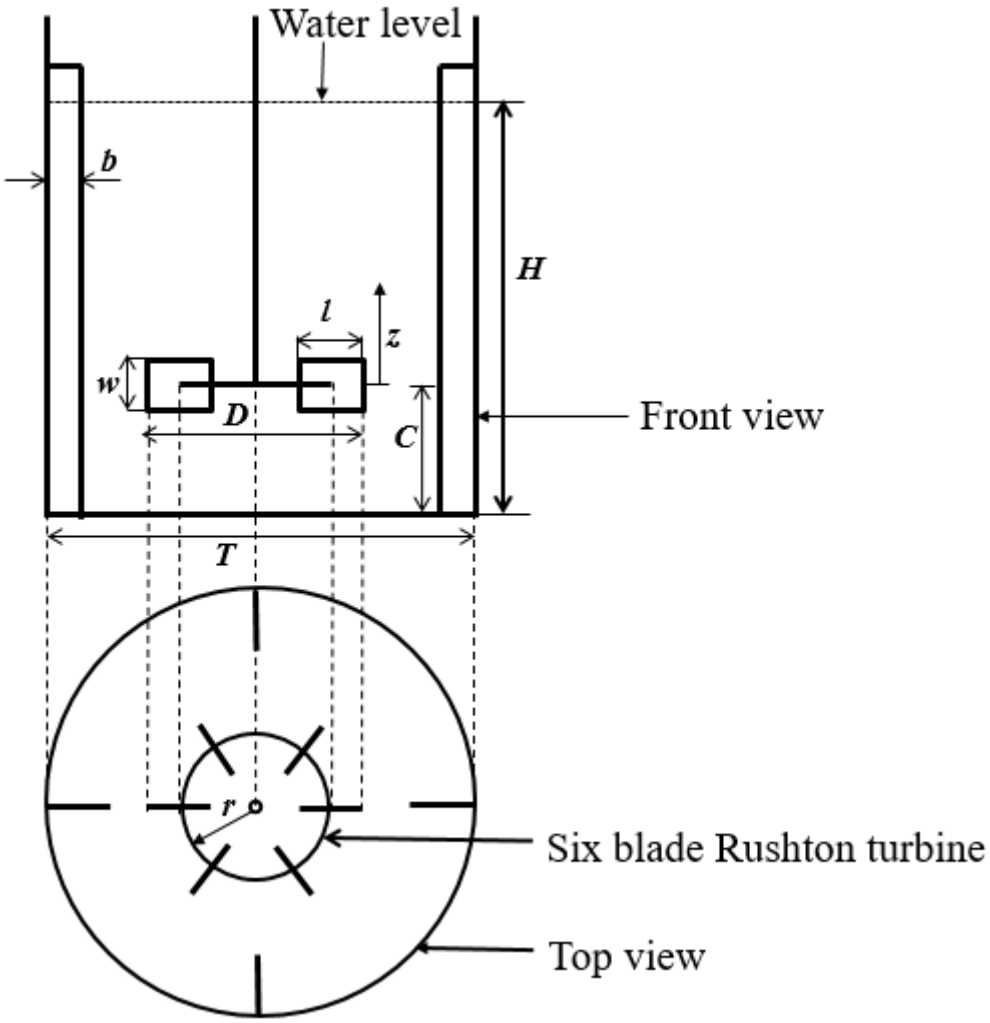

Figure 3.1 Configuration of stirred tank with Rushton turbine

Table 3.1 Stirred vessel configuration and operating conditions

Tank diameter (T)	0.3 m
Water height in tank (H)	0.3 m
Baffle width (b) = T/10	0.03 m
Impeller diameter (D)	0.1 m
Blade width (w) = D/5	0.02 m
Blade length (l) =D/4	0.025 m
Turbine location from bottom of tank (C) = T/3	0.1 m
Density of Water (ρ)	998.2 kg/m^3
Viscosity of Water (μ)	0.001003 Pa.s

3.1.2 The RPT Technique

RPT was used to study the hydrodynamics of water in stirred tank. A γ-ray emitter Sc-46 having strength of 250μCi was used as tracer particle. This particle was chosen for present work, as it is well suited for RPT experiments and same particle was used by Rammohan et al. (2001a) for investigating the flow hydrodynamics in a stirred tank. The path followed by tracer particle was tracked with the help of scintillation detectors placed around the stirred vessel. The particle was designed such that it was neutrally buoyant with the water. During experiments, the tracer particle was allowed to move freely inside the vessel. The position of the tracer particle was determined by an array of scintillation detectors that monitor the γ-rays emitted by the tracer particle. The intensity of radiation recorded at each detector decreases exponentially as the distance between the particle and detector increases and vice-versa. In order to determine the position of the tracer particle from the measured radiation intensities, a calibration step was performed prior to the RPT experiments by placing the tracer particle at various known locations. The data acquired from RPT experiments and calibration measurements was used in Monte-Carlo reconstruction algorithm to determine instantaneous position of tracer particle. The instantaneous velocities were calculated by time differentiation between two successive instantaneous positions. Further, mean velocities were evaluated by time averaging of instantaneous velocities. Following formulae are used for calculation of flow fields.

Instantaneous velocities

$$V_r = \frac{2}{\Delta t}[r_2 \cos(\theta_2 - \theta_1) - r] \tag{3.1}$$

$$V_\theta = \frac{2}{\Delta t}[r_2 \sin(\theta_2 - \theta_1)] \tag{3.2}$$

$$V_z = \frac{\Delta z}{\Delta t} \tag{3.3}$$

$$\text{where, } r = \frac{1}{2}\sqrt{r_1^2 + r_2^2 + 2r_1 r_2 \cos(\theta_1 - \theta_2)} \tag{3.4}$$

Mean velocities

$$\left\langle v_q(i,j,k) \right\rangle = \frac{1}{N(\mathrm{i,j,k})} \sum_{n=1}^{N(\mathrm{i,j,k})} v_{q,n}(i,j,k) \tag{3.5}$$

3.1.3 The RPT Setup for Stirred Tank

The RPT set up consists of 8 NaI (TI) scintillation detectors which were strategically mounted on steel supports. Four steel supports were placed around the stirred tank at an angle of 90° to each other. On each support, two detectors were mounted and their faces were kept perpendicular to the tank wall. Figure 3.2(a) depicts the photograph and Figure 3.2(b) depicts the schematic of RPT setup for the stirred tank.

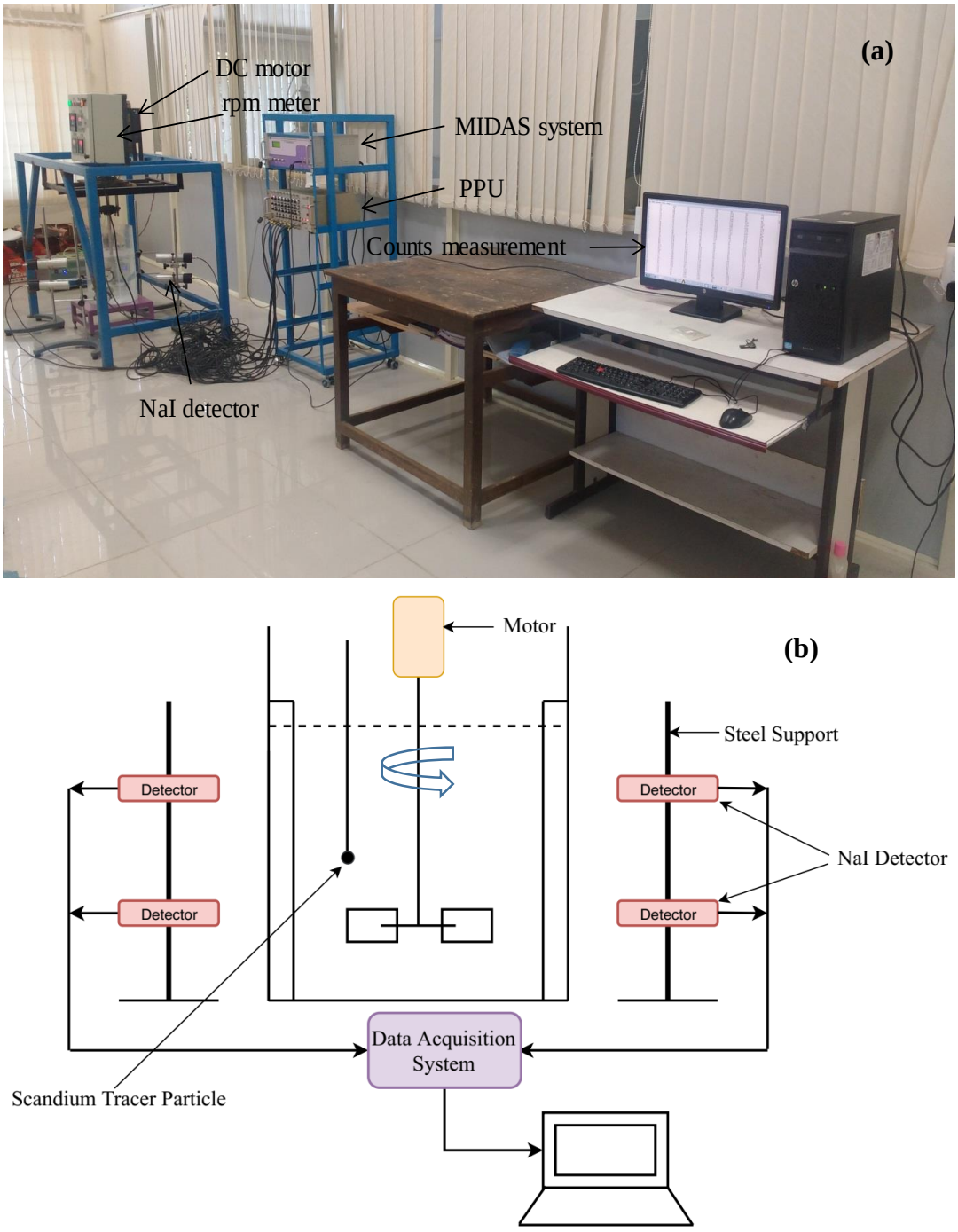

Figure 3.2 Photograph (a) and schematic (b) of RPT setup for stirred tank

The radiations emitted by radioactive tracer particle were sensed by NaI detectors and then processed by data acquisition system. Power was supplied to drive a DC motor which was connected to the rotating shaft of the impeller. With the help of a variable rpm meter, the speed of rotating impeller was controlled. High precision laser Tachometer was used for measuring the speed of rotating shaft.

3.1.4 Preparation of Neutrally Buoyant Tracer Particle

The radioactive tracer particle was made neutrally buoyant in order to mimic the water. In the preparation of neutrally buoyant tracer particle, the plastic ball having 3 mm diameter was taken and it was drilled from one side to make a hole of size slightly greater than 1 mm. After that, the radioactive particle Sc-46 of 1 mm in diameter was inserted into the hole, then the hole was sealed. The density of a neutrally buoyant tracer particle (ρ_p) was measured to be 984 kg/m^3. Figure 3.3 shows the schematic (a) and photograph (b) of preparation of neutrally buoyant tracer particle respectively.

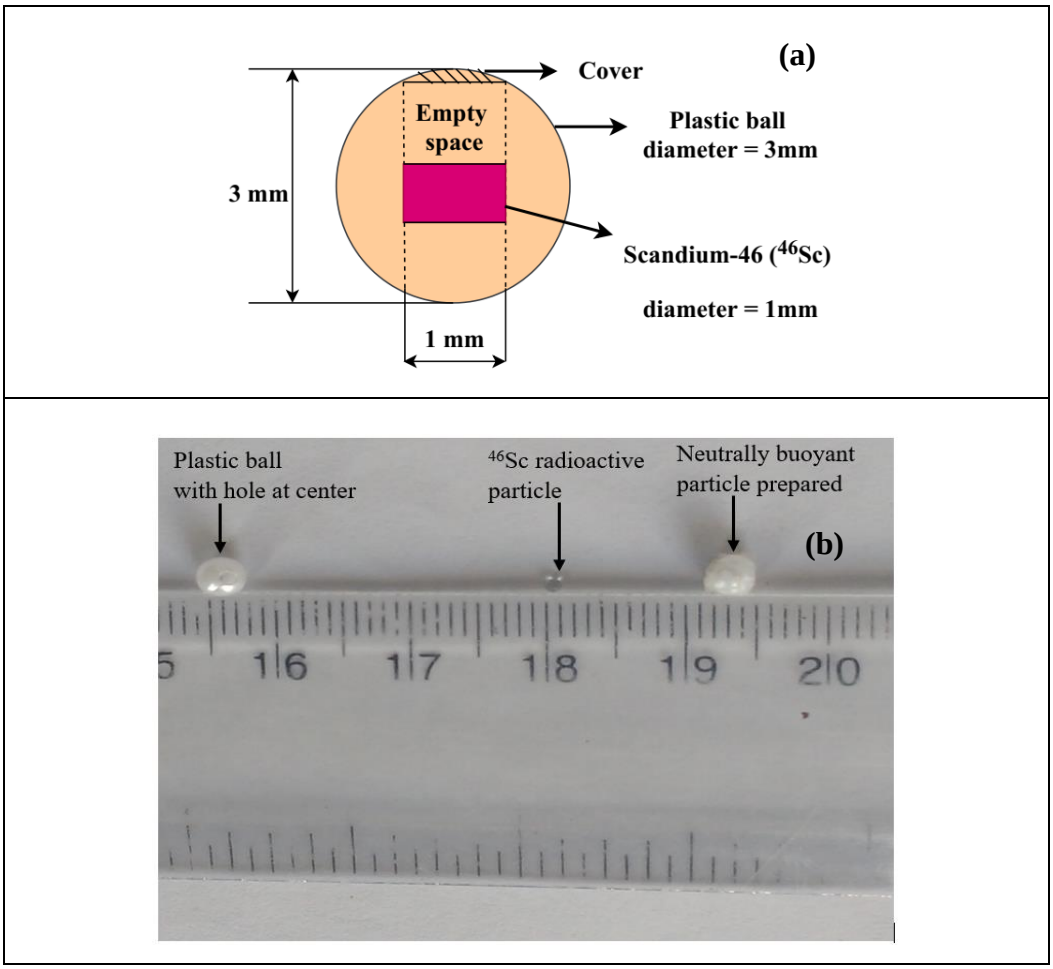

Figure 3.3 Schematic (a) and photograph (b) of preparation of neutrally buoyant tracer particle

3.1.5 Calibration of Detectors and Data Acquisition System

Before actually working on RPT experiments, it is important to test the capability of electronics parts for the desired measurement of counts emitted by a radioactive particle. Multi Input Data Acquisition System (MIDAS) unit is an interface between the data received from a detector at one end and provides the data to a computer on the other end. MIDAS unit consists of the following components:

- Power supply
- High voltage (HV) supply
- Amplifier and Single Channel Analyser (SCA) circuit for each detector

The power supply of 5V to 15V was given to provide the high voltage to each individual module. This voltage is then converted to high voltage with the help of Pulse Processing Unit (PPU) provided in MIDAS. High voltage was set at 750 V based on the specifications provided by the manufacturer.

Single Channel Analyser (SCA) is also called as a discriminator and it counts the total number of photons received at detectors between the upper (ULD - upper level discriminator) and lower (LLD - lower level discriminator) threshold. In order to verify the radiation counts measured only from Sc-46 particle, the typical energy spectrum of a source having two energy peaks of 946 KeV and 1.2 MeV were adjusted with the help of oscilloscope as shown in Figure 3.4. In this way, each channel was calibrated to the photon energy of Sc-46 particle.

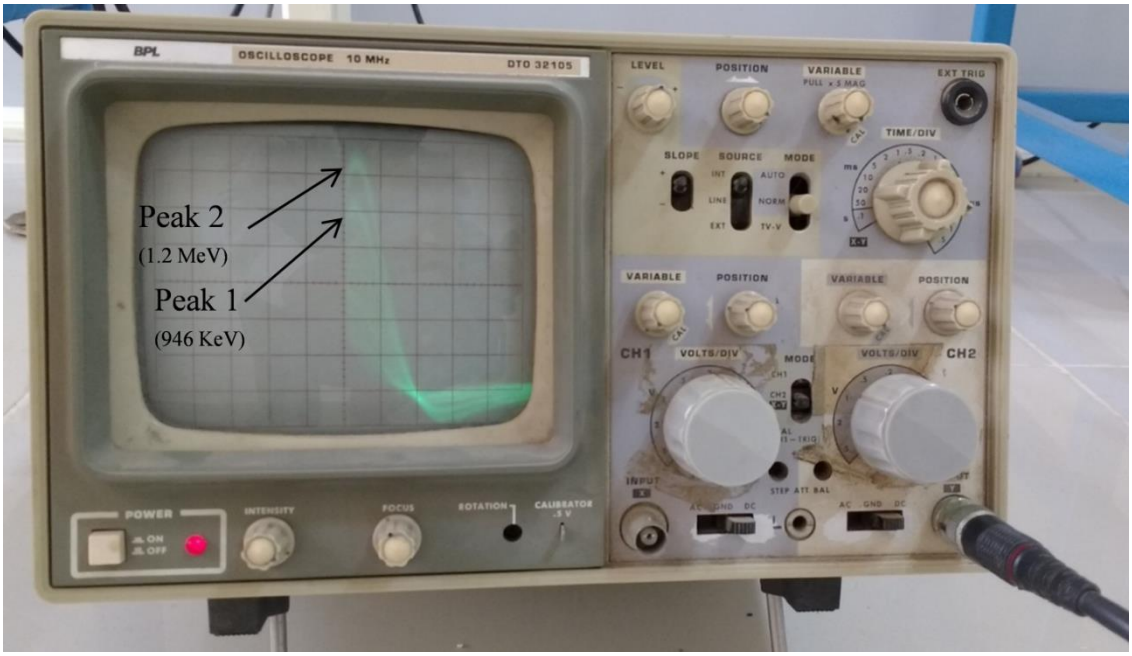

Figure 3.4 Oscilloscope showing energy peaks for Sc-46 source

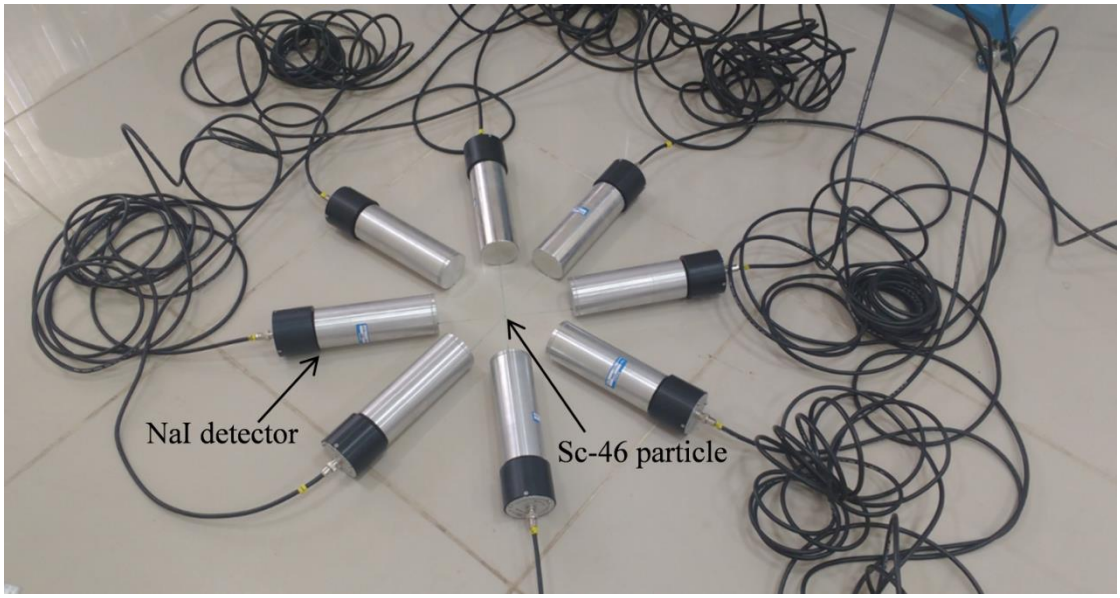

Figure 3.5 Testing of detectors to obtain the intensity versus distance map

Initially experiments have been performed for calibration of detectors. In this, a radioactive particle was placed at the center and all eight detectors were placed at equal distance from a particle in a circular fashion. Figure 3.5 depicts the testing of detectors to obtain the intensity-distance count map. The data was acquired simultaneously by all detectors at a single location of particle at frequency of 50Hz (Rammohan et al., 2001(a,b); Guha et al., 2007). Once the measurement was done at a single location of detector, all detectors were moved away from a particle with an increment of 3 cm. The measurements were done at seven different locations of detectors. Figure 3.6 show the radiation counts measured by MIDAS at a fixed location of tracer particle. There are eight channels for eight 8 detectors.

As it is well known in radiation physics, intensity reduces exponentially with the distance between particle and detector. The intensity is a function of the distance between particle and detector, and is expressed using Taylor's expansion of Beer's law:

$$I = f\left(\frac{1}{d}\right) \tag{3.6}$$

where f is a polynomial function of each detector (Devanathan et al., 1990; Degaleesan, 1997). Similar kind of analysis was done for all detectors to verify the capability of detectors. Figure 3.7 shows the plot of radiation intensity versus distance between particle and detector measured by all detectors. It can be seen that all detectors followed the exponential law of radiation intensity.

Name of the Company :
Name of the Experiment :
Experiment Date :
Dwell Time : 200 mS
Events : 10000
Comments :
Trigger : Internal
Block : 1

Event	Channel:1	Channel:2	Channel:3	Channel:4	Channel:5	Channel:6	Channel:7	Channel:8
1	3059	3013	2892	2895	3121	2855	3076	2988
2	3072	2925	2977	2858	2998	2932	3022	3098
3	2968	2980	2803	2862	3069	2851	2990	2976
4	3058	3010	2725	2871	3083	2942	3088	3032
5	3037	2991	2987	2875	3072	2798	3079	3035
6	2969	2916	2809	2932	3106	2935	3066	3049
7	3005	3032	2968	2922	3046	2848	2986	3049
8	2986	3048	2774	2907	3008	2925	3028	3066
9	3075	3078	2903	2870	3137	2946	3022	3071
10	3079	3028	2880	2895	3100	2817	3075	3077
11	2976	2928	2865	2780	3071	2862	3049	3018
12	3043	2915	2877	2998	3196	2846	3059	3039
13	2985	2992	2916	2860	3069	2866	3004	3027
14	3071	3013	2807	2942	3118	2872	3096	3008
15	2996	2969	3013	2905	3102	2975	3099	3123
16	3021	3073	2877	2834	3001	2786	3017	3038
17	2964	3116	2891	2932	3103	2859	2961	3059
18	2997	3033	2812	2959	3112	2905	3117	2985
19	3082	2891	2889	2849	3082	2921	3136	2989
20	3011	3007	2880	2902	3163	2883	3160	3069
21	3070	2955	2847	2880	3105	2801	3092	2963
22	3112	3000	2942	2899	3004	2772	2974	2945
23	2999	2991	2818	2844	3030	2854	3038	3007
24	2994	3098	2826	2921	3039	2848	3176	3023

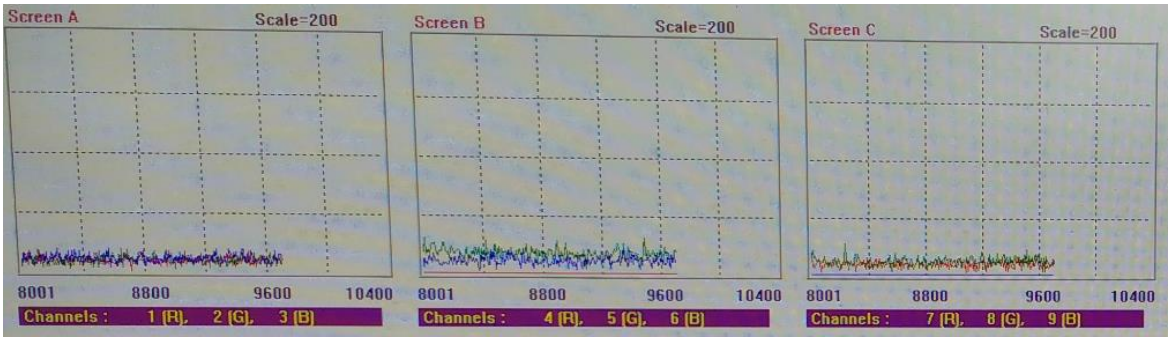

Figure 3.6 Radiation intensity counts measured by MIDAS software

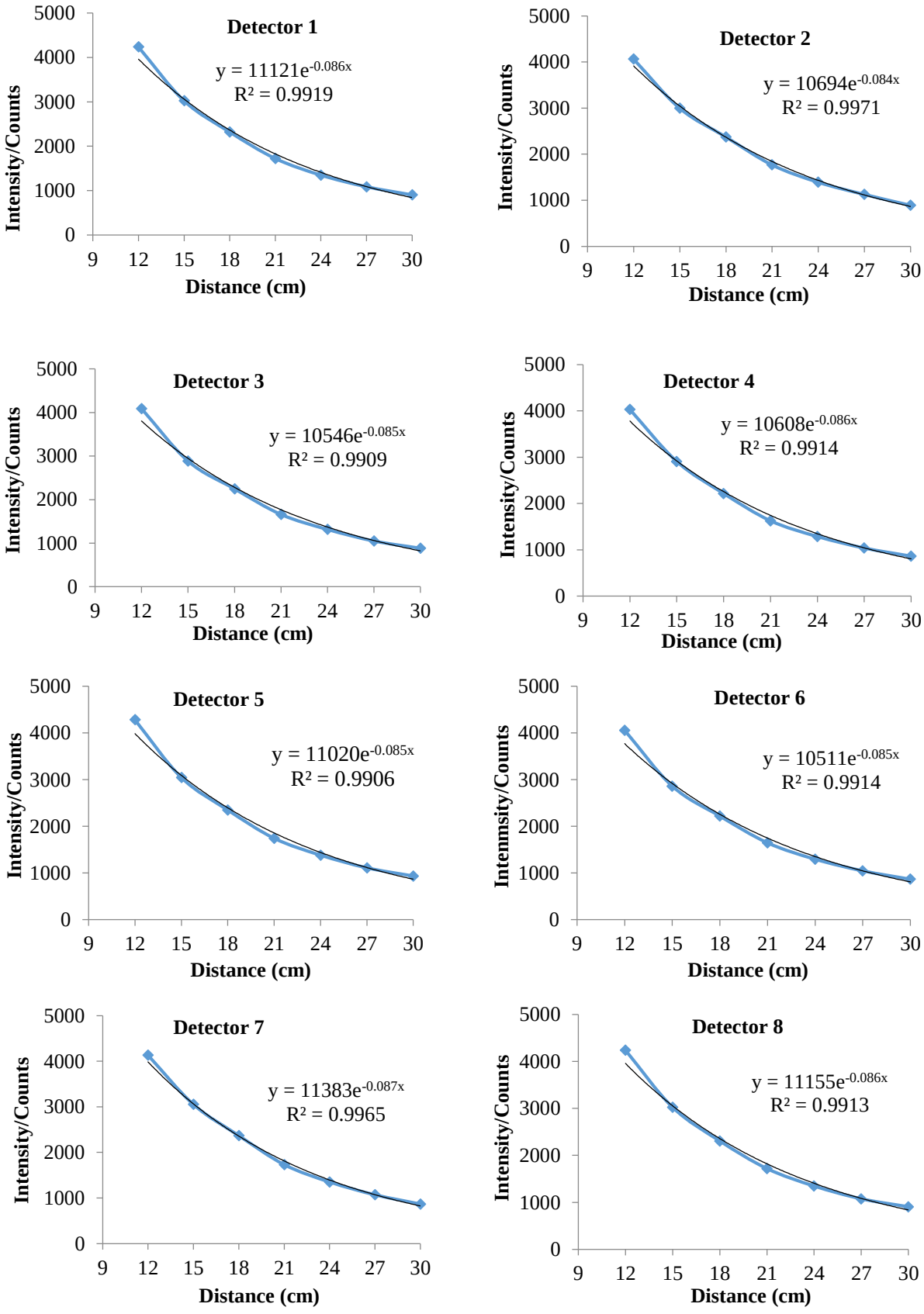

Figure 3.7 Radiation intensity (counts) versus distance plot for Detector 1 to Detector 8

3.1.6 Calibration Step in RPT Experiment

Calibration is the most important step in RPT measurement that needs to be performed prior to actual experiments. In this step, radioactive particle has to be placed at various known locations in a fluid domain and its intensity needs to be recorded by detectors placed outside the stirred tank. In order to conduct the calibration step, a traverse system was developed in such a way that tracer particle can be fixed axially and horizontally at any location in stirred tank. Figure 3.8 depicts the calibration setup developed for stirred tank in which the eight detectors used are represented by notation D_1 to D_8. Data was acquired at frequency of 50 Hz at every location of tracer particle (500 events/data points).

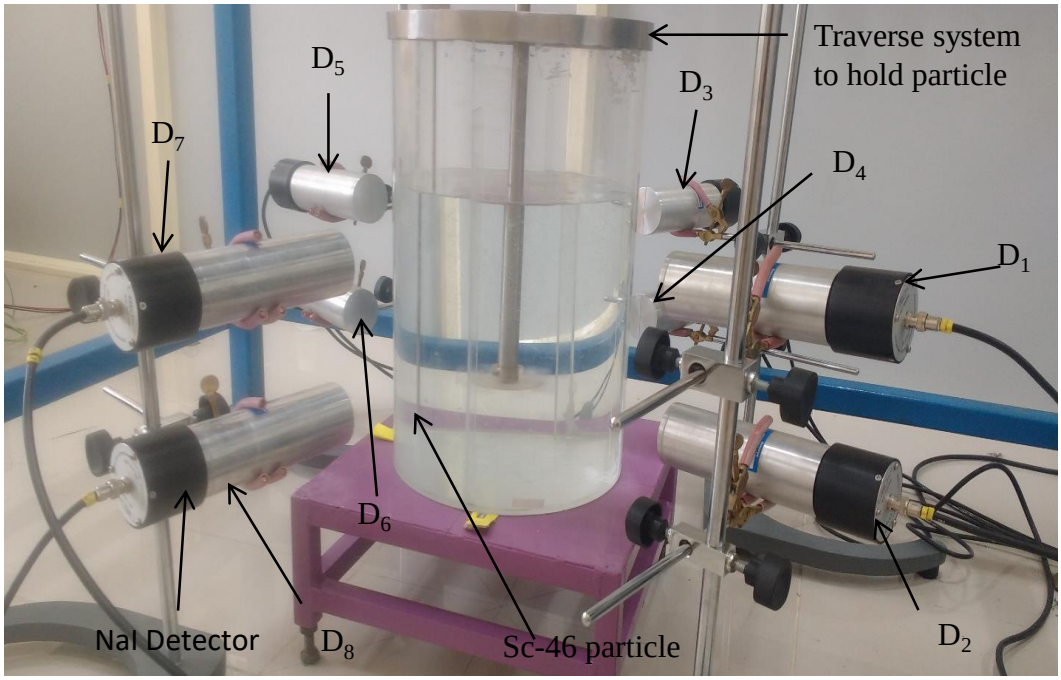

Figure 3.8 Calibration step in RPT measurement for stirred tank

3.2 Monte-Carlo Algorithm

In present work, the Monte-Carlo algorithm was used to generate the distance-count map for large number of points after calibration measurements for limited points. It is also used to obtain the instantaneous position of tracer particle by linking the calibration measurement data and actual experiment data. This algorithm uses the modelling of emission, transmission and subsequent detection of photons at detectors. In the Monte-Carlo algorithm, photon histories are tracked in their path from source, through the medium and their final detection at detector (Larachi et al., 1994; Beam et al., 1978). In this algorithm, the detector efficiencies in capturing and recording the photons were obtained by considering both the geometry and radiation

effects. The solid angle (angle created by the tracer particle with detector) was accounted to incorporate the geometry effects which considerably affects the detector counting efficiency. The photon peak counts C are calculated by the following equation (Larachi et al., 1994; Roy et al., 2002).

$$C = \frac{T_s \nu A \varepsilon_{abs} \phi}{1 + \tau_d \nu A \varepsilon_{abs} \phi} \tag{3.7}$$

Where, T_s = Sampling time (s)

ν = Number of γ-ray photons emitted per disintegration

A = Source strength (Ci)

ε_{abs} = Absolute efficiency of detector

ϕ = Photo-peak fraction

τ_d = Detector dead time (s)

And the absolute efficiency of detector is given by

$$\varepsilon_{abs} = \oiint_{\Omega} \frac{\vec{r}.\vec{n}}{r^3} \exp\left(-\sum_{j=1}^{N} \mu_j l_j \right) \left(1 - \exp\left(-\mu_D d\right)\right) d\Sigma \tag{3.8}$$

where $\vec{n}$ = Unit normal vector to the curved surface of the detector

$\vec{r}$ = Radius vector from source to detector

μ_D = The mass attenuation coefficient of the detector crystal material

d = Penetration depth of photons in the detector crystal (m)

μ_j = the mass attenuation of all materials that comes in the path of photons between the source and detector

Source strength, attenuation and dead time for each detector were obtained by the experimental values.

3.3 Analysis of Variance (ANOVA) Technique

ANOVA is the statistical technique which is used to compare the similarity of two or more data sets obtained from the experimental measurements. In present work, it is used to compare the radiation intensities obtained from different rotational speeds of impeller during the calibration

measurement in RPT experiments. The sample of ANOVA analysis is given Table 3.2; however detailed analysis is discussed in next chapter.

Table 3.2 Sample of ANOVA analysis

Source	SS	df	MS	*F*	*P-value*	$F_{critical}$
Groups	SSG	$k-1$	$MSG = \frac{SSG}{k-1}$	$\frac{MSG}{MSE}$		
Residual	SSE	$n-k$	$MSE = \frac{SSE}{n-k}$			
Total	SST	$n-1$				

There are two ways for acceptance that the data sets have equal mean. First one is the *F*, it represents the ratio of variation between data sets to the variation within the data set. Small value of *F* represents the data sets have equal mean. For equal mean, the value of *F* should be less than $F_{critical}$. Second one is the *P-value*, it should be greater than 0.05. It implies that the data sets have equal mean with confidence level of 95% (Rohatgi and Saleh, 2015).

3.4 CFD Methodology

Modelling of a stirred tank using CFD requires knowledge of many aspects of the process. First the domain of interest, in present work it is the volume occupied by the fluid inside the stirred vessel. This entire fluid domain is defined by computational grid, a collection of small sub domains or cells. The flow variables associated with the specific problem are computed in these cells. The computational grid must fit the complex geometry of stirred vessel. Another aspect is the rotation of impeller, it should be modelled in a specific way.

CFD modelling can be done by developing our own code or by using a software. In present work, Ansys Fluent software which is well known for simulating fluid flow problems has been used for CFD modelling of Rushton turbine stirred tank. Fluent is further divided into different parts, starting from creating the geometry, meshing, solution procedure and extraction of simulated data. The various steps involved in CFD modelling have been described in this section; also it is illustrated in the flowchart given (Figure 3.9).

- Design Modeller
- Impeller Rotation Model
- Meshing of CFD Model
- Model Equations and Turbulence Modelling

- Fluent Setup
- Mesh Independent Test
- Turbulence Models Comparison

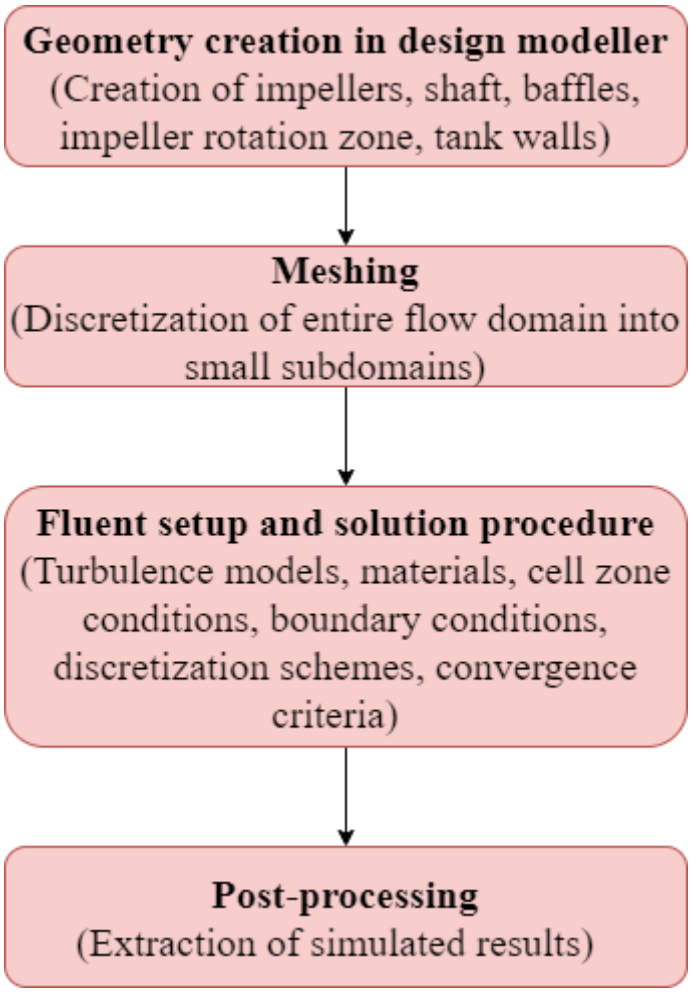

Figure 3.9 Various steps involved in CFD modelling of stirred tank

3.4.1 Design Modeller

The 3D geometry of stirred tank consisting of four equally spaced baffles, impeller mounted on a shaft was created in design modeller. After that, using Boolean operation, the solid bodies such as impeller, shaft and baffles were removed from entire fluid domain. Figure 3.10 shows the 3D geometry of stirred tank for different off bottom impeller clearances.

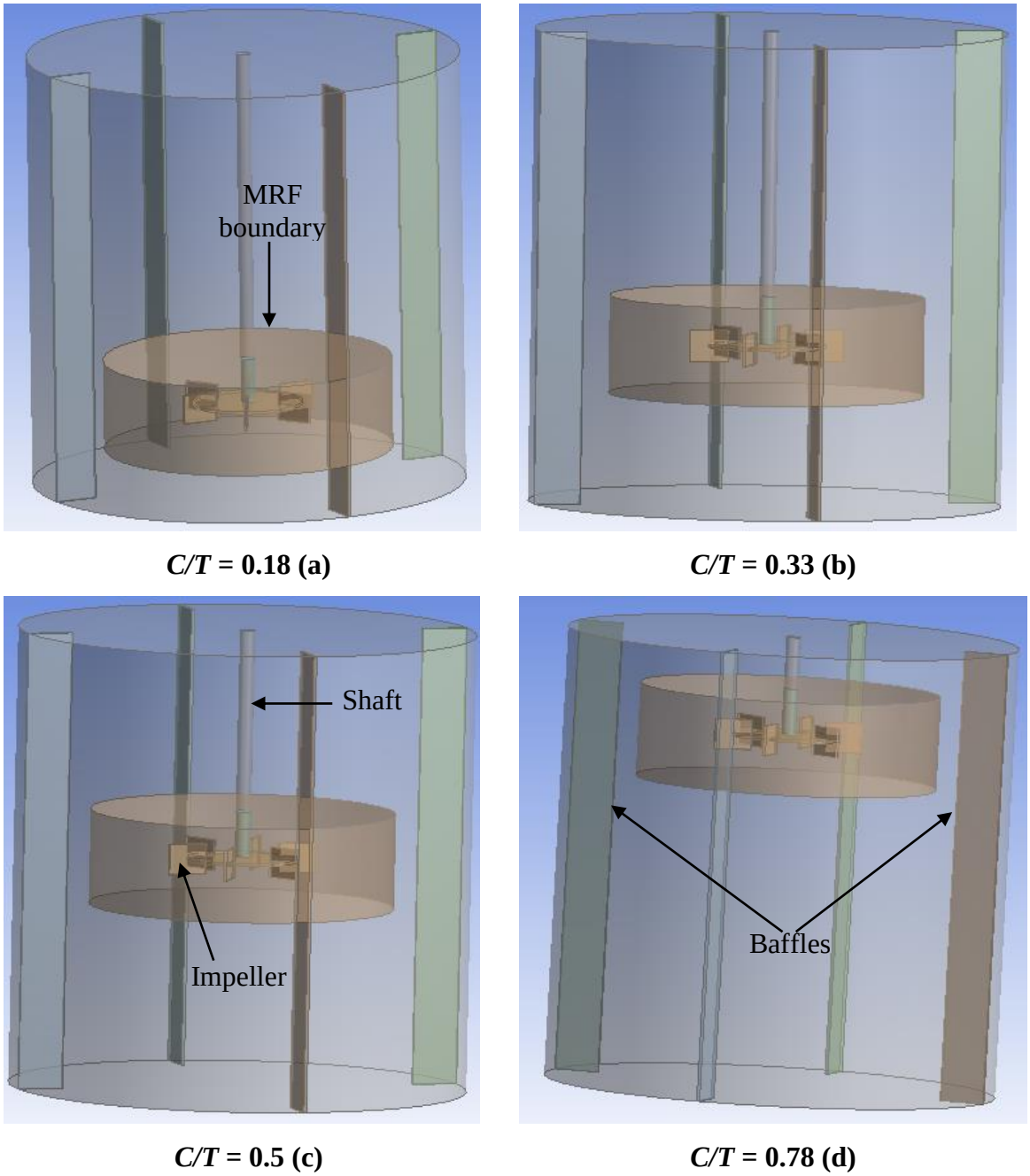

***C/T* = 0.18 (a)** **C/T = 0.33 (b)**

***C/T* = 0.5 (c)** **C/T = 0.78 (d)**

Figure 3.10 Geometry of stirred tank with different off bottom impeller clearances

3.4.2 Impeller Rotation Model

The impeller rotation was modelled by multiple reference frame (MRF) technique as suggested from literature data (Luo et al., 1994; Deglon and Meyer, 2006). It is a steady state approach. In this approach, tank is divided into two frames, i.e., a moving frame and stationary frame. The moving reference frame encapsulates the impeller and the flow confined by it, the stationary frame includes the baffles and the flow outside moving frame. The impeller is at rest in the rotating frame and the tank walls and baffles are at rest in the stationary frame. The grid

employed for an MRF solution must have a perfect surface of revolution encircling each rotating frame. This inner-rotating zone was created by slicing the fluid zone in the vicinity of the impeller from total fluid domain. Figure 3.10(a) shows the stirred tank with an MRF boundary surrounding the impeller created in the design modeller.

Due to high speed of impeller rotation, the flow variations are very sharp near the impeller. The effective region for sharp variation in flow is 1.5 times of blade height above and below the impeller disc and *D*/2 away from the impeller tip which is reported by Lee and Yianneskis, 1994. Based on this concept, the optimal dimensions of inner-rotating fluid zone (MRF boundaries) were varied radially and axially. The details of MRF boundaries are given section 4.2 (Figure 4.7 and Table 4.8).

3.4.3 Meshing of CFD Model

Generally, the partial differential equations of flow transport are not solved analytically. Therefore, the entire flow domain was divided into smaller subdomains (shapes like hexahedral and tetrahedral in 3D, quadrilaterals and triangles in 2D) to analyse fluid flows. These subdomains are called elements or cells, and the collection of all elements or cells is called a mesh or grid. Further, the discretized forms of flow equations are solved inside the each of these subdomains.

In present work, an unstructured tetrahedral mesh was produced for fluid region, while rotor and baffles have structured hexahedral mesh. Figure 3.11 shows the view of mesh used for flow domain of stirred tank, tetrahedral mesh was used for rotating zone containing impeller, while hexahedral mesh was used for stationary zone containing baffles. Optimization of mesh was done for standard configured stirred tank with six bladed Rushton turbine and four equally spaced baffles and same mesh parameters were kept for further studies. The generated optimized mesh consisted of 3,96,172 elements and 1,95,523 nodes as shown in Figure 3.12. The mesh independence study is discussed in the separate section of this chapter.

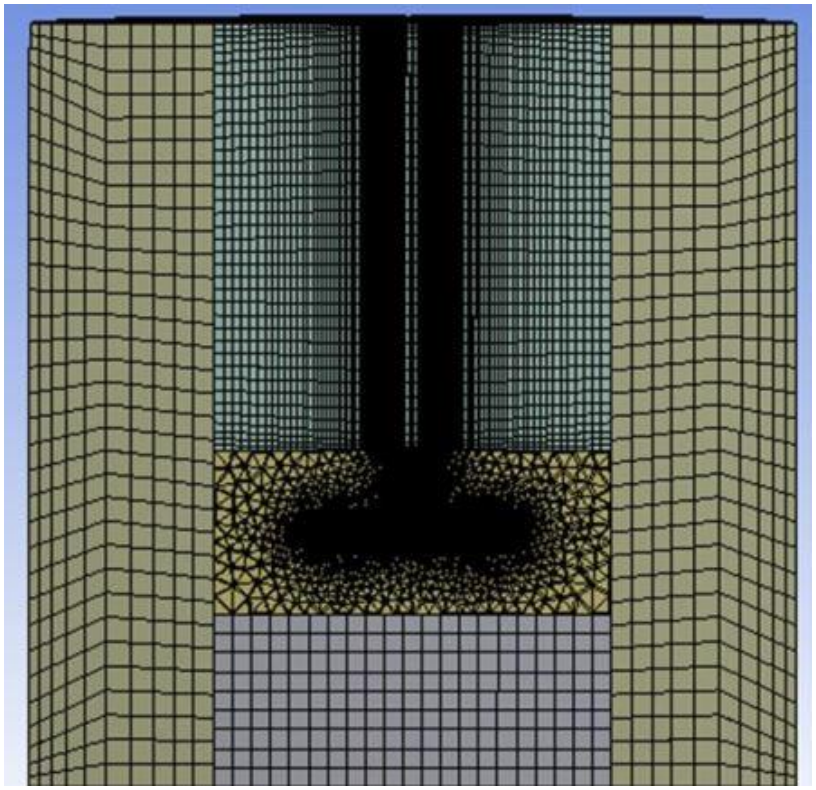

(a)

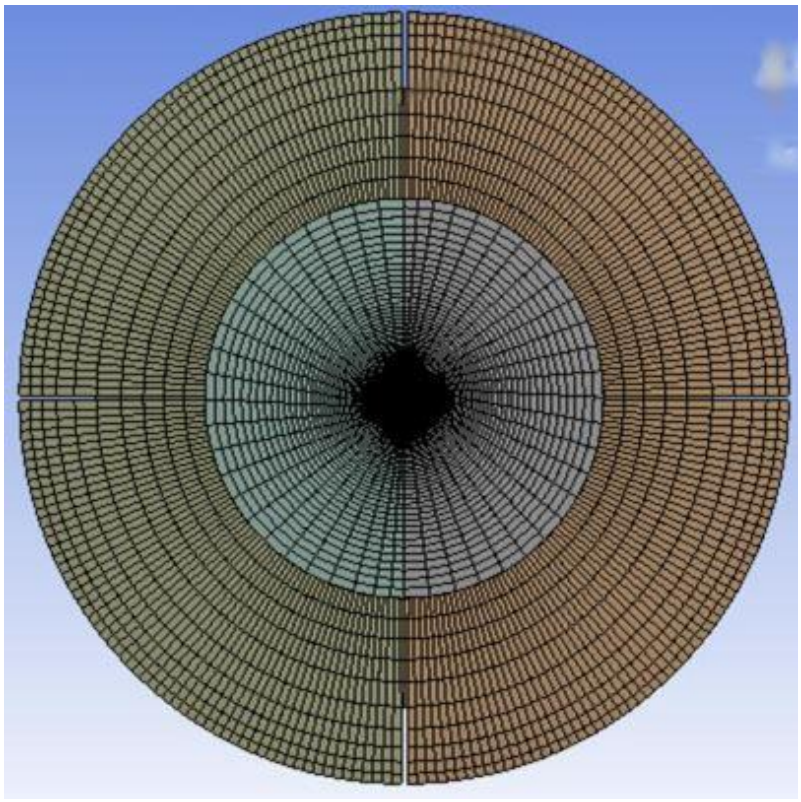

(b)

Figure 3.11 Meshing used for CFD model of stirred tank, sectional side view (a), sectional top view (b)

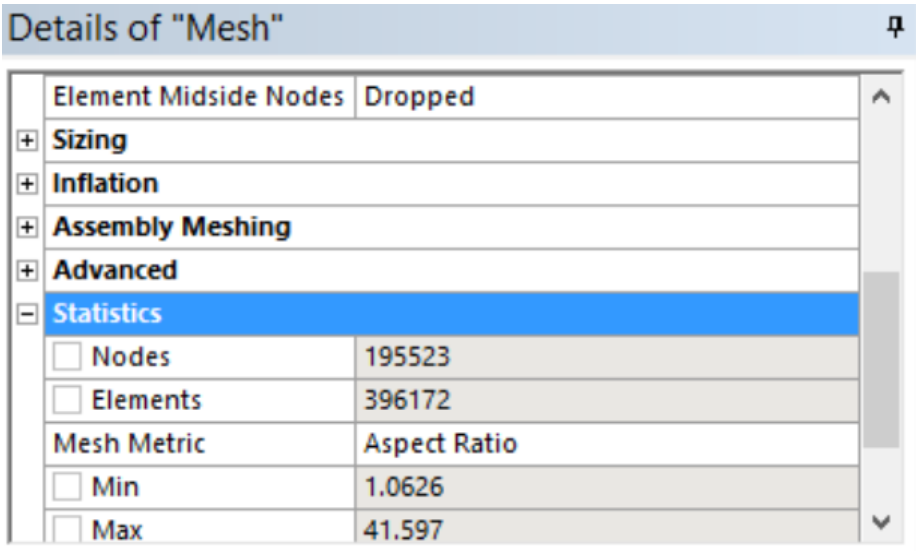

Figure 3.12 Details of mesh generated in Ansys

3.4.4 Model Equations and Turbulence Modelling

Model Equations

The basic equations used for solution of flow variables in stirred tanks are the mass and momentum conservations equations and these are referred as Navier-Stokes equations. These equations can be written as follows.

Mass Conservation or Continuity Equation

$$\frac{\partial}{\partial x_i}(\rho u_i) = 0 \tag{3.9}$$

Momentum Conservation Equation

$$\frac{\partial(\rho u_i)}{\partial t} + \frac{\partial(\rho u_i u_j)}{\partial x_j} = -\frac{\partial p}{\partial x_i} + \frac{\partial}{\partial x_j}\left[\mu\left(\frac{\partial u_i}{\partial x_j} + \frac{\partial u_j}{\partial x_i} - \frac{2}{3}\frac{\partial u_k}{\partial x_k}\delta_{ij}\right)\right] + \rho\vec{g} + \vec{F} \tag{3.10}$$

Turbulence Modelling

In the turbulence regime, when Reynolds number (N_{Re}) > 10^3, fluctuations in the mean velocity and other variables occur. In order to have a better prediction from model, their effects need to be incorporated into the CFD model. Several methods are available to incorporate turbulence in the Navier–Stokes equations. Most of these involve a process of time averaging the conservation equations. In present work, RANS approach is used for modelling of turbulence. In this, the flow variables e.g. velocity, is assumed to be sum of mean and fluctuating

components $(u_i = \bar{u}_i + u_i')$. After time averaging over many cycles of the fluctuation, terms containing factors of the fluctuating component average to zero. The only term that remains positive definite is one containing the product of two fluctuating terms in momentum equation. The modified equations after using RANS decomposition can be written as follows.

$$\frac{\partial}{\partial x_i}\left(\rho u_i\right) = 0 \tag{3.11}$$

$$\frac{\partial}{\partial t}\left(\rho u_i\right) + \frac{\partial}{\partial x_j}\left(\rho u_i u_j\right) = -\frac{\partial p}{\partial x_i} + \frac{\partial}{\partial x_j}\left[\mu\left(\frac{\partial u_i}{\partial x_j} + \frac{\partial u_j}{\partial x_i} - \frac{2}{3}\delta_{ij}\frac{\partial u_k}{\partial x_k}\right)\right] + \frac{\partial}{\partial x_i}(-\rho\overline{u_i'u_j'}) + \rho\vec{g} + \vec{F} \tag{3.12}$$

The new term $(-\rho\overline{u_i'u_j'})$ added due to the ensemble averaging in RANS momentum equation is called as Reynolds stresses. These Reynolds stresses need to be modelled appropriately and this can be done using Boussinesq hypothesis. This hypothesis relates the Reynolds stresses to the mean velocity gradients and it can be written as follows:

$$-\rho\overline{u_i'u_j'} = \mu_t\left(\frac{\partial u_i}{\partial x_j} + \frac{\partial u_j}{\partial x_i}\right) - \frac{2}{3}\left(\rho k + \mu_t\frac{\partial u_k}{\partial x_k}\right)\delta_{ij} \tag{3.13}$$

The new constant, μ_t, is the turbulence or eddy viscosity. Different turbulence models are available to compute the Reynolds stresses. The variants of *k*-*ε* turbulence models calculates the μ_t as a function of turbulence kinetic energy (*k*) and turbulence dissipation rate (*ε*) with two additional transport equations for *k* and *ε*.

In present work, the variants of *k*-*ε* turbulence models such as standard *k*-*ε*, realizable *k*-*ε* and RNG *k*-*ε* are tested for prediction of flow fields in a stirred tank. These models have similar forms of transport equation for *k* and *ε*, but have some differences are as follows:

- Calculation of turbulence viscosity
- The turbulence Prandtl numbers governing the turbulence diffusion of *k* and *ε*
- The generation and destruction terms in the *ε* equation

Standard *k*-*ε* model

It is a robust, economical and has ability to predict the flow in a reasonable accuracy. It is widely used for practical engineering flow calculations, industrial flow and heat transfer simulations. It is based on high Reynolds number. The two transport equations that need to be solved for this model are for the kinetic energy of turbulence, *k*, and the rate of dissipation of turbulence, *ε*. The model equations are given as follows:

$$\frac{\partial}{\partial t}(\rho k)+\frac{\partial}{\partial x_i}(\rho k u_i)=\frac{\partial}{\partial x_j}\left[\left(\mu+\frac{\mu_t}{\sigma_k}\right)\frac{\partial k}{\partial x_j}\right]+G_k-\rho\varepsilon \qquad (3.14)$$

$$\frac{\partial}{\partial t}(\rho \varepsilon)+\frac{\partial}{\partial x_i}(\rho \varepsilon u_i)=\frac{\partial}{\partial x_j}\left[\left(\mu+\frac{\mu_t}{\sigma_\varepsilon}\right)\frac{\partial \varepsilon}{\partial x_j}\right]+C_{1\varepsilon}\frac{\varepsilon}{k}G_k-C_{2\varepsilon}\rho\frac{\varepsilon^2}{k} \qquad (3.15)$$

where G_k represents the rate generation of turbulence kinetic energy due to mean velocity gradients, $C_{1\varepsilon}$ and $C_{2\varepsilon}$ are the model constants, σ_k and σ_ε are the turbulence Prandtl number for *k* and *ε* respectively (Pukkella et al., 2019).

The turbulence viscosity is calculated as:

$$\mu_t=\rho C_\mu\frac{k^2}{\varepsilon} \qquad (3.16)$$

Realizable *k*-*ε* model

The realizable *k*-*ε* model (Shih et al., 1995) is addition to the family of two-equation models. It differs from the standard *k*-*ε* model in two ways. First, the turbulence viscosity is computed in a different manner, making use of (Equation 3.16) but using a variable for the quantity C_μ. This is motivated by the fact that in the limit of highly strained flow, some of the normal Reynolds stresses, u_i^2, can become negative in the *k*-*ε* formulation, which is unphysical, or unrealizable. The variable form of the constant C_μ is a function of the local strain rate and rotation of the fluid and is designed to prevent unphysical values of the normal stresses from developing. The second difference is that the realizable *k*-*ε* model uses different source and sink terms in the transport equation for eddy dissipation. The resulting equation is considerably different from the one used for both the standard and RNG *k*-*ε* models.

RNG *k*-*ε* model

The RNG *k*-*ε* model obtained from statistical technique called renormalization group theory. It is similar to standard *k*-*ε* model, but the differences are given as below:

- The additional term in the dissipation rate (ε) equation with enhance the predictive capability for rapidly strained flows.
- Addition of effect of swirl flow in turbulence which increases the accuracy of swirling flows.
- Provision of analytic formula for turbulence Prandtl numbers
- The RNG model provides an analytically derived differential formula for effective viscosity that accounts for low Reynolds number effects.

The mean flow fields predicted by variants of *k-ε* models are compared with the literature data and it is provided in the separate section of this chapter.

3.4.5 Fluent Setup

After creation of geometry and mesh, we have to define the setup in Fluent with desirable values. In this section, detail setup for Ansys Fluent with parameters are described.

General

General settings (Figure 3.13) give solver options of pressure, velocity and time. Pressure-based type of solver was used. A steady state simulations were conducted.

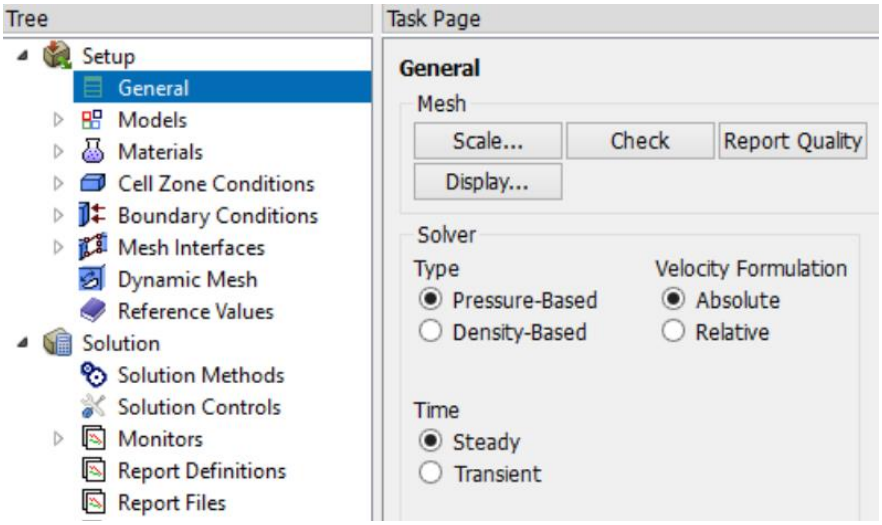

Figure 3.13 General setup in Fluent

Models

As explained earlier, RANS based standard *k-ε* turbulence model was used (Figure 3.14). Standard wall function was used to link the viscosity dominated region between the walls and the fully turbulence region (Bashiri et al., 2016).

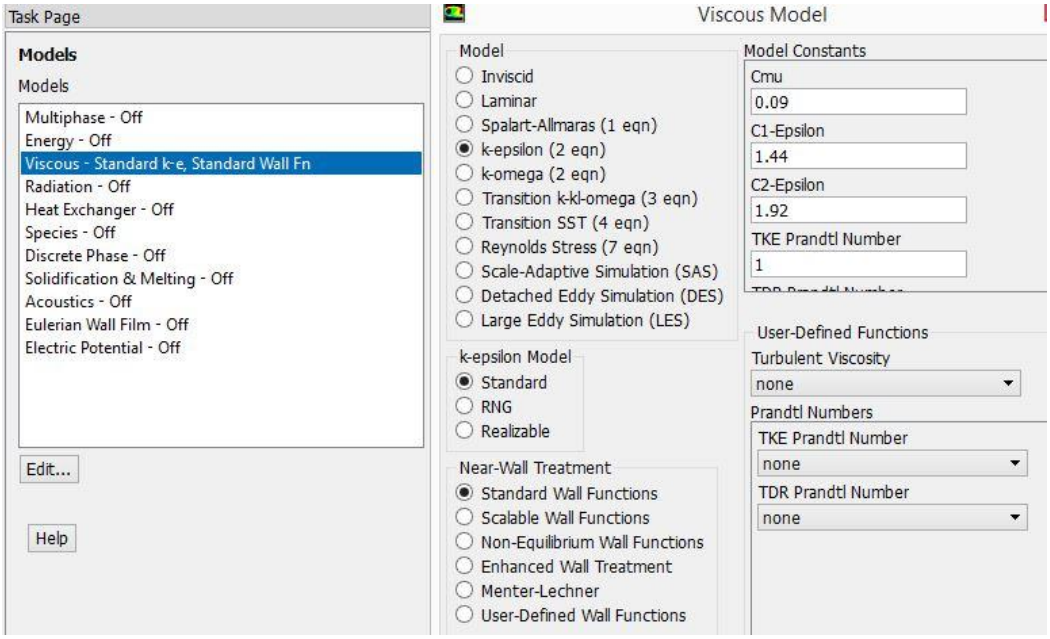

Figure 3.14 Model setup for *k-ε* turbulence model

Materials

The water was considered as working fluid. Its properties, density and dynamic viscosity were kept at 998.2 Kg/m^3 and 0.001003 Pa.s respectively (Figure 3.15).

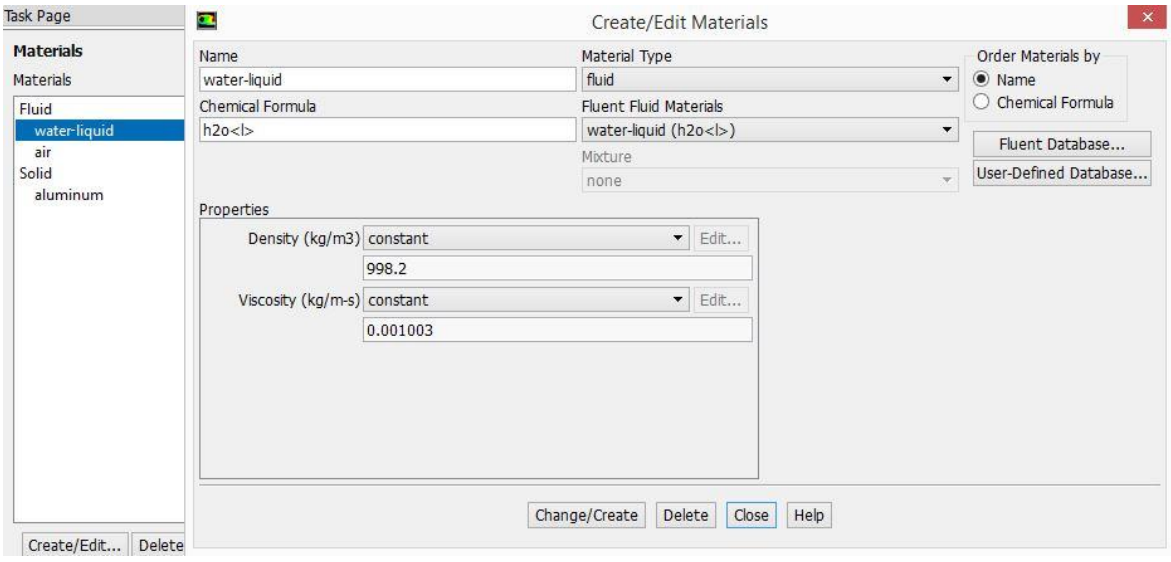

Figure 3.15 Material setup

Cell zone conditions and boundary conditions

Fluidi represents the inner-rotating fluid zone (MRF boundary) containing impeller and fluid corresponds to the volume outside the inner-rotating zone. The frame motion was enabled for

Fluidi (Figure 3.16). Table 3.3 shows the named selection and boundary conditions used for the present study.

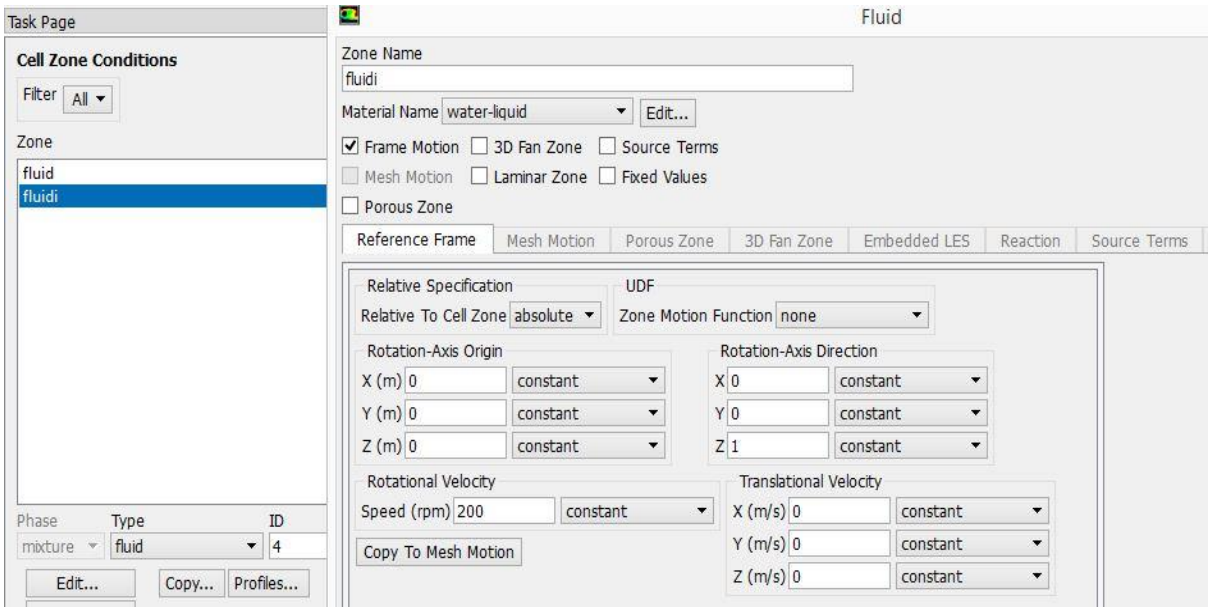

Figure 3.16 Cell zone condition setup

Table 3.3 Boundary conditions

Name	Surface	Boundary Conditions
Tank wall	Tank side and bottom surfaces	Wall
Tank top	Top surface of fluid	Symmetry
Baffle wall	All baffles and their surfaces	Wall
Rotor wall	All surfaces of impeller	Wall
Shaft wall	Cylindrical surface of shaft	Wall

Pressure velocity coupling

In three dimensional simulations, the transport equations include four equations i.e., three for velocity components (momentum) and one for pressure (continuity). Four equations with four unknown, but no explicit equation is available for calculation of pressure. For that Semi-implicit method for pressure liked equation (SIMPLE) algorithm was used to link the velocity and pressure.

In this algorithm, guessed value of pressure is provided in the momentum transport equations. Then compute the new values of velocities, but, in general it does not satisfy the continuity equation and hence corrections to the velocities are determined. From the corrected values of

velocities, correction for pressure is obtained. This corrected pressure value is replaced with original guessed pressure into the momentum transport equations and updated value of pressures is computed. Following the solution of the remaining problem variables, the iteration is complete and the entire process is repeated.

Discretization scheme

In Discretization process, the partial differential form of Navier–Stokes equations converted into algebraic equations and theses equations has to be solved by simulation in every cell. It requires an iterative solution procedure, because of the nonlinearity of the flow transport equations. The discretization methods such as finite difference, finite element, spectral element, and finite volume are generally used. In present work, finite volume method based second order upwind scheme was used for discretization of transport equations. Patankar (1980) has given the formulation of finite volume method in scalar equation of following form:

$$\frac{\partial(\rho\varphi)}{\partial t}+\frac{\partial}{\partial x_i}(\rho u_i\varphi)=\frac{\partial}{\partial x_i}(\Gamma\frac{\partial\varphi}{\partial x_i})+S \qquad (3.17)$$

The parameter Γ is used to represent the diffusion coefficient for the scalar φ. If φ is one of the components of velocity, for example, Γ would represent the viscosity. All sources are collected in the term S. Again, if φ is one of the components of velocity, S would be the sum of the pressure gradient, the gravitational force and any other additional forces that are present.

Convergence criteria

Solutions were considered converged when the residuals for continuity, velocity and turbulence quantities reached below 10^{-6} and the field values became almost identical over last 500 iterations. Figure 3.17 shows a typical convergence graph for standard configured stirred tank.

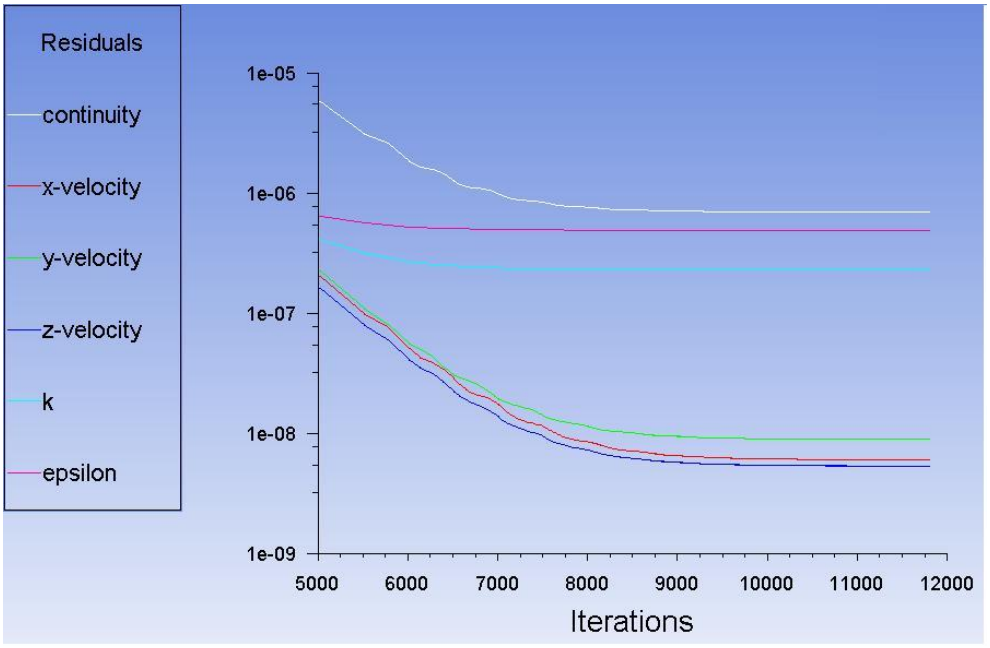

Figure 3.17 Convergence graph

3.4.6 Mesh Independence Test

Mesh independence test was performed at different mesh sizes to obtain the optimum number of cells and to minimize the numerical errors in the results obtained from CFD simulations. Table 3.4 shows the various mesh sizes used in the simulations for standard configured stirred tank. Figures 3.18 and 3.19 show the effect of grid resolution on prediction of power number and normalized profiles of mean radial velocities close to the impeller ($r/R = 1.07$) respectively. Continuous improvements in the prediction of flow fields is observed from Mesh I to III and became identical thereafter. Hence, the grid resolution having 3.9 x 10^5 elements is adequate for grid independent solutions of flow fields. Hence, the flow field predictions from Mesh III were considered for the further studies investigating the effects of various reactor parameters.

Table 3.4 Details of mesh adopted for CFD model

Mesh	Number of elements	Number of nodes	Power Number (N_p)
Mesh I	104595	115764	4.309
Mesh II	112768	118132	4.511
Mesh III	396172	195523	4.750
Mesh IV	731965	288837	4.793
Mesh V	2492445	782042	4.829

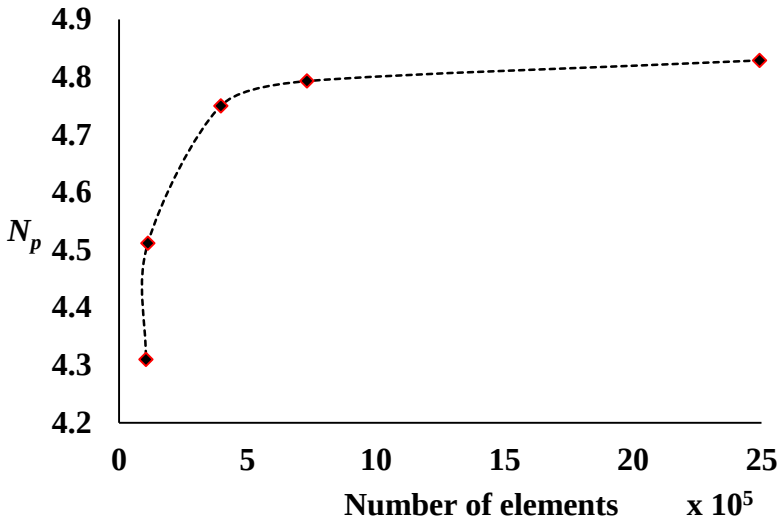

Figure 3.18 Effect of mesh size on power number

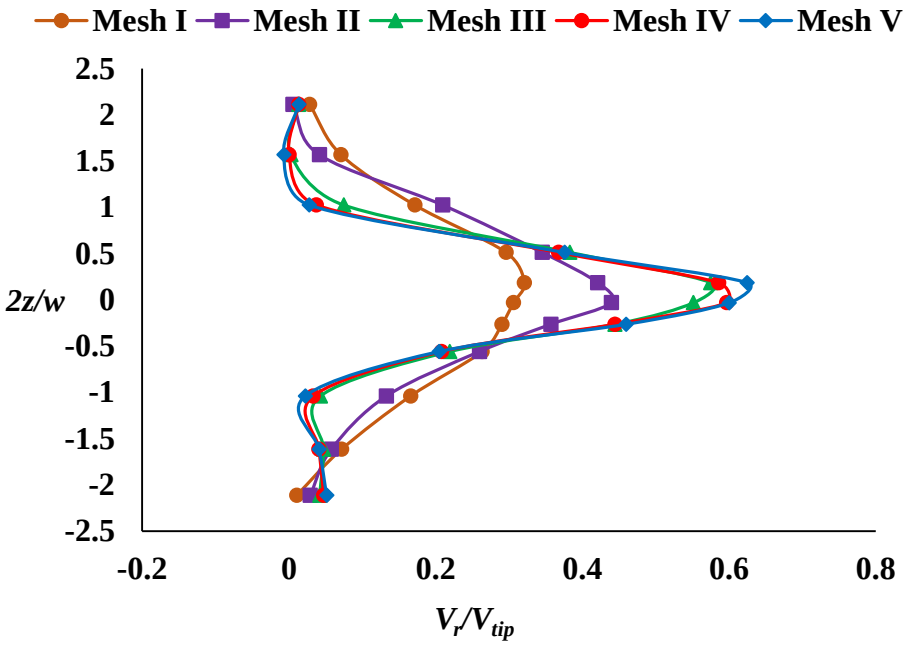

Figure 3.19 Effect of mesh size on normalized profiles of radial velocity at r/R = 1.07 and θ = 45°

3.4.7 Turbulence Models Comparison

As mentioned earlier in the turbulence models section, in present work, *k-ε* model is used for turbulence modelling. In this section, the comparison of variants *k-ε* turbulence model with the experimental literature data is provided to obtain the best model. Figures 3.20-3.22 show the comparison of standard, realizable and RNG *k-ε* turbulence models with literature data of Wu and Patterson (1989) for prediction of mean profiles of radial, tangential and axial velocities respectively.

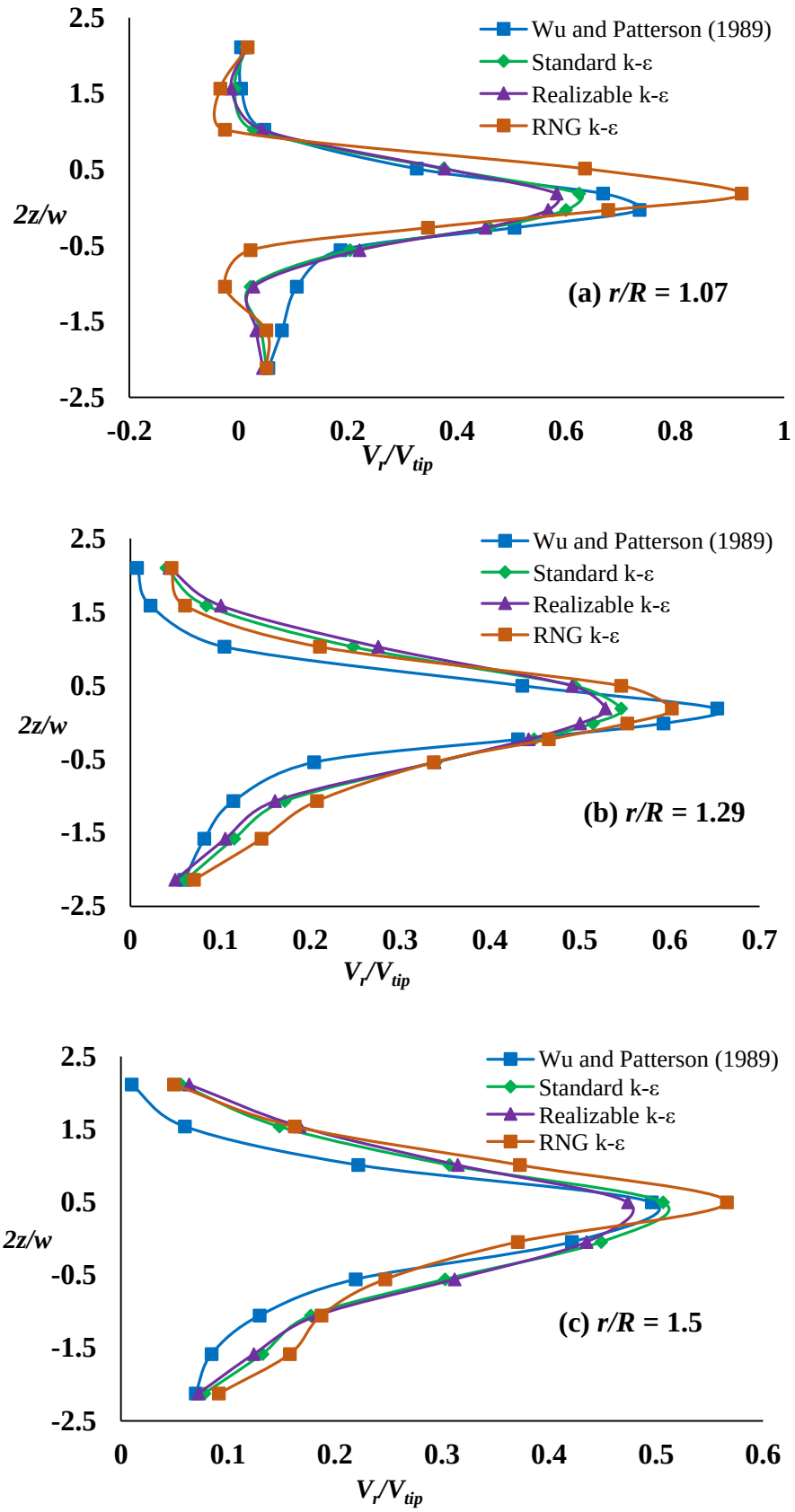

Figure 3.20 Comparison of different turbulence models for prediction of normalized mean radial velocity at different radial distances at angle $\theta = 45^{\circ}$

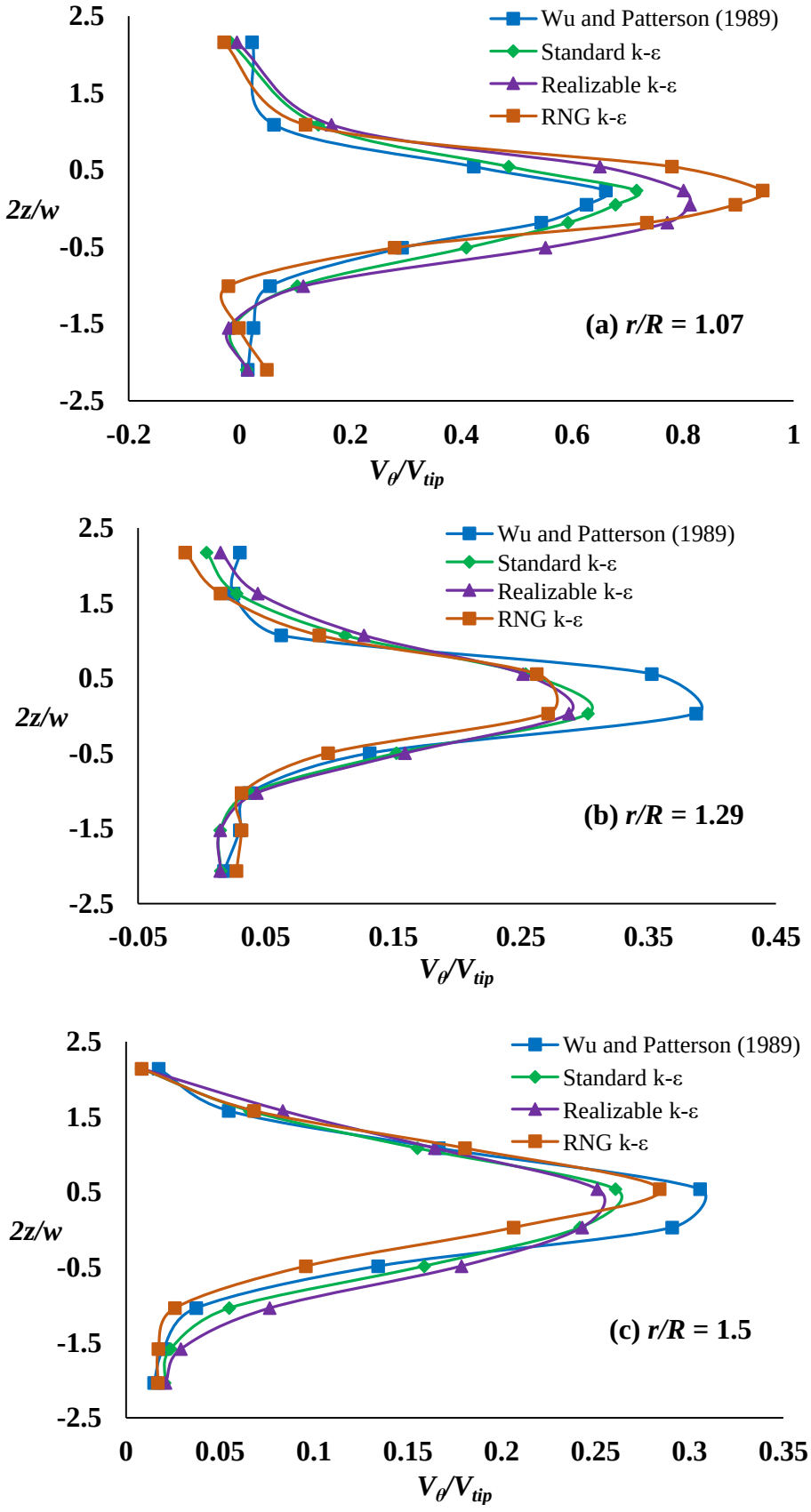

Figure 3.21 Comparison of different turbulence models for prediction of normalized mean tangential velocity at different radial distances at angle $\theta = 45^{\circ}$

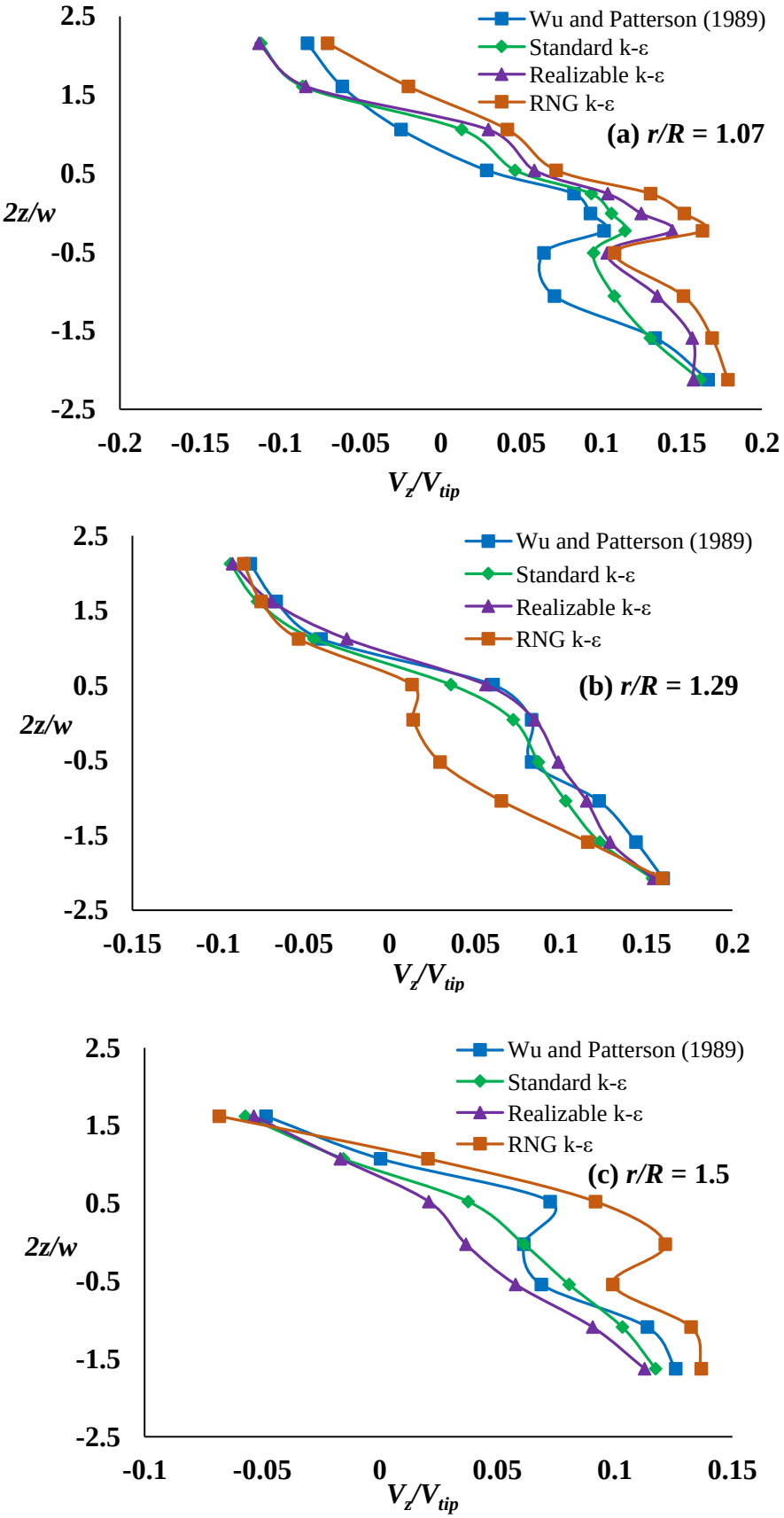

Figure 3.22 Comparison of different turbulence models for prediction of normalized mean axial velocity at different radial distances at angle $\theta = 45^{\circ}$

All turbulence models qualitatively predicted the mean velocities. The peak value of mean radial and tangential velocities near the impeller tip are high and reduces with increase in the radial distance from the impeller. In comparison between the turbulence models, the RNG *k*-*ε* model has given more under/over predictions of mean velocities as compared to the standard and realizable *k*-*ε* models. The radial and tangential velocity predictions from the standard and realizable *k*-*ε* models are highly comparable, while, standard *k*-*ε* model found in a good agreement with the literature data compared to realizable *k*-*ε* model in close comparison. The difference in the CFD results are observed because of assumption of isotropic turbulence condition associated with *k*-*ε* model (Coroneo et al., 2011).

Thus a steady state CFD model was developed for six bladed Rushton turbine stirred tank. Geometry and meshing was created using tool available in Ansys software. The optimum mesh size was found with 3,96,172 number of elements and 1,95,523 number of nodes. The impeller rotation was modelled by MRF technique as suggested from literature data. The standard *k*-*ε* turbulence model has given better predictions compared to other turbulence models. Semi Implicit Method for Pressure Linked Equations (SIMPLE) method was used for coupling of velocity and pressure. Second order upwind scheme was adopted for discretization of transport equations. The convergence criteria were kept at 10^{-6} for continuity, velocity and turbulence quantities. This optimized set of CFD parameters are considered for the further studies investigating the effects of various reactor parameters.

Chapter 4

Results and Discussion

The results obtained from RPT and CFD procedures are discussed in this chapter. It is divided into the following sections.

1. Investigation of Effect of Fluid Motion on Radiation Intensity in RPT Technique, and Comparison of RPT Results with Literature Data

In this study, the effect of fluid motion on radiation intensity during the calibration step in RPT for stirred tank is presented. The comparison of mean counts observed for different rotational speeds of impeller at different locations are investigated by statistical analysis of variance (ANOVA) method. Further, mean velocities obtained from RPT are compared with the literature data.

2. Determination of Optimal Dimensions of Inner-Rotating Fluid Zone for MRF Technique using CFD Model, and Validation of CFD Model with RPT and Literature Data

A series of CFD simulations have been conducted for various dimensions of inner-rotating fluid zone and best optimal zone has been determined by comparing the mean velocities with the literature data. Further, CFD model with optimized inner-rotating fluid zone is validated with current RPT work and literature data.

3. Investigation of Effect of Impeller Clearance on Flow Hydrodynamics in Stirred Tank using CFD Model

In this section, the location of double loop flow pattern transition to single loop at high and low impeller clearance has been investigated. Further, the flow hydrodynamic parameters at low, middle and high impeller clearances have been analyzed.

4. Investigation of Effect of Impeller Diameter on Flow Hydrodynamics in Stirred Tank using CFD Model

In this section, the flow fields at various impeller diameters have been investigated. The flow fields behind the blades at different angles have been studied.

4.1 Investigation of Effect of Fluid Motion on Radiation Intensity in RPT Technique and Comparison of RPT Results with Literature Data

In RPT technique for the stirred tank, the first and most important step is to measure radiation intensity by placing tracer particle at various known locations, known as calibration. In the literature, no data is available whether the calibration step was done under stationary or moving condition of the fluid. With this motive, calibration measurements have been conducted at various locations of tracer particle under both conditions to find the effect of fluid motion on radiation intensity. Fourteen different locations were considered which are represented from L_1 to L_{14} as shown in Figure 4.1. The locations of tracer particle were considered in such a way that these locations are well distributed in the tank volume i.e. very close to the impeller, near baffle, near the tank wall, at the fluid surface and space between tank wall to impeller tip. Once the particle location was fixed, the radiation intensity at that location was measured under stationary and rotating condition of impeller. The impeller was rotated at six different rotational speeds. The details of the calibration measurement conducted at different speeds are given in Table 4.1. Intensity data was acquired at a frequency of 50 Hz at each location of a tracer particle (500 events/data points).

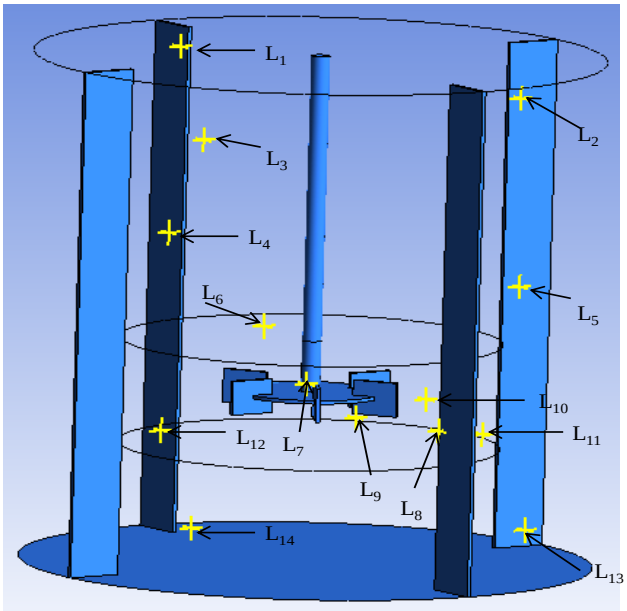

Figure 4.1 Locations of tracer particle to find the effect of fluid motion on radiation intensity

Table 4.1 Rotational speed of impeller for calibration

Rotational speed of impeller (rpm)
0 (Stationary)
109
136
161
188
214
238

4.1.1 Analysis for Effect of Fluid Motion on Radiation Intensity using ANOVA Technique

ANOVA analysis has been performed for all fourteen locations of tracer particle, however, the detailed ANOVA analysis has been presented at two locations only (details at other locations are available in Appendix). The two locations of tracer particle considered for ANOVA analysis are L_1 (at top of water surface) and L_9 (near to the impeller). The *P-value* obtained from ANOVA gives the decision of accepting the hypothesis for equal mean of counts. If the *P-value* is greater than 0.05, it means that the radiation intensity counts measured at different rotational speed have equal mean with a 95% confidence level. Also, F is another factor which shows the variability between group values. If the F is less than $F_{critical}$, it implies that the variability between mean counts is low, i.e. radiation intensity measured at a given location does not change with the velocity of water flowing around the location.

Table 4.2 shows the ANOVA analysis at location 1 (L_1 – near to water surface) for detector 1. It is found that *P-value* is greater than 0.05 and F is less than $F_{critical}$. It reveals that radiation intensities measured at L_1 for different rotational speeds are independent of motion of fluid in the stirred tank. Figure 4.2 shows the plot of variation in radiation intensity with impeller speed for particle position L_1 and detector 1. It is observed that the mean value of counts at each speed is around 110 which indicates no significant variation in counts. Similar analysis was done for the remaining seven detectors at L_1. Table 4.3 shows the summary of ANOVA analysis and percentage error between the counts observed at different speeds at L_1 for all eight detectors. It

is observed that at L_1, the criteria for equal mean is satisfied and the maximum percentage error between counts is found to be 0.567 for detector 2 among all detectors.

Table 4.2 Details of ANOVA analysis for detector 1 at L_1

Groups	*Count*	*Sum*	*Average*	*Variance*
stationary	500	55387	110.774	100.2354
109 rpm	500	55237	110.474	117.0434
136 rpm	500	55498	110.996	112.3487
161 rpm	500	55627	111.254	117.9173
188 rpm	500	55508	111.016	107.9436
214 rpm	500	55462	110.924	108.7076
238 rpm	500	55318	110.636	104.3963

Source of Variation	*SS*	*df*	*MS*	*F*	*P-value*	*F crit*
Between Groups	204.1577	6	34.02629	0.309896	0.932118	2.10118
Within Groups	383527.6	3493	109.7989			
Total	383731.8	3499				

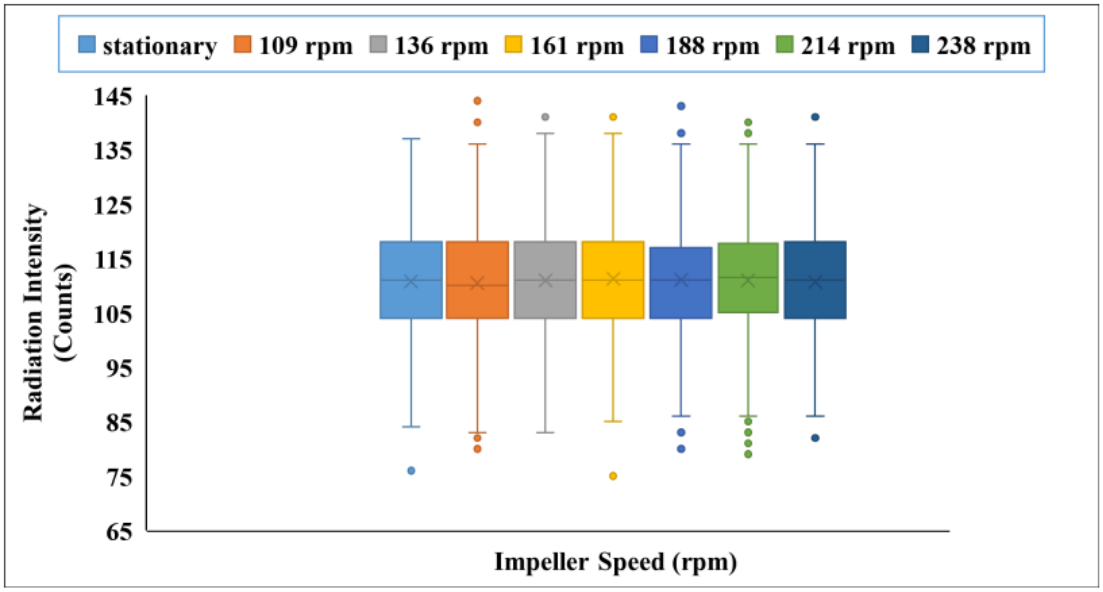

Figure 4.2 Variation of radiation intensity with impeller speed for detector 1 at L_1

Table 4.3 Summary of ANOVA analysis at L_1 for all eight detectors

Detector No.	***P-value***	***F***	$F_{critical}$	**% Error in mean counts**
1	0.932	0.309	2.101	0.433
2	0.550	0.825	2.101	**0.567**
3	0.588	0.775	2.101	0.306
4	0.168	1.516	2.101	0.523
5	0.281	1.241	2.101	0.251
6	0.743	0.583	2.101	0.338
7	0.618	0.738	2.101	0.319
8	0.831	0.469	2.101	0.511

Table 4.4 shows the ANOVA analysis at location 9 (L_9 – near to the impeller) for detector 1, where the flow variation is high. It is found that *P-value* is greater than 0.05 and *F* is less than $F_{critical}$. It reveals that the counts measured at L_9 have statistically equal mean. Figure 4.3 shows the plot of variation in radiation intensity with impeller speed at L_9 for detector 1. It is observed that the mean value of counts at each speed is 284-286 which indicates no significant variation in counts. Similar analysis was done for the remaining seven detectors at L_9. Table 4.5 shows the summary of ANOVA analysis and percentage error between the counts observed at different speeds at L_9 for all eight detectors. It is observed that at L_9, the criteria for equal means is satisfied and the maximum percentage error between counts is found to be 1.10 for detector 4 among all detectors.

Table 4.4 Details of ANOVA analysis for detector 1 at L_9

Groups	*Count*	*Sum*	*Average*	*Variance*
stationary	500	143396	286.792	262.3935
109 rpm	500	142400	284.8	245.9559
136 rpm	500	142489	284.978	246.6107
161 rpm	500	142227	284.454	250.0079
188 rpm	500	143000	286	262.9419
214 rpm	500	142850	285.7	270.8878
238 rpm	500	142661	285.322	261.9141

Source of Variation	*SS*	*df*	*MS*	*F*	*P-value*	*F crit*
Between Groups	1909.051	6	318.1752	1.236859	0.283953	2.10118
Within Groups	898555.2	3493	257.2446			
Total	900464.3	3499				

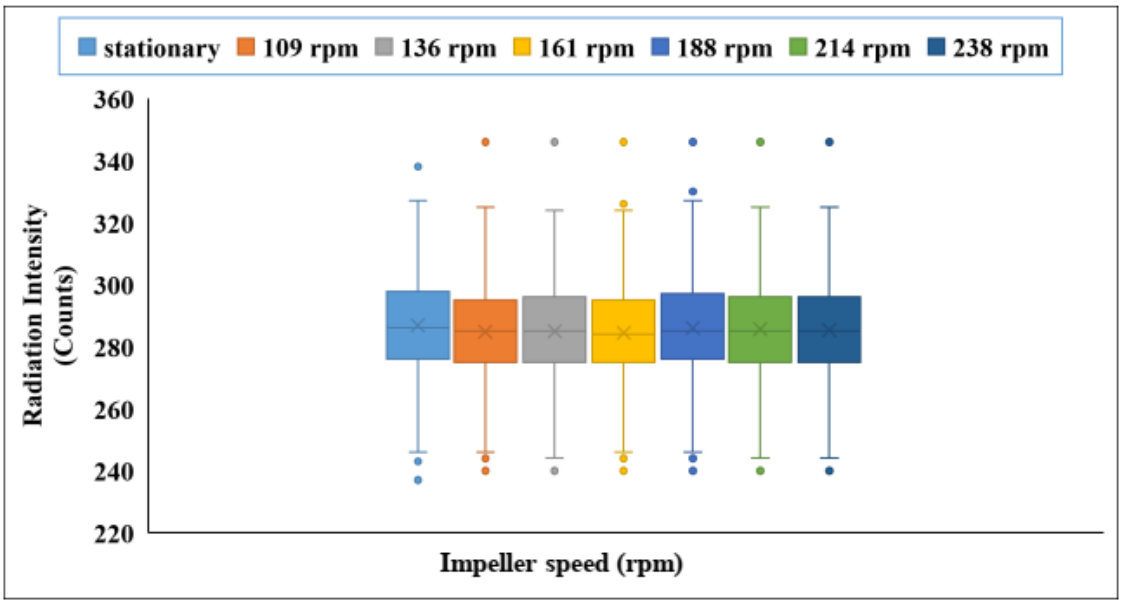

Figure 4.3 Variation of radiation intensity with impeller speed for detector 1at L_9

Table 4.5 Summary of ANOVA analysis at L_9 for all eight detectors

Detector No.	***P-value***	***F***	$F_{critical}$	**% Error in mean counts**
1	0.283	1.236	2.101	0.851
2	0.198	1.430	2.101	0.585
3	0.455	0.953	2.101	0.626
4	0.400	1.034	2.101	**1.105**
5	0.917	0.337	2.101	0.315
6	0.575	0.793	2.101	0.624
7	0.135	1.628	2.101	0.369
8	0.542	0.835	2.101	0.393

Similar ANOVA analysis has been done at all fourteen locations of tracer particle (L_1 to L_{14}) for all eight detectors. The consolidated summary of ANOVA analysis and percentage error in mean counts under the stationary and moving condition of fluid is shown in Table 4.6. At each location the detector at which the percentage error in mean counts is maximum is shown in Table 4.6.

Table 4.6 Consolidated summary of ANOVA analysis at fourteen locations

Location of particle	***P-value***	***F***	$F_{critical}$	**Maximum percentage error in counts**
1	0.550	0.825	2.101	0.567 (at detector 2)
2	0.183	1.470	2.101	**1.792 (at detector 6)**
3	0.349	1.117	2.101	0.982 (at detector 8)
4	0.218	1.380	2.101	1.312 (at detector 1)
5	0.224	1.364	2.101	0.972 (at detector 5)
6	0.128	1.654	2.101	0.830 (at detector 1)
7	0.078	1.894	2.101	1.398 (at detector 4)
8	0.796	0.516	2.101	0.983 (at detector 4)
9	0.400	1.034	2.101	1.105 (at detector 4)
10	0.494	0.899	2.101	0.979 (at detector 6)
11	0.086	1.834	2.101	1.102 (at detector 5)
12	0.897	0.371	2.101	0.654 (at detector 1)
13	0.770	0.550	2.101	0.835 (at detector 5)
14	0.311	1.183	2.101	1.070 (at detector 2)

The tracer particle locations L_6, L_7, L_8, L_9, L_{10}, L_{11} and L_{12} are in the vicinity of impeller region where the velocity gradient is sharp. Even at these locations, no change in the counts is observed with the speed of the impeller. Also, the percentage error in the measurement is found to be less than 1.79. The overall analysis shown that the radiation intensity is independent of fluid motion in the entire fluid domain in stirred tank. Hence, the calibration measurement can be done very close to impeller which helps to enhance the accuracy in measurement flow fields close to the impeller. LDA and PIV laser based techniques cannot measure the flow fields accurately within the impeller zone where the flow variation is very high due to the periodic passage of impeller. But, in RPT γ-radiations penetrate the flow and hence the flow variation does not affect the radiation intensity and flow fields can be measured close to the impeller region.

Once it is found that there is no effect of fluid motion on radiation intensity at considered fourteen locations, calibration measurement was done under stationary condition of fluid at 1362 fixed locations of a radioactive tracer particle in a stirred tank to obtain radiation intensity-position values. Then, the Monte-Carlo algorithm was used to generate the position versus

radiation intensity data for the large number of locations in fluid domain. Further, actual RPT experiments were conducted in which radioactive particle was free to move in fluid domain which produced intensity versus time data. The impeller speed was kept 200 rpm and data was acquired at a frequency of 50 Hz. The Monte-Carlo reconstruction algorithm was used to link the data obtained from calibration measurement and actual experiments which resulted in instantaneous position data of tracer particle. Instantaneous velocity data was evaluated by performing the differentiation between two successive instantaneous positions. After that mean velocities were calculated by time averaging the instantaneous velocities.

In the following section, the mean velocities obtained from RPT results are compared with LDA literature data of Wu and Patterson (1989) and LES simulated data of Zadghaffari et al. (2010).

4.1.2 Comparison of Mean Velocities

Figure 4.4 and Figure 4.5 depict the axial profiles of normalized mean radial and tangential velocities respectively at different radial positions from impeller tip. All mean velocity results are plotted along the radial direction in the plane between two baffles. The results obtained from RPT measurements were in a good agreement with the LDA data of Wu and Patterson (1989) and LES simulated data of Zadghaffari et al. (2010). The classical flow pattern for radial impellers, a jet like stream coming from Rushton turbine toward the tank wall is observed from RPT. The peak values of radial and tangential velocities near the impeller tip are high and reduce with increase in the radial distance from the impeller. The distribution of both the velocities is not symmetric at the impeller centre plane where impeller disk is placed, and shift slightly upwards, because the top surface is completely open and the impeller is not placed symmetrically within the vessel (Wu and Patterson, 1989; Bashiri et al., 2016).

The radial velocity profiles at various radial locations from the RPT are close to the LDA measurements while the peak velocities from the RPT are slightly lower (2-13%) than that from the LDA (Figure 4.4). The peak value of radial velocity close to the impeller obtained from RPT technique is much better as compared to the CARPT measurements of Rammohan et al. (2001a) where a relative difference of 34% was found when compared to the LDA measurements of Wu and Patterson (1989). However, the present RPT work has given superior measurement of the peak radial velocity close to the impeller with a relative difference of 5%. This relative deviation may be because of two reasons viz., the difference in the blade thickness and the frequency of data acquisition in LDA (Rammohan et al., 2001a).

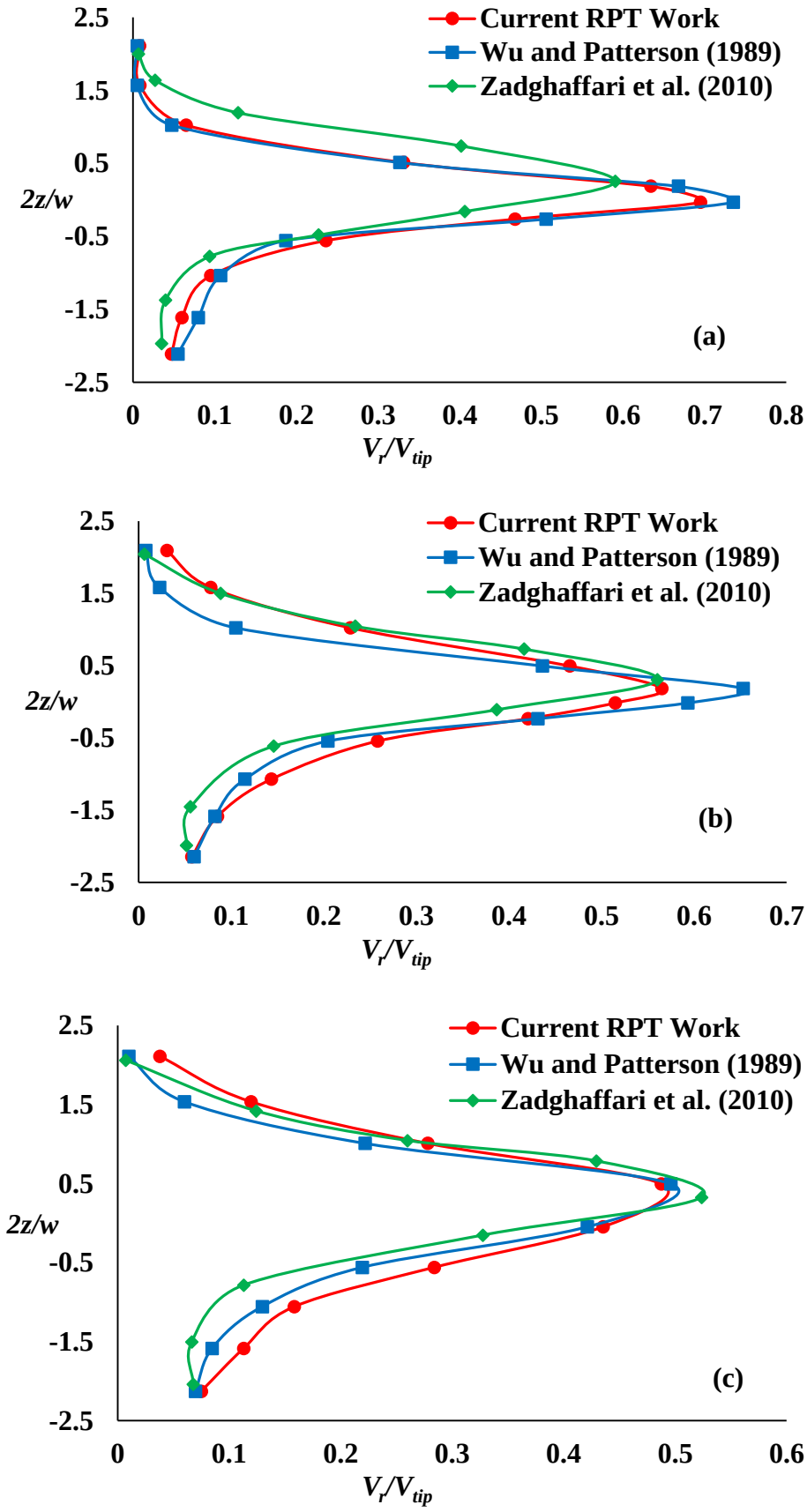

Figure 4.4 Axial profiles of normalized mean radial velocity at radial distance of r/R = 1.07 (a), 1.29 (b), 1.5 (c) and at angle $\theta = 45^{\circ}$

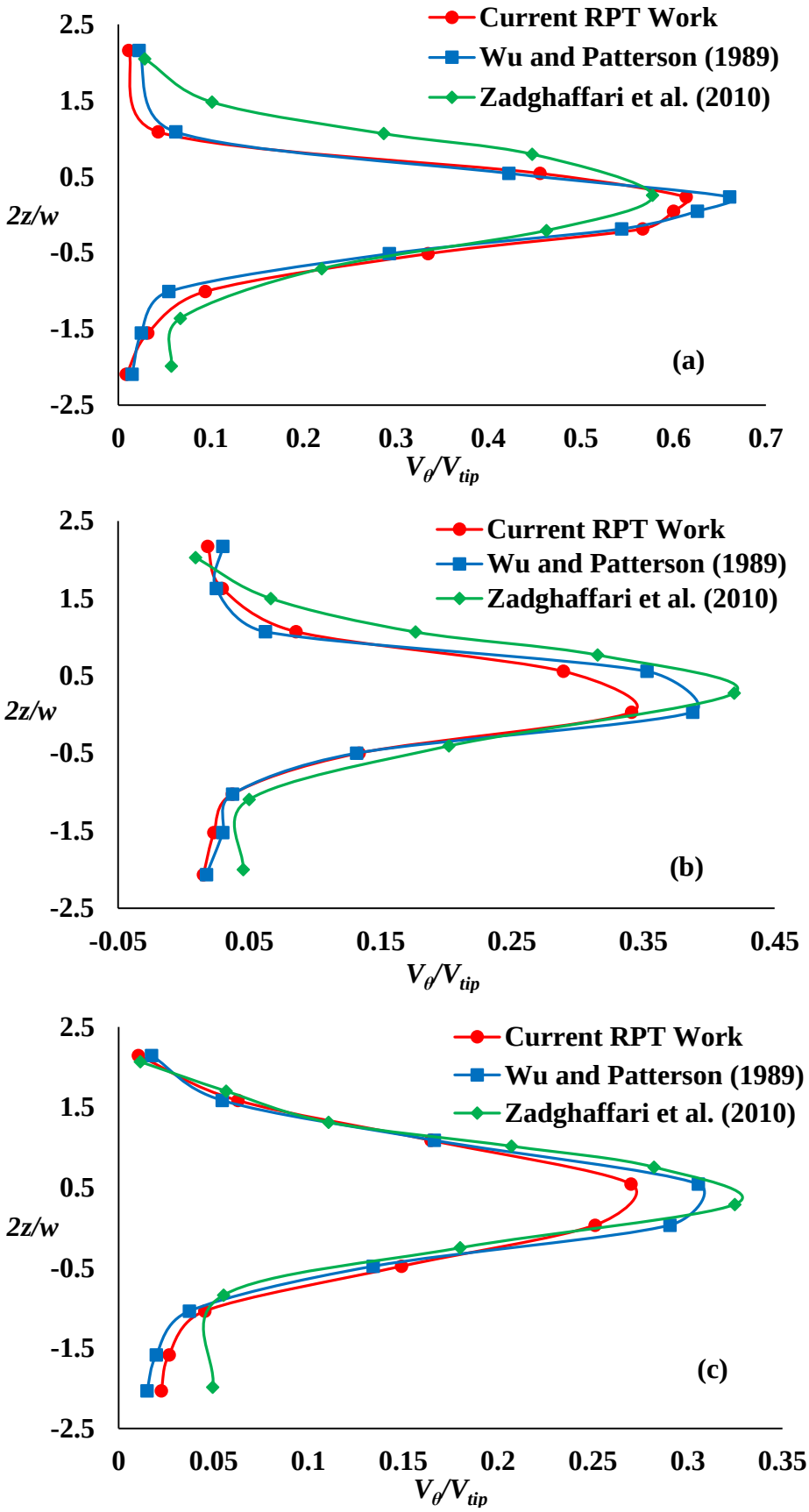

Figure 4.5 Axial profiles of normalized mean tangential velocity at radial distance of r/R = 1.07 (a), 1.29 (b), 1.5 (c) and at angle $\theta = 45^{\circ}$

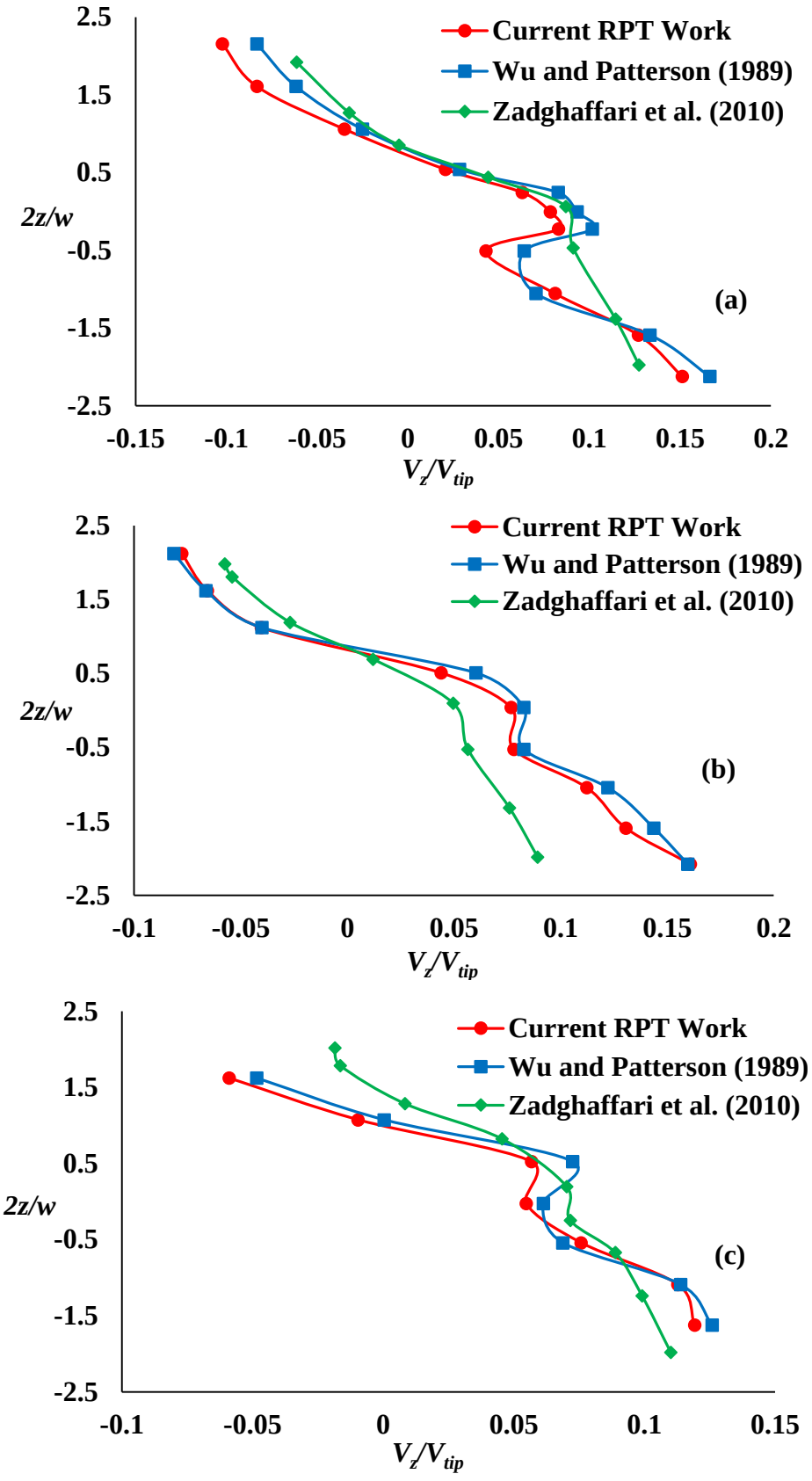

Figure 4.6 Axial profiles of normalized mean axial velocity at radial distance of r/R = 1.07 (a), 1.29 (b), 1.5 (c) and at angle $\theta = 45^{\circ}$

From Figure 4.5, it can be seen that the RPT qualitatively measured the tangential velocity as compared to the LDA measurements. The RPT has given slightly lower values of tangential velocities at the peak locations with a relative difference of 7-10%. However, this measurement is much better in comparison with the earlier CARPT measurements performed by Rammohan et al. (2001a) wherein the respective deviations were 15-25%.

Figure 4.6 depicts the axial profiles of normalized mean axial velocity at different radial positions from impeller tip. RPT accurately measured axial velocities which are almost similar with the LDA measurement. The magnitudes of axial velocity were found to be less than the radial and tangential velocities. Slight differences were observed in the peak values of the RPT in comparison with the LDA.

4.2 Determination of Optimal Dimensions of Inner-Rotating Fluid Zone for MRF Technique using CFD Model, and Validation of CFD Model with RPT and Literature Data

Following the literature, RANS based turbulence model in combination with MRF impeller rotation model is the computationally economic way for CFD modelling of stirred tank. However, the dimensions of inner-rotating fluid zone are required to be determined for MRF technique. Though various researchers have used MRF technique (Dong et al., 1994; Ciofalo et al., 1996; Deglon and Meyer, 2006; Ochieng et al., 2008; Basavarajappa et al., 2015), they have not studied the optimality of the dimensions of inner-rotating fluid zone. With this consideration the issue for the selection of inner-rotating fluid zone, in present work, a series of steady CFD simulations have been conducted to find the optimal dimension of inner-rotating fluid zone by varying diameter and height of zone. In present study, the geometry of stirred tank and operating parameters were considered as reported in the literature data of Wu and Patterson (1989). The details of dimensions used for CFD model of stirred tank are given in Table 4.7.

The dimensions of inner-rotating fluid zones for various CFD simulations are given in Table 4.8 and corresponding diagrammatic representation of inner-rotating zones is shown in Figure 4.7. The optimal inner-rotating fluid zone has been considered where simulation results for velocity predictions such as tangential velocity, radial velocity and axial velocity were found in a reasonable agreement with literature data of Wu and Patterson (1989). Further the

efficiency of CFD model with optimal MRF zone has been validated with the RPT data obtained from present work and literature data.

Table 4.7 Stirred tank dimensions and operating conditions (Wu and Patterson, 1989)

Tank diameter (T)	0.27 m
Water height in tank (H)	0.27 m
Baffle width (b) = T/10	0.027 m
Impeller diameter (D)	0.093 m
Blade width (w) = D/5	0.0186
Blade length (l) =D/4	0.02325 m
Turbine location from bottom of tank (C) = T/3	0.093 m
Density of Water (ρ)	998.2 kg/m^3
Viscosity of Water (μ)	0.001003 Pa.s

Table 4.8 Inner-rotating fluid zones and their dimensions

Inner-rotating fluid zone number	**Height (m)**	**Diameter (m)**
1	0.0392	0.0930
2	0.0410	0.1023
3	0.0429	0.1116
4	0.0503	0.1488
5	0.0540	0.1674
6	0.0578	0.1860
7	0.0615	0.2046

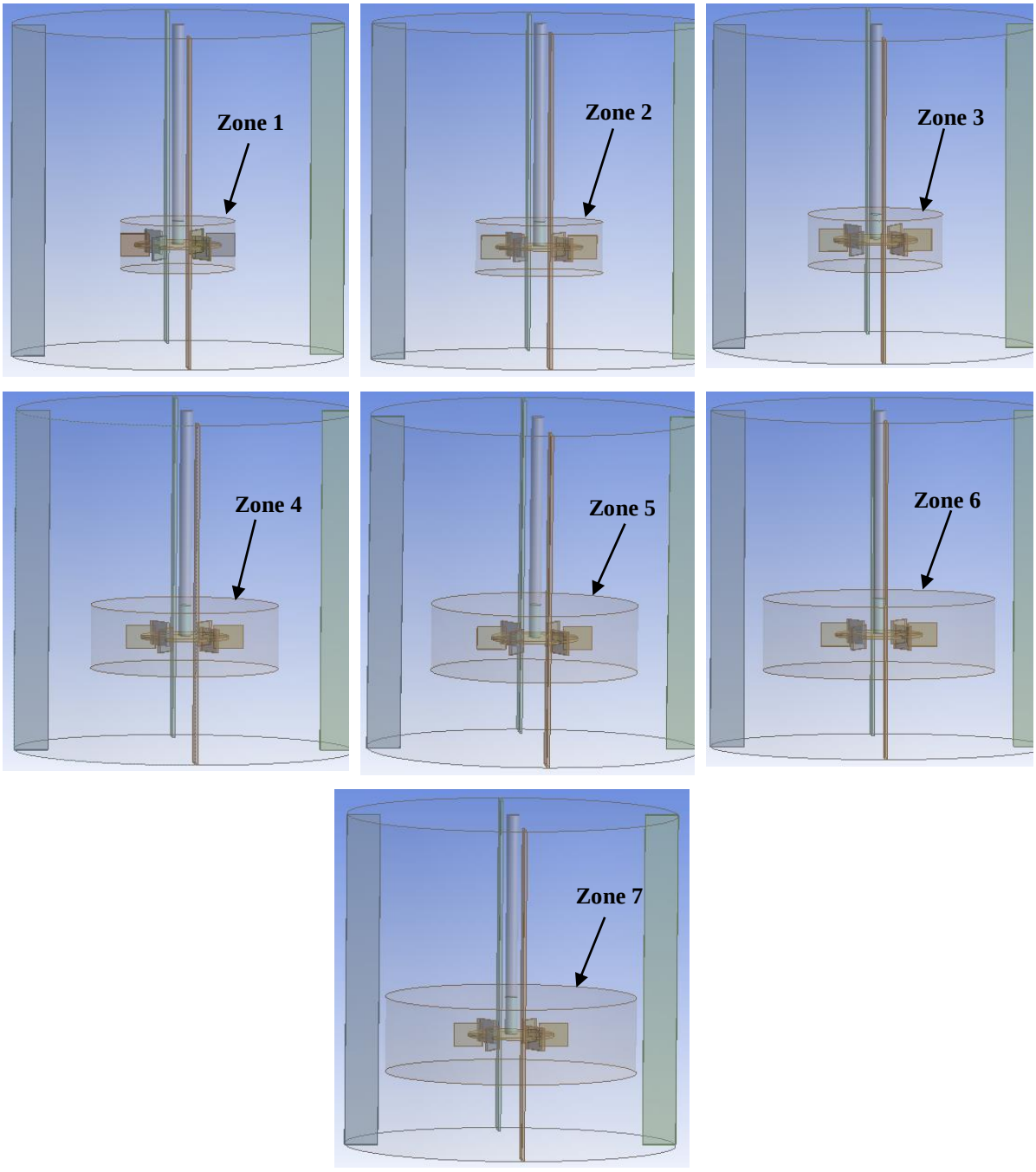

Figure 4.7 Diagrammatic representation of inner-rotating fluid zones

4.2.1 Determination of Optimal Dimensions of Inner-Rotating Fluid Zone

The comparison between CFD predictions and literature data of mean velocities at different inner-rotating zones are depicted in Figures 4.8, 4.9 and 4.10. The mean velocities have been measured at radial distance r/R of 1.07 and $\theta = 45^{\circ}$. At impeller center plane, the value of radial and tangential velocities reached to maximum, as there is sharp variation in flow fields due to continuous rotation of impeller. CFD slightly under-predicted the normalized radial velocities but qualitatively in a good agreement with literature data. This under-prediction of radial

velocity could be observed because of limitations in *k-ε* turbulence model (Basavarajappa et al., 2015). The peak value of mean radial velocity predicted by CFD at zone 6 is in a good agreement with literature data compared to other zones (Figure 4.8). In comparison of tangential velocity, axial location of peak is shifted below as compared with experiments. Also, the trend of tangential velocity observed at zone 6 is in a good agreement with literature data compared to other zones (Figure 4.9).

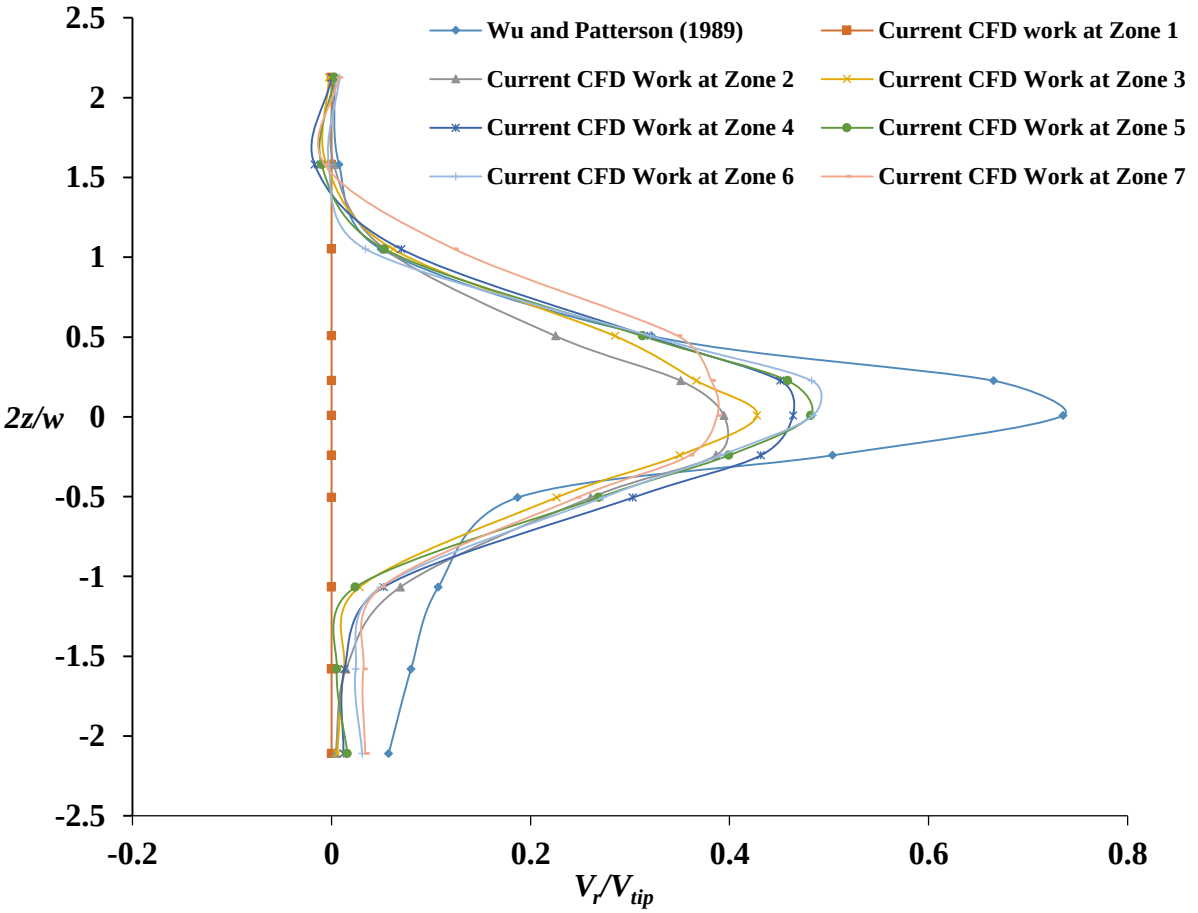

Figure 4.8 Comparison of mean radial velocity profiles between literature data and CFD predictions for different inner-rotating fluid zones

In order to find the best inner-rotating fluid zone among all seven different inner-rotating fluid zones under consideration, the CFD results of mean radial, mean tangential and mean axial velocities are quantitatively measured in terms of Root Mean Squared Error (RMSE) and correlation coefficient. RMSE and correlation coefficient are the basic statistical indicators commonly used by researchers for quantitative evaluation of model predictions. RMSE measures the difference between the values predicted by the CFD model and the values observed from the literature data. Further, correlation coefficient is estimated which describes

the strength of linear relationship between CFD model predicted values and literature data. The small value of RMSE and the large value of correlation coefficient indicate a good agreement between the CFD predictions and experimental data (Barnston, 1992).

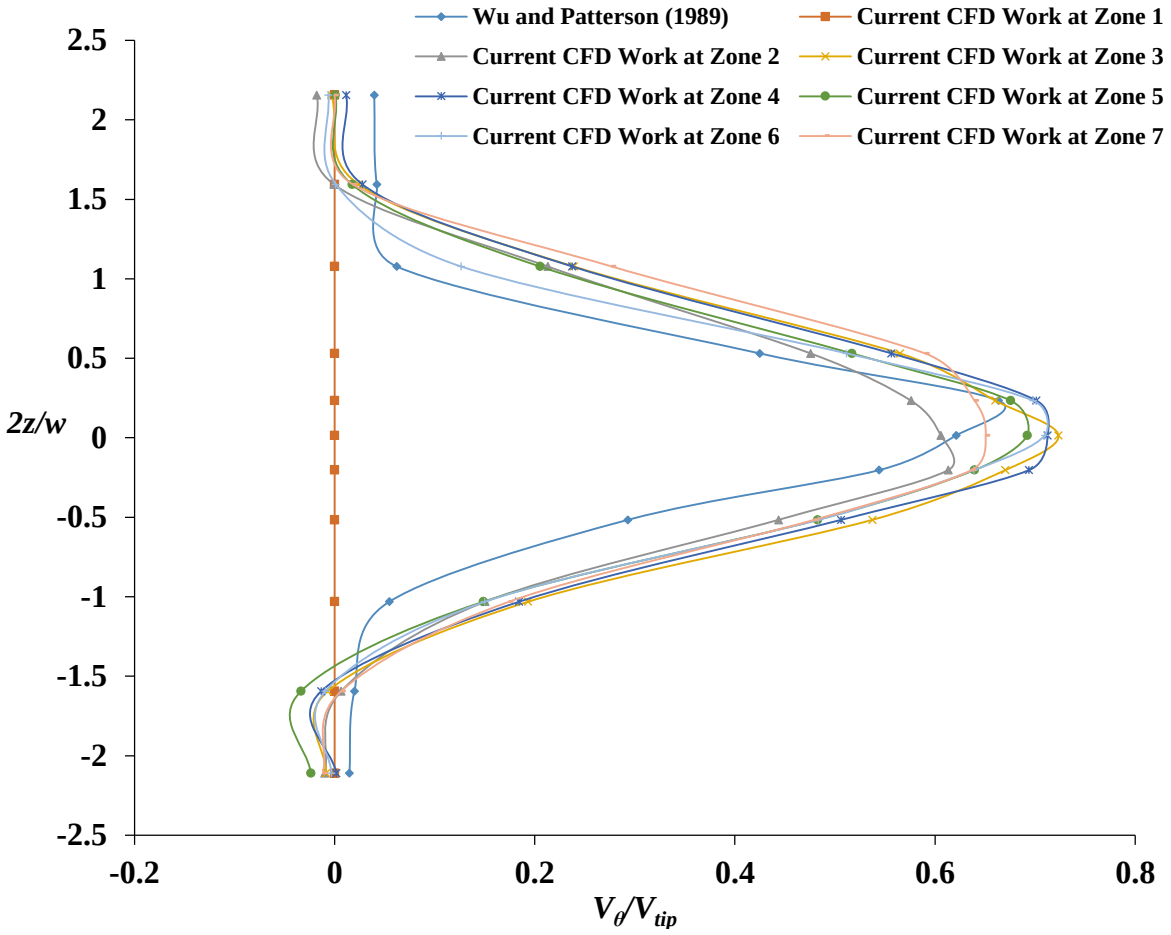

Figure 4.9 Comparison of mean tangential velocity profiles between literature data and CFD predictions for different inner-rotating fluid zones

The dimensions of inner-rotating zones are increased from zone 1 to zone 7 as shown in Table 4.8. Zone 1 is very close to impeller tip and zone 7 is near to baffles. From Figure 4.11, the RMSE in radial velocity decreased from zone 1 to zone 6 and again it increased at zone 7. Similarly, the correlation coefficient for radial velocity increased from zone 1 to zone 6 and decreased at zone 7. The best value of RMSE and correlation coefficient for radial velocity is found at zone 6. Similarly, the best value of RMSE and correlation coefficient for tangential velocity is found at zone 6 as shown in Figure 4.12. But in the case of axial velocity, correlation coefficient and RMSE are good at zone 5 but with very slight difference with zone 6 as shown in Figure 4.13. In present work, Rushton turbine (radial type) impeller is used, wherein radial and tangential components of velocity are the major factor of flow variation compared to axial

velocity. Hence, RMSE and correlation coefficient are considered based on radial and tangential velocities. From the comparison of radial and tangential velocities, CFD results at zone 6 are found qualitatively and quantitatively in a good agreement with the literature data. Hence, zone 6 is considered to the optimal inner-rotating fluid zone with the radial and axial extent of twice of impeller dimeter (D) and 1.5 times of blade height (w) above and below the impeller disk respectively. The predictive capability of CFD model with optimal inner-rotating fluid zone is validated with RPT and literature data. The detailed comparison for mean velocities, re-circulating loops, pumping number, power number and turbulence parameters is discussed in following sections.

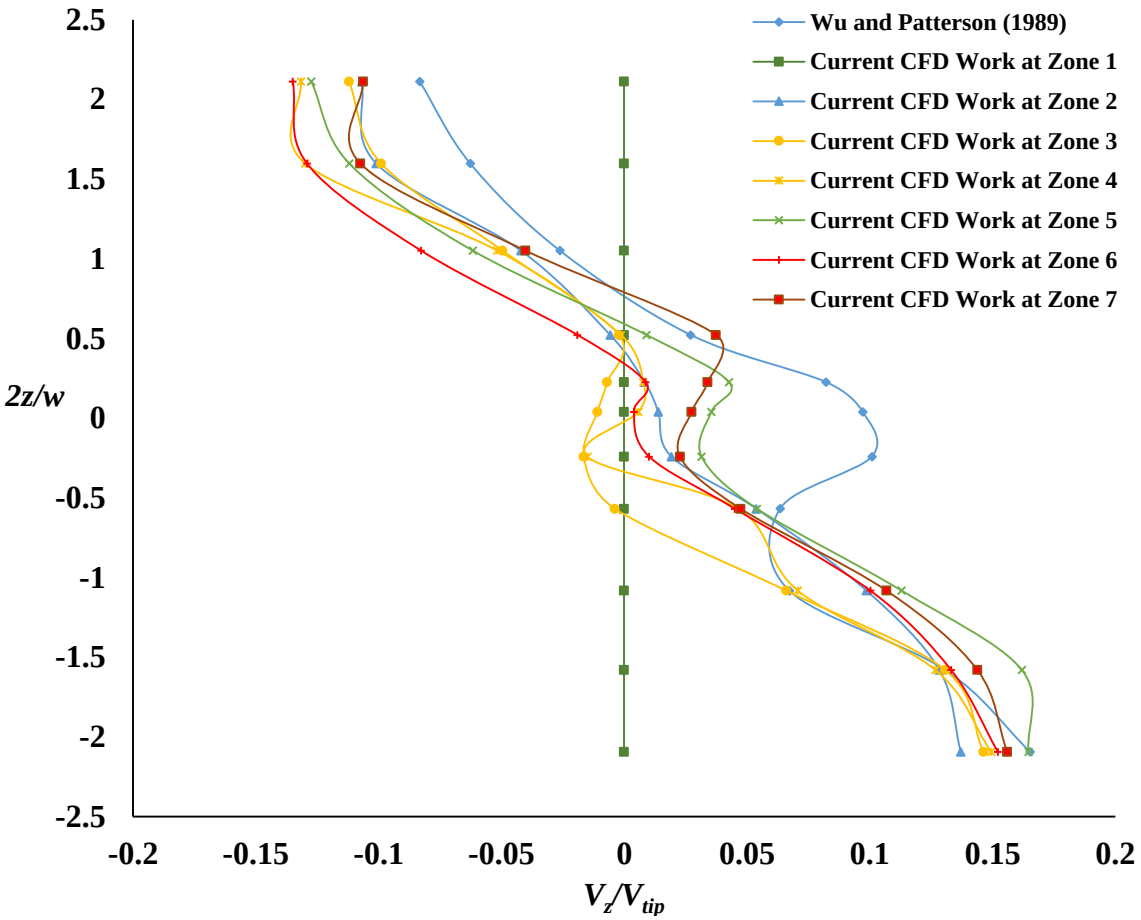

Figure 4.10 Comparison of mean axial velocity profiles between literature data and CFD predictions for different inner-rotating fluid zones

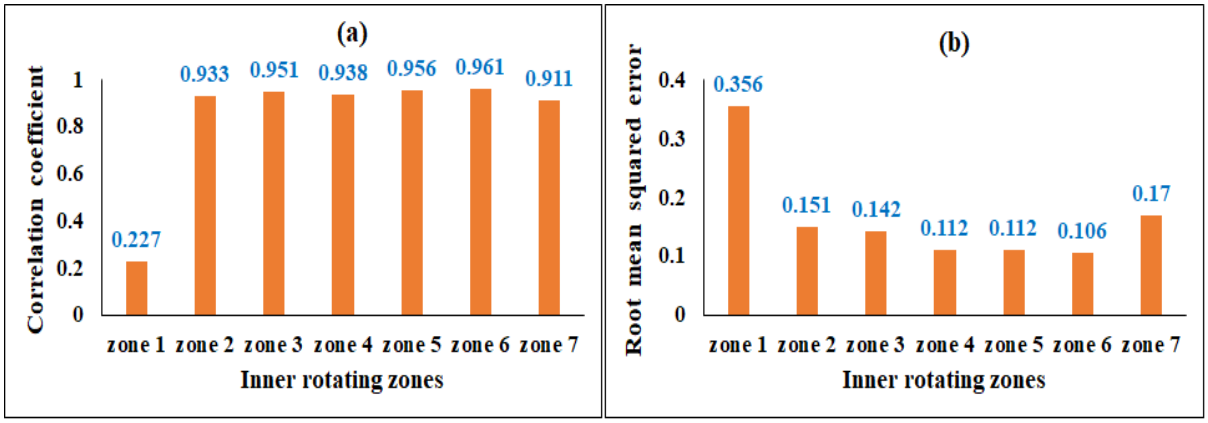

Figure 4.11 Correlation coefficient (a) and root mean squared error (b) between CFD predictions and literature data of radial velocity at different inner-rotating fluid zones

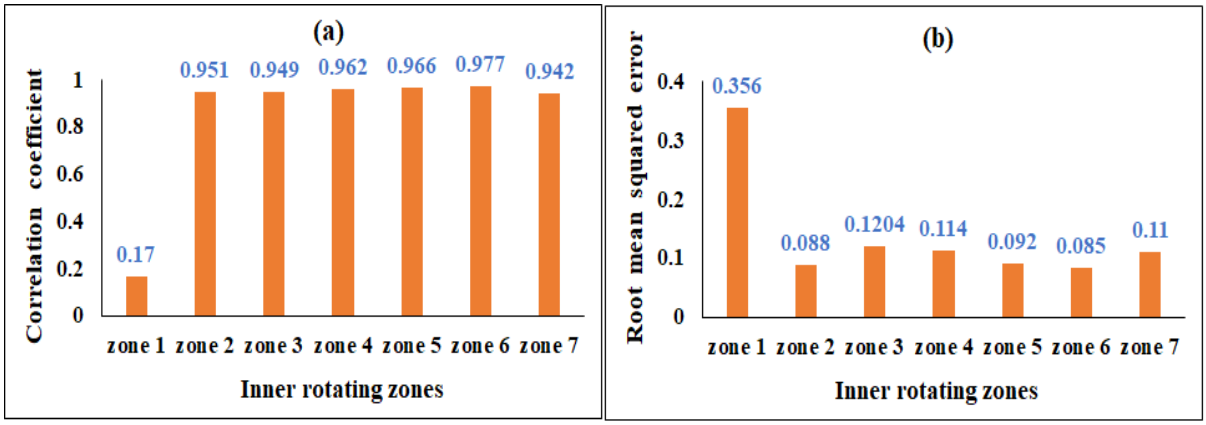

Figure 4.12 Correlation coefficient (a) and root mean squared error (b) between CFD predictions and literature data of tangential velocity at different inner-rotating fluid zones

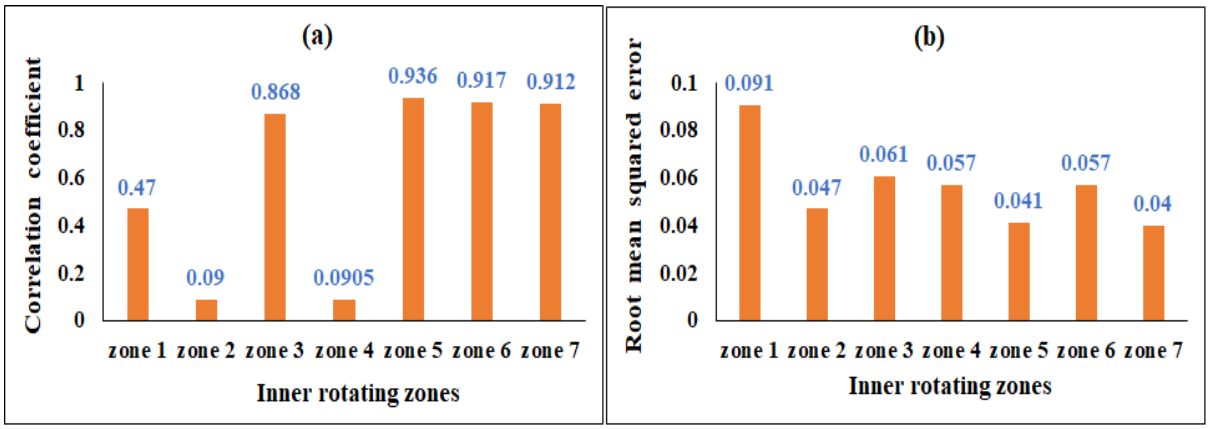

Figure 4.13 Correlation coefficient (a) and root mean squared error (b) between CFD predictions and literature data of axial velocity at different inner-rotating fluid zones

4.2.2 Validation of CFD Model with RPT and Literature Data

4.2.2.1 Prediction of Mean Velocities

Figures 4.14 - 4.16 show the comparison of CFD results with the RPT, LDA literature data of Wu and Patterson (1989) and LES simulated data of Zadghaffari et al. (2010) for radial, tangential and axial velocities at different radial locations respectively. The CFD results are found qualitatively in a good agreement with RPT and literature data. The peak value of radial and tangential velocities near the impeller tip are high and reduces with increase in the radial distance from the impeller. The radial and tangential velocity profiles close to the impeller have shown a good agreement with the respective experimental profiles above and below the impeller centre-plane while some deviations were observed in the peak values of the same. This difference in the peak velocities decreases as the radial distance from the impeller increases. At the normalized radial location of r/R = 1.5, a good agreement of peak radial and tangential velocities have been observed. This may be due to the incapability of standard k-ε model inaccurately predicting the mean velocity fields near the impeller whereas the same provides accurate predictions of the same in the bulk flow region (Basavarajappa et al., 2015). The profiles of mean velocities predicted by current standard k-ε based simulated results are found to be better in comparison with LES based simulated results of Zadghaffari et al. (2010).

The details of percentage variation between CFD predictions, RPT data and literature data close to the impeller for peak values of mean velocities is given in Table 4.9. The maximum error in the peak mean radial, tangential and axial velocities were found to be 15%, 19% and 27% respectively. The variation in the results for all mean velocities obtained from CFD model at peak points (impeller stream swept region where the velocity gradients are very sharp due to the periodic passage of impeller) may be due to the differences in the blade and disk thickness used for the modelling and that used in the literature (Coroneo et al., 2011).

Table 4.9 Percentage error in the measurements of mean velocities at peak points

Mean velocities	**Wu and Patterson (1989) and RPT**	**Wu and Patterson (1989) and CFD**	**RPT and CFD**	**Zadghaffari et al. (2010) and CFD**
Radial velocity	5.46 %	15.04 %	10.12 %	3.41%
Tangential velocity	7.09 %	8.33 %	16.61 %	19.39%
Axial velocity	18.30 %	12.79 %	27.57 %	24.56%

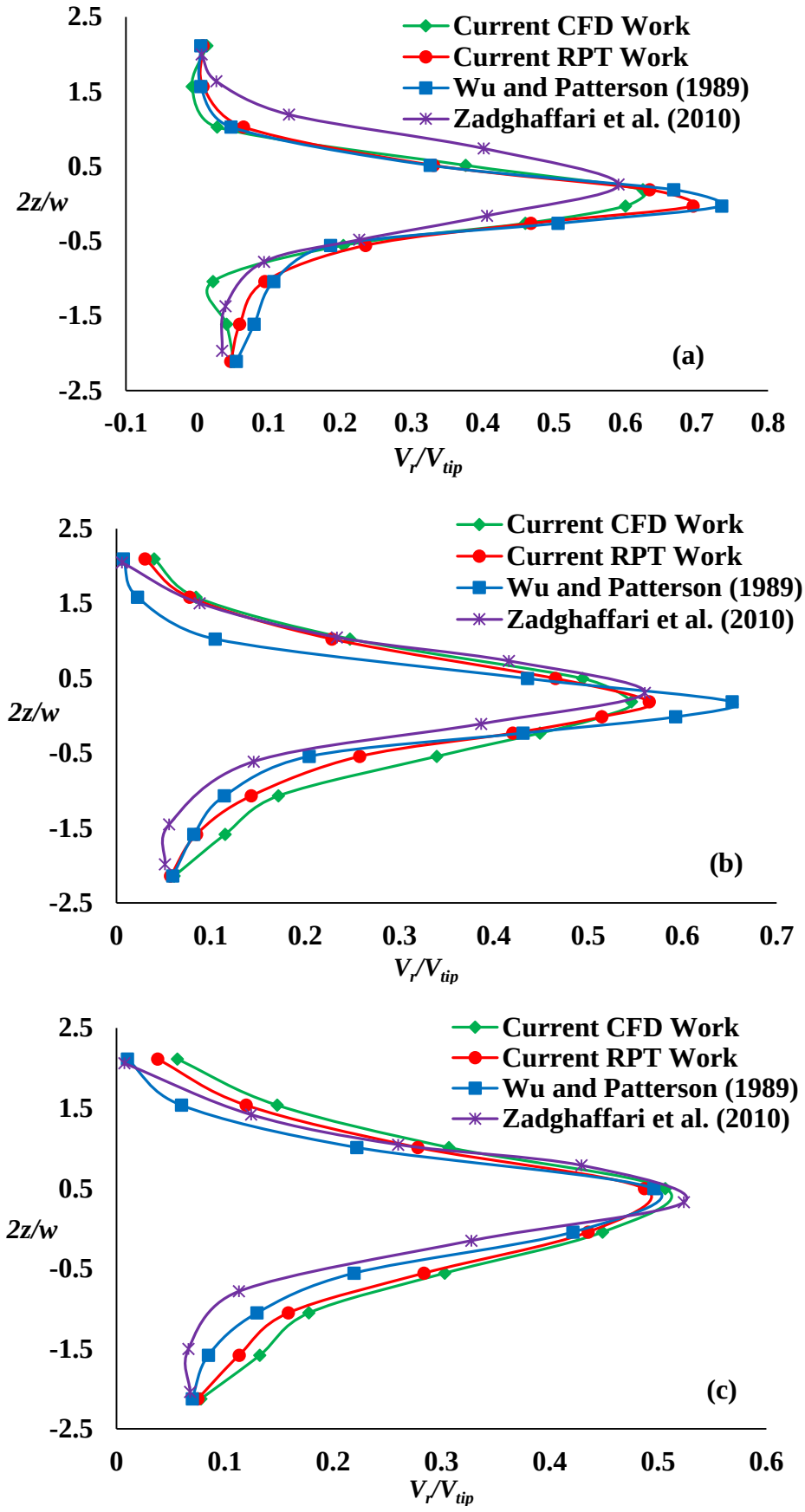

Figure 4.14 Comparison of normalized profiles of mean radial velocity at radial distance of r/R = 1.07 (a), 1.29 (b), 1.5 (c) and at angle $\theta = 45^{\circ}$

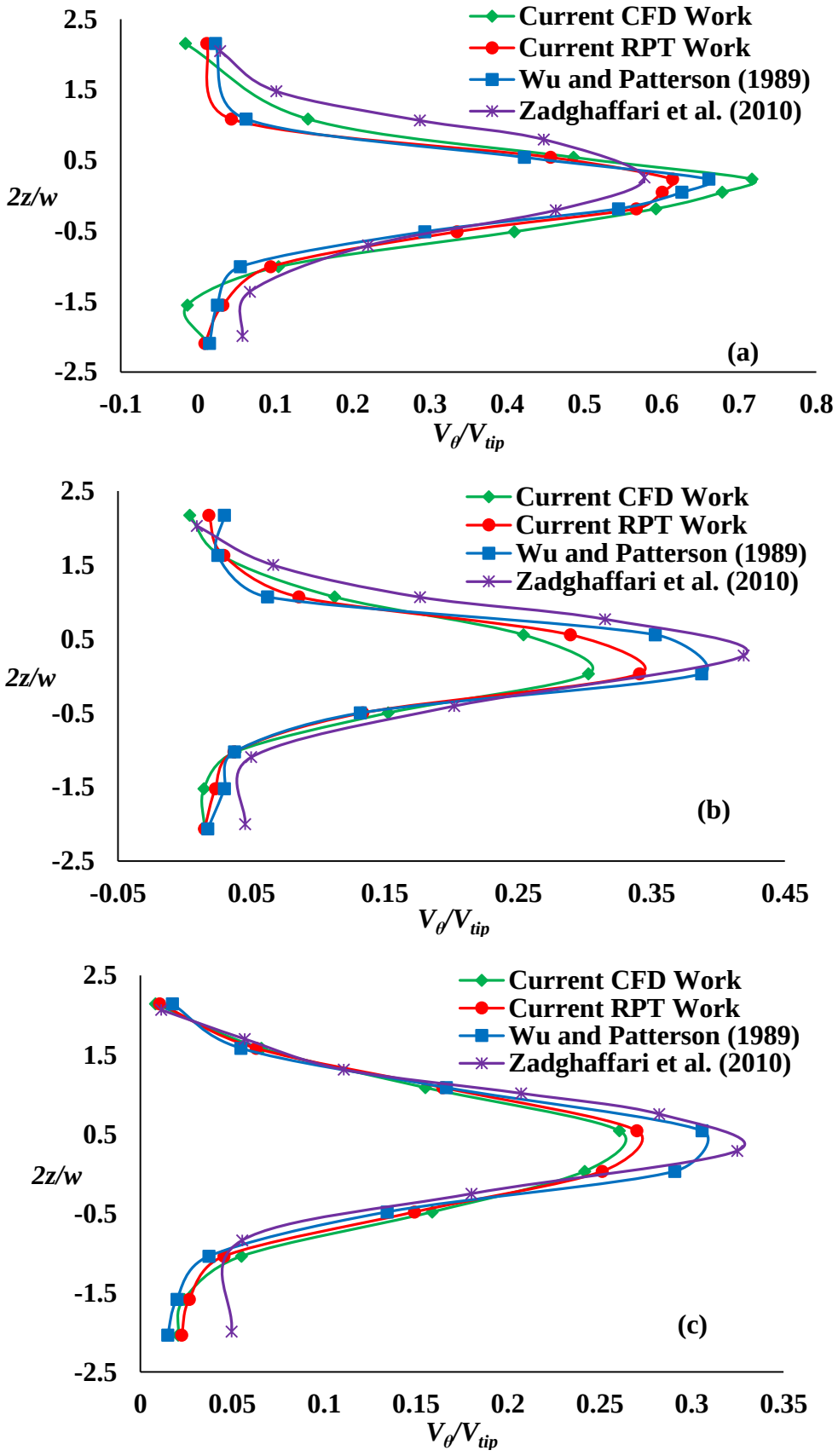

Figure 4.15 Comparison of normalized profiles of mean tangential velocity at radial distance of r/R = 1.07 (a), 1.29 (b), 1.5 (c) and at angle $\theta = 45^{\circ}$

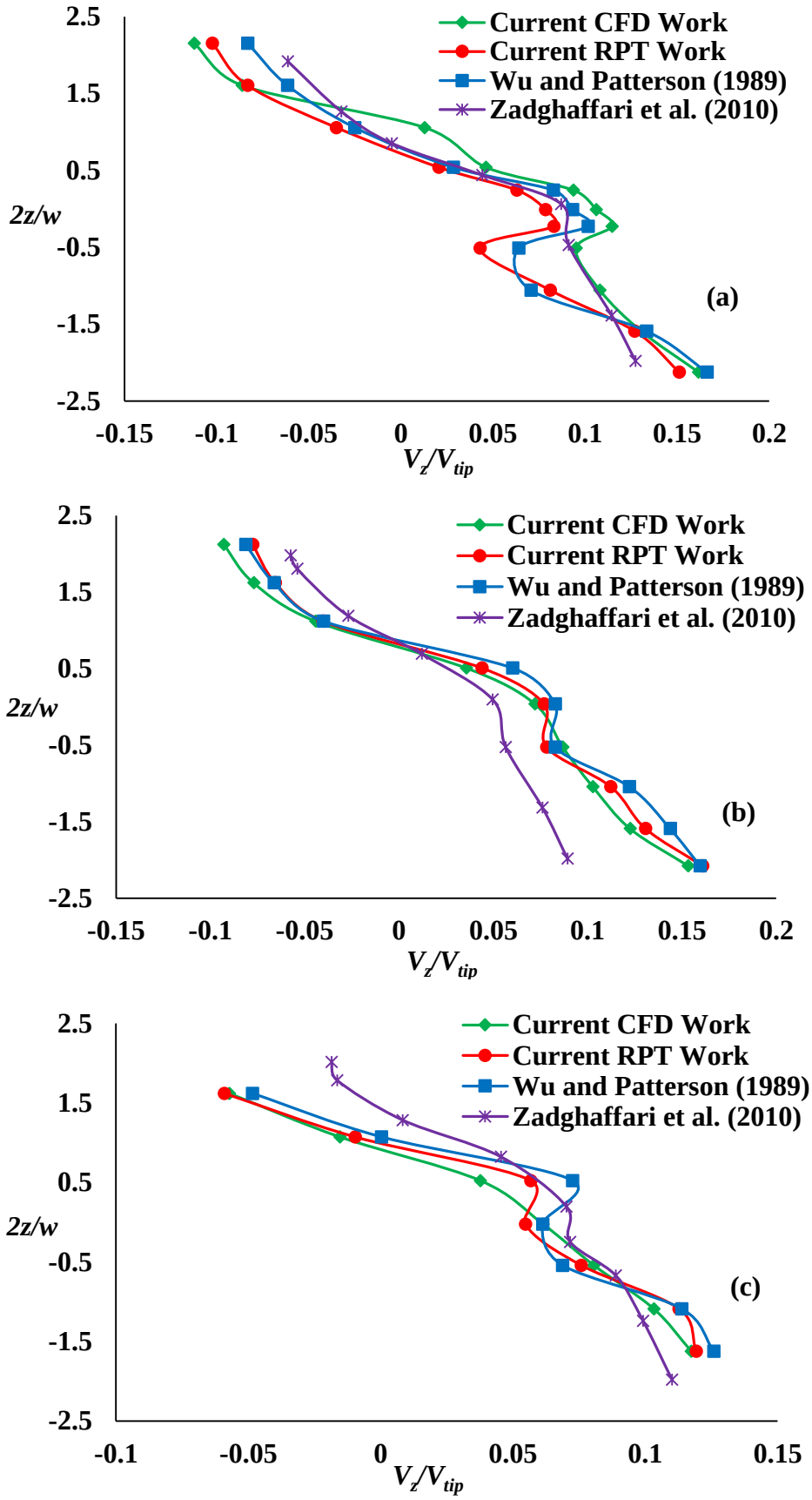

Figure 4.16 Comparison of normalized profiles of mean axial velocity at radial distance of r/R = 1.07 (a), 1.29 (b), 1.5 (c) and at angle $\theta = 45^{\circ}$

4.2.2.2 Prediction of Eye of Re-Circulating Loops

The average velocity vector along the mid-baffle plane obtained from the CFD model is shown in the Figure 4.17(a) which adequately illustrates the classic double re-circulation pattern related to the standard configured stirred tank.

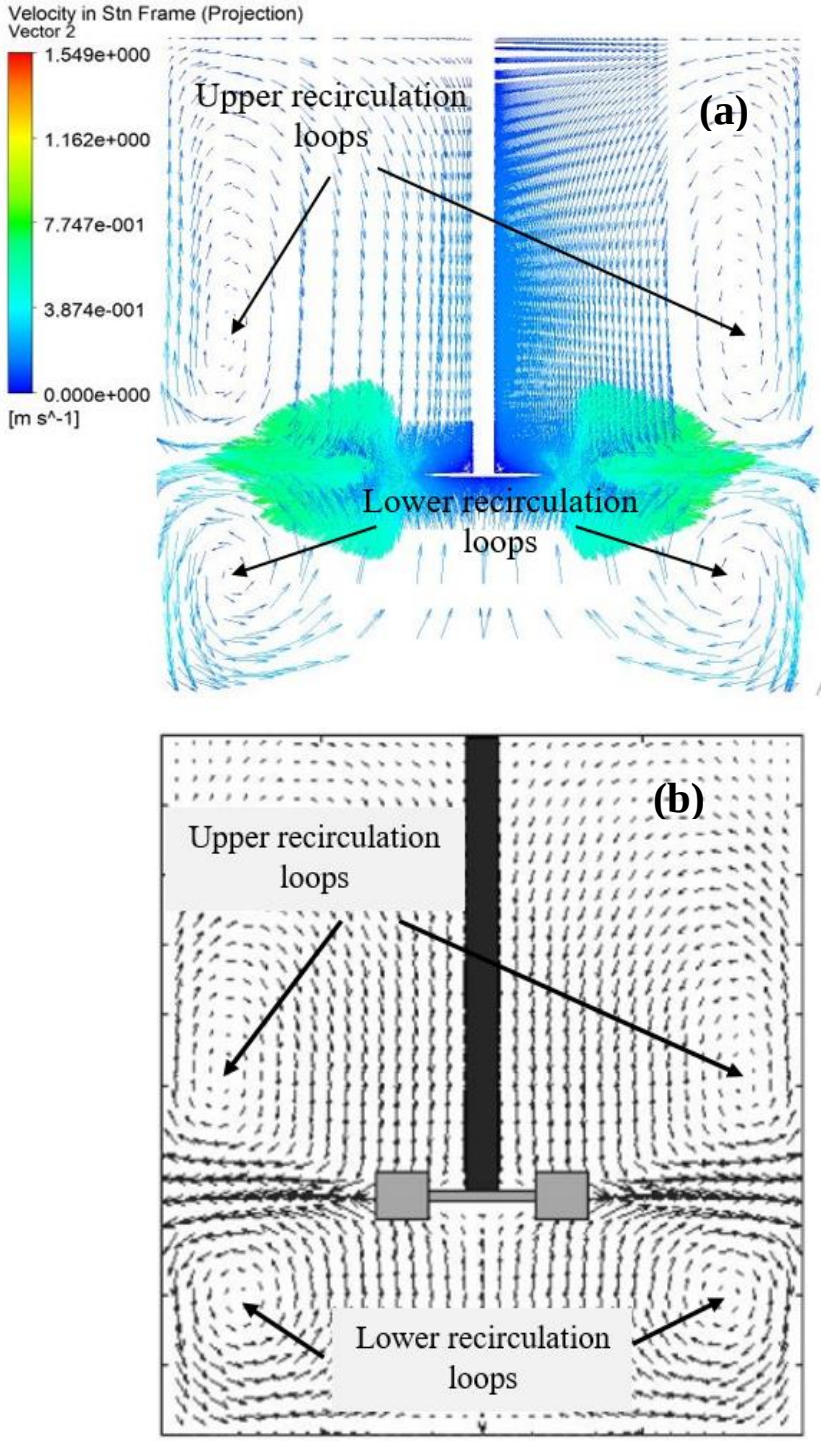

Figure 4.17 Velocity vector plot obtained from current CFD work (a) and velocity vector plot of Rammohan et al., 2001b (b)

The impeller stream goes towards the tank walls and it splits into two regions, one of them circulates towards the upper region and other towards the lower region and both finally return to impeller region. The radial and axial locations of the centres or eyes of both the re-circulating loops are accurately predicted by the CFD model when compared to the literature results as given in the Table 4.10.

The impeller discharge stream is mainly radial and characterised by high velocity magnitudes which decrease towards the periphery of the stirred tank. The discharge stream is slightly inclined upwards since the free surface is completely open and the impeller is not placed symmetrically within the vessel (Wu and Patterson, 1989; Bashiri et al., 2016). The higher magnitudes of velocity associated with the lower re-circulation loops make it stronger as compared to upper re-circulation loops and hence the former regions consume more power as compared to the latter regions (Nienow, 1968). Thus, the double re-circulation loops obtained from the present study agree with the literature data of Rammohan et al. (2001b) as shown in Figure 4.17(b).

Table 4.10 Location of eye of re-circulating loops

	Lower (*r*/*T*)	**Lower (*z*/*T*)**	**Upper (*r*/*T*)**	**Upper (*z*/*T*)**
Schaeffer et al. (1997)	0.40	0.20	0.40	0.50
Rammohan et al. (2001b)	0.40	0.20	0.40	0.50
Current CFD work	0.39	0.19	0.40	0.51

4.2.2.3 Prediction of Impeller Pumping Capacity

Radial pumping number (N_r) is one of the global flow characteristic which defines the liquid circulation rate in mixing tanks. N_r is obtained by calculating radial impeller pumping capacity (Q_r) and normalized with ND^3 (Equation 4.1). The radial pumping capacity is obtained by integrating the mean radial velocity over the two axial positions at top and bottom edge of impeller tip. Figure 4.18 shows the comparison of CFD predicted radial pumping number with literature data. The radial pumping capacity increases with increase in radial distance from the impeller tip due to the fluid entrainment (Wu and Patterson, 1989).

$$N_r = \frac{Q_r}{ND^3} = \frac{2\pi r \int_{z_1}^{z_2} V_r dz}{ND^3} \tag{4.1}$$

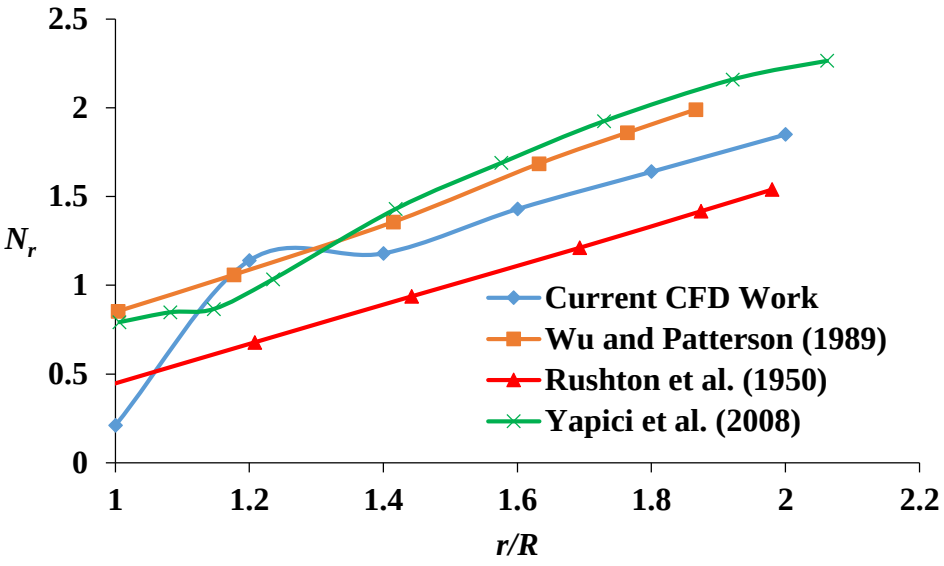

Figure 4.18 Profiles of radial pumping number in the impeller stream

The deviation in pumping number values at most of the radial locations is less than 15%. This shows a good agreement of CFD results with that of experimental results of Wu and Patterson (1989). But the pumping number near the impeller shows large variation from the experimental results and this may be due to the limitations of RANS based *k-ε* turbulence model in predicting turbulence quantities (Deglon and Meyer, 2006). Further the thickness of blade and impeller disk are not reported in the literature of Wu and Patterson (1989) which can significantly affect the pumping number predictions (Coroneo et al., 2011). The results of Rushton et al. (1950) show slight deviations from the CFD results as well as results of Wu and Patterson (1989) due to the variation in the impeller geometry, operating conditions and measurement techniques (Wu and Patterson, 1989). CFD predicted radial pumping number is found to be in a good agreement with the LES simulated data of Yapici et al. (2008).

4.2.2.4 Prediction of Power Number

Power required for stirring is the one of the key design factor from process economics point of view. In this study, the effect of Reynolds number on power consumption has been studied. The power consumption is defined in terms of dimensionless power number (Equation 4.2) where *P* is the power given by impeller to liquid for agitation. The torque (τ) required to calculate the power consumption has been obtained from CFD results.

$$power\ number\ (N_p) = \frac{P}{\rho N^3 D^5}\ where\ P = 2\pi N\tau,\ N_{\mathrm{Re}} = \frac{ND^2\rho}{\mu} \qquad (4.2)$$

Figure 4.19 shows the log-log plot of power number versus Reynolds number. In the laminar range (N_{Re}<10), N_p linearly decreases with N_{Re}. In the transitional flow regime ($10 < N_{Re} < 10^4$), slight variation in N_p was observed. In Turbulence regime ($N_{Re} > 10^4$), N_P was observed to be constant with N_{Re}. The CFD predictions of power number in the laminar and transitional regimes shows a good agreement with the experimental results of Rushton et al. (1950) and simulated data of Gillisen and Akker et al. (2012) with the deviation of less than 12%. But the average deviation in the power number predictions between CFD model and experimental results increase to 25% in the turbulence regime. This deviation is partly due to limitations of *k-ε* turbulence model and variation in the thickness of blades used in experiments and CFD model (Deglon and Meyer, 2006).

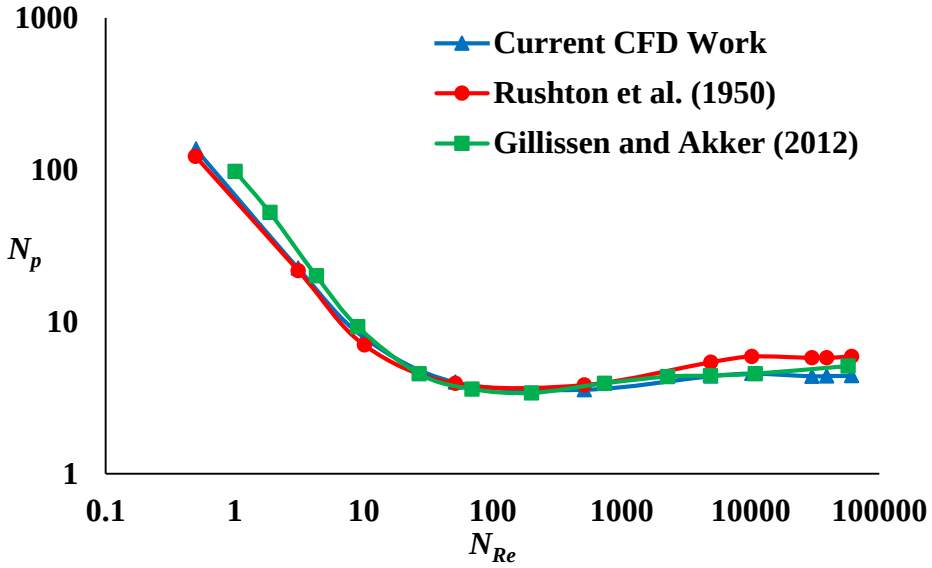

Figure 4.19 Effect of Reynolds number on power number

4.2.2.5 Prediction of Turbulence Parameters

The comparison of axial profiles of normalized turbulence kinetic energy and its dissipation rate with the experimental results of Wu and Patterson (1989) and simulated data of Singh et al. (2011) is shown in Figures 4.20 and 4.21 respectively. The axial profile of turbulence kinetic energy is in a good agreement with the experimental profile as illustrated in Figure 4.20. The double peak curve indicating the trailing vortices near upper and lower edges of the blades were properly predicted. The peak turbulence kinetic energy and its location above the impeller centre-plane were accurately predicted while the same below the impeller centre-plane were over-predicted. The over-prediction of turbulence kinetic energy below the impeller centre-plane may be due to the limitations of standard *k-ε* turbulence model as indicated by Deglon

and Meyer (2006) and Coroneo et al. (2011). The results of current CFD model are found much better compared to simulated results of Singh et al., 2011 (RSM model) wherein turbulence kinetic energy has severely under-predicted. Similar under-prediction of turbulence kinetic energy by RSM model has been reported by Murthy and Joshi (2008). The axial profiles of turbulence dissipation rate at normalized radial locations (r/R) of 1.29 and 1.5 are shown in Figures 4.21(a) and 4.21(b) respectively. The axial profiles of turbulence dissipation rate are in a close agreement with the experimental profiles and the locations of peak values are also accurately predicted. However, the turbulence dissipation rate near the impeller centre-plane is under-predicted. The under-prediction of turbulence dissipation rate near the impeller centre-plane may be due to the limitations of standard k-ε turbulence model and the assumptions involved in the RANS approach (Joshi et al., 2011).

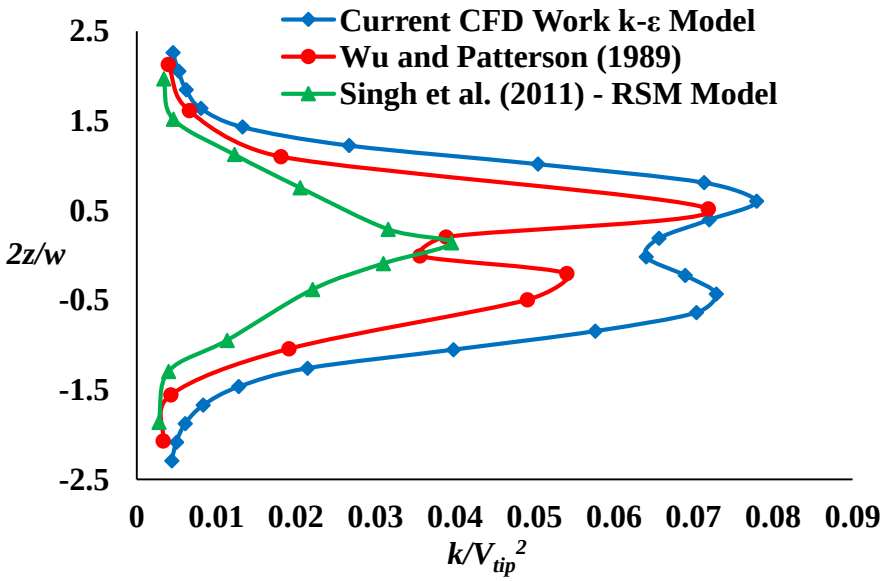

Figure 4.20 Axial profile of normalized turbulence kinetic energy at radial distance of r/R = 1.07 and at angle $\theta = 0^{\circ}$

The under/over prediction of turbulence quantities obtained from this study may be due to the assumption of isotropic turbulence condition associated with the standard k-ε turbulence model (Joshi et al., 2011). As observed from the comparison of turbulence quantities, Singh et al. (2011) have used completely anisotropic RSM (Reynolds Stress Model) for modelling the turbulence quantities, the respective predictions were also found to be much inferior as compared to the standard k-ε turbulence model. Therefore, the LES approach may be needed to obtain accurate prediction of turbulence quantities (Montante et al., 2001; Joshi et al., 2011).

But LES approach is computationally more expensive as compared to the RANS approach and hence is unsuitable in the context of practical engineering applications (Khopkar et al., 2004).

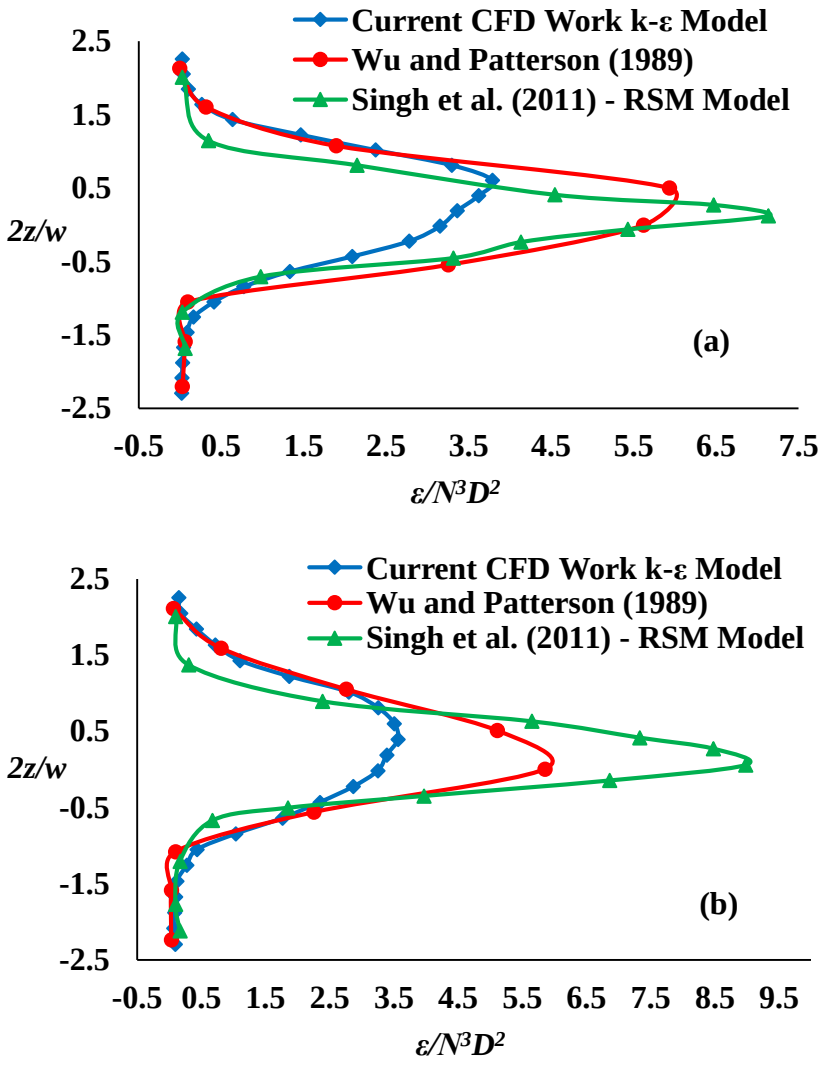

Figure 4.21 Axial profiles of normalized turbulence dissipation rate at radial distance of r/R = 1.29 (a), 1.5 (b) and at angle $\theta = 0^{\circ}$

Due to optimal selection of inner-rotating fluid zone in MRF, the CFD model has given a reasonable prediction of mean velocities, double re-circulation loop flow pattern, radial pumping number, power number and turbulence parameters. Hence, CFD model is used for investigation of effect of impeller clearance and impeller diameter on flow hydrodynamics in stirred tank. The detailed investigation is discussed in the following sections.

4.3 Investigation of Effect of Impeller Clearance on Flow Hydrodynamics in Stirred Tank using CFD Model

In stirred tanks, the location of impeller is one of the important geometrical parameters which significantly affect the flow hydrodynamics. The impeller located at bottom and middle of tank have been widely investigated, but impeller located at tank top has not been much investigated. However, many industrial applications such as aeration in wastewater treatment and other gas transfer operations require impeller to be placed near the gas-liquid interface (Patil et al., 2004; Deshmukh and Joshi, 2006; Rao et al., 2009; Devi et al., 2011; Kulkarni and Patwardhan, 2014). In standard configured stirred tank, impeller clearance is maintained at C/T = 0.33. In the present work, CFD simulations have been conducted from low to high impeller clearances (ranging from C/T = 0.15 to 0.85) and its effect on flow hydrodynamics has been investigated.

In this study, the stirred tank geometry and operating conditions were kept same as used for RPT experiments (Figure 3.1) and the impeller clearance (C) was varied. A cylindrical coordinate system was adopted, with r, z and θ indicating the radial, axial and tangential coordinates respectively. Its origin was fixed at center of tank bottom with r, z and $\theta = 0^{\circ}$, V_r, V_z and $V_{tip} = \pi ND$ represent the mean radial, mean axial and impeller tip velocity respectively.

4.3.1 Validation of CFD Simulation Results at Standard and Low Clearances

In this section, CFD simulation results of flow fields and turbulence parameters at standard and low clearances are compared with literature data. Figure 4.22 shows the comparison of normalized profiles of mean axial velocity with experimental results of Montante et al. (1999) and k-ε model based simulations of Zhu et al. (2019). The mean axial velocity was calculated for three different clearances (C/T = 0.33, 0.2 and 0.15) at axial location of 0.015m below the impeller disk and $\theta = 45^{\circ}$. A good agreement between CFD simulation results and literature data was observed. At clearance of C/T = 0.15, peak points are found to be in good agreement with experimental data, but their locations are slightly shifted. The difference in the prediction may be because of blade and disk thickness which significantly affect the flow fields (Coroneo et al., 2011).

Figure 4.23 depicts the turbulence kinetic energy at C/T = 0.15 at various axial locations below the impeller disk and compared with experimental results of Li et al. (2011) and Montante et al. (1999) as well as simulation results of Montante et al. (2001). The profiles are qualitatively in a good agreement with experimental data, but under predictions and shift in peak are

observed. It is reported that the *k*-ε model underestimates the turbulence quantities (Montante et al., 2001; Deglon and Meyer, 2006). Although *k*-ε model under predicts turbulence kinetic energy, but with the optimal selection of MRF zone, better results can be obtained as shown in Figure 4.23.

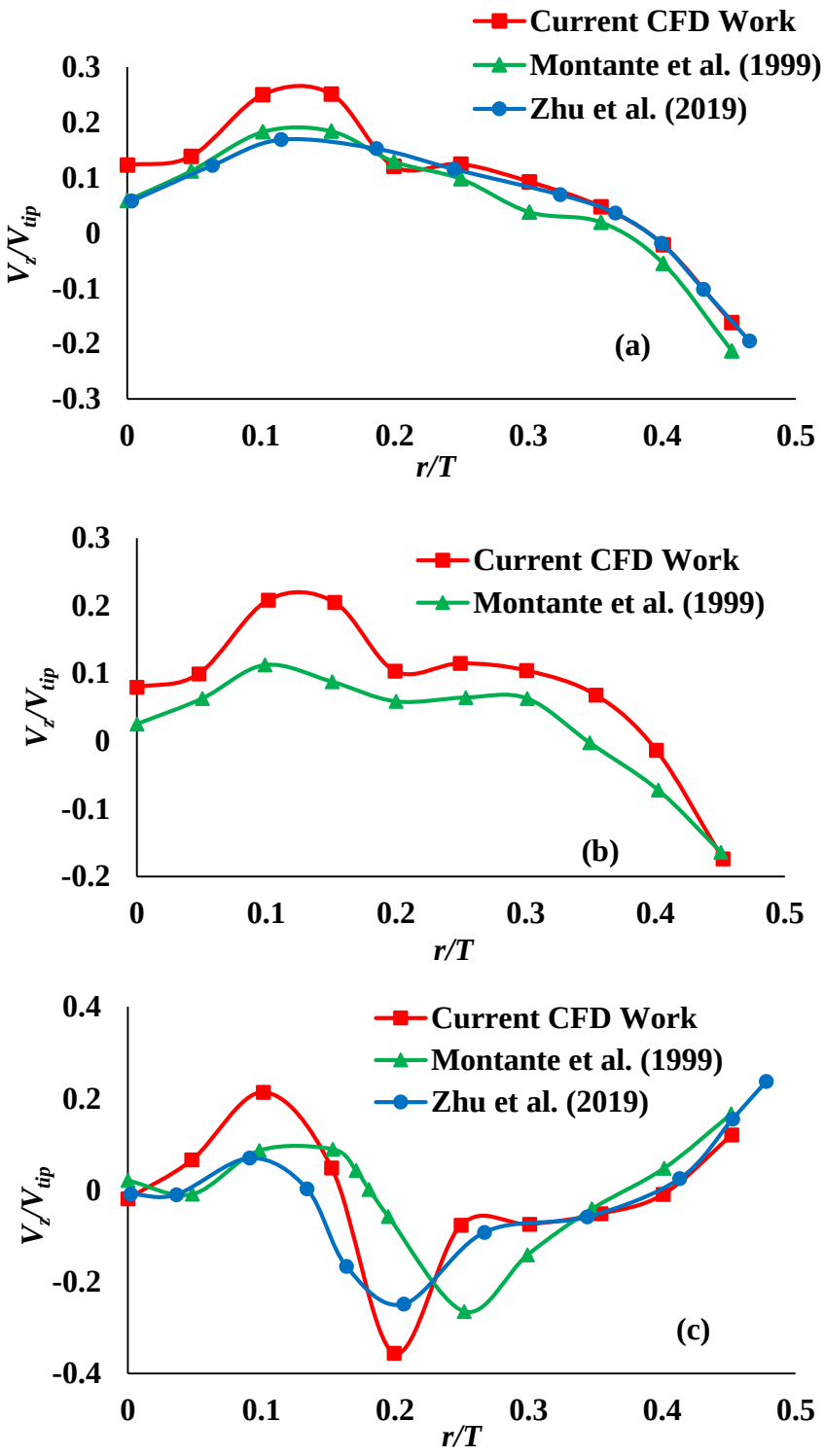

Figure 4.22 Normalized profiles of mean axial velocity at impeller center plane for *C/T* = 0.33 (a), *C/T* = 0.2 (b), *C/T* = 0.15 (c) and at $\theta = 45^{\circ}$

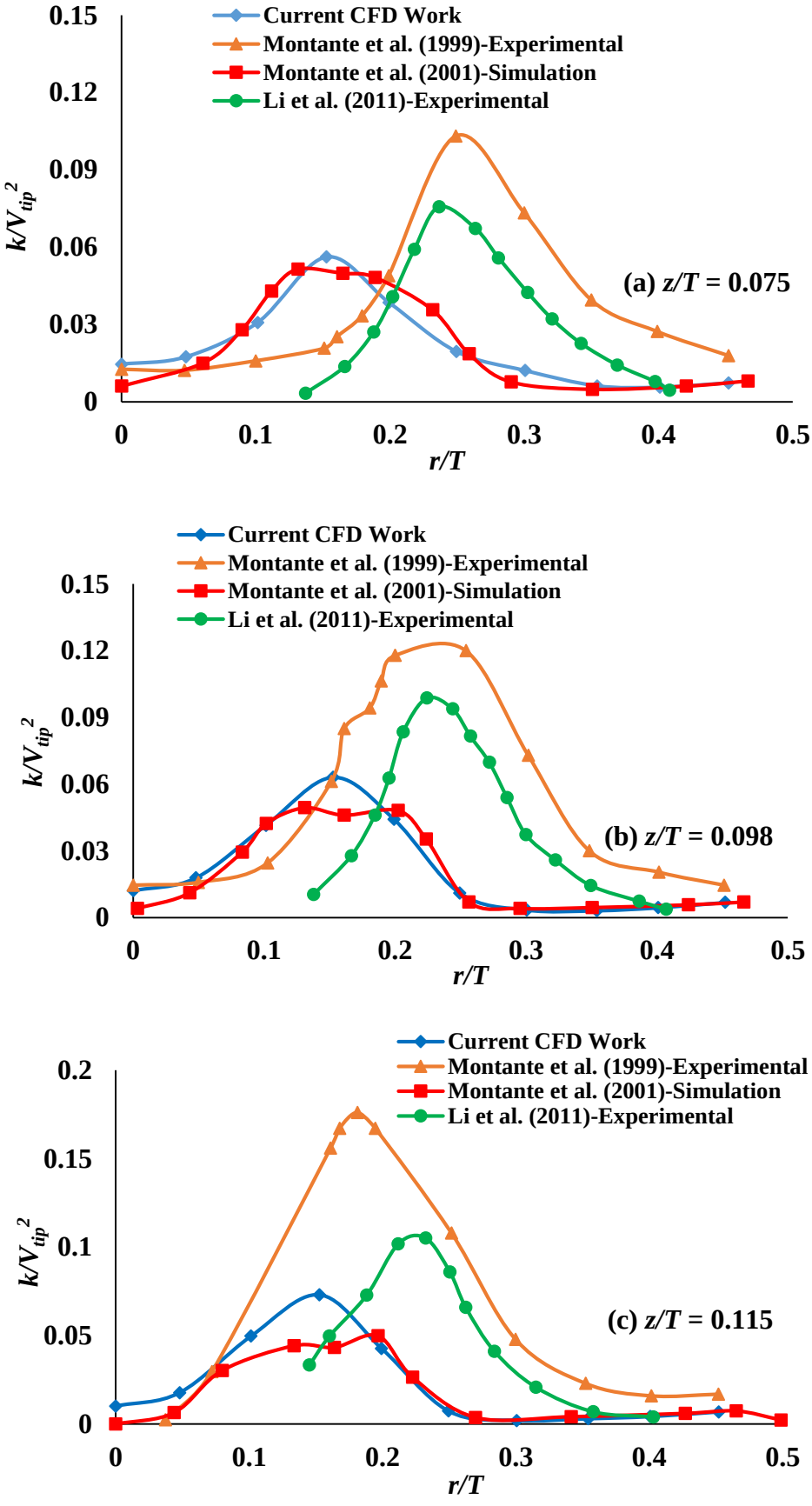

Figure 4.23 Normalized profiles of turbulence kinetic energy at various axial positions for $C/T = 0.15$ and at $\theta = 45^{\circ}$

4.3.2 Effect of Impeller Clearance on Global Flow Fields and Flow Patterns

Figures 4.24 and 4.25 show the effect of impeller clearance on power number (N_p) and radial pumping number (N_r) respectively. CFD predicted values of N_p and N_r at various impeller clearances are given in Table 4.11 and Table 4.12 respectively. The value of N_p at C/T = 0.33 (standard clearance) was found to be 4.82 which is expected for standard configuration and compared with literature data of Bates et al. (1963); Montante et al. (1999) and Coroneo et al. (2011). N_p slightly decreases with lowering the clearance up to C/T = 0.19 and it sharply dropped to 3.36 at C/T = 0.18 and later it was found to be invariant for further lower clearances. Similarly, with increase in impeller clearance, N_p was found to be invariant up to C/T = 0.77 but it suddenly dropped to 3.16 at C/T = 0.78 and was constant for further higher clearances. N_p reduces by 30% and 34% at C/T = 0.18 and 0.78 respectively in comparison with the standard clearance. The significant reduction of N_p from lower impeller clearance is due to the inhibition of power intensive lower re-circulation loops associated with the standard clearance as the impeller stream is attracted towards the tank bottom (Conti et al., 1981).

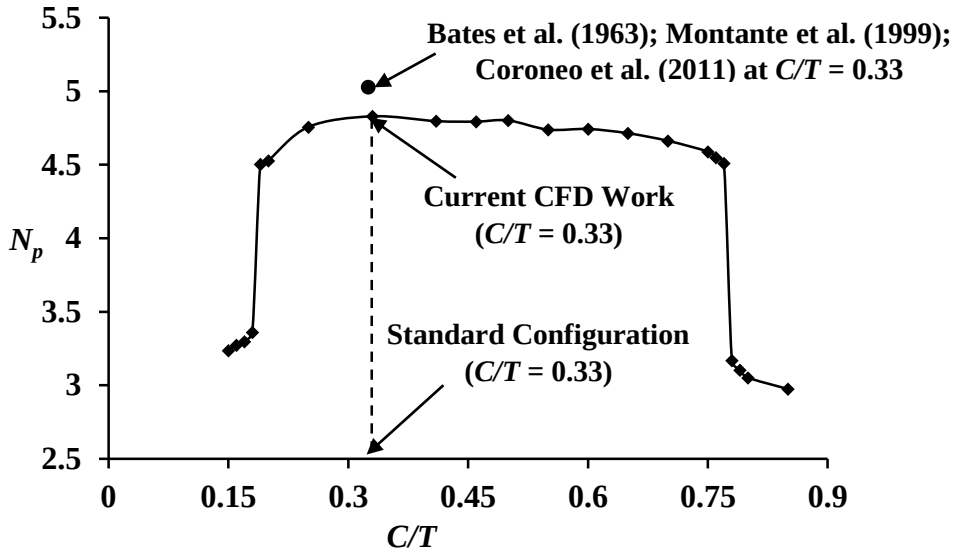

Figure 4.24 Effect of impeller clearance on power number

Table 4.11 CFD predicted power numbers at various clearances

C/T	0.15	0.16	0.17	**0.18**	0.19	0.2	0.25	0.33	0.41	0.46	0.5
N_p	3.23	3.27	3.29	**3.36**	4.50	4.52	4.75	4.82	4.79	4.79	4.80
C/T	0.55	0.6	0.65	0.7	0.75	0.76	0.77	**0.78**	0.79	0.8	0.85
N_p	4.73	4.74	4.71	4.66	4.58	4.54	4.50	**3.16**	3.10	3.05	2.97

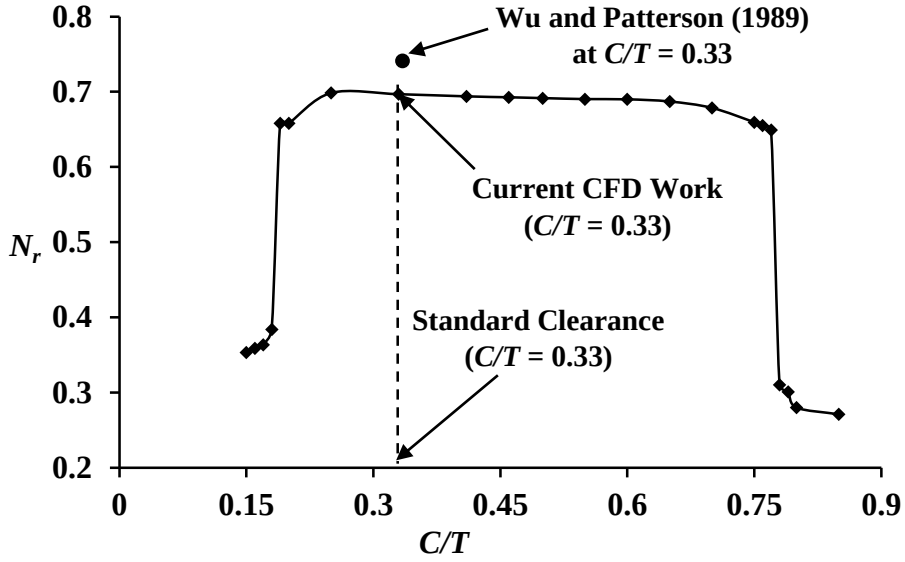

Figure 4.25 Effect of impeller clearance on radial pumping number

Table 4.12 CFD predicted radial pumping numbers at various clearances

C/T	0.15	0.16	0.17	**0.18**	0.19	0.2	0.25	0.33	0.41	0.46	0.5
N_r	0.35	0.35	0.36	**0.38**	0.65	0.65	0.69	0.69	0.69	0.69	0.69
C/T	0.55	0.6	0.65	0.7	0.75	0.76	0.77	**0.78**	0.79	0.8	0.85
N_r	0.69	0.68	0.68	0.67	0.65	0.65	0.64	**0.31**	0.30	0.27	0.27

The respective changes from double to single re-circulation loop as the impeller clearance reduces from standard conditions to low range is shown in Figure 4.26(a-d). In case of high clearances, the impeller discharge stream is inclined towards top surface and strikes on the top water surface and loses majority of the momentum and thereby producing weaker re-circulation loops below the impeller as displayed in Figure 4.26(e-f). Such type of flow pattern is very useful for exchange of gases from gaseous phase to liquid phase as it helps to increase the surface contact area between gas and liquid (Patil et al., 2004; Deshmukh and Joshi, 2006; Rao et al., 2009). Power number is highly dependent on the gas hold-up in the impeller vicinity, at higher clearances the size of this region increases and thus increases the free liquid surface area. Hence it causes the significant reduction in N_p at higher impeller clearances (Deshmukh and Joshi, 2006). Lower clearances develop minor re-circulation loops above the major re-circulation loops which are revolving in the opposite direction to that of major re-circulation loops. Similarly, higher clearances also develop such kind of minor re-circulation loops below the major re-circulation loops as shown in Figure 4.27.

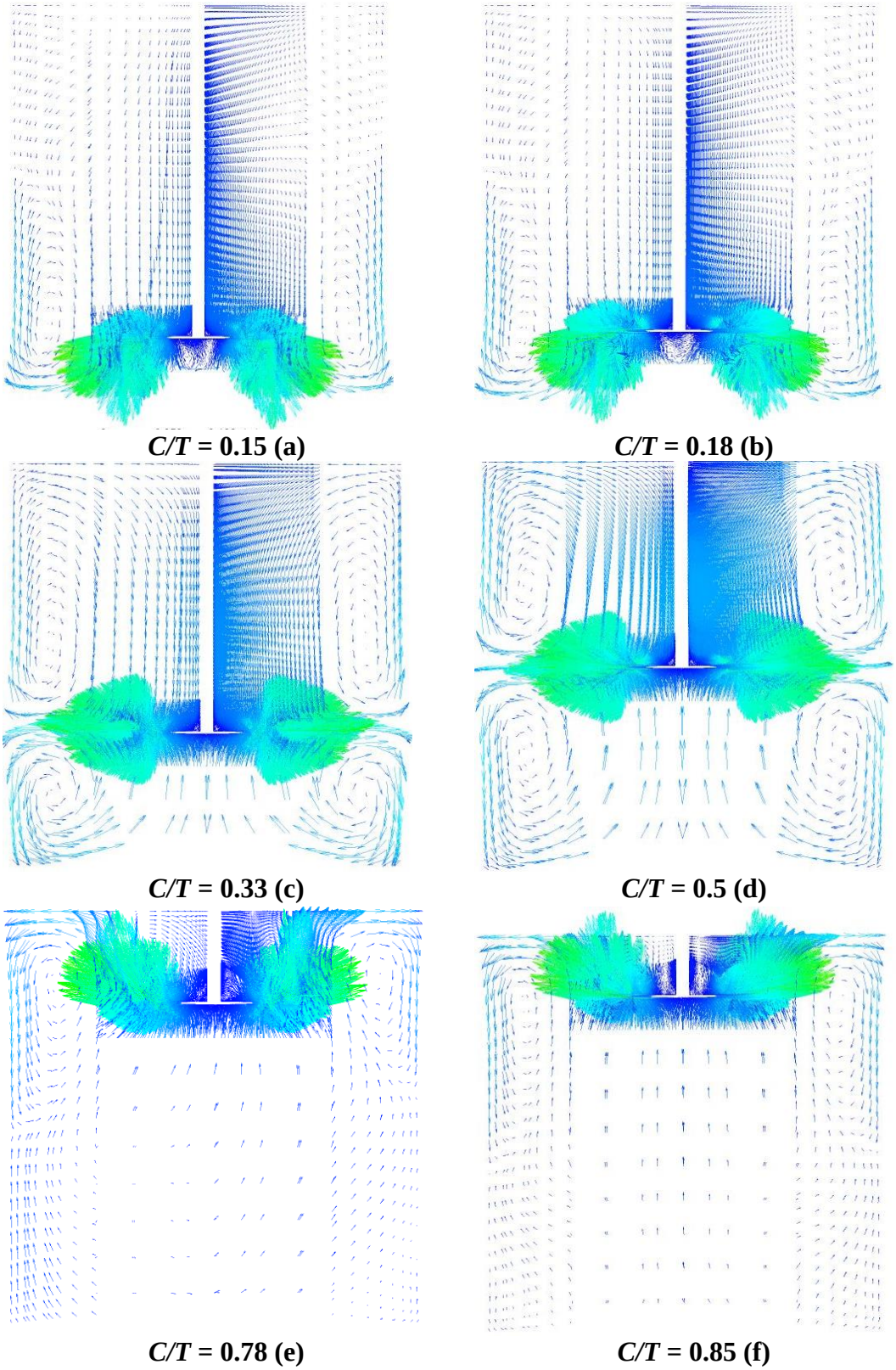

Figure 4.26 Velocity vector plots at various impeller clearances

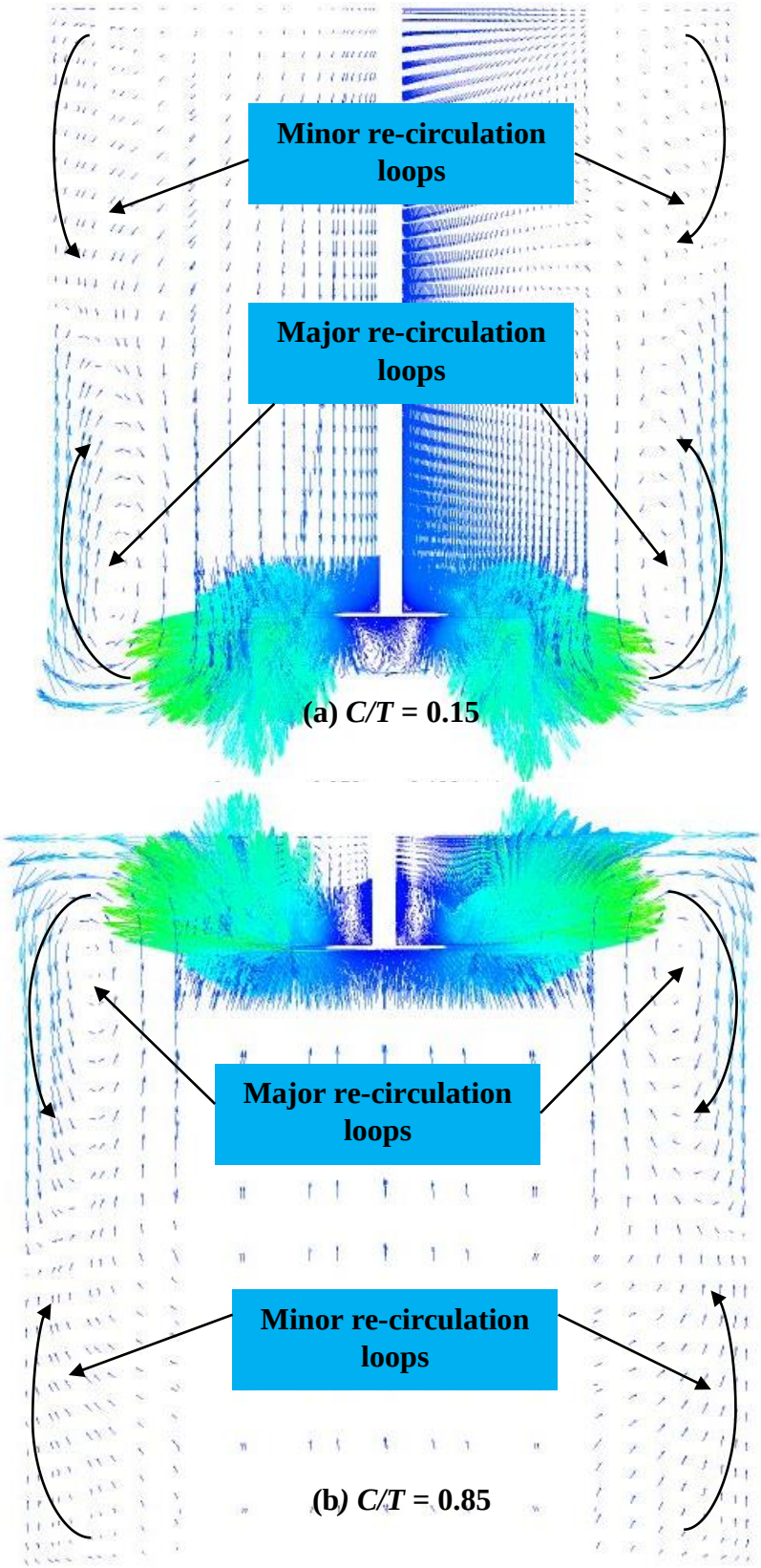

Figure 4.27 Representation of major and minor re-circulation loops at C/T = 0.15(a) and C/T = 0.85(b)

No considerable variation in the value of N_r was found for medium range clearances, but it suddenly reduced to 0.38 at C/T = 0.18 and 0.31 at C/T = 0.78 respectively (Figure 4.25). N_r reduced by 44.87% at C/T = 0.18 and 55.50% at 0.78 in comparison with the standard clearance. Also, N_r was found to be invariant for $C/T \leq 0.18$ (low clearances) and $C/T \geq 0.78$ (high clearances).

Based on the power number values, the impeller clearances can be divided into three regions i.e. high clearance region (C/T = 0.78 to 0.85), middle clearance region (C/T = 0.19 to 0.77) and low clearance region (C/T = 0.18 to 0.15) for further analysis.

4.3.3 Effect of Impeller Clearance on Mean Velocities and Turbulence Parameters

As mentioned above impeller clearances are divided into three different regions based on the power number values. This section deals with the comparison of normalized mean velocities and turbulence parameters for various impeller clearances. For this purpose, two impeller clearances from each region (C/T = 0.15, 0.18, 0.33, 0.5, 0.78 and 0.85) are considered for comparative analysis. Figures 4.28 - 4.31 depict normalized profiles of mean radial velocity, mean axial velocity, turbulence kinetic energy and turbulence dissipation rate respectively at different radial distances from impeller tip.

The middle impeller clearances produce horizontal discharge stream which characterize high magnitudes of mean radial velocity, turbulence kinetic energy and turbulence dissipation rate close to the impeller which reduce as the distance from the impeller increases (Wu and Patterson, 1989). The rate of decay of turbulence dissipation rate from r/T = 0.18 to 0.22 (Figure 4.31(a-b)) is much rapid as compared to turbulence kinetic energy and mean radial velocity. The mean radial velocity profile becomes almost constant after r/T = 0.28 (Figure 4.28d) while the turbulence quantities continuously decrease with the further increase in the radial distance towards the tank wall. The axial velocity profiles are well developed up to r/T = 0.28 (Figure 4.29d) from the impeller and decrease further. The flow fields and turbulence parameters from the middle clearances develop identical patterns with highly comparable peak values and do not show any significant variation. The magnitude of radial velocity, turbulence kinetic energy and turbulence dissipation rate from middle impeller clearances are higher than those from higher and lower impeller clearance indicating better mixing action of the respective configuration.

The higher impeller clearances cause the discharge stream to be deflected towards the water surface and develop re-circulation loops beside the impeller blades. The discharge stream is deflected in such a way that the radial velocity magnitude increases with the radial distance up to r/T = 0.28 (Figure 4.28d) and becomes constant thereafter. But the turbulence quantities especially turbulence dissipation rates were much higher near the impeller and reduce with the radial distance from the impeller blades. Again, the higher impeller clearances maintain the sufficient magnitudes of turbulence kinetic energy which is at par with the standard impeller clearance at r/T >0.25. The secondary impeller stream emanating from the trailing edge of the blades generates large undulations in the radial velocity and turbulence kinetic energy up to r/T = 0.22 (Figure 4.28b and Figure 4.30b) while the undulations in turbulence dissipation rate extend up to r/T = 0.28 (Figure 4.31d). The peak values of radial velocity, turbulence kinetic energy and turbulence dissipation rate at r/T>0.18 occur at the water surface. This leads to high momentum and turbulence action throughout the entire water surface resulting in high interfacial area between water and air. Such phenomenon is extremely suitable for surface aeration process in wastewater treatment plants which leads to superior mixing and transfer of oxygen from atmosphere to the water (Patil et al., 2004; Deshmukh and Joshi, 2006; Rao et al., 2009; Kulkarni and Patwardhan, 2014). The axial velocities near the impeller up to r/T = 0.22 (Figure 4.29b) are highly comparable with that from middle and low impeller clearances and reduce significantly with further increase in the radial distance.

The low impeller clearances maintain almost constant radial velocity magnitudes till the tank walls while turbulence kinetic energy and turbulence dissipation rate continuously decrease with the radial distance. Significant reduction in the turbulence dissipation rate occurs from r/T = 0.18 to 0.22 and continues to decay in a slow rate. The location of peak turbulence kinetic energy lowers axially for r/T > 0.22 and remains unchanged thereafter. The turbulence kinetic energy profiles up to r/T = 0.25(Figure 4.30) develop parabolic profile and maintain constant values near the tank bottom (shown by vertical line below the parabolic curve) while usual parabolic profile is observed for r/T >0.25. The fluctuations in the turbulence dissipation rate profiles (Figure 4.31) increase with the radial distance from the impeller and peak magnitudes were obtained at the tank bottom for r/T>0.25. The lower impeller clearances provide significant magnitude of axial velocity even higher than the other impeller clearances up to r/T = 0.28 and decreases further. Thus, the impellers located near the tank bottom develop strong axial pumping action and maintain sufficient value of radial velocity and turbulence quantities

(even though low magnitudes) till the tank wall which helps in solid-liquid suspension process in the agitated vessels (Armenante and Nagamine, 1998).

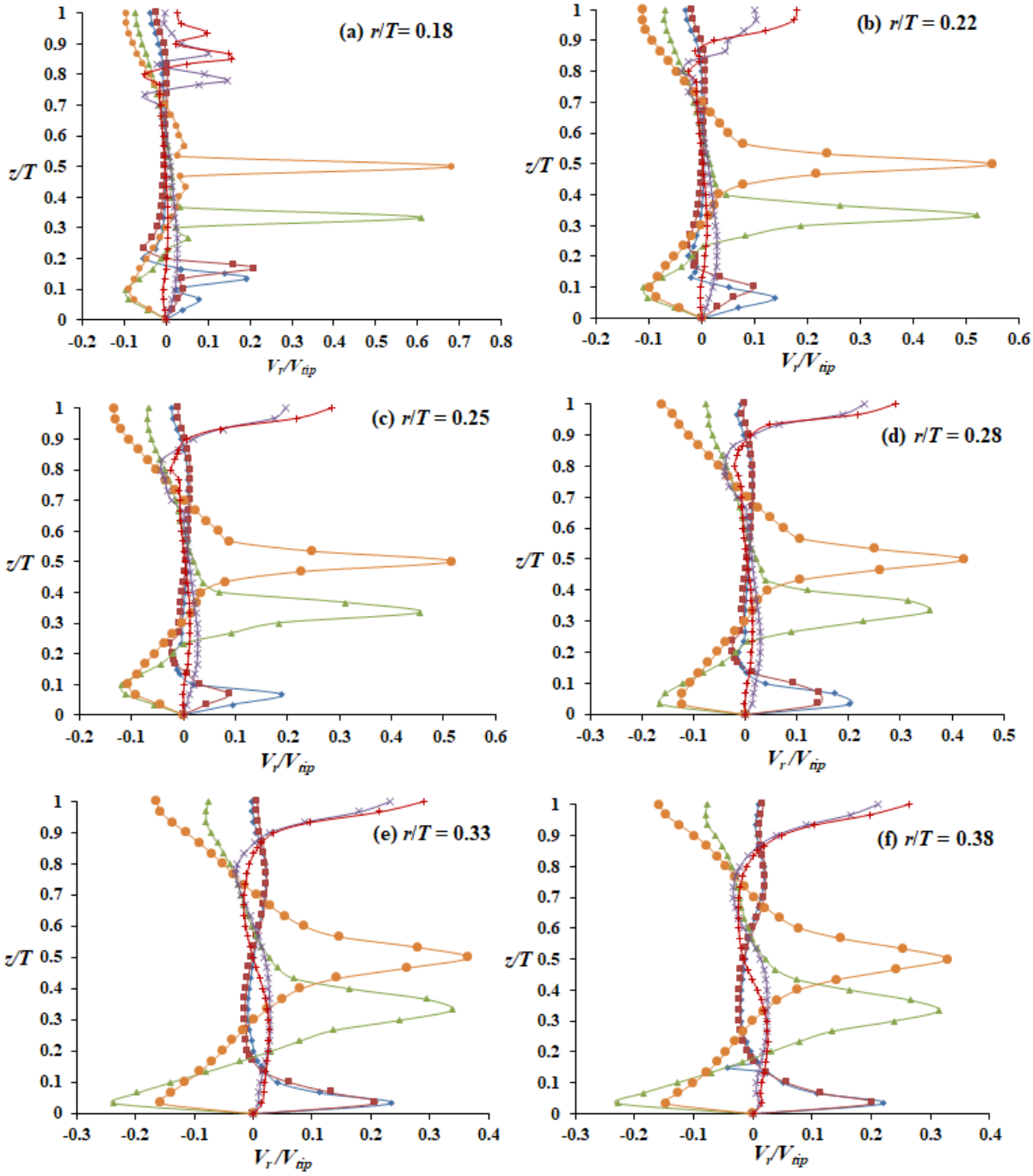

Figure 4.28 Axial profiles of normalized mean radial velocity for various clearances [*C/T* = 0.15( ), *C/T* = 0.18 ( ), *C/T* = 0.33( ), *C/T* = 0.5 ( ), *C/T* = 0.78 ( ), *C/T* = 0.85 ( )]

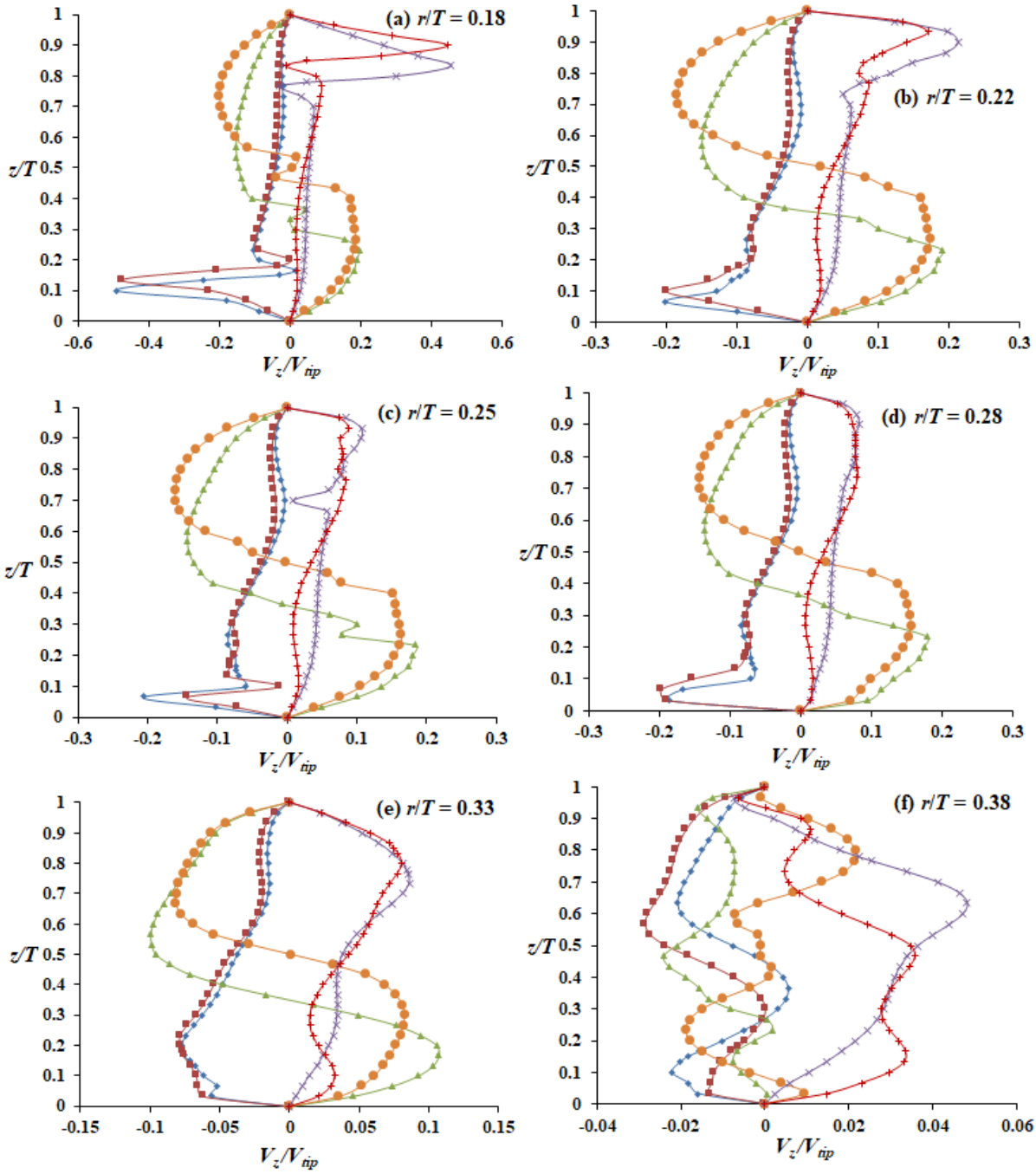

Figure 4.29 Axial profiles of normalized mean axial velocity for various clearances [C/T = 0.15( ), C/T = 0.18 ( ), C/T = 0.33( ), C/T = 0.5 ( ), C/T = 0.78 ( ), C/T = 0.85 ( )]

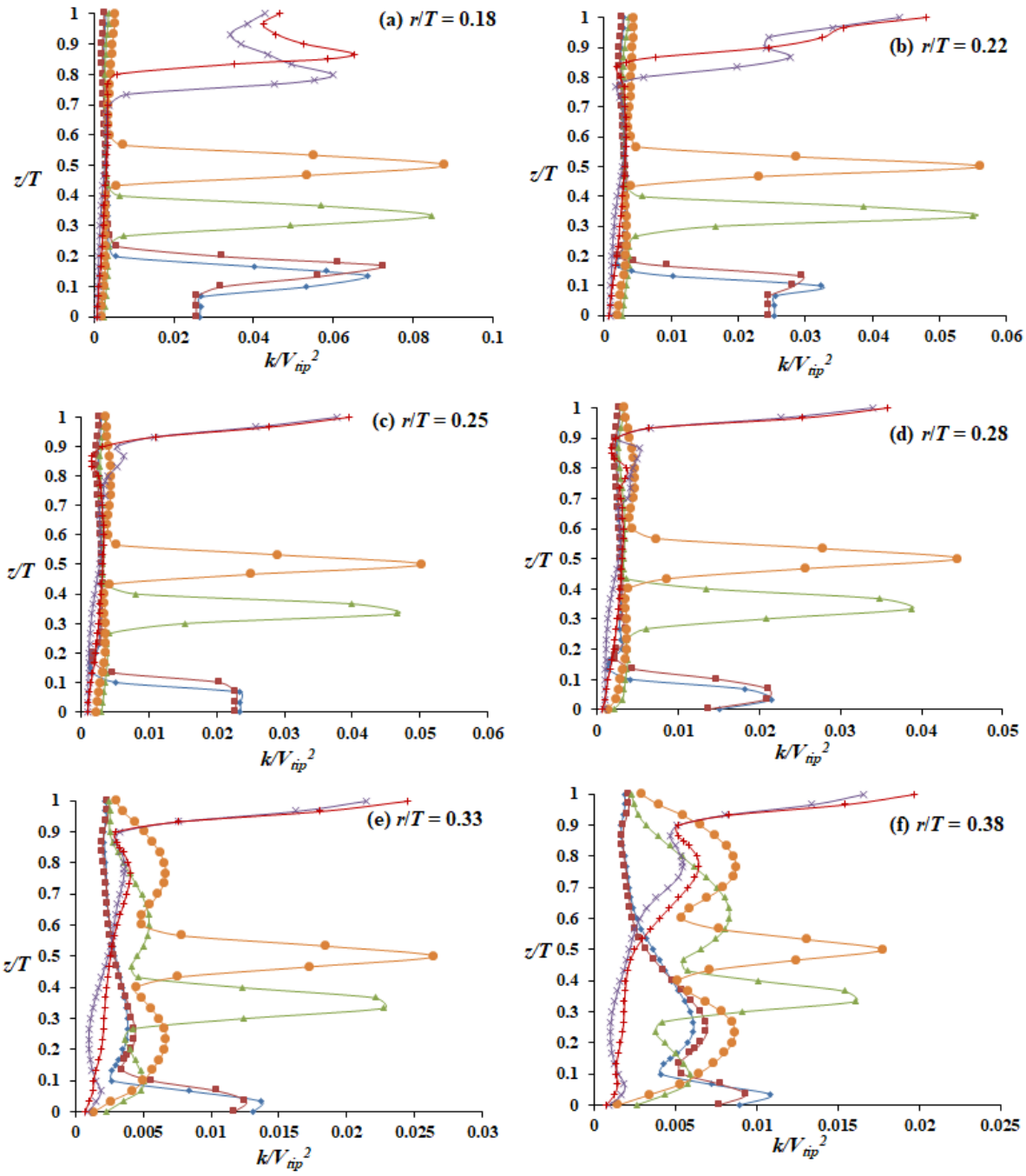

Figure 4.30 Axial profiles of normalized turbulence kinetic energy for various clearances [C/T = 0.15( ), C/T = 0.18 ( ), C/T = 0.33( ), C/T = 0.5 ( ), C/T = 0.78 ( ), C/T = 0.85 ( )]

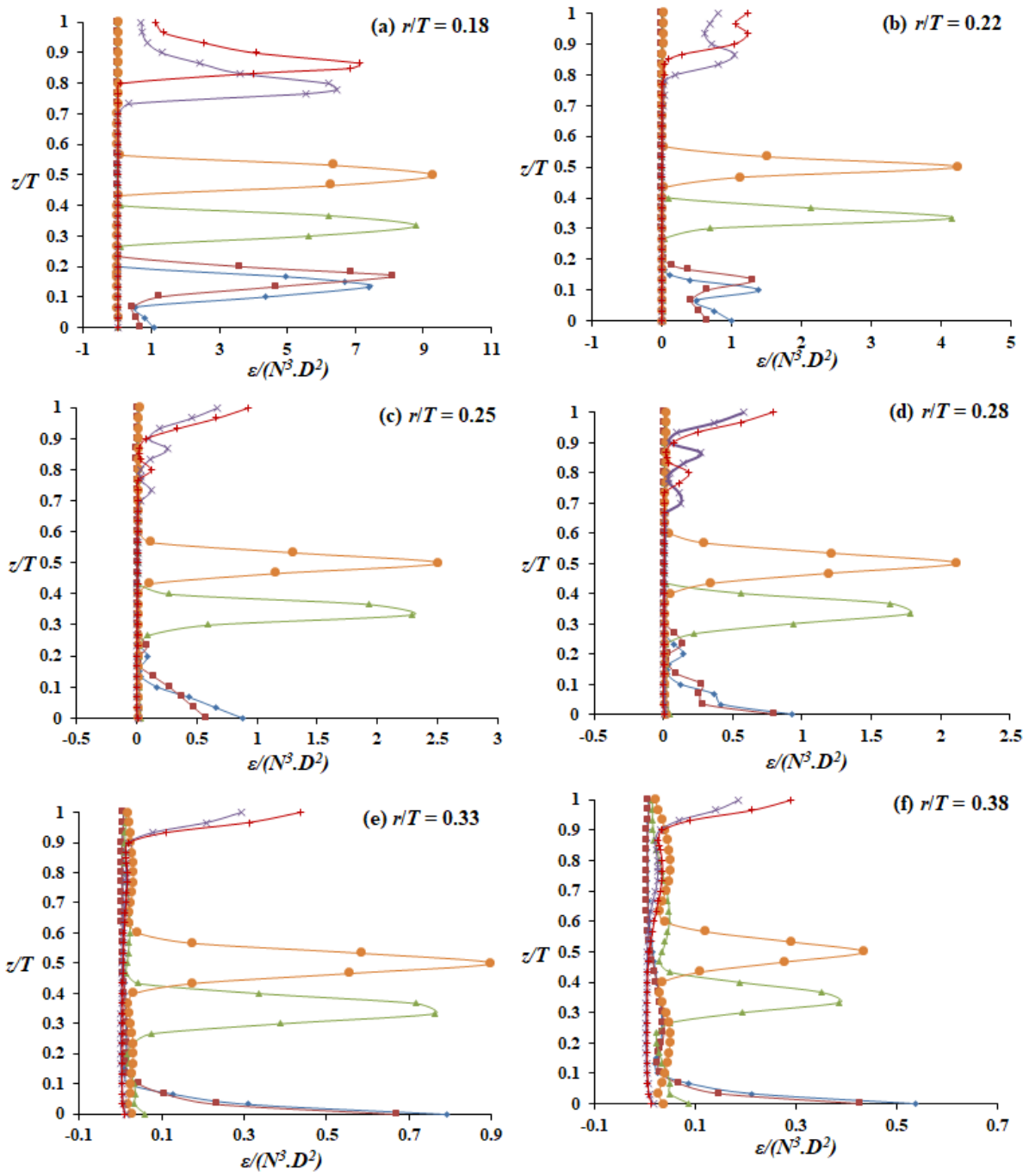

Figure 4.31 Axial profiles of normalized turbulence dissipation rate for various clearances [C/T = 0.15( ), C/T = 0.18 ( ), C/T = 0.33( ), C/T = 0.5 ( ), C/T = 0.78 ( ), C/T = 0.85 ( )]

4.4 Investigation of Effect of Impeller Diameter on Flow Hydrodynamics in Stirred Tank using CFD Model

The impeller diameter is one of the geometrical parameters which affects the flow hydrodynamics. Some of the researches (Patil et al., 2004; Deshmukh and Joshi, 2006; Rao et

al., 2009; Rao et al., 2010) have investigated the effect of impeller diameter on rate of oxygen transfer, mass transfer coefficient and power consumption. But the effect of impeller diameter on flow hydrodynamics (flow fields and turbulence parameters) has not been investigated. In present work, impeller diameter (*D/T*) was varied while keeping other parameters constant. The dimensions of stirred tank and operating conditions were kept same as used for RPT experiments (Figure 3.1). In standard configured stirred tank, impeller diameter is maintained at *D/T* = 0.33 (*D* = 0.1 m, for present geometry). In the present work, CFD simulations have been conducted for impeller diameters ranging from *D/T* = 0.2 to 0.46. Consequently, Impeller blade width (*w*) and blade length (*l*) were maintained at *D*/5 and *D*/4 respectively.

4.4.1 Effect of Impeller Diameter on Power Number and Radial Pumping Number

Power number was calculated using two different methods. In the first method, the power number ($N_{p\tau}$) was calculated by the torque produced on moving parts, viz., impeller blade, disk and shaft (Equation 4.3). In second method, it was calculated by integrating the turbulence dissipation rate through the entire fluid domain (Equation 4.4) and represented by $N_{p\varepsilon}$.

$$N_{p\tau} = \frac{2\pi N \tau}{\rho N^3 D^5} \tag{4.3}$$

$$N_{P\varepsilon} = \int \frac{\varepsilon \, dV}{N^3 D^5} \tag{4.4}$$

where, *N* represents the impeller rotational speed, τ is torque on moving parts, ρ is fluid density, *D* is the impeller diameter, ε is the turbulence dissipation rate and *V* is volume of fluid domain.

Power number increases with increase in the impeller diameter (Figure 4.32), but, the change in the magnitude of power number is small. In comparison between $N_{p\varepsilon}$ and $N_{p\tau}$, $N_{p\varepsilon}$ is observed to be under-predicted compared to $N_{p\tau}$. The reason for under-prediction of $N_{p\varepsilon}$ is *k*-ε turbulence model which predicts the lower values of turbulence dissipation rate (ε) (Deglon and Meyer, 2006; Basavarajappa et al., 2015). The overall deviation between $N_{p\tau}$ and $N_{p\varepsilon}$ is found to be 15%. Figure 4.33 shows the variation of radial pumping number (N_r) with impeller diameter. It can be observed that N_r increases with increase in the impeller diameter.

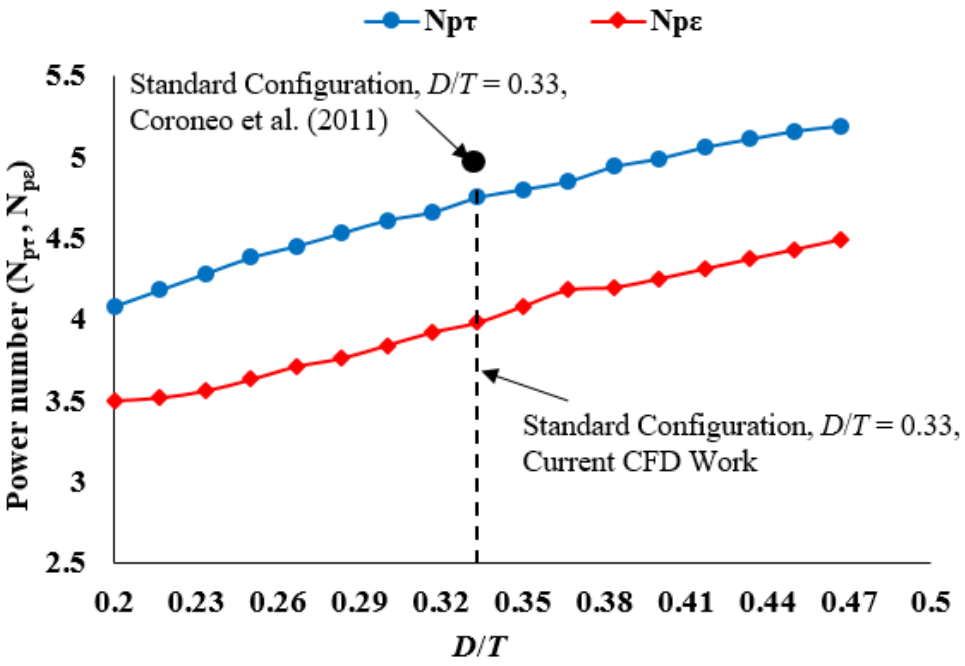

Figure 4.32 Effect of impeller diameter on power number

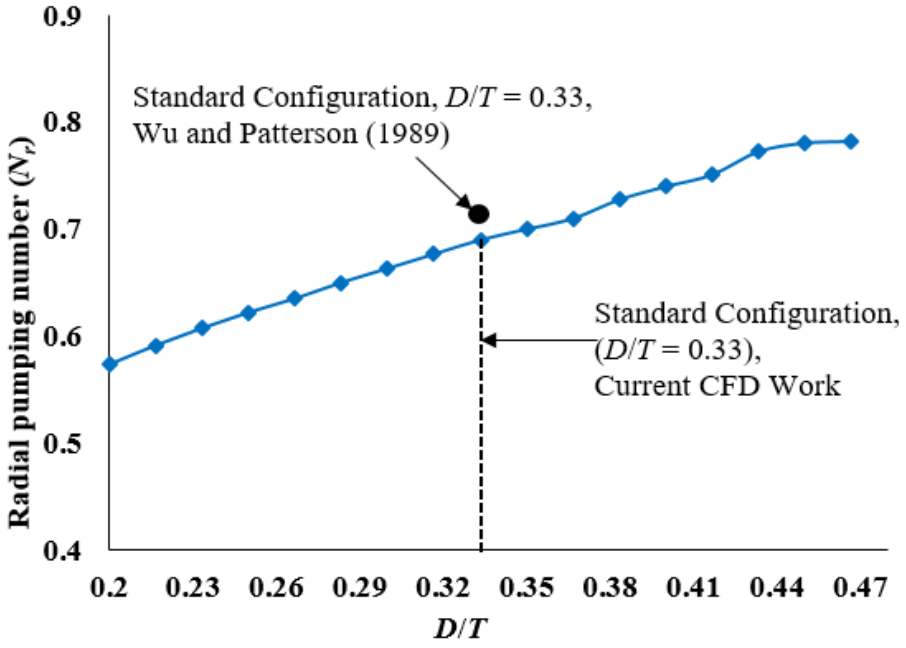

Figure 4.33 Effect of impeller diameter on radial pumping number

4.4.2 Distribution of the Mean Velocities and Turbulence Quantities in *r-θ* Plane

Figure 4.34 depicts the distribution of mean velocity in *r-θ* plane located in the mid plane of impeller. The intensity of mean velocity increases with increase in the impeller diameter. The highest peak of velocity is observed at $D/T = 0.46$. The intensity of mean velocity is more near to impeller tip and decrease gradually outside the region swept by the impeller. The baffles on

tank wall reduce the tangential velocity components and avoid the formation of the vortex around the shaft (Ammar et al., 2011).

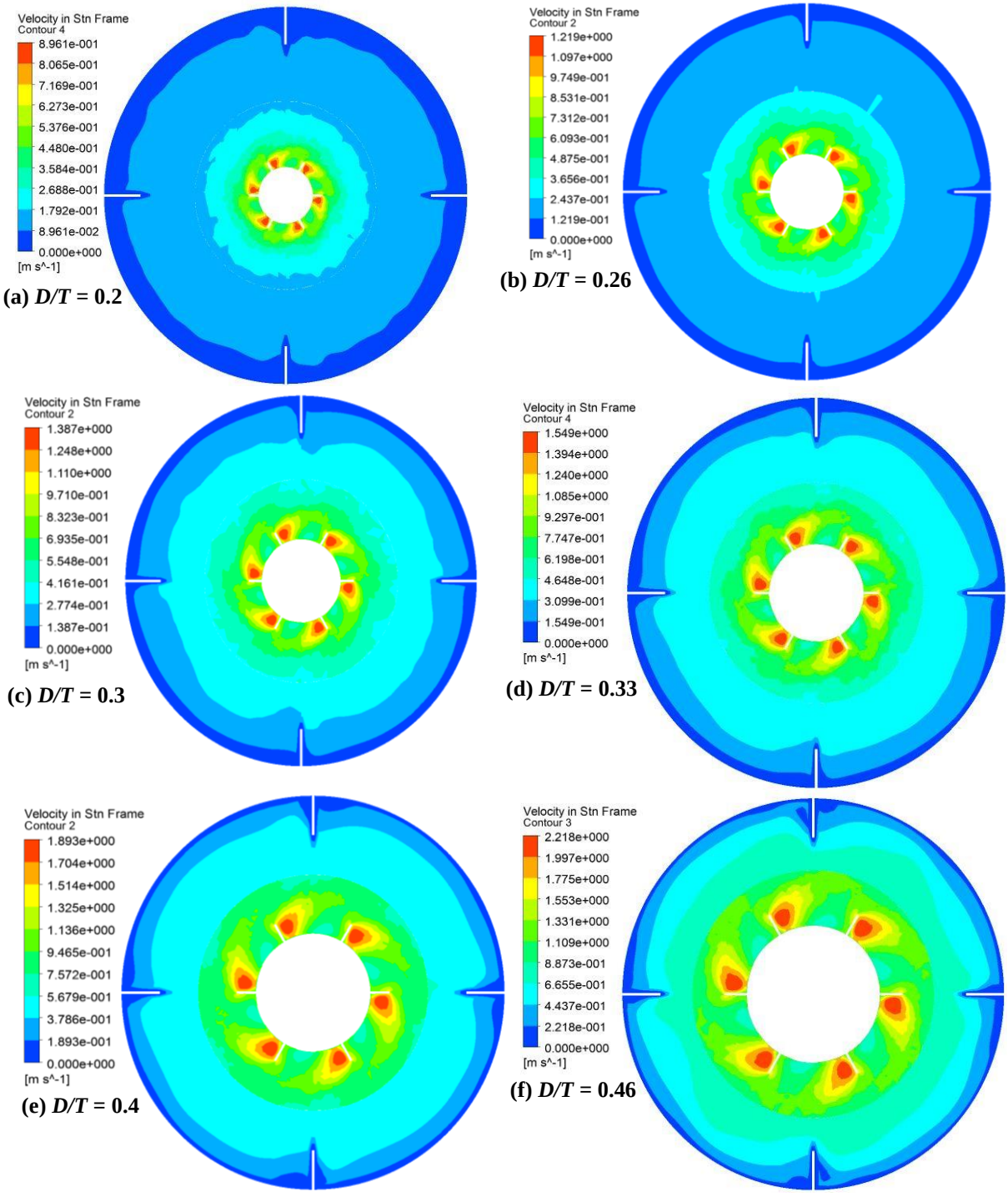

Figure 4.34 Distribution of mean velocity in *r*-θ impeller center plane for various impeller diameters

Figure 4.35 depicts the distribution of turbulence kinetic energy in *r*-θ plane located in the mid plane of impeller. It can be noted that the level of turbulence increases with increase in the

impeller diameter. The turbulence kinetic energy is highly concentrated in the region swept by the impeller and decrease gradually beyond this region. The maximum peak of turbulence kinetic energy is observed at D/T = 0.46. The low values of turbulence kinetic energy near the baffles shows that the baffles act as turbulence dissipaters (Ammar et al., 2011).

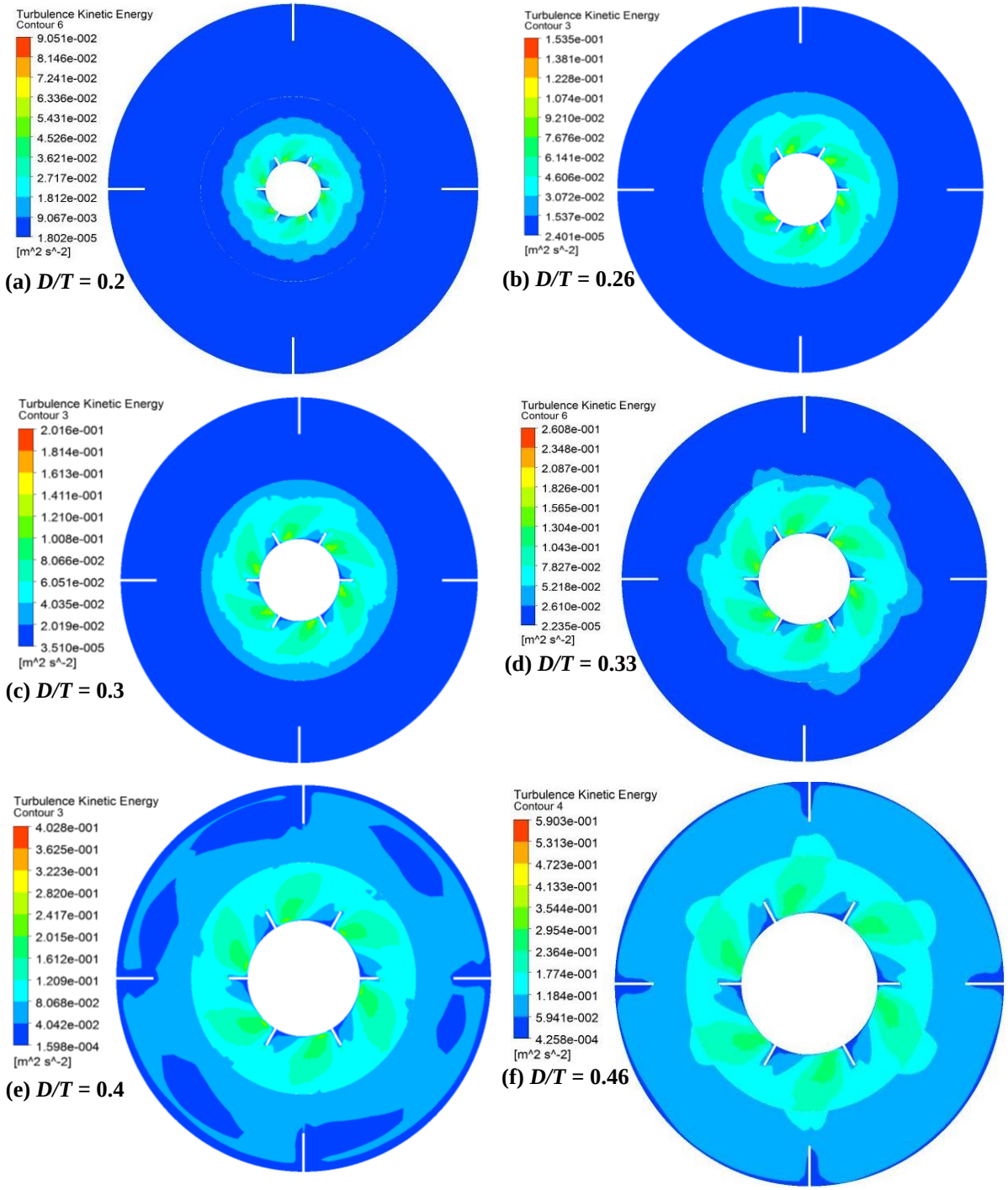

Figure 4.35 Distribution of turbulence kinetic energy in r-θ impeller center plane for various impeller diameters

4.4.3 Analysis of Flow Hydrodynamics between the Two Impeller Blades at Different Angles

This section deals with the comparison of normalized profiles of mean velocities and turbulence quantities behind the blades at different angles for different impeller diameters. The schematic representation of measurements between two blades at different angles is shown in Figure 4.36.

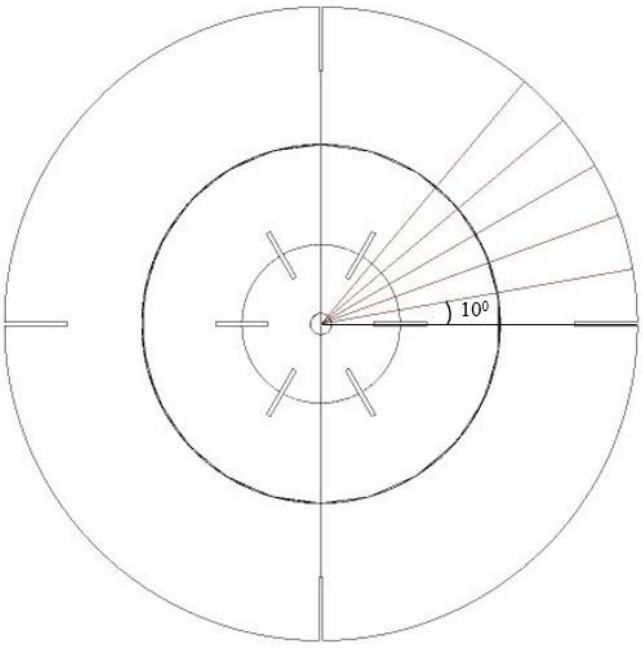

Figure 4.36 Schematic representation of measurements between two blades at different angles

Figures 4.37 and 4.38 depict the comparison of normalized profiles of mean radial and tangential velocities respectively along with the radial direction located in the impeller center plane at different angles between two blades. The intensity of radial velocity decrease gradually along the radial direction from impeller to tank wall. The peak values of radial velocity decrease from 10° to 30° and again increase from 40° to 50°, because of low velocity regions are formed between two blades (Figure 4.34). The peak values of radial velocity increase with increase in the impeller diameter, and the difference in the peak velocity values for different impeller diameters increase from 10° to 50°. The maximum peak of radial velocity is observed at 50°. The intensity of tangential velocity decrease gradually along the radial direction from impeller to tank wall. The peak values of tangential velocity increase from 10° to 50°. The peak of tangential velocity is observed high at D/T = 0.2 in comparison with other impeller diameters.

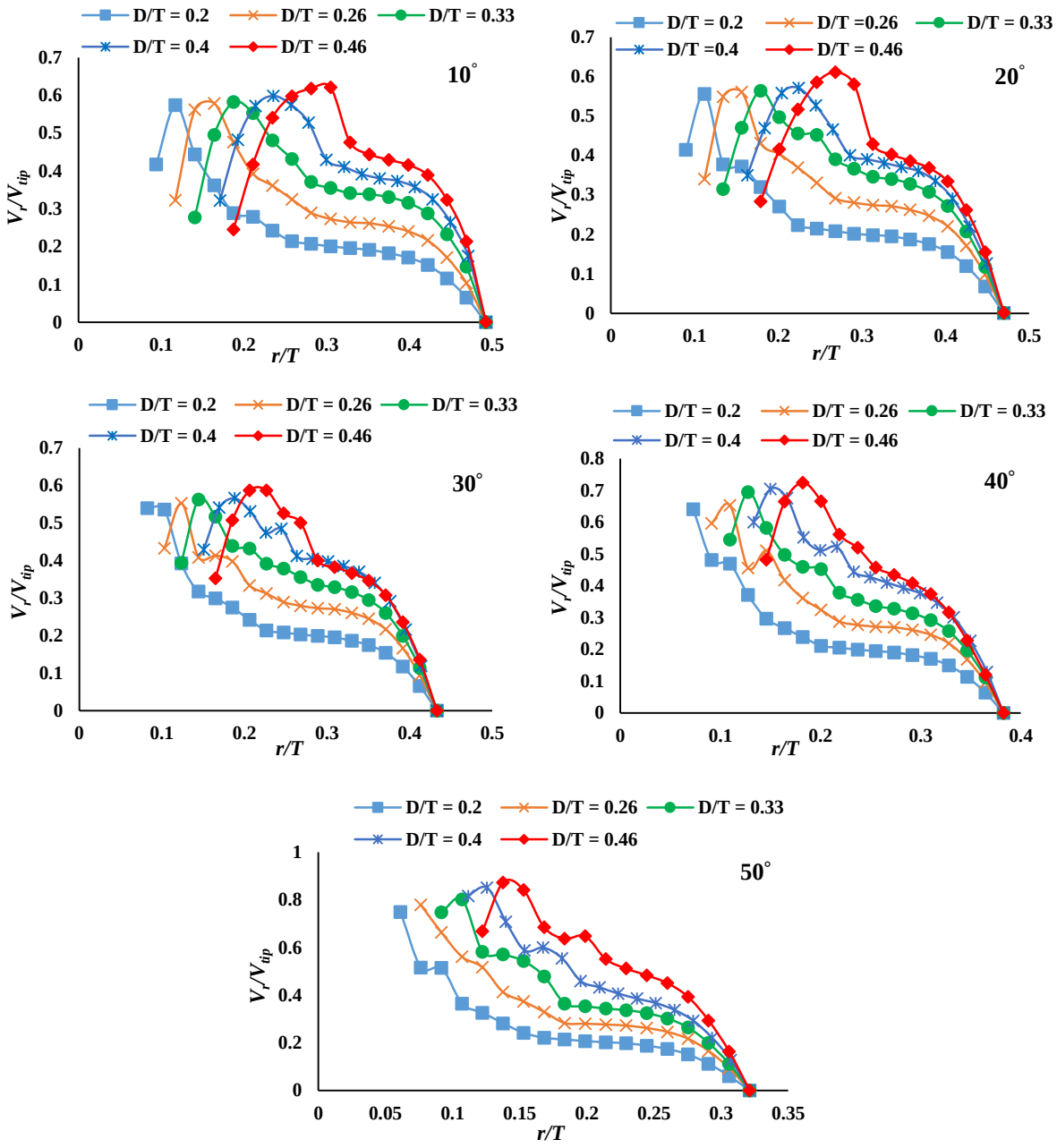

Figure 4.37 Comparison of normalized profiles of mean radial velocity along the radial direction located in the impeller center plane at different angles between two blades

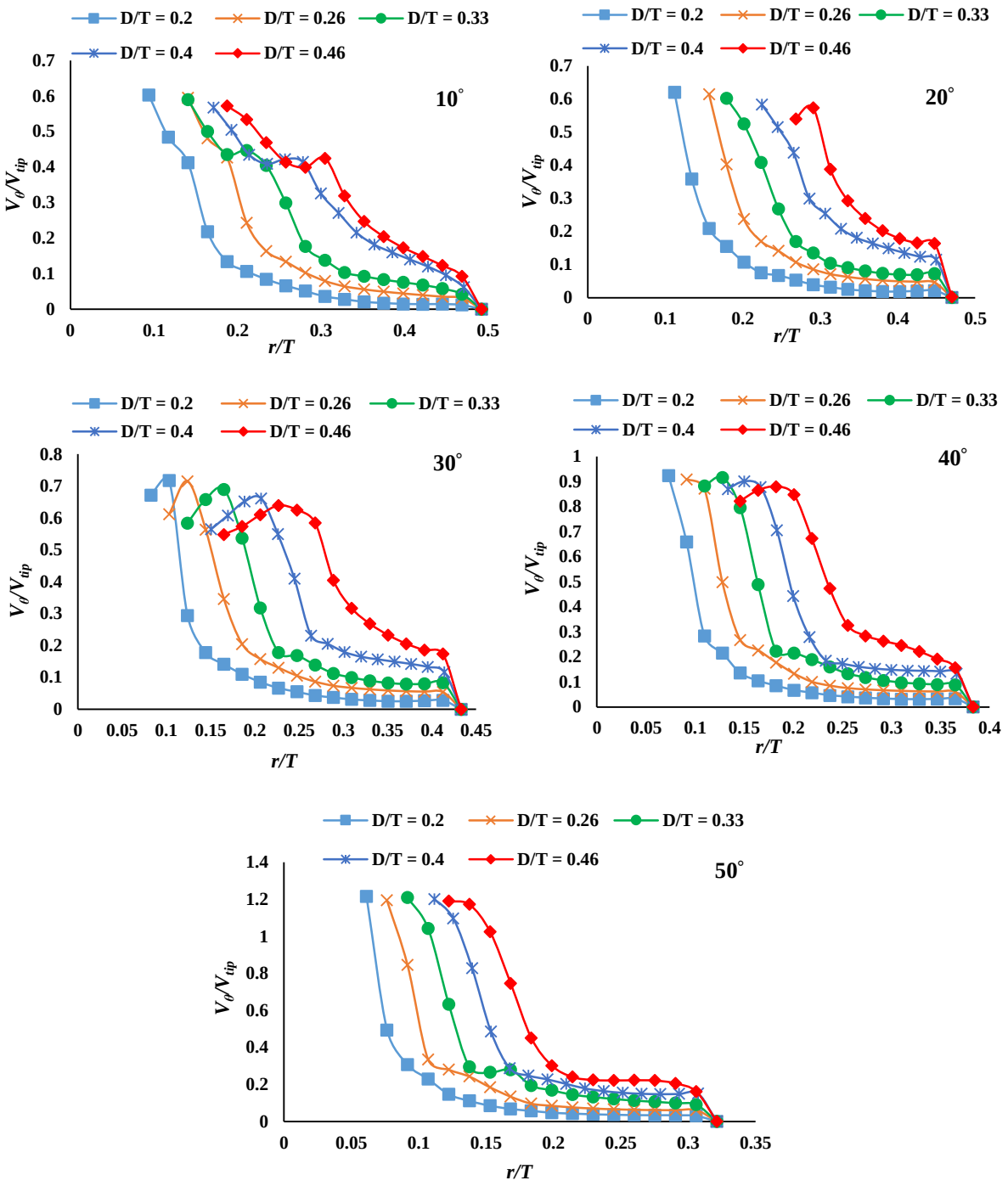

Figure 4.38 Comparison of normalized profiles of mean tangential velocity along the radial direction located in the impeller center plane at different angles between two blades

Figures 4.39 and 4.40 show the comparison of normalized profiles of turbulence kinetic energy and its dissipation rate respectively along the radial direction at different angles between two blades. The intensity of turbulence kinetic energy and its dissipation rate decrease along the radial direction from impeller. The intensity of turbulence kinetic energy increase with increase in the impeller diameter and its maximum peak is observed at *D/T* = 0.46. The peak value of

turbulence kinetic energy increased from 10° to 40° and it slightly decreased at 50°. The peak values of turbulence dissipation rate are almost constant from 10° to 30°, but significant difference in the peak values are observed for 40° and 50°. The maximum peak of turbulence dissipation rate is observed at impeller diameter of D/T = 0.46.

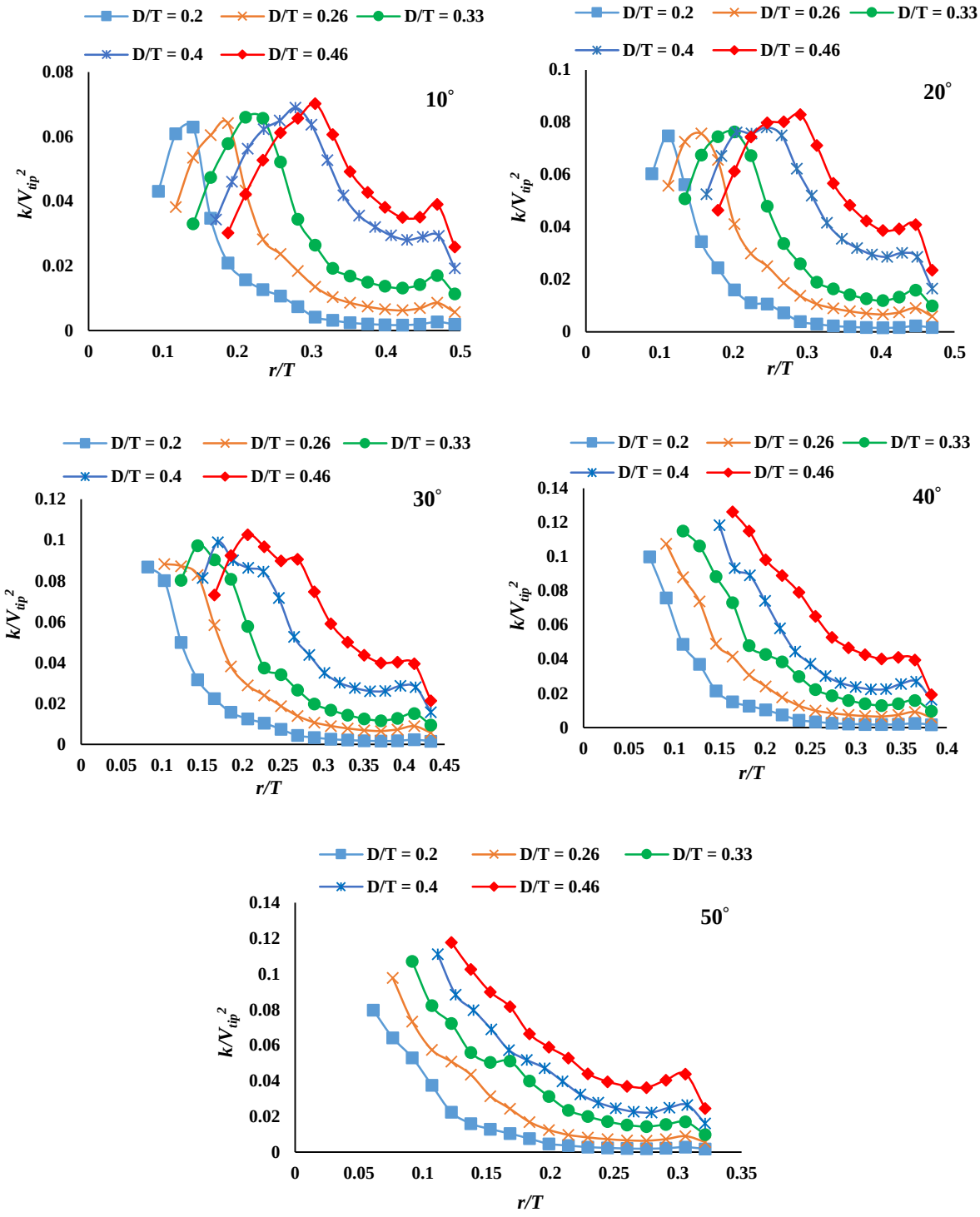

Figure 4.39 Comparison of normalized profiles of turbulence kinetic energy along the radial direction located in the impeller center plane at different angles between two blades

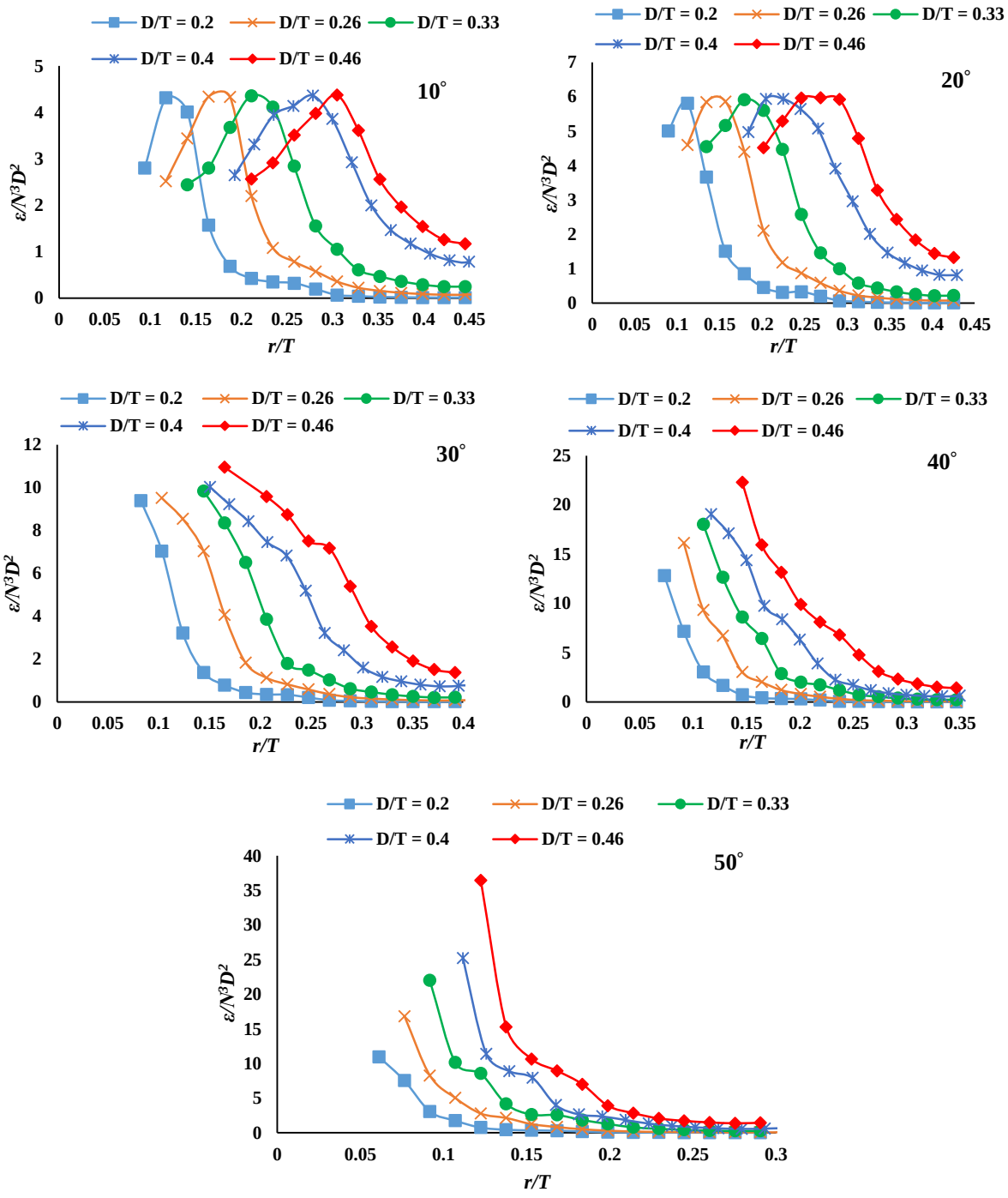

Figure 4.40 Comparison of normalized profiles of turbulence dissipation rate along the radial direction located in the impeller center plane at different angles between two blades

Chapter 5

Conclusions and Future Work

5.1 Conclusions

Experimental and numerical studies have been carried out to investigate flow hydrodynamics in a Rushton turbine stirred tank using RPT technique and steady state CFD model. The following are the conclusions drawn from the study:

Calibration Studies and Comparison of RPT with Literature Data:

- In calibration measurement of RPT technique, radiation intensity measured at a given location does not change with the velocity of water flowing around the measuring point.
- The maximum percentage error in the mean counts obtained from static fluid and moving condition of fluid was observed to be 1.79.
- Axial profiles of mean velocities such as radial, tangential and axial velocities obtained from RPT measurements were found to be in good agreement with literature data.
- Thus with the RPT technique, it is possible to get accurate estimate of velocity fields within the rotor zone which is not possible with other velocity anemometric techniques such as LDA and PIV.

Determination of Optimal Dimensions of Inner-Rotating Fluid Zone for CFD Model, and Validation of CFD Model with RPT and Literature Data:

- The zone with radial extension of twice of impeller diameter (D) and axial extension of 1.5 times of blade width (w) above and below the impeller disk was found to be optimal inner-rotating fluid zone.
- A good agreement between CFD simulations results, RPT results and literature data for mean velocities was observed. But CFD model provided under/over predictions of mean velocities at peak points.
- CFD model accurately predicted the double re-circulation loops flow pattern related to the standard configured stirred tank. The location of eye of upper and lower re-circulation loops were found in a good agreement with literature data.
- CFD model qualitatively predicted the power number and radial pumping number with the overall percentage deviation of 12% and 15% respectively.

- CFD model accurately predicted the turbulence parameters above and below impeller center plane, and the location of peak points. However, under/over predictions were observed at peak points.

Investigation of Effect of Impeller Clearance on Flow Hydrodynamics in Stirred Tank using CFD Model:

- The flow hydrodynamics developed in the stirred tank reactors is well controlled by the location of the impeller.
- The power number and radial pumping number dropped below 30% and 40% when compared to the standard clearance for the impeller clearance range of $C/T \geq 0.78$ and $C/T \leq 0.18$ respectively. The double re-circulation loop flow pattern transformed into a single re-circulation loop, beyond the mentioned clearance range.
- The higher impeller clearance produced high level of momentum transfer as well as turbulence action near the water surface which can enhance the rate of oxygen transfer to the water and it is well suited for the surface aeration process in wastewater treatment plants.
- At the middle impeller clearance, high level of momentum transfer and turbulence action is observed throughout the tank compared to other clearances. Such clearance is much suitable for the applications involving bulk mixing as they produce strong re-circulation loops above and below the impeller, and therefore such clearance can be used for gas-dispersion process.
- The lower impeller clearance provides higher magnitude of axial velocity which is ideal for suspension of solids operation at low power consumption.

Investigation of Effect of Impeller Diameter on Flow Hydrodynamics in Stirred Tank using CFD Model:

- The power number and radial pumping number increased with D/T, however, the change in magnitudes were small.
- The power number predicted by energy dissipation rate ($N_{p\varepsilon}$) found to be lower than the power number predicted by torque ($N_{p\tau}$). The overall deviation between $N_{p\tau}$ and $N_{p\varepsilon}$ is found to be 15%.
- The distribution and intensity of velocity field and turbulence kinetic energy increased with D/T.

- The peak of radial velocities and turbulence quantities observed at $D/T = 0.46$, but, the peak of tangential velocity observed at $D/T = 0.2$.
- The peak of mean velocities and turbulence parameters observed at an angle of 50° behind the blades.

5.2 Future Work

- Simulations may be conducted with the use of unsteady state Large Eddy Simulations (LES) to improve the prediction of turbulence parameters.
- Effect of number and shapes of impellers, degree of baffling may be investigated.

References

Aberoumand, S., Jafarimoghaddam, A., 2016. Mixed convection heat transfer of nanofluids inside curved tubes: An experimental study. Applied Thermal Engineering, 108, 967–979.

Al-Juwaya, T., Ali, N., Al-Dahhan, M., 2019. Investigation of hydrodynamics of binary solids mixture spouted beds using radioactive particle tracking (RPT) technique. Chemical Engineering Research and Design, 148, 21-44.

Alopaeus, V., Moilanen, P., Laakkonen, M., 2009. Analysis of stirred tanks with two-zone models AIChE Journal, 55, 2545-2552.

Ammar, M., Driss, Z., Chtourou, W., Abid, M. S., 2011. Numerical investigation of turbulence flow generated in baffled stirred vessels equipped with three different turbines in one and two-stage system. Energy, 36(8), 5081-5091.

Aubin, J., Mavros, P., Fletcher, D. F., Bertrand, J., Xuereb, C., 2001. Effect of axial agitator configuration (up-pumping, down-pumping, reverse rotation) on flow patterns generated in stirred vessels. Chemical Engineering Research and Design, 79 (8), 845–856.

ANSYS Inc., 2013. ANSYS Fluent 15 Theory Guide, Canonsburg, Pennsylvania.

Armenante, P. M., Nagamine, E. U., 1998. Effect of low off bottom impeller clearance on minimum agitation speed for complete suspension of solids in stirred tanks. Chemical Engineering Science, 53(9), 1757-1775.

Azizi, S., Yadav, A., Lau, Y. M., Hampel, U., Roy, S., Schubert, M., 2017. On the experimental investigation of gas-liquid flow in bubble columns using ultrafast X-ray tomography and radioactive particle tracking. Chemical Engineering Science, 170, 320-331.

Bakker, A., Laroche, R. D., Wang, M. H., Calabrese, R.V., 1997. Sliding mesh simulation of laminar flow in stirred reactors. Transactions of Institution of Chemical Engineers, 75, 42-44.

Barnston, A. G., 1992. Correspondence among the correlation, RMSE, and Heidke forecast verification measures; refinement of Heidke score. Weather Forecasting, 7(4), 699-709.

Bartels, C., Breuer, M., Durst, F., 2000. Proceedings of 10th European conference on mixing, Delft.

Basavarajappa, M., Draper, T., Toth, P., Ring, T. A., Miskovic, S., 2015. Numerical and experimental investigation of single phase flow characteristics in stirred tanks using Rushton turbine and floatation impeller. Minerals Engineering, 83, 156-167.

Bashiri, H., Alizadeh, E., Bertrand, F., Chauki, J., 2016. Investigation of turbulence fluid flow in stirred tanks using a non-intrusive particle tracking technique. Chemical Engineering Science, 140, 233-251.

Bates, R. L., Fondy, P. L., Corpstein, R. R., 1963. Examination of some geometric parameters of impeller power. Industrial and Engineering Chemistry Process Design and Development, 2(4), 310-314.

Beam, G. B., Wielopolski, L., Gardner, R., Verghese, P., 1978. Monte Carlo calculation of efficiencies of right-circular cylindrical NaI detectors for arbitrarily located point sources. Nuclear Instruments and Methods, 154, 501-508.

Bhusarapu, S., 2005. Solid flow mapping in gas-solid risers. D.Sc. Thesis, Washington University, USA.

Boyer, C., Duquenne A. M., Wild, G., 2002. Measuring techniques in gas–liquid and gas–liquid–solid reactors. Chemical Engineering Science, 57, 3185-3215.

Brucato, A., Ciofalo, M., Grisafi, F., Micale, G., 1998. Numerical prediction of flow fields in baffled stirred vessels: a comparison of alternative modelling approaches. Chemical Engineering Science, 53(21), 3653-3684.

Buwa, V., Dewan, A., Nassar, A. F., Durst, F., 2006. Fluid dynamics and mixing of single-phase flow in a stirred vessel with a grid disc impeller: experimental and numerical investigations. Chemical Engineering Science, 61, 2815-2822.

Cartellier, A., 1990. Optical probe for local void fraction measurements: characterization of performance. Review of Scientific Instruments, 61(2), 874-886.

Cartellier, A., 1992. Simultaneous void fraction measurement, bubble velocity, and size estimate using a single optical probe in gas-liquid two-phase flows. Review of Scientific Instruments, 63, 5442-5453.

Chaouki, J., Larachi, F., Dudukovic, M. P., 1997. Non-invasive tomographic and velocimetric monitoring of multiphase flows. Industrial and Engineering Chemistry Research, 36(11), 4476-4503.

Chara, Z., Kysela, B., Konfrst, J., Fort, I., 2016. Study of fluid flow in baffled vessels stirred by a Rushton standard impeller, Applied Mathematics and Computation, 272, 614-628.

Ciofalo, M., Brucato A., Grisafi, F., Torraca, N., 1996. Turbulence flow in closed and free surface unbaffled tanks stirred by radial impellers. Chemical Engineering Science, 51(14), 3557-3573.

Conti, R., Sicardi, S., Specchia, V., 1981. Effect of the stirrer clearance on particle suspension in agitated vessels. Chemical Engineering Journal, 22(3), 247-249.

Coroneo, M., Montante, G., Paglianti, A., Magelli, F., 2011. CFD prediction of fluid flow and mixing in stirred tanks: numerical issues about the RANS simulations. Computers and Chemical Engineering, 35, 1959-1968.

Daskopoulos, P., Harris, C. K., 1996. Three dimensional CFD simulations of turbulence flow in baffled stirred tanks: an assessment of the current position. Institution of Chemical Engineering Symposium Series, 140, 1–113.

Degaleesan, S., 1997. Fluid dynamics measurements and modeling of liquid mixing in bubble columns. D.Sc Thesis, Washington University, St. Louis, USA.

Degaleesan, S., Dudukovic, M. P., 1998. Liquid back mixing in bubble columns and the axial dispersion coefficient. AIChE Journal, 44(11), 2369-2378.

Degaleesan, S., Dudukovic, M., Pan, Y., 2001. Experimental study of gas-induced liquid-flow structures in bubble columns. AIChE Journal, 47(9), 1913-1931.

Degaleesan, S., Dudukovic, M., Pan, Y., 2002. Application of wavelet filtering to the radioactive particle tracking technique. Flow measurement and Instrumentation, 13, 31-43.

Deglon, D. A., Meyer, C. J., 2006. CFD modelling of stirred tanks numerical considerations. Minerals Engineering, 19, 1059-1068.

Deshmukh, N. A., Joshi, J. B., 2006. Surface aerators: power number, mass transfer coefficient, gas hold up profiles and flow patterns. Chemical Engineering Research and Design, 84, 1-16.

Devanathan, N., Moslemian, D., Dudukovic, M. P., 1990. Flow mapping in bubble columns using CARPT. Chemical Engineering Science, 45(8), 2285-2291.

Devanathan, N., 1991. Investigation of liquid hydrodynamics in bubble columns via computer automated radioactive particle tracking. D.Sc. Thesis, Washington University, USA.

Devanathan, N., Dudukovic, M. P., Lapin, A., Lubbert, A., 1995. Chaotic flow in bubble column reactors. Chemical Engineering Science, 50(16), 2661-2667.

Devi, T. T., Sinha, A. P., Thakre, M., Kumar B., 2011. Impeller submergence depth for stirred tanks. Bulletin of Chemical Reaction Engineering and Catalysis, 6(2), 13-128.

Dewan, A., Buwa, V., Durst, F., 2006. Performance optimizations of grids disc impellers for mixing of single phase flows in a stirred vessel. Chemical Engineering Research and Design, 84(A8), 691-702.

Dong, L., Johansen, S. T., Engh, T. A., 1994. Flow induced by an impeller in an unbaffled tank-ii. numerical modelling. Chemical Engineering Science, 49, 3511-3518.

Dube, O., Dube, D., Chaouki J., Bertrand, F., 2014. Optimization of detector positioning in the radioactive particle tracking technique. Applied Radiation and Isotopes, 89, 109-124.

Fishwick, R., Winterbottom, M., Parker, D., Fan, X., Stitt, H., 2005. The use of positron emission particle tracking in the study of multiphase stirred tank reactor hydrodynamics. The Canadian Journal of Chemical Engineering, 83, 97-103.

Fletcher, C. A. J., 1991. Computational techniques for fluid dynamics, Vol. I and II, Springer-Verlag, Berlin.

Gillissen, J. J., Van den Akker, H. E. A., 2012. Direct numerical simulation of the turbulent flow in a baffled tank driven by a Rushton turbine. AIChE Journal, 58(12), 3878-3890.

Gimbun, J., Rielly, C. D., Nagy, Z. K., Derksen, J. J., 2012. Detached eddy simulation on the turbulence flow in a stirred tank. AIChE Journal, 58 (10), 3224–3241.

Godfroy, L., Larachi, F., Kennedy, G., Grandjean, B. P. A., Chaouki, J., 1997. Online flow visualization in multiphase reactors using neural networks. Applied Radiation and Isotopes, 48(2), 225-235.

Guha, D., Dudukovic, M. P., Ramachandran, P. A., 2006. CFD based compartmental modelling of single phase stirred-tank reactors. AIChE Journal, 52, 1836-1846.

Guha, D., 2007. Hydrodynamics and mixing in single phase and liquid-solid stirred tank reactors. DSc Thesis, Washington University, Saint Louis, Missouri.

Guha, D., Ramachandran, P. A., Dudukovic, M. P., 2007. Flow field of suspended solids in a stirred tank reactor by lagrangian tracking. Chemical Engineering Science, 62, 6143-6154.

Hemrajani, R. R., Tatterson, G. B., 2004. Handbook of industrial mixing, Edited by E.L. Paul, Published by John Wiley & Sons, Inc., Hoboken, New Jersey.

Ibrahim, S., Nienow, A. W., 1995. Power curves and flow patterns for a range of impellers in Newtonian fluids: $40 < Re < 5 \times 10^5$. Chemical Engineering Research and Design, 73(A5), 485-491.

Joshi, J. B., Nere, N. K., Rane, C. V., Murthy, B. N., Mathpati, C. S., Patwardhan, A. W., Ranade, V. V., 2011. CFD simulation of stirred tanks: comparison of turbulence models, part 1-radial flow impellers. The Canadian Journal of Chemical Engineering, 89, 23-82.

Kalaga, D. V., Pant, H. J., Dalvi, S. V., Joshi, J. B., Roy, S., 2017. Investigation of hydrodynamics in bubble column with internals using radioactive particle tracking (RPT). AIChE Journal, 63(11), 4881-4894.

Kalo, L., Pant, H. J., Cassanello, M. C., Upadhyay, R. K., 2019. Time series analysis of a binary gas-solid conical fluidized bed using radioactive particle tracking (RPT) technique data. Chemical Engineering Journal, 377, 119807.

Karcz, J., Cudak, M., Szoplik, J., 2005. Stirring of a liquid in a stirred tank with an eccentrically located impeller. Chemical Engineering Science, 60, 2369-2380.

Khopkar, A. R., Rammohan, A. R., Ranade, V. V., Dudukovic, M. P., 2005. Gas–liquid flow generated by a Rushton turbine in stirred vessel: CARPT/CT measurements and CFD simulations. Chemical Engineering Science, 60, 2215-2229.

Khopkar, A. R., Mavros, P., Ranade, V. V., Bertrand, J., 2004. Simulation of flow generated by an axial-flow impeller: batch and continuous operation. Chemical Engineering Research and Design, 82(A6), 737–751.

Kondukov, N. B., Kornilaev, A. N., Skachko, I. M., Akhromenkov, A. A., Kurglov, A. S., 1964. an investigation of the parameters of moving particles in a fluidized bed by a radioisotopic method. International Journal of Chemical Engineering, 4, 37-47.

Kresta, S. M., Wood, P. E., 1991. Prediction of the three-dimensional turbulence flow in stirred tanks. AIChE Journal, 37, 448–460.

Kukukova, A., Mostek, M., Jahoda, M., Machon, V., 2005. CFD prediction of flow and homogeneisation in stirred vessel: part-i vessel with one and two impellers. Chemical Engineering and Technology, 28, 1125-1132.

Kulkarni, A. L., Patwardhan A. W., 2014. CFD modeling of gas entrainment in stirred tank systems. Chemical Engineering Research and Design, 92(7), 1227-1248.

Kumaresan, T., Joshi, J. B., 2006., Effect of impeller design on the flow pattern and mixing in stirred tanks. Chemical Engineering Journal, 115, 173-193.

Larachi, F., Kennedy, G., Chaouki, J., 1994. A γ-ray detection system for 3-D particle tracking in multiphase reactors. Nuclear Instruments and Methods in Physics Research, Sect. A, 338 (2-3), 568-576.

Larachi, F., Chauki J., Kennedy, G., 1995. 3-D mapping of solids flow fields in multiphase reactors with RPT. AIChE Journal, 41(2), 439-443.

Larachi, F., Chaouki, J., Kennedy, G., Dudukovic, M. P., 1997. Radioactive Particle tracking in Multiphase Reactors: Principles and Applications. Non-Invasive Monitoring of Multiphase Flows, 335- 406.

Lee, K. C., Yianneskis, M., 1994. The extent of periodicity of the flow in vessels stirred by Rushton impellers. AIChE Symposium Series, 90, 5-18.

Li, M., White, G., Wilkinson, D., Roberts, K. J., 2004. LDA measurements and CFD modelling of a stirred vessel with a retreat curve impeller. Industrial and Engineering Chemistry Research, 43, 6534–6547.

Li, Z., Bao, Y., Gao, Z., 2011. PIV experiments and large eddy simulations of single loop flow fields in Rushton turbine stirred tanks. Chemical Engineering Science, 66(6), 1219-1231.

Ligarani, P. M., Singer, B. A., Baun, L. R., 1989. Miniature five-hole pressure probe for measurement of three mean velocity components in low-speed flows. Journal of Physics E Scientific Instruments, 22, 868-876.

Lin, J., Chen, M., Chao, B., 1985. A novel radioactive particle tracking facility for measurement of solids motion in gas fluidized beds. AIChE Journal, 31(3), 465-472.

Luo, J. Y., Gosman, A. D., Issa, R. I., Middleton, J. C., Fitzgerald, M. K., 1993. Full flow field computation of mixing in baffled stirred vessels. Chemical Engineering Research and Design, 71, 342–344.

Luo, J. Y., Issa, R. I., Gosman, A. D., 1994. Prediction of impeller-induced flows in mixing vessels using multiple frames of reference. IChE Symposium Series, 136, 549–556.

McCabe, W. L., Smith, J. C., Harriott, P., 1993. Unit operations of chemical engineering. McGraw-Hill Chemical Engineering Series, Singapore.

Meek, C. C., 1972. Statistical characterization of dilute particulate suspensions in turbulence fluid field. Ph.D. Thesis, University of Illinois, Urbana, IL.

Montante, G., Lee, K. C., Brucato, A., Yianneskis, M., 1999. An experimental study of double to single loop transition in stirred vessels. The Canadian Journal of Chemical Engineering, 77(4), 649-659.

Montante, G., Lee, K. C., Brucato, A., Yianneskis, M., 2001. Numerical simulations of the dependency of flow pattern on impeller clearance in stirred vessels. Chemical Engineering Science, 56(12), 3751-3770.

Montante, G., Bakker, A., Paglianti, A., Magelli, F, 2006. Effect of the shaft eccentricity on the hydrodynamics of unbaffled stirred tanks. Chemical Engineering Science, 61(9), 2807-2814.

Moslemian, M., Chen, M., Chao, B. T., 1989. Experimental and numerical simulations of solids mixing in a gas solid fluidized bed. Particulate Science and Technology, 7, 335-355.

Muller, U. R., 1992. Comparison of turbulence measurements with single, X and Triple hot-wire probes, Experiments in Fluids, 13, 208-216.

Murthy, B., Joshi, J., 2008. Assessment of standard, RSM and LES turbulence models in a baffled stirred vessel agitated by various impeller designs. Chemical Engineering Science, 63(22), 5468–5495.

Naude, I., Xuereb, C., Bertrand, J., 1998. Direct prediction of the flows induced by a propeller in an agitated vessel using an unstructured mesh. The Canadian Journal of Chemical Engineering, 76, 631–640.

Nienow, A.W., 1968. Suspensions of solid particles in turbine agitated baffled vessels. Chemical Engineering Science, 23(12), 1453-1459.

Nurtono, T., Setyawan, H., Altway, A., Winardi, S., 2008. Numerical analysis of macro-instability characteristic in a stirred tank by means of large eddy simulations: off-bottom clearance effect. Chemical Product and Process Modeling, 3(1), 1-24.

Ochieng, A., Onyango, M. S., Kumar, A., Kiriamiti, K., Musonge, P., 2008. Mixing in a tank stirred by a Rushton turbine at low clearance. Chemical Engineering and Processing: Process Intensification, 47(5), 842-851.

Patankar, S. V., 1980. Numerical heat transfer and fluid flow. Hemisphere, Washington, DC.

Patil, H., Patel, A. K., Pant, H. J., Venu Vinod, A., 2018. CFD simulation model for mixing tank using multiple reference frame impeller rotation. ISH Journal of Hydraulic Engineering, 1-10.

Patil, S. S., Deshmukh, N. A., Joshi, J. B., 2004. Mass transfer characteristics of surface aerators and gas inducing impellers. Industrial and Engineering Chemistry Research, 43, 2765-2774.

Placek, J., Talvarides, L. L., Smith, G. W., Fort, I., 1986. Turbulence flow in stirred tanks, part ii: a two scale model of turbulence. AIChE Journal, 32, 1771-1786.

Perng, C. Y., Murthy, J. Y., 1994. A moving deforming mesh technique for simulation of flow in mixing tanks. Proceedings 8th European Conference on Mixing, 37-39.

Pericleous, K. A., Patel, M. K., 1987. The modelling of tangential and axial agitators in chemical reactors. Physico-Chemical Hydrodynamics, 8, 105-123.

Pukkella, A. K., Vysyaraju, R., Tammishetti, V., Rai, B., Subramanian, S., 2019. Improved mixing of solid suspensions in stirred tanks with interface baffles: CFD simulation and experimental validation. Chemical Engineering Journal, 358, 621-633.

Rammohan, A. R., Kemoun, A., Al-Dahhan, M. H., Dudukovic, M. P., 2001a. Characterization of single phase flows in stirred tanks via computer automated radioactive particle tracking (CARPT). Transactions of Institution of Chemical Engineers, 79(A), 831-844.

Rammohan, A. R., Kemoun, A., Al-Dahhan, M. H., Dudukovic, M. P., 2001b. A lagrangian description of flows in stirred tanks via computer automated radioactive particle tracking. Chemical Engineering Science, 56, 2629-2639.

Rammohan, A., 2002. Characterization of single and multiphase flow in stirred tank reactor. D.Sc. Thesis, Washington University, USA.

Ranade, V. V., 1995, Computational fluid dynamics for reactor engineering. Reviews in Chemical Engineering, 11, 229-289.

Ranade, V. V., 2002. Computational flow modeling for chemical reactor engineering, Academic Press, New York.

Ranade, V. V., Dommeti, S. M. S., 1996. Computational snapshot of flow generated by axial impellers in baffled stirred vessels. Transactions of Institution of Chemical Engineers, 74, 476-484.

Ranade, V. V., Joshi, J. B., 1990. Flow generated by a disc turbine part I: experimental. Transactions of Institution of Chemical Engineers, 68, 19–33.

Rao, A. R. K., Patel, A. K., Kumar, B., 2009. Oxygen transfer in circular surface aeration tanks. Environmental Technology, 30(7), 747-753.

Rao, A. R. K., Patel, A. K., Kumar, B., 2010. Power characteristics of surface aerators. Journal of Chemical Technology and Biotechnology, 85, 805-813.

Rohatgi, V. K., Md. Ehsanes Saleh, A. K., 2015. An introduction to probability and statistics. Wiley Series in Probability and Statistics, New Delhi, India.

Roy, S., Larachi, F., Al-Dahhan, M., Dudukovic, M. P., 2002. Optimal design of radioactive particle tracking experiments for flow mapping in opaque multiphase reactors. Applied Radiation and Isotopes, 56, 485-503.

Roy, S., Acharya, S., Cloeter, M. D., 2010. Flow structure and the effect of macro-instabilities in a pitched-blade stirred tank. Chemical Engineering Science, 65, 3009-3024.

Rushton, J. H., Costich, E. W., Everett, H. J., 1950. Power characteristics of mixing impellers –part II. Chemical Engineering Progress, 46, 467-476.

Sahu, A. K., Kumar, P., Joshi, J. B., 1998. Simulation of flow in stirred vessels with axial flow impeller: zonal modelling and optimization of parameters. Industrial and Engineering Chemistry Research, 37, 2116–2130.

Schaeffer, M., Hofken, M., Durst, F., 1997. Detailed LDV measurements for visualization of the flow field within a stirred tank reactor equipped with a Rushton turbine. Transactions of Institution of Chemical Engineers, 75(A), 729-736.

Schafer, M. M., Yianneskis, M., Durst, F., 1998. Trailing vortices behind 45° pitched blade impeller AIChE Journal, 44, 1233–1246.

Sharma, L., Nigam, K. D. P., Roy, S., 2017. Investigation of two-phase (oil-water) flow in coiled geometries using radioactive particle tracking-time of flight (RPT-TOF) and radioactive particle tracking-volume fraction (RPT-VOF) measurements. Chemical Engineering Science, 170, 422-436.

Sheng, J., Meng, H., Fox, R. O., 2000. A large eddy PIV method for turbulence dissipation rate estimation. Chemical Engineering Science, 55(20), 4423-4434.

Shih, T. H., Liou, W. W., Shabbir, A., Zhu, J., 1995. A new k-ε eddy-viscosity model for high Reynolds number turbulence flows: model development and validation, Computers and Fluids, 24(3), 227-238.

Singh, H., Fletcher, D. F., Nijdam, J. J., 2011. An assessment of different turbulence models for predicting flow in a baffled tank stirred with a Rushton turbine. Chemical Engineering Science, 66 (23), 5976–5988.

Tatterson, G. B., 1991. Fluid mixing and gas dispersion in agitated tanks, McGraw- Hill, New York.

Tabor, A., Gosman, A. D., Issa, R. A., 1998. Numerical simulation of the flow in a mixing vessel stirred by a Rushton turbine. Institution of Chemical Engineering Symposium Series, 140, 25-34.

Torre, J. P., Fletcher, D. F., Lasuye, T., Xuereb, C., 2007. Single and multiphase CFD approaches for modelling partially baffled stirred vessels: comparison of experimental data with numerical predictions, Chemical Engineering Science, 62(22), 6246-6262.

Upadhyay, R. K., 2010. Investigation of multiphase reactors using radioactive particle tracking. PhD Thesis, Indian Institute of Technology Delhi, India.

Upadhyay, R., Roy S., 2010. Investigation of hydrodynamics of binary fluidized beds via radioactive particle tracking and dual source densitometry. The Canadian Journal of Chemical Engineering, 88, 601-610.

Versteeg, H. K., Malalasekera, W., 1995. An introduction to computational fluid dynamics the finite volume method. Longman Scientific and Technical, England.

Walas, S. M., 1990. Chemical Process Equipment. Butterworth-Heinemann Series in Chemical Engineering, USA.

Wildman, R. D., Blackburn, S., Benton, D. M., McNeil, P. A., Parker, D. J., 1999. Investigation of paste flow using positron emission particle tracking. Powder Technology, 103, 220-229.

Wilson, S. V., Luis, E. B., Delson B., 2014. An alternative method for tracking a radioactive particle inside a fluid. Applied Radiation and Isotopes, 85, 139-146.

Wu, H., Patterson, G., 1989. Laser-Doppler measurements of turbulence flow parameters in a stirred mixer. Chemical Engineering Science, 44, 2207-2221.

Xue, J., Al-Dahhan, M. H., Dudukovic M. P., Mudde R. F., 2008. Four-point optical probe for measurement of bubble dynamics: validation of the technique. Flow Measurement and Instrumentation, 19, 293-300.

Yang, Y. B., Devanathan, N., Dudukovic, M. P., 1992. Liquid back mixing in bubble columns. Chemical Engineering Science, 47, 2859-2864.

Yang, Y. B., Devanathan, N., Dudukovic, M. P., 1993. Liquid backmixing in bubble columns via computer-automated radioactive particle tracking (CARPT). Experiments in Fluids, 16, 1-9.

Yapici, K., Karasozen, B., Schafer, M., Uludug, Y., 2008. Numerical investigation of the effect of Rushton type turbine design factors on agitated tank flow characteristics. Chemical Engineering and Processing: Process Intensification, 47, 1340-134.

Zadghaffari, R., Moghaddas, J. S., Revstedt, J., 2010. Large-eddy simulation of turbulent flow in a stirred tank driven by a Rushton turbine. Computers & Fluids, 39, 1183-1190.

Zhu, Q., Xiao, H., Chen, A., Geng, S., Huang, Q., 2019. CFD study on double to single loop flow pattern transition and its influence on macro mixing efficiency in fully baffled tank stirred by a Rushton turbine. Chinese Journal of Chemical Engineering, 27(5), 993-1000.

Appendix – A.1

Detailed ANOVA analysis at all 14 locations for all 8 detectors

Table A.1 ANOVA analysis and percentage error in mean counts at L_1 for Detector 1

SUMMARY

Groups	*Count*	*Sum*	*Average*	*Variance*
stationary	500	55387	110.774	100.2354
109 rpm	500	55237	110.474	117.0434
136 rpm	500	55498	110.996	112.3487
161 rpm	500	55627	111.254	117.9173
188 rpm	500	55508	111.016	107.9436
214 rpm	500	55462	110.924	108.7076
238 rpm	500	55318	110.636	104.3963

ANOVA

Source of Variation	*SS*	*df*	*MS*	*F*	*P-value*	*F crit*
Between Groups	204.1577	6	34.02629	0.309896	0.932118	2.10118
Within Groups	383527.6	3493	109.7989			
Total	383731.8	3499				

rpm (motion & stationary)	**% error in counts**
109 and stationary	0.270
136 and stationary	0.200
161 and stationary	**0.433**
188 and stationary	0.218
214 and stationary	0.135
238 and stationary	0.124

Table A.2 ANOVA analysis and percentage error in mean counts at L_1 for Detector 2

SUMMARY

Groups	*Count*	*Sum*	*Average*	*Variance*
stationary	500	154944	309.888	291.6588
109 rpm	500	154884	309.768	248.419
136 rpm	500	155374	310.748	276.77
161 rpm	500	155520	311.04	281.9022
188 rpm	500	155179	310.358	274.5509
214 rpm	500	155450	310.9	254.2345
238 rpm	500	155824	311.648	251.5873

ANOVA

Source of Variation	*SS*	*df*	*MS*	*F*	*P-value*	*F crit*
Between Groups	1329.163	6	221.5271	0.82522	0.550158	2.10118
Within Groups	937682.2	3493	268.4461			
Total	939011.4	3499				

rpm (motion & stationary)	**% error in counts**
109 and stationary	0.038
136 and stationary	0.277
161 and stationary	0.371
188 and stationary	0.151
214 and stationary	0.326
238 and stationary	**0.567**

Table A.3 ANOVA analysis and percentage error in mean counts at L_1 for Detector 3

SUMMARY

Groups	*Count*	*Sum*	*Average*	*Variance*
stationary	500	187354	374.708	342.2152
109 rpm	500	187532	375.064	350.557
136 rpm	500	186803	373.606	317.2132
161 rpm	500	187191	374.382	349.4029
188 rpm	500	186779	373.558	332.6559
214 rpm	500	187773	375.546	339.3025
238 rpm	500	187296	374.592	347.4043

ANOVA

Source of Variation	*SS*	*df*	*MS*	*F*	*P-value*	*F crit*
Between Groups	1582.094	6	263.6823	0.775943	0.58873	2.10118
Within Groups	1186997	3493	339.8216			
Total	1188579	3499				

rpm (motion & stationary)	**% error in counts**
109 and stationary	0.095
136 and stationary	0.294
161 and stationary	0.087
188 and stationary	**0.306**
214 and stationary	0.223
238 and stationary	0.030

Table A.4 ANOVA analysis and percentage error in mean counts at L_1 for Detector 4

SUMMARY

Groups	*Count*	*Sum*	*Average*	*Variance*
stationary	500	318449	636.898	481.19
109 rpm	500	319042	638.084	454.542
136 rpm	500	319089	638.178	421.8781
161 rpm	500	318751	637.502	407.3687
188 rpm	500	318857	637.714	534.6976
214 rpm	500	318286	636.572	464.8986
238 rpm	500	320116	640.232	508.8439

ANOVA

Source of Variation	*SS*	*df*	*MS*	*F*	*P-value*	*F crit*
Between Groups	4253.947	6	708.9912	1.516133	0.16857	2.10118
Within Groups	1633436	3493	467.6313			
Total	1637690	3499				

rpm (motion & stationary)	**% error in counts**
109 and stationary	0.186
136 and stationary	0.200
161 and stationary	0.094
188 and stationary	0.128
214 and stationary	0.051
238 and stationary	**0.523**

Table A.5 ANOVA analysis and percentage error in mean counts at L_1 for Detector 5

SUMMARY

Groups	*Count*	*Sum*	*Average*	*Variance*
stationary	500	192977	385.954	328.9899
109 rpm	500	193453	386.906	365.0072
136 rpm	500	193434	386.868	327.0487
161 rpm	500	192491	384.982	384.2782
188 rpm	500	192508	385.016	348.5969
214 rpm	500	192533	385.066	349.4846
238 rpm	500	193458	386.916	378.1292

ANOVA

Source of Variation	*SS*	*df*	*MS*	*F*	*P-value*	*F crit*
Between Groups	2640.094	6	440.0156	1.241211	0.281762	2.10118
Within Groups	1238286	3493	354.505			
Total	1240926	3499				

rpm (motion & stationary)	**% error in counts**
109 and stationary	0.246
136 and stationary	0.236
161 and stationary	**0.251**
188 and stationary	0.243
214 and stationary	0.230
238 and stationary	0.249

Table A.6 ANOVA analysis and percentage error in mean counts at L_1 for Detector 6

SUMMARY

Groups	*Count*	*Sum*	*Average*	*Variance*
stationary	500	296856	593.712	434.0131
109 rpm	500	297726	595.452	449.7993
136 rpm	500	297766	595.532	470.6904
161 rpm	500	297860	595.72	455.9615
188 rpm	500	297125	594.25	423.3702
214 rpm	500	297592	595.184	530.2907
238 rpm	500	297492	594.984	490.0839

ANOVA

Source of Variation	*SS*	*df*	*MS*	*F*	*P-value*	*F crit*
Between Groups	1628.674	6	271.4456	0.583896	0.743487	2.10118
Within Groups	1623850	3493	464.887			
Total	1625479	3499				

rpm (motion & stationary)	**% error in counts**
109 and stationary	0.293
136 and stationary	0.306
161 and stationary	**0.338**
188 and stationary	0.090
214 and stationary	0.247
238 and stationary	0.214

Table A.7 ANOVA analysis and percentage error in mean counts at L_1 for Detector 7

SUMMARY

Groups	*Count*	*Sum*	*Average*	*Variance*
stationary	500	180344	360.688	291.7021
109 rpm	500	180715	361.43	279.6284
136 rpm	500	180610	361.22	288.4485
161 rpm	500	180670	361.34	311.3671
188 rpm	500	179767	359.534	289.9207
214 rpm	500	180618	361.236	285.5755
238 rpm	500	180420	360.84	309.6617

ANOVA

Source of Variation	*SS*	*df*	*MS*	*F*	*P-value*	*F crit*
Between Groups	1302.138	6	217.023	0.738782	0.618371	2.10118
Within Groups	1026096	3493	293.7577			
Total	1027398	3499				

rpm (motion & stationary)	**% error in counts**
109 and stationary	0.205
136 and stationary	0.147
161 and stationary	0.180
188 and stationary	**0.319**
214 and stationary	0.151
238 and stationary	0.042

Table A.8 ANOVA analysis and percentage error in mean counts at L_1 for Detector 8

SUMMARY

Groups	*Count*	*Sum*	*Average*	*Variance*
stationary	500	60011	120.022	112.0296
109 rpm	500	60191	120.382	123.6594
136 rpm	500	60082	120.164	118.8107
161 rpm	500	60318	120.636	122.8452
188 rpm	500	59805	119.61	106.1181
214 rpm	500	60105	120.21	109.3085
238 rpm	500	59965	119.93	113.8809

ANOVA

Source of Variation	*SS*	*df*	*MS*	*F*	*P-value*	*F crit*
Between Groups	324.4417	6	54.07362	0.469242	0.83157	2.10118
Within Groups	402519.6	3493	115.2361			
Total	402844	3499				

rpm (motion & stationary)	**% error in counts**
109 and stationary	0.299
136 and stationary	0.118
161 and stationary	**0.511**
188 and stationary	0.343
214 and stationary	0.156
238 and stationary	0.076

Table A.9 ANOVA analysis and percentage error in mean counts at L_2 for Detector 1

SUMMARY

Groups	*Count*	*Sum*	*Average*	*Variance*
stationary	500	296787	593.574	471.1228
109 rpm	500	296764	593.528	535.4241
136 rpm	500	297216	594.432	534.6026
161 rpm	500	297017	594.034	496.3175
188 rpm	500	296392	592.784	502.7068
214 rpm	500	297287	594.574	525.4394
238 rpm	500	296431	592.862	475.8026

ANOVA

Source of Variation	*SS*	*df*	*MS*	*F*	*P-value*	*F crit*
Between Groups	1498.112	6	249.6853	0.493531	0.813648	2.10118
Within Groups	1767166	3493	505.9165			
Total	1768665	3499				

rpm (motion & stationary)	**% error in counts**
109 and stationary	0.007
136 and stationary	0.144
161 and stationary	0.077
188 and stationary	0.133
214 and stationary	**0.168**
238 and stationary	0.119

Table A.10 ANOVA analysis and percentage error in mean counts at L_2 for Detector 2

SUMMARY

Groups	*Count*	*Sum*	*Average*	*Variance*
stationary	500	437039	874.078	630.9097
109 rpm	500	435927	871.854	600.0808
136 rpm	500	436404	872.808	640.5202
161 rpm	500	435799	871.598	625.6397
188 rpm	500	435829	871.658	548.2896
214 rpm	500	436598	873.196	606.3904
238 rpm	500	435778	871.556	611.9067

ANOVA

Source of Variation	*SS*	*df*	*MS*	*F*	*P-value*	*F crit*
Between Groups	2909.799	6	484.9665	0.796195	0.572764	2.10118
Within Groups	2127605	3493	609.1053			
Total	2130515	3499				

rpm (motion & stationary)	**% error in counts**
109 and stationary	0.254
136 and stationary	0.145
161 and stationary	0.283
188 and stationary	0.276
214 and stationary	0.100
238 and stationary	**0.288**

Table A.11 ANOVA analysis and percentage error in mean counts at L_2 for Detector 3

SUMMARY

Groups	*Count*	*Sum*	*Average*	*Variance*
stationary	500	95223	190.446	182.5883
109 rpm	500	95085	190.17	167.1233
136 rpm	500	94782	189.564	173.6773
161 rpm	500	94712	189.424	194.3048
188 rpm	500	95324	190.648	172.6574
214 rpm	500	95073	190.146	186.4496
238 rpm	500	95133	190.266	189.7187

ANOVA

Source of Variation	*SS*	*df*	*MS*	*F*	*P-value*	*F crit*
Between Groups	599.33943	6	99.8899	0.552087	0.768679	2.10118
Within Groups	631993.17	3493	180.9313			
Total	632592.51	3499				

rpm (motion & stationary)	**% error in counts**
109 and stationary	0.144
136 and stationary	0.463
161 and stationary	**0.536**
188 and stationary	0.106
214 and stationary	0.157
238 and stationary	0.094

Table A.12 ANOVA analysis and percentage error in mean counts at L_2 for Detector 4

SUMMARY

Groups	*Count*	*Sum*	*Average*	*Variance*
stationary	500	130293	260.586	259.3333
109 rpm	500	130354	260.708	250.2793
136 rpm	500	129850	259.7	235.7295
161 rpm	500	130514	261.028	235.1415
188 rpm	500	130750	261.5	256.1102
214 rpm	500	130288	260.576	242.5934
238 rpm	500	130162	260.324	293.1453

ANOVA

Source of Variation	*SS*	*df*	*MS*	*F*	*P-value*	*F crit*
Between Groups	942.3777	6	157.063	0.620335	0.714215	2.10118
Within Groups	884393.9	3493	253.1904			
Total	885336.3	3499				

rpm (motion & stationary)	**% error in counts**
109 and stationary	0.046
136 and stationary	0.340
161 and stationary	0.169
188 and stationary	**0.350**
214 and stationary	0.003
238 and stationary	0.100

Table A.13 ANOVA analysis and percentage error in mean counts at L_2 for Detector 5

SUMMARY

Groups	*Count*	*Sum*	*Average*	*Variance*
stationary	500	33276	66.552	66.352
109 rpm	500	32935	65.87	63.98908
136 rpm	500	33188	66.376	63.67397
161 rpm	500	32972	65.944	64.69024
188 rpm	500	32920	65.84	68.59158
214 rpm	500	32933	65.866	67.31067
238 rpm	500	32782	65.564	65.31253

ANOVA

Source of Variation	*SS*	*df*	*MS*	*F*	*P-value*	*F crit*
Between Groups	349.8737	6	58.31229	0.887515	0.502968	2.10118
Within Groups	229500.1	3493	65.70287			
Total	229850	3499				

rpm (motion & stationary)	**% error in counts**
109 and stationary	1.024
136 and stationary	0.264
161 and stationary	0.913
188 and stationary	1.069
214 and stationary	1.030
238 and stationary	**1.484**

Table A.14 ANOVA analysis and percentage error in mean counts at L_2 for Detector 6

SUMMARY

Groups	*Count*	*Sum*	*Average*	*Variance*
stationary	500	39931	79.862	77.83863
109 rpm	500	39821	79.642	74.05795
136 rpm	500	39576	79.152	61.01493
161 rpm	500	39748	79.496	76.12624
188 rpm	500	39628	79.256	73.18884
214 rpm	500	39213	78.426	76.84622
238 rpm	500	39513	79.026	86.59451

ANOVA

Source of Variation	SS	df	MS	F	P-value	F crit
Between Groups	662.8937	6	110.4823	1.471227	0.183882	2.10118
Within Groups	262308	3493	75.09533			
Total	262970.9	3499				

rpm (motion & stationary)	**% error in counts**
109 and stationary	0.275
136 and stationary	0.889
161 and stationary	0.458
188 and stationary	0.758
214 and stationary	**1.798**
238 and stationary	1.046

Table A.15 ANOVA analysis and percentage error in mean counts at L_2 for Detector 7

SUMMARY

Groups	*Count*	*Sum*	*Average*	*Variance*
stationary	500	288914	577.828	399.8301
109 rpm	500	289214	578.428	386.3094
136 rpm	500	288603	577.206	393.4465
161 rpm	500	289588	579.176	436.1774
188 rpm	500	289292	578.584	386.7244
214 rpm	500	288806	577.612	409.4203
238 rpm	500	288957	577.914	450.1709

ANOVA

Source of Variation	*SS*	*df*	*MS*	*F*	*P-value*	*F crit*
Between Groups	1322.623	6	220.4372	0.53914	0.778801	2.10118
Within Groups	1428177	3493	408.8684			
Total	1429500	3499				

rpm (motion & stationary)	**% error in counts**
109 and stationary	0.103
136 and stationary	0.107
161 and stationary	**0.233**
188 and stationary	0.130
214 and stationary	0.037
238 and stationary	0.014

Table A.16 ANOVA analysis and percentage error in mean counts at L_2 for Detector 8

SUMMARY

Groups	*Count*	*Sum*	*Average*	*Variance*
stationary	500	134529	269.058	249.8183
109 rpm	500	133488	266.976	246.2239
136 rpm	500	134089	268.178	241.1446
161 rpm	500	133580	267.16	246.7198
188 rpm	500	134611	269.222	221.131
214 rpm	500	134191	268.382	196.7255
238 rpm	500	134622	269.244	255.3231

ANOVA

Source of Variation	*SS*	*df*	*MS*	*F*	*P-value*	*F crit*
Between Groups	2693.955	6	448.9926	1.896671	0.077646	2.10118
Within Groups	826886	3493	236.7266			
Total	829580	3499				

rpm (motion & stationary)	**% error in counts**
109 and stationary	**0.773**
136 and stationary	0.327
161 and stationary	0.705
188 and stationary	0.060
214 and stationary	0.251
238 and stationary	0.069

Table A.17 ANOVA analysis and percentage error in mean counts at L_3 for Detector 1

SUMMARY

Groups	*Count*	*Sum*	*Average*	*Variance*
stationary	500	73196	146.392	133.5294
109 rpm	500	72822	145.644	128.2057
136 rpm	500	72813	145.626	147.8218
161 rpm	500	73137	146.274	127.8667
188 rpm	500	72723	145.446	131.5382
214 rpm	500	73019	146.038	145.9925
238 rpm	500	72536	145.072	132.4798

ANOVA

Source of Variation	*SS*	*df*	*MS*	*F*	*P-value*	*F crit*
Between Groups	670.0149	6	111.6691	0.825054	0.550287	2.10118
Within Groups	472769.6	3493	135.3477			
Total	473439.6	3499				

rpm (motion & stationary)	**% error in counts**
109 and stationary	0.510
136 and stationary	0.523
161 and stationary	0.080
188 and stationary	0.646
214 and stationary	0.241
238 and stationary	**0.901**

Table A.18 ANOVA analysis and percentage error in mean counts at L_3 for Detector 2

SUMMARY

Groups	*Count*	*Sum*	*Average*	*Variance*
stationary	500	184912	369.824	372.6463
109 rpm	500	184890	369.78	337.2261
136 rpm	500	185061	370.122	335.0252
161 rpm	500	184840	369.68	316.7391
188 rpm	500	184835	369.67	310.6945
214 rpm	500	184749	369.498	310.9078
238 rpm	500	184943	369.886	307.9289

ANOVA

Source of Variation	*SS*	*df*	*MS*	*F*	*P-value*	*F crit*
Between Groups	115.88	6	19.31333	0.059006	0.999189	2.10118
Within Groups	1143293	3493	327.3097			
Total	1143409	3499				

rpm (motion & stationary)	**% error in counts**
109 and stationary	0.011
136 and stationary	0.080
161 and stationary	0.038
188 and stationary	0.041
214 and stationary	**0.088**
238 and stationary	0.016

Table A.19 ANOVA analysis and percentage error in mean counts at L_3 for Detector 3

SUMMARY

Groups	*Count*	*Sum*	*Average*	*Variance*
stationary	500	321399	642.798	453.1515
109 rpm	500	321388	642.776	457.9457
136 rpm	500	321745	643.49	518.038
161 rpm	500	320955	641.91	471.5169
188 rpm	500	322622	645.244	515.5716
214 rpm	500	321744	643.488	490.8676
238 rpm	500	322376	644.752	499.245

ANOVA

Source of Variation	*SS*	*df*	*MS*	*F*	*P-value*	*F crit*
Between Groups	4077.056	6	679.5093	1.396387	0.212024	2.10118
Within Groups	1699762	3493	486.6195			
Total	1703839	3499				

rpm (motion & stationary)	**% error in counts**
109 and stationary	0.003
136 and stationary	0.107
161 and stationary	0.138
188 and stationary	**0.380**
214 and stationary	0.107
238 and stationary	0.303

Table A.20 ANOVA analysis and percentage error in mean counts at L_3 for Detector 4

SUMMARY

Groups	*Count*	*Sum*	*Average*	*Variance*
stationary	500	450754	901.508	595.8096
109 rpm	500	450234	900.468	599.6803
136 rpm	500	448876	897.752	519.5296
161 rpm	500	449629	899.258	544.6888
188 rpm	500	449422	898.844	536.5287
214 rpm	500	449689	899.378	557.0051
238 rpm	500	449461	898.922	554.3967

ANOVA

Source of Variation	*SS*	*df*	*MS*	*F*	*P-value*	*F crit*
Between Groups	4421.451	6	736.9086	1.320071	0.244323	2.10118
Within Groups	1949912	3493	558.2341			
Total	1954333	3499				

rpm (motion & stationary)	**% error in counts**
109 and stationary	0.115
136 and stationary	**0.416**
161 and stationary	0.249
188 and stationary	0.295
214 and stationary	0.236
238 and stationary	0.286

Table A.21 ANOVA analysis and percentage error in mean counts at L_3 for Detector 5

SUMMARY

Groups	*Count*	*Sum*	*Average*	*Variance*
stationary	500	208565	417.13	385.5803
109 rpm	500	207994	415.988	366.2243
136 rpm	500	208218	416.436	355.7173
161 rpm	500	208153	416.306	356.0485
188 rpm	500	208335	416.67	329.1795
214 rpm	500	208491	416.982	393.8454
238 rpm	500	208425	416.85	380.4163

ANOVA

Source of Variation	*SS*	*df*	*MS*	*F*	*P-value*	*F crit*
Between Groups	489.1754	6	81.52924	0.222323	0.969724	2.10118
Within Groups	1280939	3493	366.7159			
Total	1281428	3499				

rpm (motion & stationary)	**% error in counts**
109 and stationary	**0.273**
136 and stationary	0.166
161 and stationary	0.197
188 and stationary	0.110
214 and stationary	0.035
238 and stationary	0.067

Table A.22 ANOVA analysis and percentage error in mean counts at L_3 for Detector 6

SUMMARY

Groups	*Count*	*Sum*	*Average*	*Variance*
stationary	500	255195	510.39	433.3366
109 rpm	500	254379	508.758	437.6107
136 rpm	500	255275	510.55	394.1117
161 rpm	500	254732	509.464	424.2452
188 rpm	500	255675	511.35	426.7169
214 rpm	500	255327	510.654	408.3991
238 rpm	500	255214	510.428	432.1651

ANOVA

Source of Variation	*SS*	*df*	*MS*	*F*	*P-value*	*F crit*
Between Groups	2177.442	6	362.907	0.859217	0.524162	2.10118
Within Groups	1475336	3493	422.3693			
Total	1477514	3499				

rpm (motion & stationary)	**% error in counts**
109 and stationary	**0.319**
136 and stationary	0.031
161 and stationary	0.181
188 and stationary	0.188
214 and stationary	0.051
238 and stationary	0.007

Table A.23 ANOVA analysis and percentage error in mean counts at L_3 for Detector 7

SUMMARY

Groups	*Count*	*Sum*	*Average*	*Variance*
stationary	500	173673	347.346	322.4833
109 rpm	500	173381	346.762	294.7268
136 rpm	500	173765	347.53	284.8468
161 rpm	500	173505	347.01	294.2143
188 rpm	500	173732	347.464	292.8384
214 rpm	500	173415	346.83	320.9109
238 rpm	500	173551	347.102	309.8112

ANOVA

Source of Variation	*SS*	*df*	*MS*	*F*	*P-value*	*F crit*
Between Groups	278.1274	6	46.35457	0.15307	0.988503	2.10118
Within Groups	1057796	3493	302.8331			
Total	1058074	3499				

rpm (motion & stationary)	**% error in counts**
109 and stationary	**0.168**
136 and stationary	0.052
161 and stationary	0.096
188 and stationary	0.033
214 and stationary	0.148
238 and stationary	0.070

Table A.24 ANOVA analysis and percentage error in mean counts at L_3 for Detector 8

SUMMARY

Groups	*Count*	*Sum*	*Average*	*Variance*
stationary	500	56084	112.168	118.2122
109 rpm	500	56167	112.334	119.6578
136 rpm	500	55986	111.972	119.0333
161 rpm	500	56265	112.53	113.5562
188 rpm	500	56470	112.94	102.6978
214 rpm	500	56635	113.27	115.8247
238 rpm	500	55960	111.92	104.9675

ANOVA

Source of Variation	*SS*	*df*	*MS*	*F*	*P-value*	*F crit*
Between Groups	760.6137	6	126.769	1.117681	0.34914	2.10118
Within Groups	396180.8	3493	113.4214			
Total	396941.4	3499				

rpm (motion & stationary)	**% error in counts**
109 and stationary	0.147
136 and stationary	0.174
161 and stationary	0.322
188 and stationary	0.688
214 and stationary	**0.982**
238 and stationary	0.221

Table A.25 ANOVA analysis and percentage error in mean counts at L_4 for Detector 1

SUMMARY

Groups	*Count*	*Sum*	*Average*	*Variance*
stationary	500	57128	114.256	104.1748
109 rpm	500	56629	113.258	105.8471
136 rpm	500	56376	112.752	108.3191
161 rpm	500	56653	113.306	113.9162
188 rpm	500	57087	114.174	102.0719
214 rpm	500	56573	113.146	122.6139
238 rpm	500	56705	113.41	107.3566

ANOVA

Source of Variation	*SS*	*df*	*MS*	*F*	*P-value*	*F crit*
Between Groups	904.6657	6	150.7776	1.380929	0.218265	2.10118
Within Groups	381385.5	3493	109.1857			
Total	382290.2	3499				

rpm (motion & stationary)	**% error in counts**
109 and stationary	0.873
136 and stationary	**1.316**
161 and stationary	0.831
188 and stationary	0.071
214 and stationary	0.971
238 and stationary	0.740

Table A.26 ANOVA analysis and percentage error in mean counts at L_4 for Detector 2

SUMMARY

Groups	*Count*	*Sum*	*Average*	*Variance*
stationary	500	158033	316.066	270.755
109 rpm	500	157177	314.354	297.981
136 rpm	500	158213	316.426	274.433
161 rpm	500	157397	314.794	269.471
188 rpm	500	156911	313.822	284.932
214 rpm	500	157449	314.898	262.945
238 rpm	500	157548	315.096	259.51

ANOVA

Source of Variation	*SS*	*df*	*MS*	*F*	*P-value*	*F crit*
Between Groups	2503.59	6	417.265	1.52126	0.16689	2.10118
Within Groups	958094	3493	274.29			
Total	960597	3499				

rpm (motion & stationary)	**% error in counts**
109 and stationary	0.541
136 and stationary	0.113
161 and stationary	0.402
188 and stationary	**0.709**
214 and stationary	0.369
238 and stationary	0.306

Table A.27 ANOVA analysis and percentage error in mean counts at L_4 for Detector 3

SUMMARY

Groups	*Count*	*Sum*	*Average*	*Variance*
stationary	500	142596	285.192	243.2937
109 rpm	500	143321	286.642	261.1922
136 rpm	500	143201	286.402	265.6477
161 rpm	500	143018	286.036	260.9486
188 rpm	500	143104	286.208	265.4396
214 rpm	500	143254	286.508	269.7334
238 rpm	500	143988	287.976	268.2279

ANOVA

Source of Variation	*SS*	*df*	*MS*	*F*	*P-value*	*F crit*
Between Groups	2089.395	6	348.2325	1.328782	0.240445	2.10118
Within Groups	915407.1	3493	262.069			
Total	917496.5	3499				

rpm (motion & stationary)	**% error in counts**
109 and stationary	0.508
136 and stationary	0.424
161 and stationary	0.295
188 and stationary	0.356
214 and stationary	0.461
238 and stationary	**0.976**

Table A.28 ANOVA analysis and percentage error in mean counts at L_4 for Detector 4

SUMMARY

Groups	*Count*	*Sum*	*Average*	*Variance*
stationary	500	161879	323.758	251.3301
109 rpm	500	162483	324.966	269.2914
136 rpm	500	161782	323.564	272.8115
161 rpm	500	162180	324.36	273.4132
188 rpm	500	162369	324.738	297.4082
214 rpm	500	162500	325	306.3447
238 rpm	500	161841	323.682	299.1913

ANOVA

Source of Variation	*SS*	*df*	*MS*	*F*	*P-value*	*F crit*
Between Groups	1173.119	6	195.5198	0.694814	0.653847	2.10118
Within Groups	982925.4	3493	281.3986			
Total	984098.5	3499				

rpm (motion & stationary)	**% error in counts**
109 and stationary	0.373
136 and stationary	0.059
161 and stationary	0.185
188 and stationary	0.302
214 and stationary	**0.383**
238 and stationary	0.023

Table A.29 ANOVA analysis and percentage error in mean counts at L_4 for Detector 5

SUMMARY

Groups	*Count*	*Sum*	*Average*	*Variance*
stationary	500	348482	696.964	575.0648
109 rpm	500	348925	697.85	560.0115
136 rpm	500	349167	698.334	517.5696
161 rpm	500	349256	698.512	380.7233
188 rpm	500	349787	699.574	517.6318
214 rpm	500	349552	699.104	517.6365
238 rpm	500	349954	699.908	508.8813

ANOVA

Source of Variation	*SS*	*df*	*MS*	*F*	*P-value*	*F crit*
Between Groups	3115.375	6	519.2291	1.015957	0.412753	2.10118
Within Groups	1785182	3493	511.0741			
Total	1788297	3499				

rpm (motion & stationary)	**% error in counts**
109 and stationary	0.127
136 and stationary	0.196
161 and stationary	0.222
188 and stationary	0.374
214 and stationary	0.307
238 and stationary	**0.422**

Table A.30 ANOVA analysis and percentage error in mean counts at L_4 for Detector 6

SUMMARY

Groups	*Count*	*Sum*	*Average*	*Variance*
stationary	500	380273	760.546	569.5911
109 rpm	500	382206	764.412	580.1065
136 rpm	500	382880	765.76	600.792
161 rpm	500	382052	764.104	584.1535
188 rpm	500	382687	765.374	578.4831
214 rpm	500	382227	764.454	565.1061
238 rpm	500	382825	765.65	5216.537

ANOVA

Source of Variation	*SS*	*df*	*MS*	*F*	*P-value*	*F crit*
Between Groups	9634.527	6	1605.754	1.292764	0.256809	2.10118
Within Groups	4338690	3493	1242.11			
Total	4348324	3499				

rpm (motion & stationary)	**% error in counts**
109 and stationary	0.508
136 and stationary	**0.685**
161 and stationary	0.467
188 and stationary	0.634
214 and stationary	0.513
238 and stationary	0.671

Table A.31 ANOVA analysis and percentage error in mean counts at L_4 for Detector 7

SUMMARY

Groups	*Count*	*Sum*	*Average*	*Variance*
stationary	500	310803	621.606	455.5459
109 rpm	500	310871	621.742	421.0455
136 rpm	500	311614	623.228	400.7535
161 rpm	500	311047	622.094	404.6184
188 rpm	500	310796	621.592	428.5787
214 rpm	500	310839	621.678	424.8079
238 rpm	500	311804	623.608	440.6837

ANOVA

Source of Variation	*SS*	*df*	*MS*	*F*	*P-value*	*F crit*
Between Groups	2126.051	6	354.3419	0.833456	0.54381	2.10118
Within Groups	1485041	3493	425.1477			
Total	1487167	3499				

rpm (motion & stationary)	**% error in counts**
109 and stationary	0.021
136 and stationary	0.260
161 and stationary	0.078
188 and stationary	0.002
214 and stationary	0.011
238 and stationary	**0.322**

Table A.32 ANOVA analysis and percentage error in mean counts at L_4 for Detector 8

SUMMARY

Groups	*Count*	*Sum*	*Average*	*Variance*
stationary	500	142289	284.578	279.2344
109 rpm	500	141846	283.692	251.4841
136 rpm	500	142030	284.06	286.1006
161 rpm	500	142305	284.61	277.1522
188 rpm	500	141687	283.374	255.461
214 rpm	500	142026	284.052	255.1797
238 rpm	500	142020	284.04	262.4713

ANOVA

Source of Variation	*SS*	*df*	*MS*	*F*	*P-value*	*F crit*
Between Groups	588.64	6	98.10667	0.367818	0.899663	2.10118
Within Groups	931674.6	3493	266.7262			
Total	932263.2	3499				

rpm (motion & stationary)	**% error in counts**
109 and stationary	0.311
136 and stationary	0.182
161 and stationary	0.011
188 and stationary	**0.423**
214 and stationary	0.184
238 and stationary	0.189

Table A.33 ANOVA analysis and percentage error in mean counts at L_5 for Detector 1

SUMMARY

Groups	*Count*	*Sum*	*Average*	*Variance*
stationary	500	324653	649.306	482.822
109 rpm	500	326327	652.654	528.864
136 rpm	500	325869	651.738	546.6026
161 rpm	500	325308	650.616	498.1248
188 rpm	500	325295	650.59	560.5951
214 rpm	500	325155	650.31	511.2684
238 rpm	500	325518	651.036	496.5238

ANOVA

Source of Variation	*SS*	*df*	*MS*	*F*	*P-value*	*F crit*
Between Groups	3431.295	6	571.8826	1.104386	0.35704	2.10118
Within Groups	1808776	3493	517.8287			
Total	1812207	3499				

rpm (motion & stationary)	**% error in counts**
109 and stationary	**0.515**
136 and stationary	0.374
161 and stationary	0.201
188 and stationary	0.197
214 and stationary	0.154
238 and stationary	0.266

Table A.34 ANOVA analysis and percentage error in mean counts at L_5 for Detector 2

SUMMARY

Groups	*Count*	*Sum*	*Average*	*Variance*
stationary	500	416012	832.024	590.5165
109 rpm	500	417447	834.894	619.2573
136 rpm	500	415618	831.236	543.4151
161 rpm	500	416622	833.244	589.4874
188 rpm	500	416884	833.768	536.7196
214 rpm	500	416928	833.856	603.1215
238 rpm	500	417115	834.23	529.5482

ANOVA

Source of Variation	*SS*	*df*	*MS*	*F*	*P-value*	*F crit*
Between Groups	4911.002	6	818.5003	1.428068	0.199699	2.10118
Within Groups	2002021	3493	573.1522			
Total	2006932	3499				

rpm (motion & stationary)	**% error in counts**
109 and stationary	**0.344**
136 and stationary	0.094
161 and stationary	0.146
188 and stationary	0.209
214 and stationary	0.220
238 and stationary	0.265

Table A.35 ANOVA analysis and percentage error in mean counts at L_5 for Detector 3

SUMMARY

Groups	*Count*	*Sum*	*Average*	*Variance*
stationary	500	64435	128.87	130.8989
109 rpm	500	64181	128.362	127.3016
136 rpm	500	64168	128.336	111.8909
161 rpm	500	64338	128.676	128.5882
188 rpm	500	64366	128.732	126.5132
214 rpm	500	64253	128.506	126.1663
238 rpm	500	63967	127.934	119.0197

ANOVA

Source of Variation	*SS*	*df*	*MS*	*F*	*P-value*	*F crit*
Between Groups	293.512	6	48.91867	0.393427	0.883676	2.10118
Within Groups	434319	3493	124.3398			
Total	434612.5	3499				

rpm (motion & stationary)	**% error in counts**
109 and stationary	0.394
136 and stationary	0.414
161 and stationary	0.150
188 and stationary	0.107
214 and stationary	0.282
238 and stationary	**0.726**

Table A.36 ANOVA analysis and percentage error in mean counts at L_5 for Detector 4

SUMMARY

Groups	*Count*	*Sum*	*Average*	*Variance*
stationary	500	64254	128.508	138.2224
109 rpm	500	64117	128.234	114.1756
136 rpm	500	64204	128.408	130.7711
161 rpm	500	64004	128.008	116.6452
188 rpm	500	64818	129.636	133.2861
214 rpm	500	64233	128.466	132.8305
238 rpm	500	64105	128.21	122.4308

ANOVA

Source of Variation	*SS*	*df*	*MS*	*F*	*P-value*	*F crit*
Between Groups	848.4857	6	141.4143	1.114298	0.351138	2.10118
Within Groups	443292.5	3493	126.9088			
Total	444140.9	3499				

rpm (motion & stationary)	**% error in counts**
109 and stationary	0.213
136 and stationary	0.077
161 and stationary	0.389
188 and stationary	**0.877**
214 and stationary	0.032
238 and stationary	0.231

Table A.37 ANOVA analysis and percentage error in mean counts at L_5 for Detector 5

SUMMARY

Groups	*Count*	*Sum*	*Average*	*Variance*
stationary	500	59756	119.512	94.94775
109 rpm	500	59814	119.628	112.6389
136 rpm	500	59300	118.6	110.0762
161 rpm	500	59523	119.046	91.45479
188 rpm	500	59668	119.336	115.9069
214 rpm	500	59185	118.37	108.1213
238 rpm	500	59175	118.35	113.6668

ANOVA

Source of Variation	*SS*	*df*	*MS*	*F*	*P-value*	*F crit*
Between Groups	873.6869	6	145.6145	1.364869	0.224909	2.10118
Within Groups	372659.5	3493	106.6875			
Total	373533.2	3499				

rpm (motion & stationary)	**% error in counts**
109 and stationary	0.097
136 and stationary	0.763
161 and stationary	0.389
188 and stationary	0.147
214 and stationary	0.955
238 and stationary	**0.972**

Table A.38 ANOVA analysis and percentage error in mean counts at L_5 for Detector 6

SUMMARY

Groups	*Count*	*Sum*	*Average*	*Variance*
stationary	500	58734	117.468	114.4178
109 rpm	500	58697	117.394	119.1891
136 rpm	500	58496	116.992	135.1943
161 rpm	500	58975	117.95	126.26
188 rpm	500	58457	116.914	125.2732
214 rpm	500	58593	117.186	105.3661
238 rpm	500	58836	117.672	109.7439

ANOVA

Source of Variation	*SS*	*df*	*MS*	*F*	*P-value*	*F crit*
Between Groups	411.216	6	68.536	0.574248	0.751172	2.10118
Within Groups	416886.8	3493	119.3492			
Total	417298	3499				

rpm (motion & stationary)	**% error in counts**
109 and stationary	0.062
136 and stationary	0.405
161 and stationary	0.410
188 and stationary	**0.471**
214 and stationary	0.240
238 and stationary	0.173

Table A.39 ANOVA analysis and percentage error in mean counts at L_5 for Detector 7

SUMMARY

Groups	*Count*	*Sum*	*Average*	*Variance*
stationary	500	369546	739.092	708.224
109 rpm	500	368112	736.224	774.8395
136 rpm	500	369199	738.398	757.0377
161 rpm	500	368199	736.398	723.695
188 rpm	500	367656	735.312	863.9385
214 rpm	500	369554	739.108	781.9282
238 rpm	500	368278	736.556	765.578

ANOVA

Source of Variation	*SS*	*df*	*MS*	*F*	*P-value*	*F crit*
Between Groups	7081.386	6	1180.231	1.536976	0.161844	2.10118
Within Groups	2682245	3493	767.8916			
Total	2689327	3499				

rpm (motion & stationary)	**% error in counts**
109 and stationary	0.388
136 and stationary	0.093
161 and stationary	0.364
188 and stationary	**0.511**
214 and stationary	0.002
238 and stationary	0.343

Table A.40 ANOVA analysis and percentage error in mean counts at L_5 for Detector 8

SUMMARY

Groups	*Count*	*Sum*	*Average*	*Variance*
stationary	500	358574	717.148	494.463
109 rpm	500	358044	716.088	619.9602
136 rpm	500	357867	715.734	520.2638
161 rpm	500	357719	715.438	505.6294
188 rpm	500	357863	715.726	485.522
214 rpm	500	357726	715.452	553.9035
238 rpm	500	357349	714.698	509.2934

ANOVA

Source of Variation	*SS*	*df*	*MS*	*F*	*P-value*	*F crit*
Between Groups	1681.083	6	280.1806	0.531647	0.784617	2.10118
Within Groups	1840829	3493	527.005			
Total	1842510	3499				

rpm (motion & stationary)	**% error in counts**
109 and stationary	0.147
136 and stationary	0.197
161 and stationary	0.238
188 and stationary	0.198
214 and stationary	0.236
238 and stationary	**0.341**

Table A.41 ANOVA analysis and percentage error in mean counts at L_6 for Detector 1

SUMMARY

Groups	*Count*	*Sum*	*Average*	*Variance*
stationary	500	110869	221.738	213.1236
109 rpm	500	111573	223.146	209.4476
136 rpm	500	110754	221.508	221.056
161 rpm	500	111790	223.58	181.0377
188 rpm	500	111030	222.06	238.7058
214 rpm	500	111710	223.42	216.5687
238 rpm	500	111366	222.732	192.5974

ANOVA

Source of Variation	*SS*	*df*	*MS*	*F*	*P-value*	*F crit*
Between Groups	2087.706	6	347.951	1.654055	0.128237	2.10118
Within Groups	734795.9	3493	210.3624			
Total	736883.6	3499				

rpm (motion & stationary)	**% error in counts**
109 and stationary	0.634
136 and stationary	0.103
161 and stationary	**0.830**
188 and stationary	0.145
214 and stationary	0.758
238 and stationary	0.448

Table A.42 ANOVA analysis and percentage error in mean counts at L_6 for Detector 2

SUMMARY

Groups	*Count*	*Sum*	*Average*	*Variance*
stationary	500	232724	465.448	384.4963
109 rpm	500	232839	465.678	402.6636
136 rpm	500	232936	465.872	345.9195
161 rpm	500	233260	466.52	380.7711
188 rpm	500	233254	466.508	371.3767
214 rpm	500	233663	467.326	410.1721
238 rpm	500	233890	467.78	414.8172

ANOVA

Source of Variation	*SS*	*df*	*MS*	*F*	*P-value*	*F crit*
Between Groups	2239.283	6	373.2138	0.963944	0.448027	2.10118
Within Groups	1352398	3493	387.1738			
Total	1354637	3499				

rpm (motion & stationary)	**% error in counts**
109 and stationary	0.049
136 and stationary	0.091
161 and stationary	0.230
188 and stationary	0.227
214 and stationary	0.403
238 and stationary	**0.501**

Table A.43 ANOVA analysis and percentage error in mean counts at L_6 for Detector 3

SUMMARY

Groups	*Count*	*Sum*	*Average*	*Variance*
stationary	500	215802	431.604	353.7387
109 rpm	500	215372	430.744	400.8442
136 rpm	500	215003	430.006	383.6453
161 rpm	500	214958	429.916	345.9769
188 rpm	500	215195	430.39	373.0239
214 rpm	500	214898	429.796	426.6517
238 rpm	500	214881	429.762	351.6527

ANOVA

Source of Variation	*SS*	*df*	*MS*	*F*	*P-value*	*F crit*
Between Groups	1340.507	6	223.4179	0.5934	0.735887	2.10118
Within Groups	1315131	3493	376.5048			
Total	1316472	3499				

rpm (motion & stationary)	**% error in counts**
109 and stationary	0.199
136 and stationary	0.370
161 and stationary	0.391
188 and stationary	0.281
214 and stationary	0.418
238 and stationary	**0.426**

Table A.44 ANOVA analysis and percentage error in mean counts at L_6 for Detector 4

SUMMARY

Groups	*Count*	*Sum*	*Average*	*Variance*
stationary	500	185928	371.856	323.9672
109 rpm	500	186880	373.76	315.7379
136 rpm	500	186321	372.642	337.4527
161 rpm	500	186051	372.102	346.4084
188 rpm	500	185630	371.26	329.0625
214 rpm	500	186220	372.44	324.5635
238 rpm	500	186125	372.25	328.0316

ANOVA

Source of Variation	*SS*	*df*	*MS*	*F*	*P-value*	*F crit*
Between Groups	1791.152	6	298.5253	0.906496	0.488999	2.10118
Within Groups	1150307	3493	329.3177			
Total	1152098	3499				

rpm (motion & stationary)	**% error in counts**
109 and stationary	**0.512**
136 and stationary	0.211
161 and stationary	0.066
188 and stationary	0.160
214 and stationary	0.157
238 and stationary	0.105

Table A.45 ANOVA analysis and percentage error in mean counts at L_6 for Detector 5

SUMMARY

Groups	*Count*	*Sum*	*Average*	*Variance*
stationary	500	212789	425.578	370.1001
109 rpm	500	212457	424.914	419.4776
136 rpm	500	211881	423.762	391.2839
161 rpm	500	211948	423.896	372.9751
188 rpm	500	211773	423.546	380.1362
214 rpm	500	212463	424.926	387.2911
238 rpm	500	211979	423.958	349.7918

ANOVA

Source of Variation	*SS*	*df*	*MS*	*F*	*P-value*	*F crit*
Between Groups	1753.691	6	292.2818	0.765979	0.596638	2.10118
Within Groups	1332857	3493	381.5794			
Total	1334611	3499				

rpm (motion & stationary)	**% error in counts**
109 and stationary	0.156
136 and stationary	0.426
161 and stationary	0.395
188 and stationary	**0.477**
214 and stationary	0.153
238 and stationary	0.380

Table A.46 ANOVA analysis and percentage error in mean counts at L_6 for Detector 6

SUMMARY

Groups	*Count*	*Sum*	*Average*	*Variance*
stationary	500	175548	351.096	336.0228
109 rpm	500	175708	351.416	354.4158
136 rpm	500	174925	349.85	292.741
161 rpm	500	175625	351.25	301.755
188 rpm	500	175640	351.28	292.5828
214 rpm	500	175488	350.976	325.8952
238 rpm	500	175984	351.968	292.4479

ANOVA

Source of Variation	*SS*	*df*	*MS*	*F*	*P-value*	*F crit*
Between Groups	1241.715	6	206.9525	0.659727	0.682309	2.10118
Within Groups	1095734	3493	313.6943			
Total	1096976	3499				

rpm (motion & stationary)	**% error in counts**
109 and stationary	0.091
136 and stationary	**0.354**
161 and stationary	0.043
188 and stationary	0.052
214 and stationary	0.034
238 and stationary	0.248

Table A.47 ANOVA analysis and percentage error in mean counts at L_6 for Detector 7

SUMMARY

Groups	*Count*	*Sum*	*Average*	*Variance*
stationary	500	274352	548.704	480.5094
109 rpm	500	273967	547.934	419.0237
136 rpm	500	274247	548.494	436.4829
161 rpm	500	273486	546.972	388.6365
188 rpm	500	274140	548.28	388.6148
214 rpm	500	273570	547.14	395.0986
238 rpm	500	274109	548.218	391.4213

ANOVA

Source of Variation	*SS*	*df*	*MS*	*F*	*P-value*	*F crit*
Between Groups	1328.403	6	221.4006	0.534454	0.782442	2.10118
Within Groups	1446994	3493	414.2553			
Total	1448322	3499				

rpm (motion & stationary)	**% error in counts**
109 and stationary	0.140
136 and stationary	0.038
161 and stationary	**0.315**
188 and stationary	0.077
214 and stationary	0.285
238 and stationary	0.088

Table A.48 ANOVA analysis and percentage error in mean counts at L_6 for Detector 8

SUMMARY

Groups	*Count*	*Sum*	*Average*	*Variance*
stationary	500	126763	253.526	214.0614
109 rpm	500	127080	254.16	236.6998
136 rpm	500	127188	254.376	221.9505
161 rpm	500	126294	252.588	242.375
188 rpm	500	126768	253.536	217.4516
214 rpm	500	126793	253.586	229.9385
238 rpm	500	127486	254.972	236.9251

ANOVA

Source of Variation	*SS*	*df*	*MS*	*F*	*P-value*	*F crit*
Between Groups	1745.755	6	290.9591	1.273422	0.265957	2.10118
Within Groups	798101.6	3493	228.486			
Total	799847.3	3499				

rpm (motion & stationary)	**% error in counts**
109 and stationary	0.250
136 and stationary	0.335
161 and stationary	0.369
188 and stationary	0.003
214 and stationary	0.023
238 and stationary	**0.570**

Table A.49 ANOVA analysis and percentage error in mean counts at L_7 for Detector 1

SUMMARY

Groups	*Count*	*Sum*	*Average*	*Variance*
stationary	500	115764	231.528	189.869
109 rpm	500	116378	232.756	224.7941
136 rpm	500	115705	231.41	193.4608
161 rpm	500	115543	231.086	219.3814
188 rpm	500	115609	231.218	228.3552
214 rpm	500	115025	230.05	220.5767
238 rpm	500	115217	230.434	222.4145

ANOVA

Source of Variation	*SS*	*df*	*MS*	*F*	*P-value*	*F crit*
Between Groups	2247.218	6	374.5363	1.749175	0.105647	2.10118
Within Groups	747926.9	3493	214.1216			
Total	750174.1	3499				

rpm (motion & stationary)	**% error in counts**
109 and stationary	0.530
136 and stationary	0.050
161 and stationary	0.190
188 and stationary	0.133
214 and stationary	**0.638**
238 and stationary	0.472

Table A.50 ANOVA analysis and percentage error in mean counts at L_7 for Detector 2

SUMMARY

Groups	*Count*	*Sum*	*Average*	*Variance*
stationary	500	226254	452.508	361.1522
109 rpm	500	227421	454.842	356.498
136 rpm	500	227233	454.466	370.8024
161 rpm	500	226156	452.312	385.5137
188 rpm	500	226567	453.134	387.6954
214 rpm	500	226557	453.114	386.7425
238 rpm	500	226444	452.888	373.1818

ANOVA

Source of Variation	*SS*	*df*	*MS*	*F*	*P-value*	*F crit*
Between Groups	2784.391	6	464.0651	1.239119	0.282814	2.10118
Within Groups	1308171	3493	374.5123			
Total	1310956	3499				

rpm (motion & stationary)	**% error in counts**
109 and stationary	**0.515**
136 and stationary	0.432
161 and stationary	0.043
188 and stationary	0.138
214 and stationary	0.133
238 and stationary	0.083

Table A.51 ANOVA analysis and percentage error in mean counts at L_7 for Detector 3

SUMMARY

Groups	*Count*	*Sum*	*Average*	*Variance*
stationary	500	88850	177.7	189.1283
109 rpm	500	88756	177.512	170.8075
136 rpm	500	88405	176.81	170.7314
161 rpm	500	88702	177.404	184.7783
188 rpm	500	88602	177.204	151.6898
214 rpm	500	88249	176.498	184.0701
238 rpm	500	88785	177.57	165.3638

ANOVA

Source of Variation	*SS*	*df*	*MS*	*F*	*P-value*	*F crit*
Between Groups	579.0469	6	96.50781	0.555295	0.766159	2.10118
Within Groups	607068	3493	173.7956			
Total	607647.1	3499				

rpm (motion & stationary)	**% error in counts**
109 and stationary	0.105
136 and stationary	0.500
161 and stationary	0.166
188 and stationary	0.279
214 and stationary	**0.676**
238 and stationary	0.073

Table A.52 ANOVA analysis and percentage error in mean counts at L_7 for Detector 4

SUMMARY

Groups	*Count*	*Sum*	*Average*	*Variance*
stationary	500	75273	150.546	137.2865
109 rpm	500	74220	148.44	151.0325
136 rpm	500	74519	149.038	159.6038
161 rpm	500	74493	148.986	144.3866
188 rpm	500	75128	150.256	138.4153
214 rpm	500	74679	149.358	148.8676
238 rpm	500	74794	149.588	131.4772

ANOVA

Source of Variation	*SS*	*df*	*MS*	*F*	*P-value*	*F crit*
Between Groups	1641.475	6	273.5792	1.894088	0.078072	2.10118
Within Groups	504523.6	3493	144.4385			
Total	506165.1	3499				

rpm (motion & stationary)	**% error in counts**
109 and stationary	**1.398**
136 and stationary	1.001
161 and stationary	1.036
188 and stationary	0.192
214 and stationary	0.781
238 and stationary	0.636

Table A.53 ANOVA analysis and percentage error in mean counts at L_7 for Detector 5

SUMMARY

Groups	*Count*	*Sum*	*Average*	*Variance*
stationary	500	194103	388.206	351.5667
109 rpm	500	194131	388.262	329.4523
136 rpm	500	192991	385.982	291.8534
161 rpm	500	193574	387.148	367.3568
188 rpm	500	193385	386.77	406.6023
214 rpm	500	192994	385.988	325.7313
238 rpm	500	192847	385.694	310.9422

ANOVA

Source of Variation	*SS*	*df*	*MS*	*F*	*P-value*	*F crit*
Between Groups	3379.53	6	563.255	1.654196	0.128201	2.10118
Within Groups	1189369	3493	340.5007			
Total	1192749	3499				

rpm (motion & stationary)	**% error in counts**
109 and stationary	0.014
136 and stationary	0.572
161 and stationary	0.272
188 and stationary	0.369
214 and stationary	0.571
238 and stationary	**0.647**

Table A.54: ANOVA analysis and percentage error in mean counts at L_7 for Detector 6

SUMMARY

Groups	*Count*	*Sum*	*Average*	*Variance*
stationary	500	152144	304.288	276.5381
109 rpm	500	151039	302.078	284.5731
136 rpm	500	151185	302.37	272.8708
161 rpm	500	151878	303.756	258.4814
188 rpm	500	151887	303.774	302.2554
214 rpm	500	151668	303.336	273.6304
238 rpm	500	151500	303	273.4589

ANOVA

Source of Variation	*SS*	*df*	*MS*	*F*	*P-value*	*F crit*
Between Groups	1911.403	6	318.5672	1.148399	0.331372	2.10118
Within Groups	968962.3	3493	277.4012			
Total	970873.7	3499				

rpm (motion & stationary)	**% error in counts**
109 and stationary	**0.726**
136 and stationary	0.630
161 and stationary	0.174
188 and stationary	0.168
214 and stationary	0.312
238 and stationary	0.423

Table A.55 ANOVA analysis and percentage error in mean counts at L_7 for Detector 7

SUMMARY

Groups	*Count*	*Sum*	*Average*	*Variance*
stationary	500	393622	787.244	512.1688
109 rpm	500	394182	788.364	555.6388
136 rpm	500	394148	788.296	533.5274
161 rpm	500	395152	790.304	526.0677
188 rpm	500	394569	789.138	483.4258
214 rpm	500	393047	786.094	480.9471
238 rpm	500	393651	787.302	516.8485

ANOVA

Source of Variation	*SS*	*df*	*MS*	*F*	*P-value*	*F crit*
Between Groups	5718.248	6	953.0413	1.848707	0.085905	2.10118
Within Groups	1800703	3493	515.5177			
Total	1806422	3499				

rpm (motion & stationary)	**% error in counts**
109 and stationary	0.142
136 and stationary	0.133
161 and stationary	**0.388**
188 and stationary	0.240
214 and stationary	0.146
238 and stationary	0.007

Table A.56 ANOVA analysis and percentage error in mean counts at L_7 for Detector 8

SUMMARY

Groups	*Count*	*Sum*	*Average*	*Variance*
stationary	500	306259	612.518	466.0217
109 rpm	500	306414	612.828	550.6838
136 rpm	500	307321	614.642	452.2864
161 rpm	500	306958	613.916	465.6843
188 rpm	500	306858	613.716	488.4282
214 rpm	500	307330	614.66	499.1868
238 rpm	500	307233	614.466	529.9047

ANOVA

Source of Variation	*SS*	*df*	*MS*	*F*	*P-value*	*F crit*
Between Groups	2248.947	6	374.8246	0.76003	0.601374	2.10118
Within Groups	1722646	3493	493.1708			
Total	1724895	3499				

rpm (motion & stationary)	**% error in counts**
109 and stationary	0.050
136 and stationary	**0.346**
161 and stationary	0.228
188 and stationary	0.195
214 and stationary	0.349
238 and stationary	0.318

Table A.57 ANOVA analysis and percentage error in mean counts at L_8 for Detector 1

SUMMARY

Groups	*Count*	*Sum*	*Average*	*Variance*
stationary	500	193772	387.544	352.6494
109 rpm	500	193022	386.044	360.3427
136 rpm	500	192635	385.27	347.6203
161 rpm	500	192705	385.41	347.0881
188 rpm	500	192510	385.02	355.8192
214 rpm	500	192754	385.508	355.6412
238 rpm	500	194411	388.822	7171.589

ANOVA

Source of Variation	*SS*	*df*	*MS*	*F*	*P-value*	*F crit*
Between Groups	6029.515	6	1004.919	0.757144	0.603675	2.10118
Within Groups	4636084	3493	1327.25			
Total	4642114	3499				

rpm (motion & stationary)	**% error in counts**
109 and stationary	0.401
136 and stationary	0.599
161 and stationary	0.618
188 and stationary	0.658
214 and stationary	0.584
238 and stationary	**0.668**

Table A.58 ANOVA analysis and percentage error in mean counts at L_8 for Detector 2

SUMMARY

Groups	*Count*	*Sum*	*Average*	*Variance*
stationary	500	277623	555.246	445.2239
109 rpm	500	276038	552.076	418.2587
136 rpm	500	277103	554.206	462.3443
161 rpm	500	277114	554.228	450.5772
188 rpm	500	276755	553.51	425.1923
214 rpm	500	276605	553.21	407.1282
238 rpm	500	279157	558.314	15081.95

ANOVA

Source of Variation	*SS*	*df*	*MS*	*F*	*P-value*	*F crit*
Between Groups	11855.75	6	1975.958	0.781864	0.584047	2.10118
Within Groups	8827645	3493	2527.239			
Total	8839501	3499				

rpm (motion & stationary)	**% error in counts**
109 and stationary	**0.610**
136 and stationary	0.217
161 and stationary	0.185
188 and stationary	0.313
214 and stationary	0.390
238 and stationary	0.433

Table A.59 ANOVA analysis and percentage error in mean counts at L_8 for Detector 3

SUMMARY

Groups	*Count*	*Sum*	*Average*	*Variance*
stationary	500	53634	107.268	90.45308
109 rpm	500	53607	107.214	107.0944
136 rpm	500	53931	107.862	108.7965
161 rpm	500	53859	107.718	116.279
188 rpm	500	53647	107.294	91.53063
214 rpm	500	53743	107.486	102.6952
238 rpm	500	54237	108.474	632.8029

ANOVA

Source of Variation	*SS*	*df*	*MS*	*F*	*P-value*	*F crit*
Between Groups	605.1869	6	100.8645	0.564998	0.758505	2.10118
Within Groups	623576.3	3493	178.5217			
Total	624181.4	3499				

rpm (motion & stationary)	**% error in counts**
109 and stationary	0.070
136 and stationary	**0.428**
161 and stationary	0.359
188 and stationary	0.020
214 and stationary	0.160
238 and stationary	0.160

Table A.60 ANOVA analysis and percentage error in mean counts at L_8 for Detector 4

SUMMARY

Groups	*Count*	*Sum*	*Average*	*Variance*
stationary	500	43420	86.84	85.53747
109 rpm	500	43705	87.41	80.83156
136 rpm	500	43493	86.986	81.44469
161 rpm	500	43554	87.108	85.39112
188 rpm	500	43548	87.096	80.86852
214 rpm	500	43853	87.706	79.9675
238 rpm	500	43909	87.818	412.8345

ANOVA

Source of Variation	*SS*	*df*	*MS*	*F*	*P-value*	*F crit*
Between Groups	415.6469	6	69.27448	0.534717	0.782239	2.10118
Within Groups	452530.8	3493	129.5536			
Total	452946.5	3499				

rpm (motion & stationary)	**% error in counts**
109 and stationary	0.601
136 and stationary	0.099
161 and stationary	0.301
188 and stationary	0.340
214 and stationary	**0.983**
238 and stationary	0.195

Table A.61 ANOVA analysis and percentage error in mean counts at L_8 for Detector 5

SUMMARY

Groups	*Count*	*Sum*	*Average*	*Variance*
stationary	500	93416	186.832	173.6631
109 rpm	500	93451	186.902	186.3331
136 rpm	500	93134	186.268	159.5914
161 rpm	500	92912	185.824	184.0531
188 rpm	500	93395	186.79	193.573
214 rpm	500	93681	187.362	156.1553
238 rpm	500	93774	187.548	1877.763

ANOVA

Source of Variation	*SS*	*df*	*MS*	*F*	*P-value*	*F crit*
Between Groups	1060.847	6	176.8078	0.422245	0.864643	2.10118
Within Groups	1462635	3493	418.7332			
Total	1463696	3499				

rpm (motion & stationary)	**% error in counts**
109 and stationary	0.108
136 and stationary	0.269
161 and stationary	0.489
188 and stationary	0.026
214 and stationary	0.350
238 and stationary	**0.519**

Table A.62 ANOVA analysis and percentage error in mean counts at L_8 for Detector 6

SUMMARY

Groups	*Count*	*Sum*	*Average*	*Variance*
stationary	500	72712	145.424	133.395
109 rpm	500	73331	146.662	132.2362
136 rpm	500	72621	145.242	135.5545
161 rpm	500	73142	146.284	137.4021
188 rpm	500	72636	145.272	131.9339
214 rpm	500	73188	146.376	125.7822
238 rpm	500	73611	147.222	1036.013

ANOVA

Source of Variation	*SS*	*df*	*MS*	*F*	*P-value*	*F crit*
Between Groups	1778.347	6	296.3912	1.132303	0.340598	2.10118
Within Groups	914326.1	3493	261.7595			
Total	916104.4	3499				

rpm (motion & stationary)	**% error in counts**
109 and stationary	**0.861**
136 and stationary	0.110
161 and stationary	0.693
188 and stationary	0.009
214 and stationary	0.694
238 and stationary	0.372

Table A.63 ANOVA analysis and percentage error in mean counts at L_8 for Detector 7

SUMMARY

Groups	*Count*	*Sum*	*Average*	*Variance*
stationary	500	367431	734.862	720.039
109 rpm	500	365868	731.736	788.2708
136 rpm	500	366621	733.242	785.4584
161 rpm	500	367266	734.532	742.2936
188 rpm	500	366766	733.532	830.0771
214 rpm	500	366767	733.534	696.1532
238 rpm	500	371237	742.474	26487.66

ANOVA

Source of Variation	*SS*	*df*	*MS*	*F*	*P-value*	*F crit*
Between Groups	36989.04	6	6164.84	1.389821	0.214657	2.10118
Within Groups	15493924	3493	4435.707			
Total	15530913	3499				

rpm (motion & stationary)	**% error in counts**
109 and stationary	**0.386**
136 and stationary	0.206
161 and stationary	0.003
188 and stationary	0.130
214 and stationary	0.124
238 and stationary	0.104

Table A.64 ANOVA analysis and percentage error in mean counts at L_8 for Detector 8

SUMMARY

Groups	*Count*	*Sum*	*Average*	*Variance*
stationary	500	504085	1008.17	590.7586
109 rpm	500	503485	1006.97	598.5542
136 rpm	500	502662	1005.324	569.8026
161 rpm	500	502312	1004.624	572.5477
188 rpm	500	503260	1006.52	588.9515
214 rpm	500	503391	1006.782	568.0265
238 rpm	500	508625	1017.25	52221.57

ANOVA

Source of Variation	*SS*	*df*	*MS*	*F*	*P-value*	*F crit*
Between Groups	54433.03	6	9072.172	1.13992	0.336209	2.10118
Within Groups	27799396	3493	7958.602			
Total	27853829	3499				

rpm (motion & stationary)	**% error in counts**
109 and stationary	0.106
136 and stationary	0.270
161 and stationary	**0.349**
188 and stationary	0.148
214 and stationary	0.139
238 and stationary	0.094

Table A.65 ANOVA analysis and percentage error in mean counts at L_9 for Detector 1

SUMMARY

Groups	*Count*	*Sum*	*Average*	*Variance*
stationary	500	143396	286.792	262.3935
109 rpm	500	142400	284.8	245.9559
136 rpm	500	142489	284.978	246.6107
161 rpm	500	142227	284.454	250.0079
188 rpm	500	143000	286	262.9419
214 rpm	500	142850	285.7	270.8878
238 rpm	500	142661	285.322	261.9141

ANOVA

Source of Variation	*SS*	*df*	*MS*	*F*	*P-value*	*F crit*
Between Groups	1909.051	6	318.1752	1.236859	0.283953	2.10118
Within Groups	898555.2	3493	257.2446			
Total	900464.3	3499				

rpm (motion & stationary)	**% error in counts**
109 and stationary	0.694
136 and stationary	0.632
161 and stationary	**0.815**
188 and stationary	0.276
214 and stationary	0.380
238 and stationary	0.512

Table A.66 ANOVA analysis and percentage error in mean counts at L_9 for Detector 2

SUMMARY

Groups	*Count*	*Sum*	*Average*	*Variance*
stationary	500	251624	503.248	393.9063
109 rpm	500	251067	502.134	438.4409
136 rpm	500	251522	503.044	422.1744
161 rpm	500	250152	500.304	436.4886
188 rpm	500	250789	501.578	433.3226
214 rpm	500	251645	503.29	406.535
238 rpm	500	250849	501.698	418.7202

ANOVA

Source of Variation	*SS*	*df*	*MS*	*F*	*P-value*	*F crit*
Between Groups	3617.627	6	602.9379	1.4309	0.198627	2.10118
Within Groups	1471844	3493	421.3697			
Total	1475462	3499				

rpm (motion & stationary)	**% error in counts**
109 and stationary	0.221
136 and stationary	0.040
161 and stationary	**0.584**
188 and stationary	0.331
214 and stationary	0.008
238 and stationary	0.307

Table A.67 ANOVA analysis and percentage error in mean counts at L_9 for Detector 3

SUMMARY

Groups	*Count*	*Sum*	*Average*	*Variance*
stationary	500	89808	179.616	170.1769
109 rpm	500	89245	178.49	162.1662
136 rpm	500	89770	179.54	182.9102
161 rpm	500	89496	178.992	187.4508
188 rpm	500	89797	179.594	158.422
214 rpm	500	90112	180.224	164.4267
238 rpm	500	89504	179.008	146.529

ANOVA

Source of Variation	*SS*	*df*	*MS*	*F*	*P-value*	*F crit*
Between Groups	957.484	6	159.5807	0.95306	0.455632	2.10118
Within Groups	584868.9	3493	167.4403			
Total	585826.3	3499				

rpm (motion & stationary)	**% error in counts**
109 and stationary	**0.626**
136 and stationary	0.042
161 and stationary	0.347
188 and stationary	0.012
214 and stationary	0.338
238 and stationary	0.338

Table A.68 ANOVA analysis and percentage error in mean counts at L_9 for Detector 4

SUMMARY

Groups	*Count*	*Sum*	*Average*	*Variance*
stationary	500	52177	104.354	93.49568
109 rpm	500	52632	105.264	95.66163
136 rpm	500	52446	104.892	95.98831
161 rpm	500	52196	104.392	95.39713
188 rpm	500	52754	105.508	111.3687
214 rpm	500	52383	104.766	99.879
238 rpm	500	52222	104.444	94.91269

ANOVA

Source of Variation	*SS*	*df*	*MS*	*F*	*P-value*	*F crit*
Between Groups	609.1194	6	101.5199	1.034857	0.400387	2.10118
Within Groups	342664.9	3493	98.10044			
Total	343274	3499				

rpm (motion & stationary)	**% error in counts**
109 and stationary	0.872
136 and stationary	0.515
161 and stationary	0.036
188 and stationary	**1.105**
214 and stationary	0.394
238 and stationary	0.086

Table A.69 ANOVA analysis and percentage error in mean counts at L_9 for Detector 5

SUMMARY

Groups	*Count*	*Sum*	*Average*	*Variance*
stationary	500	148851	297.702	237.8649
109 rpm	500	148804	297.608	265.0284
136 rpm	500	148853	297.706	270.3683
161 rpm	500	149321	298.642	248.3626
188 rpm	500	148814	297.628	267.5728
214 rpm	500	149184	298.368	270.2531
238 rpm	500	149094	298.188	250.0888

ANOVA

Source of Variation	*SS*	*df*	*MS*	*F*	*P-value*	*F crit*
Between Groups	523.3269	6	87.22114	0.337405	0.917385	2.10118
Within Groups	902959.9	3493	258.5056			
Total	903483.2	3499				

rpm (motion & stationary)	**% error in counts**
109 and stationary	0.031
136 and stationary	0.001
161 and stationary	**0.315**
188 and stationary	0.024
214 and stationary	0.223
238 and stationary	0.163

Table A.70 ANOVA analysis and percentage error in mean counts at L_9 for Detector 6

SUMMARY

Groups	*Count*	*Sum*	*Average*	*Variance*
stationary	500	111831	223.662	208.0639
109 rpm	500	111133	222.266	204.7608
136 rpm	500	111609	223.218	223.77
161 rpm	500	111896	223.792	197.8605
188 rpm	500	111804	223.608	218.6637
214 rpm	500	111480	222.96	227.5375
238 rpm	500	111959	223.918	209.35

ANOVA

Source of Variation	*SS*	*df*	*MS*	*F*	*P-value*	*F crit*
Between Groups	1013.19	6	168.865	0.793322	0.575019	2.10118
Within Groups	743513.1	3493	212.858			
Total	744526.3	3499				

rpm (motion & stationary)	**% error in counts**
109 and stationary	**0.624**
136 and stationary	0.198
161 and stationary	0.058
188 and stationary	0.024
214 and stationary	0.313
238 and stationary	0.114

Table A.71 ANOVA analysis and percentage error in mean counts at L_9 for Detector 7

SUMMARY

Groups	*Count*	*Sum*	*Average*	*Variance*
stationary	500	383144	766.288	452.4459
109 rpm	500	381728	763.456	495.0943
136 rpm	500	383361	766.722	563.8003
161 rpm	500	382259	764.518	447.4045
188 rpm	500	381937	763.874	511.3608
214 rpm	500	382786	765.572	448.1772
238 rpm	500	382107	764.214	462.3289

ANOVA

Source of Variation	*SS*	*df*	*MS*	*F*	*P-value*	*F crit*
Between Groups	4717.619	6	786.2699	1.628075	0.135112	2.10118
Within Groups	1686925	3493	482.9446			
Total	1691643	3499				

rpm (motion & stationary)	**% error in counts**
109 and stationary	**0.369**
136 and stationary	0.056
161 and stationary	0.230
188 and stationary	0.315
214 and stationary	0.093
238 and stationary	0.270

Table A.72 ANOVA analysis and percentage error in mean counts at L_9 for Detector 8

SUMMARY

Groups	*Count*	*Sum*	*Average*	*Variance*
stationary	500	310680	621.36	417.9383
109 rpm	500	310142	620.284	470.845
136 rpm	500	309864	619.728	483.3487
161 rpm	500	309470	618.94	471.3351
188 rpm	500	310057	620.114	499.9168
214 rpm	500	310334	620.668	514.9918
238 rpm	500	309458	618.916	465.548

ANOVA

Source of Variation	*SS*	*df*	*MS*	*F*	*P-value*	*F crit*
Between Groups	2381.051	6	396.8418	0.835727	0.542066	2.10118
Within Groups	1658638	3493	474.8462			
Total	1661019	3499				

rpm (motion & stationary)	**% error in counts**
109 and stationary	0.173
136 and stationary	0.262
161 and stationary	0.389
188 and stationary	0.200
214 and stationary	0.111
238 and stationary	**0.393**

Table A.73 ANOVA analysis and percentage error in mean counts at L_{10} for Detector 1

SUMMARY

Groups	*Count*	*Sum*	*Average*	*Variance*
stationary	500	269945	539.89	417.2845
109 rpm	500	270166	540.332	436.8354
136 rpm	500	268790	537.58	447.1539
161 rpm	500	269789	539.578	421.9879
188 rpm	500	269706	539.412	467.6415
214 rpm	500	269836	539.672	456.3852
238 rpm	500	269632	539.264	461.4973

ANOVA

Source of Variation	*SS*	*df*	*MS*	*F*	*P-value*	*F crit*
Between Groups	2272.346	6	378.7243	0.852767	0.529051	2.10118
Within Groups	1551284	3493	444.1122			
Total	1553556	3499				

rpm (motion & stationary)	**% error in counts**
109 and stationary	0.081
136 and stationary	**0.427**
161 and stationary	0.057
188 and stationary	0.088
214 and stationary	0.040
238 and stationary	0.115

Table A.74 ANOVA analysis and percentage error in mean counts at L_{10} for Detector 2

SUMMARY

Groups	*Count*	*Sum*	*Average*	*Variance*
stationary	500	361999	723.998	554.9118
109 rpm	500	361412	722.824	479.5802
136 rpm	500	360337	720.674	515.627
161 rpm	500	361546	723.092	567.6027
188 rpm	500	360513	721.026	542.7789
214 rpm	500	361603	723.206	560.2761
238 rpm	500	361183	722.366	440.99

ANOVA

Source of Variation	*SS*	*df*	*MS*	*F*	*P-value*	*F crit*
Between Groups	4354.351	6	725.7252	1.387329	0.215663	2.10118
Within Groups	1827222	3493	523.1095			
Total	1831576	3499				

rpm (motion & stationary)	**% error in counts**
109 and stationary	0.162
136 and stationary	**0.459**
161 and stationary	0.125
188 and stationary	0.410
214 and stationary	0.103
238 and stationary	0.225

Table A.75 ANOVA analysis and percentage error in mean counts at L_{10} for Detector 3

SUMMARY

Groups	*Count*	*Sum*	*Average*	*Variance*
stationary	500	164475	328.95	289.27
109 rpm	500	164008	328.016	332.4005
136 rpm	500	164009	328.018	314.6069
161 rpm	500	164076	328.152	304.8386
188 rpm	500	164320	328.64	319.5174
214 rpm	500	164569	329.138	295.2014
238 rpm	500	163837	327.674	321.0578

ANOVA

Source of Variation	*SS*	*df*	*MS*	*F*	*P-value*	*F crit*
Between Groups	890.1417	6	148.357	0.477056	0.82586	2.10118
Within Groups	1086269	3493	310.9847			
Total	1087160	3499				

rpm (motion & stationary)	**% error in counts**
109 and stationary	0.283
136 and stationary	0.283
161 and stationary	0.242
188 and stationary	0.094
214 and stationary	0.057
238 and stationary	**0.387**

Table A.76 ANOVA analysis and percentage error in mean counts at L_{10} for Detector 4

SUMMARY

Groups	*Count*	*Sum*	*Average*	*Variance*
stationary	500	120922	241.844	219.9916
109 rpm	500	120349	240.698	213.2132
136 rpm	500	120254	240.508	217.9699
161 rpm	500	120744	241.488	215.2524
188 rpm	500	120883	241.766	238.0714
214 rpm	500	120844	241.688	204.5037
238 rpm	500	120552	241.104	236.3058

ANOVA

Source of Variation	*SS*	*df*	*MS*	*F*	*P-value*	*F crit*
Between Groups	863.5309	6	143.9218	0.651943	0.688624	2.10118
Within Groups	771108.7	3493	220.7583			
Total	771972.2	3499				

rpm (motion & stationary)	**% error in counts**
109 and stationary	0.473
136 and stationary	**0.552**
161 and stationary	0.147
188 and stationary	0.032
214 and stationary	0.064
238 and stationary	0.305

Table A.77 ANOVA analysis and percentage error in mean counts at L_{10} for Detector 5

SUMMARY

Groups	*Count*	*Sum*	*Average*	*Variance*
stationary	500	82345	164.69	158.042
109 rpm	500	82079	164.158	150.8307
136 rpm	500	81953	163.906	155.0753
161 rpm	500	81938	163.876	152.2732
188 rpm	500	82189	164.378	169.7747
214 rpm	500	81993	163.986	136.078
238 rpm	500	82016	164.032	157.3577

ANOVA

Source of Variation	*SS*	*df*	*MS*	*F*	*P-value*	*F crit*
Between Groups	259.4989	6	43.24981	0.28047	0.946397	2.10118
Within Groups	538636.3	3493	154.2045			
Total	538895.8	3499				

rpm (motion & stationary)	**% error in counts**
109 and stationary	0.323
136 and stationary	0.476
161 and stationary	**0.494**
188 and stationary	0.189
214 and stationary	0.427
238 and stationary	0.399

Table A.78 ANOVA analysis and percentage error in mean counts at L_{10} for Detector 6

SUMMARY

Groups	*Count*	*Sum*	*Average*	*Variance*
stationary	500	51466	102.932	97.62663
109 rpm	500	51037	102.074	103.1909
136 rpm	500	51141	102.282	105.261
161 rpm	500	51362	102.724	107.4106
188 rpm	500	51406	102.812	105.2111
214 rpm	500	50962	101.924	103.0884
238 rpm	500	50965	101.93	106.9951

ANOVA

Source of Variation	*SS*	*df*	*MS*	*F*	*P-value*	*F crit*
Between Groups	561.6469	6	93.60781	0.899107	0.494413	2.10118
Within Groups	363663.1	3493	104.112			
Total	364224.7	3499				

rpm (motion & stationary)	**% error in counts**
109 and stationary	0.833
136 and stationary	0.631
161 and stationary	0.202
188 and stationary	0.116
214 and stationary	**0.979**
238 and stationary	0.973

Table A.79 ANOVA analysis and percentage error in mean counts at L_{10} for Detector 7

SUMMARY

Groups	*Count*	*Sum*	*Average*	*Variance*
stationary	500	282694	565.388	341.8171
109 rpm	500	283780	567.56	369.1046
136 rpm	500	283200	566.4	408.6132
161 rpm	500	283728	567.456	418.1243
188 rpm	500	282438	564.876	413.1028
214 rpm	500	283080	566.16	399.798
238 rpm	500	282790	565.58	419.9956

ANOVA

Source of Variation	*SS*	*df*	*MS*	*F*	*P-value*	*F crit*
Between Groups	3132.699	6	522.1166	1.319164	0.24473	2.10118
Within Groups	1382507	3493	395.7937			
Total	1385640	3499				

rpm (motion & stationary)	**% error in counts**
109 and stationary	**0.384**
136 and stationary	0.178
161 and stationary	0.365
188 and stationary	0.090
214 and stationary	0.136
238 and stationary	0.033

Table A.80 ANOVA analysis and percentage error in mean counts at L_{10} for Detector 8

SUMMARY

Groups	*Count*	*Sum*	*Average*	*Variance*
stationary	500	156345	312.69	287.04
109 rpm	500	156411	312.822	294.4673
136 rpm	500	155951	311.902	311.1988
161 rpm	500	156393	312.786	266.0202
188 rpm	500	156237	312.474	299.2438
214 rpm	500	155772	311.544	288.7776
238 rpm	500	156217	312.434	303.0437

ANOVA

Source of Variation	*SS*	*df*	*MS*	*F*	*P-value*	*F crit*
Between Groups	697.7114	6	116.2852	0.397112	0.881301	2.10118
Within Groups	1022846	3493	292.8273			
Total	1023544	3499				

rpm (motion & stationary)	**% error in counts**
109 and stationary	0.042
136 and stationary	0.252
161 and stationary	0.030
188 and stationary	0.069
214 and stationary	**0.366**
238 and stationary	0.081

Table A.81 ANOVA analysis and percentage error in mean counts at L_{11} for Detector 1

SUMMARY

Groups	*Count*	*Sum*	*Average*	*Variance*
stationary	500	352172	704.344	643.3564
109 rpm	500	352727	705.454	612.1602
136 rpm	500	353422	706.844	594.0558
161 rpm	500	353202	706.404	561.3795
188 rpm	500	353336	706.672	584.1086
214 rpm	500	353039	706.078	630.8897
238 rpm	500	352970	705.94	550.9583

ANOVA

Source of Variation	*SS*	*df*	*MS*	*F*	*P-value*	*F crit*
Between Groups	2183.658	6	363.943	0.609925	0.722611	2.10118
Within Groups	2084277	3493	596.7012			
Total	2086461	3499				

rpm (motion & stationary)	**% error in counts**
109 and stationary	0.157
136 and stationary	**0.354**
161 and stationary	0.292
188 and stationary	0.330
214 and stationary	0.246
238 and stationary	0.226

Table A.82 ANOVA analysis and percentage error in mean counts at L_{11} for Detector 2

SUMMARY

Groups	*Count*	*Sum*	*Average*	*Variance*
stationary	500	380357	760.714	531.2226
109 rpm	500	380619	761.238	480.1978
136 rpm	500	380492	760.984	533.0539
161 rpm	500	381417	762.834	490.8161
188 rpm	500	380994	761.988	504.2203
214 rpm	500	380861	761.722	474.2252
238 rpm	500	380399	760.798	518.6906

ANOVA

Source of Variation	*SS*	*df*	*MS*	*F*	*P-value*	*F crit*
Between Groups	1752.722	6	292.1203	0.578877	0.747489	2.10118
Within Groups	1762681	3493	504.6323			
Total	1764433	3499				

rpm (motion & stationary)	**% error in counts**
109 and stationary	0.068
136 and stationary	0.035
161 and stationary	**0.278**
188 and stationary	0.167
214 and stationary	0.132
238 and stationary	0.011

Table A.83 ANOVA analysis and percentage error in mean counts at L_{11} for Detector 3

SUMMARY

Groups	*Count*	*Sum*	*Average*	*Variance*
stationary	500	147949	295.898	278.9936
109 rpm	500	148243	296.486	243.4647
136 rpm	500	148776	297.552	269.859
161 rpm	500	147999	295.998	272.6393
188 rpm	500	148492	296.984	299.9036
214 rpm	500	147748	295.496	305.2004
238 rpm	500	148422	296.844	267.8834

ANOVA

Source of Variation	*SS*	*df*	*MS*	*F*	*P-value*	*F crit*
Between Groups	1536.775	6	256.1291	0.925158	0.475468	2.10118
Within Groups	967034	3493	276.8491			
Total	968570.8	3499				

rpm (motion & stationary)	**% error in counts**
109 and stationary	0.198
136 and stationary	**0.558**
161 and stationary	0.033
188 and stationary	0.367
214 and stationary	0.135
238 and stationary	0.319

Table A.84 ANOVA analysis and percentage error in mean counts at L_{11} for Detector 4

SUMMARY

Groups	*Count*	*Sum*	*Average*	*Variance*
stationary	500	102731	205.462	197.3272
109 rpm	500	102565	205.13	175.929
136 rpm	500	102469	204.938	211.1284
161 rpm	500	102194	204.388	174.7991
188 rpm	500	102568	205.136	185.3362
214 rpm	500	102690	205.38	175.7391
238 rpm	500	102746	205.492	178.01

ANOVA

Source of Variation	*SS*	*df*	*MS*	*F*	*P-value*	*F crit*
Between Groups	445.5977	6	74.26629	0.400429	0.879149	2.10118
Within Groups	647836.2	3493	185.467			
Total	648281.8	3499				

rpm (motion & stationary)	**% error in counts**
109 and stationary	0.161
136 and stationary	0.255
161 and stationary	**0.522**
188 and stationary	0.158
214 and stationary	0.039
238 and stationary	0.014

Table A.85 ANOVA analysis and percentage error in mean counts at L_{11} for Detector 5

SUMMARY

Groups	*Count*	*Sum*	*Average*	*Variance*
stationary	500	62875	125.75	116.7169
109 rpm	500	62182	124.364	120.4805
136 rpm	500	62350	124.7	114.0782
161 rpm	500	62793	125.586	115.1569
188 rpm	500	62584	125.168	124.0679
214 rpm	500	62941	125.882	126.2927
238 rpm	500	63102	126.204	121.7339

ANOVA

Source of Variation	*SS*	*df*	*MS*	*F*	*P-value*	*F crit*
Between Groups	1324.955	6	220.8259	1.843449	0.086857	2.10118
Within Groups	418424.9	3493	119.7896			
Total	419749.9	3499				

rpm (motion & stationary)	**% error in counts**
109 and stationary	**1.102**
136 and stationary	0.834
161 and stationary	0.130
188 and stationary	0.462
214 and stationary	0.104
238 and stationary	0.361

Table A.86 ANOVA analysis and percentage error in mean counts at L_{11} for Detector 6

SUMMARY

Groups	*Count*	*Sum*	*Average*	*Variance*
stationary	500	34764	69.528	69.7928
109 rpm	500	34673	69.346	72.13455
136 rpm	500	34537	69.074	67.34722
161 rpm	500	34519	69.038	67.40336
188 rpm	500	34865	69.73	70.51814
214 rpm	500	34468	68.936	67.6993
238 rpm	500	34490	68.98	67.10581

ANOVA

Source of Variation	*SS*	*df*	*MS*	*F*	*P-value*	*F crit*
Between Groups	281.1634	6	46.86057	0.680546	0.665414	2.10118
Within Groups	240518.6	3493	68.85731			
Total	240799.8	3499				

rpm (motion & stationary)	**% error in counts**
109 and stationary	0.261
136 and stationary	0.652
161 and stationary	0.704
188 and stationary	0.290
214 and stationary	**0.851**
238 and stationary	0.788

Table A.87 ANOVA analysis and percentage error in mean counts at L_{11} for Detector 7

SUMMARY

Groups	*Count*	*Sum*	*Average*	*Variance*
stationary	500	260975	521.95	395.8712
109 rpm	500	261140	522.28	431.1599
136 rpm	500	260547	521.094	370.899
161 rpm	500	260250	520.5	399.02
188 rpm	500	260886	521.772	439.3788
214 rpm	500	260670	521.34	413.0826
238 rpm	500	260635	521.27	396.6785

ANOVA

Source of Variation	*SS*	*df*	*MS*	*F*	*P-value*	*F crit*
Between Groups	1057.936	6	176.3227	0.433668	0.856821	2.10118
Within Groups	1420199	3493	406.5843			
Total	1421257	3499				

rpm (motion & stationary)	**% error in counts**
109 and stationary	0.063
136 and stationary	0.166
161 and stationary	**0.277**
188 and stationary	0.034
214 and stationary	0.116
238 and stationary	0.130

Table A.88 ANOVA analysis and percentage error in mean counts at L_{11} for Detector 8

SUMMARY

Groups	*Count*	*Sum*	*Average*	*Variance*
stationary	500	155580	311.16	259.5976
109 rpm	500	154858	309.716	297.1697
136 rpm	500	155060	310.12	264.8112
161 rpm	500	155081	310.162	291.2342
188 rpm	500	155205	310.41	283.7855
214 rpm	500	154380	308.76	282.8842
238 rpm	500	154672	309.344	273.9696

ANOVA

Source of Variation	*SS*	*df*	*MS*	*F*	*P-value*	*F crit*
Between Groups	1793.783	6	298.9639	1.071307	0.377237	2.10118
Within Groups	974772.5	3493	279.0646			
Total	976566.3	3499				

rpm (motion & stationary)	**% error in counts**
109 and stationary	0.464
136 and stationary	0.334
161 and stationary	0.320
188 and stationary	0.241
214 and stationary	**0.771**
238 and stationary	0.583

Table A.89 ANOVA analysis and percentage error in mean counts at L_{12} for Detector 1

SUMMARY

Groups	*Count*	*Sum*	*Average*	*Variance*
stationary	500	64155	128.31	112.8035
109 rpm	500	64363	128.726	119.8306
136 rpm	500	64559	129.118	122.8458
161 rpm	500	64575	129.15	111.1177
188 rpm	500	64438	128.876	130.9505
214 rpm	500	64315	128.63	123.5201
238 rpm	500	64502	129.004	125.0661

ANOVA

Source of Variation	*SS*	*df*	*MS*	*F*	*P-value*	*F crit*
Between Groups	269.4749	6	44.91248	0.371557	0.897386	2.10118
Within Groups	422221.1	3493	120.8763			
Total	422490.5	3499				

rpm (motion & stationary)	**% error in counts**
109 and stationary	0.324
136 and stationary	0.629
161 and stationary	**0.654**
188 and stationary	0.441
214 and stationary	0.249
238 and stationary	0.540

Table A.90 ANOVA analysis and percentage error in mean counts at L_{12} for Detector 2

SUMMARY

Groups	*Count*	*Sum*	*Average*	*Variance*
stationary	500	141158	282.316	231.8438
109 rpm	500	140916	281.832	261.5549
136 rpm	500	141676	283.352	251.932
161 rpm	500	141164	282.328	269.8882
188 rpm	500	140712	281.424	231.1946
214 rpm	500	140729	281.458	241.5032
238 rpm	500	140854	281.708	235.0047

ANOVA

Source of Variation	*SS*	*df*	*MS*	*F*	*P-value*	*F crit*
Between Groups	1374.706	6	229.1176	0.930874	0.471365	2.10118
Within Groups	859737.8	3493	246.1316			
Total	861112.5	3499				

rpm (motion & stationary)	**% error in counts**
109 and stationary	0.171
136 and stationary	**0.366**
161 and stationary	0.004
188 and stationary	0.315
214 and stationary	0.303
238 and stationary	0.215

Table A.91 ANOVA analysis and percentage error in mean counts at L_{12} for Detector 3

SUMMARY

Groups	*Count*	*Sum*	*Average*	*Variance*
stationary	500	191893	383.786	342.8138
109 rpm	500	192162	384.324	349.5702
136 rpm	500	191806	383.612	351.3642
161 rpm	500	192116	384.232	345.433
188 rpm	500	192189	384.378	346.5322
214 rpm	500	191713	383.426	317.0987
238 rpm	500	191838	383.676	304.4118

ANOVA

Source of Variation	*SS*	*df*	*MS*	*F*	*P-value*	*F crit*
Between Groups	443.3554	6	73.89257	0.219431	0.970707	2.10118
Within Groups	1176255	3493	336.7463			
Total	1176698	3499				

rpm (motion & stationary)	**% error in counts**
109 and stationary	0.140
136 and stationary	0.045
161 and stationary	0.116
188 and stationary	**0.154**
214 and stationary	0.093
238 and stationary	0.028

Table A.92 ANOVA analysis and percentage error in mean counts at L_{12} for Detector 4

SUMMARY

Groups	*Count*	*Sum*	*Average*	*Variance*
stationary	500	134495	268.99	223.5209
109 rpm	500	134758	269.516	267.4246
136 rpm	500	134706	269.412	251.9542
161 rpm	500	134722	269.444	246.7564
188 rpm	500	134450	268.9	242.7395
214 rpm	500	134558	269.116	225.4294
238 rpm	500	134276	268.552	243.9191

ANOVA

Source of Variation	*SS*	*df*	*MS*	*F*	*P-value*	*F crit*
Between Groups	366.9194	6	61.15324	0.251549	0.958839	2.10118
Within Groups	849170.3	3493	243.1063			
Total	849537.2	3499				

rpm (motion & stationary)	**% error in counts**
109 and stationary	**0.195**
136 and stationary	0.156
161 and stationary	0.168
188 and stationary	0.033
214 and stationary	0.046
238 and stationary	0.162

Table A.93 ANOVA analysis and percentage error in mean counts at L_{12} for Detector 5

SUMMARY

Groups	*Count*	*Sum*	*Average*	*Variance*
stationary	500	363569	727.138	502.8527
109 rpm	500	363639	727.278	524.5779
136 rpm	500	363839	727.678	546.0865
161 rpm	500	364132	728.264	521.9141
188 rpm	500	365128	730.256	553.8502
214 rpm	500	364106	728.212	594.5241
238 rpm	500	363705	727.41	504.038

ANOVA

Source of Variation	*SS*	*df*	*MS*	*F*	*P-value*	*F crit*
Between Groups	3456.166	6	576.0276	1.07587	0.374405	2.10118
Within Groups	1870174	3493	535.4062			
Total	1873630	3499				

rpm (motion & stationary)	**% error in counts**
109 and stationary	0.019
136 and stationary	0.074
161 and stationary	0.154
188 and stationary	**0.428**
214 and stationary	0.147
238 and stationary	0.037

Table A.94 ANOVA analysis and percentage error in mean counts at L_{12} for Detector 6

SUMMARY

Groups	*Count*	*Sum*	*Average*	*Variance*
stationary	500	221188	442.376	390.0587
109 rpm	500	220590	441.18	349.2461
136 rpm	500	221953	443.906	390.9871
161 rpm	500	221258	442.516	387.5488
188 rpm	500	220761	441.522	401.9815
214 rpm	500	221524	443.048	374.5147
238 rpm	500	221393	442.786	520.9902

ANOVA

Source of Variation	*SS*	*df*	*MS*	*F*	*P-value*	*F crit*
Between Groups	2534.758	6	422.4596	1.050399	0.390402	2.10118
Within Groups	1404848	3493	402.1896			
Total	1407383	3499				

rpm (motion & stationary)	**% error in counts**
109 and stationary	0.270
136 and stationary	**0.345**
161 and stationary	0.031
188 and stationary	0.193
214 and stationary	0.151
238 and stationary	0.092

Table A.95 ANOVA analysis and percentage error in mean counts at L_{12} for Detector 7

SUMMARY

Groups	*Count*	*Sum*	*Average*	*Variance*
stationary	500	239591	479.182	393.2594
109 rpm	500	238704	477.408	324.8713
136 rpm	500	238764	477.528	376.6706
161 rpm	500	239458	478.916	340.9428
188 rpm	500	238603	477.206	373.3743
214 rpm	500	238855	477.71	365.06
238 rpm	500	238418	476.836	359.7847

ANOVA

Source of Variation	*SS*	*df*	*MS*	*F*	*P-value*	*F crit*
Between Groups	2334.159	6	389.0265	1.074674	0.375146	2.10118
Within Groups	1264448	3493	361.9947			
Total	1266782	3499				

rpm (motion & stationary)	**% error in counts**
109 and stationary	0.370
136 and stationary	0.345
161 and stationary	0.055
188 and stationary	0.412
214 and stationary	0.307
238 and stationary	**0.489**

Table A.96 ANOVA analysis and percentage error in mean counts at L_{12} for Detector 8

SUMMARY

Groups	*Count*	*Sum*	*Average*	*Variance*
stationary	500	121634	243.268	202.3489
109 rpm	500	120908	241.816	222.9801
136 rpm	500	122107	244.214	226.5012
161 rpm	500	121365	242.73	191.5322
188 rpm	500	121673	243.346	257.3891
214 rpm	500	121215	242.43	236.7586
238 rpm	500	121496	242.992	216.2725

ANOVA

Source of Variation	*SS*	*df*	*MS*	*F*	*P-value*	*F crit*
Between Groups	1729.555	6	288.2592	1.298647	0.254077	2.10118
Within Groups	775337.5	3493	221.9689			
Total	777067	3499				

rpm (motion & stationary)	**% error in counts**
109 and stationary	**0.596**
136 and stationary	0.388
161 and stationary	0.221
188 and stationary	0.032
214 and stationary	0.344
238 and stationary	0.113

Table A.97 ANOVA analysis and percentage error in mean counts at L_{13} for Detector 1

SUMMARY

Groups	*Count*	*Sum*	*Average*	*Variance*
stationary	500	338277	676.554	1084.56
109 rpm	500	337976	675.952	1083.348
136 rpm	500	338715	677.43	1174.502
161 rpm	500	337831	675.662	1155.266
188 rpm	500	338133	676.266	1110.496
214 rpm	500	338439	676.878	1090.925
238 rpm	500	338679	677.358	1149.1

ANOVA

Source of Variation	*SS*	*df*	*MS*	*F*	*P-value*	*F crit*
Between Groups	1376.37	6	229.395	0.204603	0.975474	2.10118
Within Groups	3916251	3493	1121.171			
Total	3917627	3499				

rpm (motion & stationary)	**% error in counts**
109 and stationary	0.088
136 and stationary	0.129
161 and stationary	**0.131**
188 and stationary	0.042
214 and stationary	0.047
238 and stationary	0.118

Table A.98 ANOVA analysis and percentage error in mean counts at L_{13} for Detector 2

SUMMARY

Groups	*Count*	*Sum*	*Average*	*Variance*
stationary	500	320789	641.578	569.6632
109 rpm	500	320971	641.942	596.2992
136 rpm	500	320811	641.622	573.0933
161 rpm	500	320939	641.878	577.0412
188 rpm	500	321216	642.432	594.2619
214 rpm	500	320717	641.434	624.5267
238 rpm	500	320222	640.444	593.2173

ANOVA

Source of Variation	*SS*	*df*	*MS*	*F*	*P-value*	*F crit*
Between Groups	1124.459	6	187.4098	0.31779	0.928023	2.10118
Within Groups	2059923	3493	589.729			
Total	2061048	3499				

rpm (motion & stationary)	**% error in counts**
109 and stationary	0.056
136 and stationary	0.006
161 and stationary	0.046
188 and stationary	0.133
214 and stationary	0.022
238 and stationary	**0.176**

Table A.99 ANOVA analysis and percentage error in mean counts at L_{13} for Detector 3

SUMMARY

Groups	*Count*	*Sum*	*Average*	*Variance*
stationary	500	150851	301.702	283.2998
109 rpm	500	149992	299.984	267.4707
136 rpm	500	150399	300.798	258.5543
161 rpm	500	150412	300.824	277.6844
188 rpm	500	150429	300.858	268.078
214 rpm	500	150088	300.176	262.999
238 rpm	500	150364	300.728	272.4629

ANOVA

Source of Variation	*SS*	*df*	*MS*	*F*	*P-value*	*F crit*
Between Groups	918.9177	6	153.153	0.567068	0.756867	2.10118
Within Groups	943384	3493	270.0784			
Total	944302.9	3499				

rpm (motion & stationary)	**% error in counts**
109 and stationary	**0.569**
136 and stationary	0.299
161 and stationary	0.291
188 and stationary	0.279
214 and stationary	0.505
238 and stationary	0.322

Table A.100 ANOVA analysis and percentage error in mean counts at L_{13} for Detector 4

SUMMARY

Groups	*Count*	*Sum*	*Average*	*Variance*
stationary	500	88061	176.122	185.5141
109 rpm	500	88150	176.3	174.2064
136 rpm	500	88050	176.1	179.6413
161 rpm	500	87795	175.59	187.4087
188 rpm	500	88080	176.16	183.1968
214 rpm	500	88347	176.694	176.337
238 rpm	500	87553	175.106	191.4256

ANOVA

Source of Variation	*SS*	*df*	*MS*	*F*	*P-value*	*F crit*
Between Groups	794.3577	6	132.393	0.72531	0.629204	2.10118
Within Groups	637587.3	3493	182.5329			
Total	638381.6	3499				

rpm (motion & stationary)	**% error in counts**
109 and stationary	0.101
136 and stationary	0.012
161 and stationary	0.302
188 and stationary	0.021
214 and stationary	0.324
238 and stationary	**0.576**

Table A.101 ANOVA analysis and percentage error in mean counts at L_{13} for Detector 5

SUMMARY

Groups	*Count*	*Sum*	*Average*	*Variance*
stationary	500	43662	87.324	141.5902
109 rpm	500	43916	87.832	147.7994
136 rpm	500	43622	87.244	146.5576
161 rpm	500	43297	86.594	140.2897
188 rpm	500	43754	87.508	150.026
214 rpm	500	43754	87.508	144.6232
238 rpm	500	43498	86.996	149.7795

ANOVA

Source of Variation	*SS*	*df*	*MS*	*F*	*P-value*	*F crit*
Between Groups	481.4269	6	80.23781	0.550293	0.770088	2.10118
Within Groups	509312.1	3493	145.8094			
Total	509793.6	3499				

rpm (motion & stationary)	**% error in counts**
109 and stationary	0.581
136 and stationary	0.091
161 and stationary	**0.835**
188 and stationary	0.210
214 and stationary	0.210
238 and stationary	0.375

Table A.102 ANOVA analysis and percentage error in mean counts at L_{13} for Detector 6

SUMMARY

Groups	*Count*	*Sum*	*Average*	*Variance*
stationary	500	29725	59.45	87.1498
109 rpm	500	29808	59.616	84.26107
136 rpm	500	29579	59.158	77.99703
161 rpm	500	29808	59.616	80.91437
188 rpm	500	29706	59.412	83.36499
214 rpm	500	29659	59.318	86.68224
238 rpm	500	29784	59.568	85.17573

ANOVA

Source of Variation	*SS*	*df*	*MS*	*F*	*P-value*	*F crit*
Between Groups	86.57371	6	14.42895	0.172493	0.984235	2.10118
Within Groups	292187.1	3493	83.64932			
Total	292273.6	3499				

rpm (motion & stationary)	**% error in counts**
109 and stationary	0.279
136 and stationary	**0.491**
161 and stationary	0.279
188 and stationary	0.063
214 and stationary	0.222
238 and stationary	0.198

Table A.103 ANOVA analysis and percentage error in mean counts at L_{13} for Detector 7

SUMMARY

Groups	*Count*	*Sum*	*Average*	*Variance*
stationary	500	177286	354.572	411.1511
109 rpm	500	176721	353.442	388.692
136 rpm	500	176906	353.812	432.165
161 rpm	500	176812	353.624	424.2511
188 rpm	500	176596	353.192	416.5082
214 rpm	500	176785	353.57	404.4821
238 rpm	500	176614	353.228	423.972

ANOVA

Source of Variation	*SS*	*df*	*MS*	*F*	*P-value*	*F crit*
Between Groups	656.3937	6	109.399	0.263955	0.953701	2.10118
Within Groups	1447709	3493	414.4602			
Total	1448366	3499				

rpm (motion & stationary)	**% error in counts**
109 and stationary	0.318
136 and stationary	0.214
161 and stationary	0.267
188 and stationary	**0.389**
214 and stationary	0.282
238 and stationary	0.379

Table A.104 ANOVA analysis and percentage error in mean counts at L_{13} for Detector 8

SUMMARY

Groups	*Count*	*Sum*	*Average*	*Variance*
stationary	500	94185	188.37	168.0732
109 rpm	500	94378	188.756	170.3211
136 rpm	500	94433	188.866	167.2345
161 rpm	500	94483	188.966	174.8024
188 rpm	500	94178	188.356	185.7007
214 rpm	500	94214	188.428	168.2894
238 rpm	500	93972	187.944	161.2914

ANOVA

Source of Variation	*SS*	*df*	*MS*	*F*	*P-value*	*F crit*
Between Groups	381.8309	6	63.63848	0.372555	0.896775	2.10118
Within Groups	596660.7	3493	170.8161			
Total	597042.5	3499				

rpm (motion & stationary)	**% error in counts**
109 and stationary	0.204
136 and stationary	0.263
161 and stationary	**0.316**
188 and stationary	0.007
214 and stationary	0.0307
238 and stationary	0.226

Table A.105 ANOVA analysis and percentage error in mean counts at L_{14} for Detector 1

SUMMARY

Groups	*Count*	*Sum*	*Average*	*Variance*
stationary	500	65793	131.586	133.0527
109 rpm	500	65826	131.652	140.6282
136 rpm	500	65765	131.53	132.3939
161 rpm	500	65812	131.624	146.1589
188 rpm	500	65685	131.37	136.2696
214 rpm	500	65858	131.716	135.3861
238 rpm	500	65549	131.098	136.9784

ANOVA

Source of Variation	*SS*	*df*	*MS*	*F*	*P-value*	*F crit*
Between Groups	135.5554	6	22.59257	0.164589	0.986065	2.10118
Within Groups	479473	3493	137.2668			
Total	479608.6	3499				

rpm (motion & stationary)	**% error in counts**
109 and stationary	0.050
136 and stationary	0.042
161 and stationary	0.028
188 and stationary	0.164
214 and stationary	0.098
238 and stationary	**0.370**

Table A.106 ANOVA analysis and percentage error in mean counts at L_{14} for Detector 2

SUMMARY

Groups	*Count*	*Sum*	*Average*	*Variance*
stationary	500	133090	266.18	277.6389
109 rpm	500	134518	269.036	358.4716
136 rpm	500	133923	267.846	329.3931
161 rpm	500	133787	267.574	322.9865
188 rpm	500	133613	267.226	317.7544
214 rpm	500	134047	268.094	320.6144
238 rpm	500	133958	267.916	320.1052

ANOVA

Source of Variation	*SS*	*df*	*MS*	*F*	*P-value*	*F crit*
Between Groups	2279.472	6	379.912	1.183545	0.311868	2.10118
Within Groups	1121235	3493	320.9949			
Total	1123515	3499				

rpm (motion & stationary)	**% error in counts**
109 and stationary	**1.072**
136 and stationary	0.625
161 and stationary	0.523
188 and stationary	0.392
214 and stationary	0.719
238 and stationary	0.652

Table A.107 ANOVA analysis and percentage error in mean counts at L_{14} for Detector 3

SUMMARY

Groups	*Count*	*Sum*	*Average*	*Variance*
stationary	500	179523	359.046	340.0039
109 rpm	500	179703	359.406	332.9711
136 rpm	500	178920	357.84	320.7078
161 rpm	500	179199	358.398	319.1218
188 rpm	500	178966	357.932	339.5745
214 rpm	500	179138	358.276	340.4407
238 rpm	500	179680	359.36	363.317

ANOVA

Source of Variation	*SS*	*df*	*MS*	*F*	*P-value*	*F crit*
Between Groups	1297.638	6	216.273	0.642539	0.696249	2.10118
Within Groups	1175712	3493	336.591			
Total	1177010	3499				

rpm (motion & stationary)	**% error in counts**
109 and stationary	0.100
136 and stationary	**0.335**
161 and stationary	0.180
188 and stationary	0.310
214 and stationary	0.214
238 and stationary	0.087

Table A.108 ANOVA analysis and percentage error in mean counts at L_{14} for Detector 4

SUMMARY

Groups	*Count*	*Sum*	*Average*	*Variance*
stationary	500	102401	204.802	156.4637
109 rpm	500	102259	204.518	154.7432
136 rpm	500	102182	204.364	162.3161
161 rpm	500	102066	204.132	164.4354
188 rpm	500	102719	205.438	153.8499
214 rpm	500	102227	204.454	157.0941
238 rpm	500	102522	205.044	148.2906

ANOVA

Source of Variation	*SS*	*df*	*MS*	*F*	*P-value*	*F crit*
Between Groups	599.7074	6	99.95124	0.637681	0.700185	2.10118
Within Groups	547499.3	3493	156.7419			
Total	548099	3499				

rpm (motion & stationary)	**% error in counts**
109 and stationary	0.138
136 and stationary	0.213
161 and stationary	**0.327**
188 and stationary	0.310
214 and stationary	0.169
238 and stationary	0.118

Table A.109 ANOVA analysis and percentage error in mean counts at L_{14} for Detector 5

SUMMARY

Groups	*Count*	*Sum*	*Average*	*Variance*
stationary	500	231250	462.5	730.8998
109 rpm	500	231968	463.936	823.6352
136 rpm	500	231119	462.238	728.3501
161 rpm	500	232251	464.502	772.8357
188 rpm	500	230622	461.244	656.1848
214 rpm	500	231561	463.122	751.1414
238 rpm	500	232147	464.294	878.8653

ANOVA

Source of Variation	*SS*	*df*	*MS*	*F*	*P-value*	*F crit*
Between Groups	4317.879	6	719.6465	0.943019	0.462715	2.10118
Within Groups	2665614	3493	763.1303			
Total	2669932	3499				

rpm (motion & stationary)	**% error in counts**
109 and stationary	0.310
136 and stationary	0.056
161 and stationary	**0.432**
188 and stationary	0.271
214 and stationary	0.134
238 and stationary	0.387

Table A.110 ANOVA analysis and percentage error in mean counts at L_{14} for Detector 6

SUMMARY

Groups	*Count*	*Sum*	*Average*	*Variance*
stationary	500	118698	237.396	271.3298
109 rpm	500	118346	236.692	291.0913
136 rpm	500	118163	236.326	293.4867
161 rpm	500	118419	236.838	276.0839
188 rpm	500	118304	236.608	310.828
214 rpm	500	118096	236.192	305.1214
238 rpm	500	118329	236.658	318.991

ANOVA

Source of Variation	*SS*	*df*	*MS*	*F*	*P-value*	*F crit*
Between Groups	453.2674	6	75.54457	0.255844	0.957094	2.10118
Within Groups	1031399	3493	295.276			
Total	1031852	3499				

rpm (motion & stationary)	**% error in counts**
109 and stationary	0.296
136 and stationary	0.450
161 and stationary	0.235
188 and stationary	0.331
214 and stationary	**0.507**
238 and stationary	0.310

Table A.111 ANOVA analysis and percentage error in mean counts at L_{14} for Detector 7

SUMMARY

Groups	*Count*	*Sum*	*Average*	*Variance*
stationary	500	187291	374.582	329.6746
109 rpm	500	187018	374.036	329.7422
136 rpm	500	187019	374.038	342.7501
161 rpm	500	187251	374.502	300.5992
188 rpm	500	187014	374.028	351.2217
214 rpm	500	187796	375.592	314.4304
238 rpm	500	187710	375.42	324.5647

ANOVA

Source of Variation	*SS*	*df*	*MS*	*F*	*P-value*	*F crit*
Between Groups	1313.758	6	218.9596	0.668438	0.675239	2.10118
Within Groups	1144198	3493	327.569			
Total	1145512	3499				

rpm (motion & stationary)	**% error in counts**
109 and stationary	0.145
136 and stationary	0.145
161 and stationary	0.021
188 and stationary	0.147
214 and stationary	**0.269**
238 and stationary	0.223

Table A.112 ANOVA analysis and percentage error in mean counts at L_{14} for Detector 8

SUMMARY

Groups	*Count*	*Sum*	*Average*	*Variance*
stationary	500	90932	181.864	196.2019
109 rpm	500	90553	181.106	198.5038
136 rpm	500	90791	181.582	190.6967
161 rpm	500	90793	181.586	195.209
188 rpm	500	90413	180.826	190.4687
214 rpm	500	90620	181.24	193.798
238 rpm	500	90922	181.844	193.9155

ANOVA

Source of Variation	*SS*	*df*	*MS*	*F*	*P-value*	*F crit*
Between Groups	456.4389	6	76.07314	0.391901	0.884654	2.10118
Within Groups	678038	3493	194.1134			
Total	678494.4	3499				

rpm (motion & stationary)	**% error in counts**
109 and stationary	0.416
136 and stationary	0.155
161 and stationary	0.152
188 and stationary	**0.570**
214 and stationary	0.343
238 and stationary	0.010

List of Publications

International Journals

1. Harshal Patil, Ajey Kumar Patel, Harish J. Pant and A. Venu Vinod. "Numerical Modelling of Stirred Tank and its Validation by Radioactive Particle Tracking (RPT) Technique". ISH Journal of Hydraulic Engineering, DOI: 10.1080/09715010.2020.1797543.
2. Harshal Patil, Ajey Kumar Patel, Harish J. Pant and A. Venu Vinod. "CFD Simulation Model for Mixing Tank Using Multiple Reference Frame Impeller Rotation". ISH Journal of Hydraulic Engineering: 2018, 1-10, DOI:10.1080/09715010.2018.1535921.

Conference Proceedings

1. Harshal Patil, Ajey Kumar Patel, K. Devarajan and A. Venu Vinod, "Comparison of Different off Bottom Impeller Clearances to Investigate the Effect on Hydrodynamics in Rushton Turbine Stirred Tank", *International Conference on New Frontiers in Chemical, Energy and Environmental Engineering, INCEEE-2019,* 15-16 February 2019, NIT Warangal.
2. Harshal Patil, Ajey Kumar Patel, Harish J. Pant and A. Venu Vinod, "Effect of Fluid Motion on Radiation Intensity in RPT Technique during Calibration: A Case of Stirred Tank", *NAARRI International Conference on Advanced Applications of Radiation Technology, NICSTAR-2018,* 5-7 March 2018, Mumbai.
3. Harshal Patil, Ajey Kumar Patel, Harish J. Pant and A. Venu Vinod, "CFD Simulation Model for Mixing Tank using Multiple Reference Frame Impeller Rotation", *22nd International Conference on Hydraulics, Water Resources and Coastal Engineering, HYDRO-2017,* 21- 23 December 2017, Ahmedabad.
4. G. Singh, A. K. Patel, H. S. Patil, A. Venu Vinod and H. J. Pant, "Comparison of Different Turbulent Models to Simulate Flows in Fully Baffled Stirred Tank", *68th Annual Session of the Indian Institute of Chemical Engineers, CHEMCON-2015,* 27-30 December 2015, Indian Institute of Technology, Guwahati.

Curriculum Vitae

Name: Patil Harshal Somnath

Gender: Male

Nationality: Indian

Academic Profile:

M.Tech: Chemical Engineering from Vishwakarma Institute of Technology, Pune University, Pune, Maharashtra, India, (2013).

B.E: Chemical Engineering from Pravara Rural Engineering College, Loni, Pune University, Pune, Maharashtra, India, (2011).